

**Structural insights into redox enzymes of anaerobic aromatic
degradation and flavin-based electron bifurcation**

Dissertation

zur Erlangung des Doktorgrades
der Naturwissenschaften

vorgelegt beim Fachbereich 15

Biowissenschaften

der Johann Wolfgang Goethe-Universität

in Frankfurt am Main

von

Kanwal Kayastha

aus Varanasi, India

Frankfurt am Main (2021)

(D30)

vom Fachbereich 15 – Biowissenschaften der
Johann Wolfgang Goethe-Universität als Dissertation angenommen.

Dekan: Prof. Dr. Sven Klimpel

1. Gutachter: Prof. Dr. Volker Müller

Institut für Molekulare Biowissenschaften, Johann Wolfgang Goethe-Universität

2. Gutachter: PD Dr. Ulrich Ermler

Molekulare Membranbiologie, Max-Planck-Institut für Biophysik

Datum der Disputation:

Diese Doktorarbeit wurde vom Juli 2016 bis zum Juni 2021 unter Leitung von PD Dr. Ulrich Ermler in der Abteilung für Molekulare Membranbiologie (Direktor: Prof. Dr. Dr. hc Hartmut Michel) am Max-Planck-Institut für Biophysik in Frankfurt am Main durchgeführt.

Eidesstattliche Erklärung

Hiermit versichere ich, dass ich die vorliegende Arbeit selbständig angefertigt habe und keine weiteren Hilfsmittel und Quellen als die hier aufgeführten verwendet habe.



(Kanwal Kayastha)

Frankfurt am Main, den

Publications:

Ernst C[#], **Kayastha K[#]**, Koch T, Venceslau SS, Pereira IAC, Demmer U, Ermler U, Dahl C. Structural and spectroscopic characterization of a HdrA-like subunit from *Hyphomicrobium denitrificans*. FEBS J. 2021 Mar;288(5):1664-1678.

Willistein M, Bechtel DF, Müller CS, Demmer U, Heimann L, **Kayastha K**, Schünemann V, Pierik AJ, Ullmann GM, Ermler U, Boll M. Low potential enzymatic hydride transfer via highly cooperative and inversely functionalized flavin cofactors. Nat Commun. 2019 May 6;10(1):2074.

Demmer JK, Bertsch J, Öppinger C, Wohlers H, **Kayastha K**, Demmer U, Ermler U, Müller V. Molecular basis of the flavin-based electron-bifurcating caffeyl-CoA reductase reaction. FEBS Lett. 2018 Feb;592(3):332-342.

Manuscripts in preparation:

Kayastha K[#], Geiger RA[#], Ermler U, Boll M. Structural insights into enzymatic decarboxylation by phthaloyl-CoA decarboxylase (Pcd) complex.

Kayastha K[#], Katsyv A[#], Himmrichs C, Ermler U, Müller V. Electron Microscopy structure of the flavin-based electron-confurcating Ldh/EtfAB complex from *Acetobacterium woodii*.

Review article:

Kayastha K, Vitt S, Buckel W, Ermler U. Flavins in the electron bifurcation process. Arch Biochem Biophys. 2021 Apr 15;701:108796.

Research report:

Kayastha K, Demmer JK., Müller V, Buckel W, Ermler U. Acyl-CoA dehydrogenase/electron-transferring flavoprotein complexes: Structural determinants of a flavin-based electron bifurcation (2018)

https://www.biophys.mpg.de/2384291/research_report_12587617?c=2320827

[#] refers to co-first authored manuscripts.

Table of contents

I. Summary	i
II. Zusammenfassung	v
III. List of figures	ix
IV. List of tables	xi
V. Abbreviation	xii
VI. Introduction	
A. Overall energy metabolism	-1-
B. Energy metabolism in the absence of O ₂	-2-
C. Flavin-based electron bifurcation (FBEB)	-4-
D. Anaerobic degradation of aromatic compounds	-6-
VII. Materials and Methods	
A. Chemicals	-8-
B. Prokaryotic cell strains and plasmids	-9-
C. PCR	-10-
D. Transformation of <i>E. coli</i> cells	-11-
E. Isolation of plasmid DNA from <i>E. coli</i>	-11-
F. Determination of DNA concentration	-12-
G. DNA sequencing	-12-
H. In-fusion HD cloning	-12-
I. Site-directed mutagenesis	-14-
J. Agarose gel electrophoresis	-14-
K. Anaerobic heterologous gene expression in <i>E. coli</i>	-15-
L. Anaerobic protein purification	
a) Strep-tag Affinity chromatography	-16-

b) Size exclusion chromatography	-17-
M. Protein concentration measurement	-19-
N. Denaturing polyacrylamide gel electrophoresis	-19-
O. Non-denaturing polyacrylamide gel electrophoresis	-20-
P. Immunoblotting (Western Blot)	-21-
Q. Chemical cross-linking	-22-
R. Crystallization	-24-
S. Single-particle EM	
a) Single-particle negative-staining EM	-25-
b) Single-particle cryo-EM	-27-
T. Data collection and structure refinement	
a) Crystallography	-29-
b) Single-particle cryo-EM	-30-
• Chapter A. Pcd	
1. Introduction	-33-
2. Materials and methods	-35-
3. Results	-39-
4. Discussion	-50-
• Chapter B. Ldh/EtfAB	
1. Introduction	-55-
2. Materials and methods	-57-
3. Results	-60-
4. Discussion	-69-
• Chapter C. sHdrA	
1. Introduction	-72-
2. Materials and methods	-73-
3. Results	-74-

4. Discussion	-80-
VIII. Future prospects	-86-
IX. References	-87-
X. Appendices	
A. PrDOS result of Pcd complex	-101-
B. Multiple sequence alignment of Pcd complex	-102-
C. Multiple sequence alignment of Ldh/EtfAB complex	-103-
D. Manuscript of the review article	-105-
E. Manuscript of Naphthoyl-CoA reductase (NCR)	-116-
F. Manuscript of Caffeyl-CoA reductase (CarCDE)	-126-
XI. Acknowledgments	-137-
XII. Curriculum vitae	-139-

I. Summary

The main aim of this thesis work was to elucidate the catalytic mechanism of several enzyme complexes on the basis of their three-dimensional structure. All investigated enzyme complexes occur in the anaerobic energy metabolism and have an essential function by the challenging degradation of aromatic compounds and the flavin-based electron bifurcation (FBEB)/confurcation, an energy-coupling mechanism. More specifically, I studied the phthaloyl-CoA decarboxylase of *Thauera chlorobenzoica* (Pcd) involved in phthalate ester decomposition, the FBEB protein complexes lactate dehydrogenase/electron-transfer flavoprotein (Ldh/EtfAB) of *Acetobacterium woodii*, the heterodisulfide-related subunit HdrA of the sulfur-oxidizing bacteria *Hyphomicrobium denitrificans* (sHdrA). In addition, I contributed to the structure determination of the caffeyl-CoA reductase- EtfAB complex of *A. woodii* and the naphthoyl-CoA reductase of the sulfate-respiring enrichment culture N47 (mentioned in the Appendix E and F).

The mentioned protein complexes were structurally analyzed either by classical X-ray crystallography or single-particle electron cryo-microscopy. Classical X-ray crystallography has been proven to be very useful and successful for proteins or protein complexes which are characterized by a moderate biological flexibility, a high availability, a low heterogeneity and a limited size. For this reason, X-ray crystallography was successful in our case for sHdrA with a molecular mass of ca. 79 kDa. For the protein complexes beyond a molecular mass of 100 kDa, as Ldh/EtfAB (250 kDa) and Pcd (360 kDa) we therefore applied single-particle electron cryo-microscopy for successful structure determination.

I. Summary

Pcd hosting a prenylated FMN (pr-FMN) catalyzes the anaerobic, light-sensitive decarboxylation of phthaloyl-CoA to benzoyl-CoA, which gets further degraded into acetyl-CoA. The cryo-EM structure of active holo-Pcd complex was determined up to 2.43 Å in the empty state, to 2.0 Å in complex with the substrate analog 2-CN-benzoyl-CoA and to 2.3 Å in complex with the product benzoyl-CoA. The densities indicated the binding mode and conformations of pr-FMN and the CoA compounds and the conversion from a preformed into an active conformation basically realized by rigidification of an expanded loop segment. The active site geometry of the facing pr-FMN and substrate analog/benzyl rings argues for a 1,3-dipolar addition for the decarboxylation reaction implicating two unusual dearomatisation steps. An alternative scenario that avoids the second dearomatisation step was suggested.

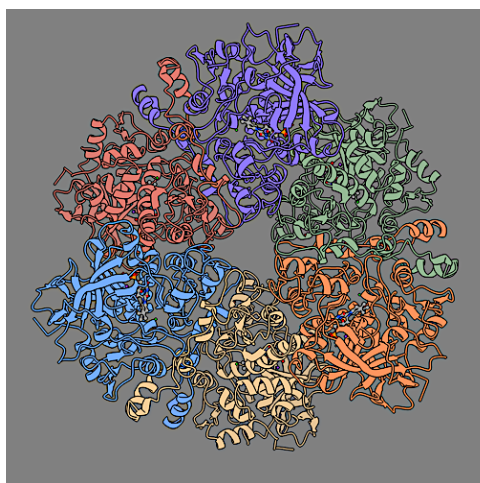


Fig. S-I. PDB model of the active-holo Pcd complex. 6 monomers are colored in different colors containing prFMN, Fe molecule, K^+ ion in each monomer.

The Ldh/EtfAB complex catalyzes the oxidation of lactate into pyruvate with NAD^+ as electron acceptor driven by the oxidation of energy-rich reduced ferredoxin within a flavin-based electron confurcation framework. The cryo-EM structure of the Ldh/EtfAB complex was determined at 2.43 Å resolution revealing a heterohexameric complex subdivided into a central Ldh dimer with two EtfAB

modules attached to its periphery. Each of the subunits contains one FAD and EtfA, in addition, one [4Fe-4S] cluster. The structure is present in the D (dehydrogenase)-state in which the a-FAD of EtfA and l-FAD of Ldh are in an electron-conducting distance. Two aspartate residues contact both isoalloxazine rings and may thus adjust their redox potentials to that of the substrate. Adjacent to N5 of l-FAD a putative density was found for lactate that was connected to metal binding site via a H₂O molecule.

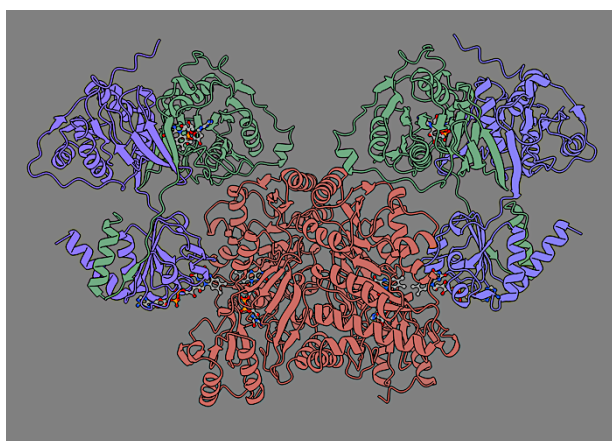


Fig. S-II. PDB model of Ldh/EtfAB complex. Each subunit contains one FAD co-factor, Ldh subunits contain one Fe molecule each.

sHdrA constitutes the core of the sHdr(AA'B1B2C1C2) complex, which is predicted to catalyze the oxidation of protein-bound sulfane sulfur to sulfite. It was assumed that this enzyme complex performs a bifurcating reaction as the structurally highly related methanogenic Hdr(ABC)₂ complex. The X-ray structure of sHdrA was determined at 1.4 Å resolution, as a homodimer containing two [4Fe-4S] clusters and two FAD molecules. Detailed structural data of the isoalloxazine environment and UV/Vis spectral data indicating a stable flavo-semiquinone excluded a FBEB reaction for the sHdr(AA'B1B2C1C2) complex. On this basis an alternative

I. Summary

mechanism was postulated by which one sHdrBC lobe produces sulfite and the other takes over the four electrons and reduces NAD^+ via a lipoamide thiol/disulfide converter. HdrA is only used as single electron transfer module and FAD might serve as electron-storage device.

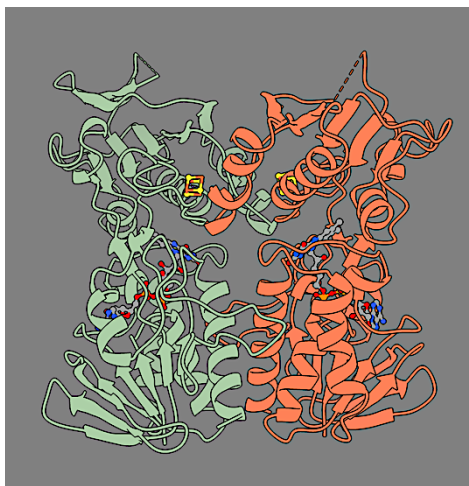


Fig. S-III. PDB model of sHdrA. Each monomer contains 1 FAD co-factor and 1 [4Fe-4S] cluster.

II. Zusammenfassung

Das Hauptziel dieser Arbeit war die Aufklärung der Katalysemechanismen von mehreren Enzymkomplexen auf Grundlage ihrer dreidimensionalen Struktur. Alle untersuchten Enzymkomplexe sind Teil des anaeroben Energiemetabolismus und haben eine essentielle Funktion entweder beim Abbau von aromatischen Verbindungen oder bei der Flavin-basierten Elektronenbifurkation (FBEB)/konfurkation, einem Energiekopplungsvorgang. Im Einzelnen habe ich die Phthaloyl-CoA-Decarboxylase aus *Thauera chlorobenzoica* (Pcd), ein Schlüsselenzym des anaeroben Phthalsäureesterabbaus, den FBEB Komplex Laktatdehydrogenase-Elektrontransfer-Flavoprotein (Ldh/EtfAB) aus *Acetobacterium woodii* (Ldh/EtfAB) und die Heterodisulfidreduktase ähnliche Untereinheit HdrA aus dem schwefeloxidierenden Bakterium *Hyphomicrobium denitrificans* (sHdrA) untersucht. Zusätzlich habe ich zur Strukturbestimmung des Caffeyl-CoA/EtfAB - Komplexes aus *A. woodii* und der Naphthoyl-CoA - Reduktase aus der Kultur N47 beigetragen (im Appendix erwähnt).

Die genannten Proteinkomplexe wurden entweder mittels Röntgenkristallographie oder Einzelteilchen-Elektronenkryomikroskopie strukturell charakterisiert. Die klassische Röntgenkristallographie ist sehr nützlich und erfolgreich für Proteine oder Proteinkomplexe, die eine geringere biologische Flexibilität, eine hohe Verfügbarkeit, eine geringe Heterogenität und nur eine begrenzte Größe aufweisen. Aus diesem Grund wurde die Röntgenkristallographie für sHdrA mit einer Molekülmasse von ca. 79 kDa zur erfolgreichen Strukturbestimmung ausgewählt. Für die Proteinkomplexe mit mehr als 100 kDa

II. Zusammenfassung

Molekülmasse wie Ldh/EtfAB (250 kDa) und Pcd (360 kDa) verwendeten wir dagegen die Einzelteilchen-Elektronenkryomikroskopie.

Die prenyliertes FMN (pr-FMN) haltige Pcd katalysiert die anaerobe, lichtempfindliche Dekarboxylierung von Phthaloyl-CoA zu Benzoyl-CoA, das schließlich zu Acetyl-CoA abgebaut wird. Die Cryo-EM-Struktur des aktiven hexameren holo-Pcd-Komplexes wurde bis zu 2,43 Å Auflösung im leeren Zustand, bis 2,0 Å im Komplex mit dem Substratanalogen 2-CN-Benzoyl-CoA und bis 2,3 Å im Komplex mit dem Produkt Benzoyl-CoA gelöst. Die Dichtekarte zeigte die Art der Bindung von pr-FMN und der CoA-Verbindung sowie die Umwandlung des katalytischen Zentrums von einer vorgeformten in eine aktive Konformation. Dies wird primär durch einen, CoA-Bindung induzierten, Einfriervorgang eines Schleifensegments erreicht. Die Geometrie der sich gegenüberstehenden pr-FMN und Substrataromaten – Ringe deuten auf eine 1,3-dipolare Cycloaddition hin, die zwei schwierige Dearomatisierungsschritte verlangt.

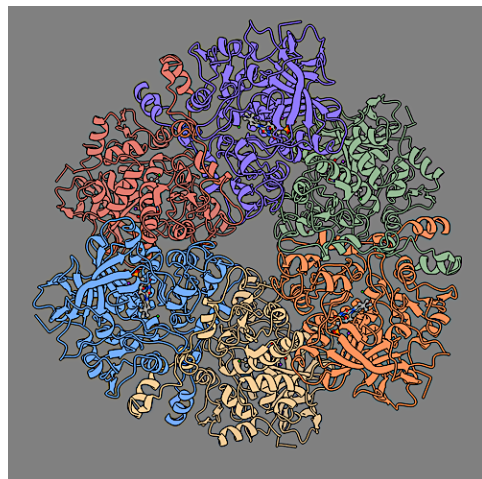


Abb. Z-I. PDB-Modell des Pcd-Komplexes

Der Ldh/EtfAB-Komplex katalysiert die Oxidation von Laktat zu Pyruvat mit NAD^+ als Elektronenakzeptor. Diese endergone Reaktion wird durch die parallele

Oxidation von reduziertem Ferredoxin innerhalb einer Flavin-basierten Elektronenkofaktation angetrieben. Die Kryo-EM-Struktur des Ldh/EtfAB-Komplexes wurde bei 2,43 Å Auflösung gelöst. Der heterohexamere Komplex ist in einem zentralen Ldh-Dimer mit zwei peripher assoziierten EtfAB Einheiten unterteilt. Die Struktur liegt im D (Dehydrogenase)- Zustand vor, bei dem zwischen a-FAD und l-FAD ein schneller Elektronentransfer stattfinden kann. Zwei Aspartate kontaktieren die beide Isoalloxazinringe und könnten so ihr Redoxpotential an dasjenige des Substrats annähern. Eine mögliche, der Form von Laktat entsprechende Dichte wurde benachbart zum Flavin N5 identifiziert. Interessanterweise wäre dieses Laktat über ein Wassermolekül mit einem Metallion verbunden.

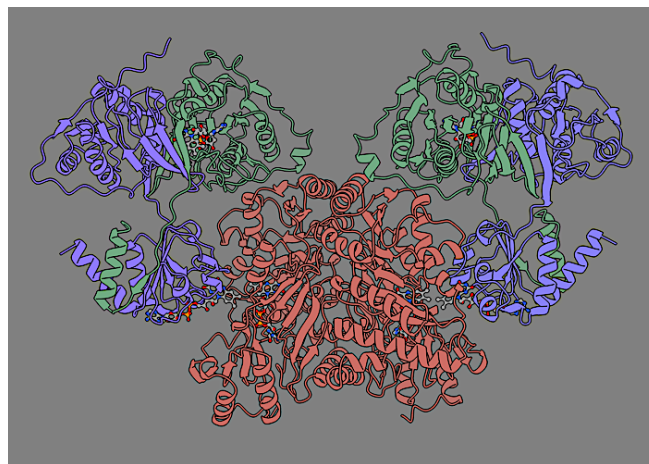


Abb. Z-II. PDB-Modell des Ldh/EtfAB-Komplexes

SHdrA stellt die Kernuntereinheit des sHdr(AA'B1B2C1C2)-Komplexes dar, welcher die Oxidation eines proteingebundenen Sulfanschwefels zu Sulfit katalysieren könnte. Dieser Enzymkomplex wurde in Analogie zu dem strukturell sehr verwandten methanogenen Enzym als bifurkierend angenommen. Die Röntgenstruktur von sHdrA wurde bei 1,4 Å Auflösung gelöst. Der Homodimer enthält zwei [4Fe-4S]-Cluster und zwei FAD-Moleküle. Die Proteinumgebung des

II. Zusammenfassung

Isoallozinrings und UV/vis spektroskopische Daten belegten eindeutig ein stabiles Flavosemiquinon, was im Widerspruch zur Vorstellung von den Eigenschaften eines bifurkierenden Flavins steht. Angesichts dieses überraschenden Befundes wurde ein neuer Mechanismus vorgeschlagen, bei dem der sHdrB1C1-Zweig Sulfit produziert und der sHdrB2C2-Zweig vier einzelne Elektronen übernimmt sowie NAD^+ mit Hilfe eines Liponamidthiol/disulfid-Konverters zu NADH reduziert. SHdrA wäre somit ein Elektronentransfermodul und FAD ein Elektronenspeichereinheit.

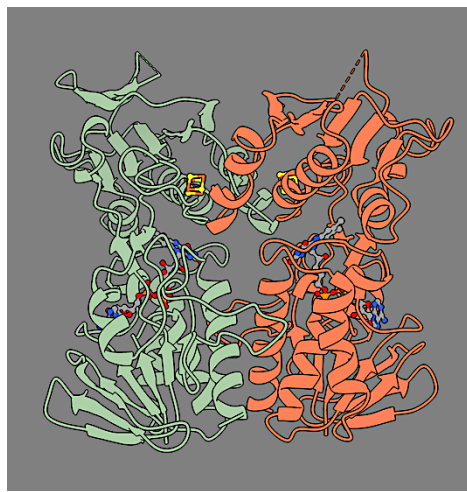


Abb. Z-III. PDB-Modell von sHdrA.

III. List of Figures

- Fig. S-I. PDB model of Pcd complex
- Fig. S-II. PDB model of Ldh/EtfAB complex
- Fig. S-III. PDB model of sHdrA complex
- Abb. Z-I. PDB-Modell der Pcd-Komplex
- Abb. Z-II. PDB-Modell des Ldh/EtfAB-Komplex
- Abb. Z-III. PDB-Modell des sHdrA
- Fig. 1. Ethanol-acetate formation of *Clostridium kluyveri*
- Fig. 2. Energetic scheme of FBEB
- Fig. 3. Degradation of aromates in O₂-free habitats
- Fig. 4. In-fusion HD cloning protocol overview
- Fig. 5. SDS-PAGE gels showing effects of different chemical cross-linkers on the Ldh-EtfAB complex.
- Fig. 6. (A) Crystallization plates; (B) Crystallization methods; (C) OryxNano crystallization robot
- Fig. 7. Flow-diagram of Negative-staining grid preparation process
- Fig. 8. Single-particle Negative-staining diagrammatic steps
- Fig. 9. Flow-diagram showing cryo-EM sample preparation steps
- Fig. 10. General workflow for cryo-EM grid preparation
- Fig. 11. Anaerobic degradation of phthalic acid
- Fig. 12. Micrograph from active holo-Pcd complex negative-staining
- Fig. 13. Single-particle cryo-EM data analysis of active holo-Pcd complex
- Fig. 14. Single-particle cryo-EM data analysis of Pcd-2CN-benzoyl-CoA complex
- Fig. 15. Single-particle cryo-EM data analysis of Pcd-benzoyl-CoA complex
- Fig. 16. Cryo-EM map showing overall shape and subunit arrangement of Pcd complex
- Fig. 17. Fold of a Pcd complex subunit
- Fig. 18. prFMN binding mode
- Fig. 19. Binding mode of the inhibitor 2-CN-benzoyl-CoA

III. List of figures

- Fig. 20. The active site geometry of the isoalloxazine and CN-benzoyl-CoA rings
- Fig. 21. Catalytic cycle of the phthaloyl-CoA decarboxylation
- Fig. 22. Lactate fermentation pathway involving Ldh/EtfAB complex in *Acetobacterium woodii*
- Fig. 23. Single-particle negative staining, cryo-EM micrographs, selected 2D classes of Ldh/EtfAB complex
- Fig. 24. Single-particle cryo-EM data analysis of Ldh/EtfAB complex
- Fig. 25. Single-particle cryo-EM map showing overall Ldh/EtfAB complex structure
- Fig. 26. Structure of Ldh subunit
- Fig. 27. Structural states of Ldh/EtfAB complex
- Fig. 28. Ldh-EtfAB interfaces
- Fig. 29. Mechanism of (Ldh/EtfAB)₂ reaction
- Fig. 30. Structure of the HdrA dimer of *Hyphomicrobium denitrificans*
- Fig. 31. Structure of the FAD binding site in sHdrA
- Fig. 32. Structure of the [4Fe-4S] cluster binding mode of sHdrA
- Fig. 33. Postulated model of the sHdr complex
- Fig. 34. Reaction scheme of the sHdr complex
- Fig. 35. PrDOS result for Pcd complex

IV. List of Tables

- Table 1. Chemical names, formulae, mass and manufacturers
- Table 2. Bacterial cell strains and plasmids for cloning with usage
- Table 3. PCR reagents
- Table 4. PCR protocol
- Table 5. Site-directed mutagenesis PCR reaction
- Table 6. Buffers for Strep-tag affinity purification
- Table 7. Buffers for Size exclusion chromatography
- Table 8. SDS-PAGE buffers
- Table 9. Buffers for Western blotting
- Table 10. Cross-linkers, their lengths, concentration ranges used in the experiment
- Table 11. Software and servers for data processing, refinement, and visualization
- Table 12. Software, tools, services used for cryo-EM data collection and image processing
- Table 13. Cryo-EM data collection analysis, refinement statistics of active holo-Pcd, Pcd-2-CN-benzoyl-CoA and Pcd-benzoyl-CoA
- Table 14. Cryo-EM data collection analysis, refinement statistics of Ldh/EtfAB complex
- Table 15. sHdrA crystallization, data collection and refinement statistics details

V. Abbreviations

2-CNB	2-cyano-benzoyl-CoA
A	absorbance
AP	alkaline phosphatase
ATP	adenosine triphosphate
Bcd/EtfAB	butyryl-CoA dehydrogenase/ electron transferring flavoproteinAB
BCIP	5-Bromo-4-chloro-3-indolyl phosphate disodium salt
BSA	bovine serum albumin
CN-PAGE	clear native-polyacrylamide gel electrophoresis
CoA	coenzyme A
cryo-EM	electron cryo-microscopy
CV	column volume
Cymal-6	6-Cyclohexyl-1-Hexyl- β -D-Maltoside
ddH ₂ O	double distilled water
DMSO	dimethyl sulfoxide
DNA	deoxyribonucleic acid
DNase	deoxyribonuclease
dNTPs	deoxyribose nucleotide triphosphate
DTE	dithioerythritol
DTT	dithiothreitol
EDTA	ethylenediaminetetraacetic acid
EtBr	ethidium bromide
FAD	flavin adenine dinucleotide
g	gravitational acceleration (9.80665 m/s ²)
HF	high fidelity
IPTG	isopropyl β - d-1-thiogalactopyranoside
kb	kilobase
kDa	kiloDalton (1000 Dalton)
LB	lysogeny broth
Ldh/EtfAB	lactate dehydrogenase/ electron transferring flavoprotein AB

MES	2-morpholin-4-ylethanesulfonic acid
MOPS	3-Morpholinopropane-1-sulfonic acid
MWCO	molecular weight cutoff
NAD	nicotinamide adenine dinucleotide
OD	optical density
Pcd	phthalate-CoA decarboxylase
PCR	polymerase chain reaction
prFMN	prenylated flavin adenine mononucleotide
PVDF	polyvinylidene difluoride
rmsd	root mean square deviation
rpm	revolutions per minute
SAD	single wavelength anomalous dispersion
SDS	sodium dodecyl sulfate
SDS-PAGE	sodium dodecyl sulfate-polyacrylamide gel electrophoresis
SDT	sodium dithionite
SOC	superoptimal broth with catabolite repression
TAE	tris-base, acetic acid, EDTA
TBST	tris buffered saline with tween
U	enzyme unit
UV	ultraviolet
V	volts
v/v	volume/volume
w/v	weight/volume

VI. Introduction

A. Overall energy metabolism

The cycle of matter on earth is predominantly conducted by microorganisms. In principle, biomass is synthesized by photosynthetic organisms, green plants, and cyanobacteria, from simple inorganic molecules like CO_2 , CH_4 , H_2O , NH_4^+ , and SH^- powered by the light energy of the sun. The produced energy-rich organic compounds are degraded back to the starting compounds by all other organisms for extracting energy¹.

The universal energy carrier and energy currency of the cell is ATP, which stores the energy in an energy-rich phosphoanhydride, P-O-P bond². While photosynthetic organisms produce ATP by light energy-driven proton gradient formation via the reaction center and ATP synthase, chemotrophic organisms oxidize organic compounds in aerobic habitats finally to CO_2 and in anaerobic habitats to CO_2 and CH_4 . Chemotrophic organisms use both ion gradient phosphorylation and substrate-level phosphorylation for ATP synthesis albeit in different proportions. In substrate-level phosphorylation, a phosphate group of a phosphorylated metabolite is transferred onto ADP. In ion gradient phosphorylation the free energy of an exergonic chemical (mostly redox) reaction is coupled with an uphill ion transport across the cell membrane³. Subsequently, the chemiosmotic energy is converted into ATP. Ion gradient phosphorylation has the advantage that reactions with a moderate driving force can contribute to energy conservation⁴. Each living cell contains the enzymatic capability to use the energy stored in ATP for growth, basal metabolism, reproduction, and motility.

In contrast to higher organisms, microorganisms occupy all possible niches on earth and developed during evolution an enormous capability to flexibly adapt to extreme and variable environmental conditions and to mineralize all chemicals synthesized by nature. Degradation proceeds by a fascinating mix of pathways shared by many organisms but also by specialized metabolic routes only developed by a few species.

B. Energy metabolism in the absence of O₂

Ecosystems like rice fields, freshwater sediments, tundra areas, swamps, oceanic areas near hydrothermal vents, and intestinal tracts of ruminants and termites as well as rice fields, biogas plants and sewage digesters operated by man are free of oxygen as this rather nonpolar gas is insoluble in larger amounts and quickly eliminated by O₂ consuming microorganisms. In the absence of O₂ and a few other suitable electron acceptors, like nitrate and sulfate, required for ion gradient phosphorylation, a process termed fermentation occurs, which preferentially applies substrate-level phosphorylation for ATP synthesis⁵. Only some organisms developed a specialized pathway to use an exergonic reaction for ion-gradient formation (Fig. 1)

In fermentation, balanced oxidation and reduction reactions are accomplished by oxidation of one and the reduction of another organic substrate or an internal metabolite derived during oxidation. Without a powerful electron acceptor, a complete degradation to CO₂ is not feasible and only a fraction of the energy stored in the substrate can be conserved. In addition, only a few reactions in the oxidation but not in the reduction branch of fermentation are sufficiently exergonic to use energy by substrate-level phosphorylation such that normally only 2 or less ATP per

substrate molecule are formed (for example see ethanol-acetate fermentation in Fig. 1). Recently, an energy coupling mechanism termed flavin-based electron bifurcation (FBEB) was discovered (next chapter) that can indirectly use exergonic reduction reactions for energy conservation⁶ by driving the endergonic reduction of ferredoxin. The obtained energy-rich compound ferredoxin can be applied for powering thermodynamically unfavorable reduction reactions or for building up a transmembrane ion gradient by exergonically reduce H^+ or NAD^+ via the multisubunit membrane complexes Ech and Rnf, respectively^{7,8} (Fig. 1). FBEB significantly increases the energy yield of anaerobic microorganisms operating at the energetic limit of life and provides the thermodynamic basis to metabolize substrates with lower energy yields⁹. It is worth mentioning that FBEB is only effective in anaerobic ecosystems as O_2 competes with ferredoxin for energy-rich electrons.

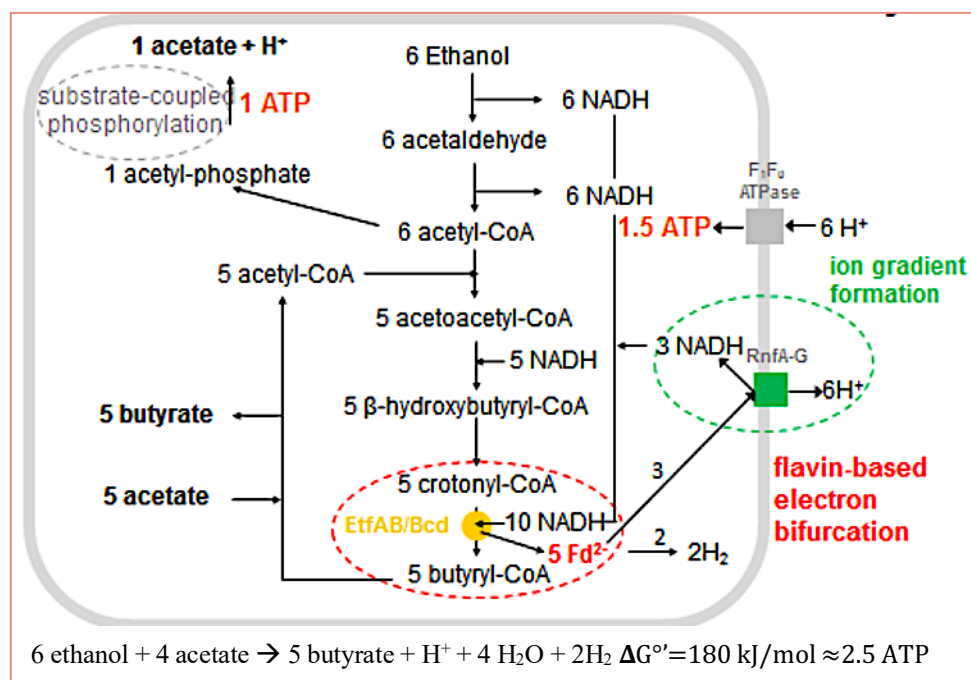


Fig. 1. Ethanol-acetate formation of *Clostridium kluyveri*. The overall degradation process proceeds via the equation: 6 ethanol + 4 acetate to 5 butyrate + H^+ + 4 H_2O + 2 H_2 . This pathway exemplarily illustrates the cooperation of substrate-coupled phosphorylation, FBEB and ion-gradient formation-driven ATP synthesis to form ca. 2.5 ATP⁶.

O₂ is not only essential as an optimal final electron acceptor for the oxidation of organic matter to CO₂ but also as reactive Fe^{2+/3+} - or flavin-activated species in challenging oxidation reactions, for example, to oxidatively attack inert compounds like mono- and multi-cyclic aromates, (see below), long aliphatic hydrocarbons and lignin. Anaerobic microorganism cannot utilize O₂ and developed alternative catalytic capabilities to reductively crack substances difficult to attack¹⁰.

C. Flavin-Based Electron Bifurcation (FBEB)

Anaerobic microorganisms operate at the thermodynamic limit of life, mainly due to the inability to use O₂ as the final electron acceptor in oxidative respiration. To maximize the energy yield, the cells developed in primordial times an energy coupling mechanism termed FBEB by which an exergonic oxidation drives an endergonic reduction both using the same electron donor endowed with a medium redox potential^{6,11,12}. While the high-potential electron acceptors and electron donors are variable, the low-potential electron acceptor is normally a ferredoxin (or a ferredoxin-like domain of a larger oxidoreductase) or e.g., under Fe-depleted conditions a flavodoxin¹³. The energy-splitting and coupling agent is a flavin termed electron-bifurcating flavin (Fig. 2). Upon reduction to FADH⁻ the two electrons endowed with different one-electron redox potentials flow into different directions and are thus available for two distinct energetically dissimilar pathways. Conceptionally, the one-electron redox-potentials are adjusted such that the first electron transfer to the high-potential acceptor is endergonic and the second to ferredoxin exergonic¹⁴. Accordingly, the first electron transfer is slow but when it occurs the extremely fast second electron transfer abstracts the remaining electron of

FAD^{•-} before the thermodynamically favorable back reaction of the first electron to the high potential acceptor takes place¹⁵. This mechanism also suppresses deleterious side reactions from energized FAD^{•-}. In addition, the back reaction of the ferredoxin reduction is prevented by its endergonicity such the directionality of both electron transfer steps is ensured and a short circuit, the 2 x 1e transfer to the high-potential electron acceptor is minimized. The strict directionality and cooperativity of the two-electron transfer events within the FBEB device still allow reversibility of the total FBEB process^{9,13,16–19}.

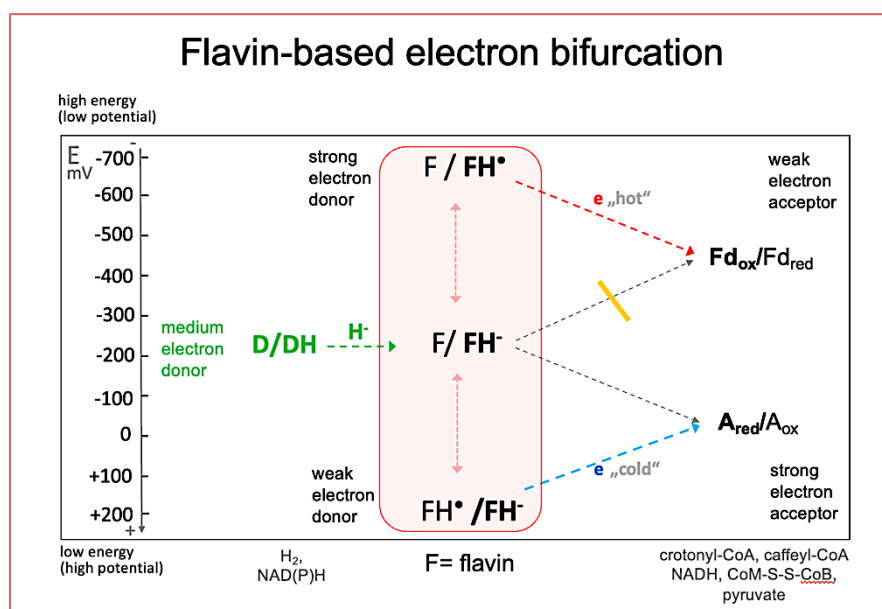


Fig. 2. Energetic scheme of FBEB. FBEB is based on the property of flavins to accomplish a coupled two-electron acceptance e.g., in form of H⁻ from a hydride donor DH (e.g., NADH) and two single electron transfers of different energy levels. So, a weak and strong electron acceptor can be delivered.

D. Anaerobic degradation of aromatic compounds

Aromatic compounds are ubiquitous in nature found as phenylalanine, tyrosine, and tryptophan in proteins of all organisms and as secondary products of plants and as lignin of trees^{20,21} in huge amounts. A significant amount of aromates accumulated on earth originates from fossil fuels such as petroleum products like benzene, toluene, ethylbenzene, and xylene (BTEX group) and polycyclic aromatic compounds due to their incomplete combustion or accidental discharge into aquatic and terrestrial environments during the transport, use, and disposal. These aromatic pollutants are harmful for both environment and human health. An additional severe problem is their stability and inertness which makes their degradation to a great chemical challenge and has to be accomplished differently in O₂-containing and O₂-free habitats. In aerobic microorganisms the aromatic ring is hydroxylated by monooxygenases and in this activated form oxidatively dearomatized and cleaved by dioxygenases; both oxidases use the energy-rich electron acceptor O₂ as co-substrate²² activated by one or two irons. Aromatic compounds also occur in anaerobic environments and, in particular, bacteria (but also fungi) developed alternative solutions for reductive degradation in the absence of O₂. In most cases, different aromatic compounds are degraded by channeling them to the central metabolite benzoyl-CoA (Fig. 3) and from there via dienoyl-CoA finally to three acetyl-CoA and one CO₂ by the modified β -oxidation pathway²⁰. Two strategies were developed to metabolize benzoyl-CoA: Facultative anaerobic microorganism use ATP and obligate anaerobic microorganism²³⁻²⁵, probably the energy-coupling FBEB mechanism²⁶ for providing the energy for attacking the inert and electron-rich ring. The two reactions are catalyzed by class I and II benzoyl-CoA reductases which

crack the aromatic ring by a Birch-like scenario where $2e$ and $2H^+$ are subsequently donated to the aromatic ring²⁷.

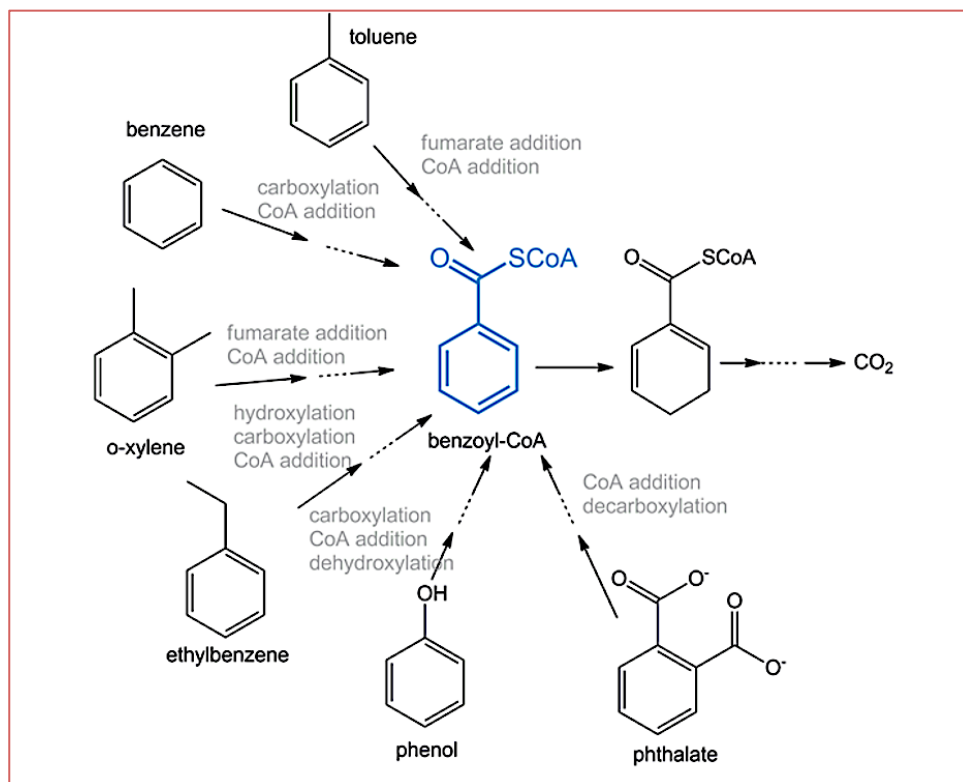


Fig. 3. Degradation of aromates in O₂-free habitats. Diverse aromatic compounds are converted to the central metabolite benzoyl-CoA which is finally mineralized to CO₂.

VII. Materials and Methods

A. Chemicals

Summary of common chemicals used in the study of proteins mentioned in this thesis are listed following table:

Table 1. Chemical names, formulae, mass and manufacturers

Name	Molecular formula	Molecular mass, M_r (g/mol)	Manufacturer
Sodium chloride	NaCl	58.44	Merck
Potassium chloride	KCl	74.55	Merck
Ethylenediaminetetraacetic acid (EDTA)	$C_{16}H_{14}N_2Na_2O_8 \cdot 2H_2O$	372.24	Invitrogen
Dithiothreitol (DTT)	$C_4H_{10}O_2S_2$	154.25	AppliChem
Nitrotetrazolium Blue chloride (NBT)	$C_{40}H_{30}N_{10}O_6 \cdot 2Cl$	817.64	Sigma
Dimethylsulfoxid (DMSO)	C_2H_6OS	78.13	Roth
5-Bromo-4-chloro-3-indolyl phosphate disodium salt (BCIP)	$C_8H_4BrClNO_4P \cdot 2Na$	370.43	Sigma
Glycerol	$C_3H_8O_3$	92.09	Roth
Uranyl formate (UF)	$UO_2(CHO_2)_2 \cdot H_2O$	378.08	Sigma
Collodion solution			Sigma
Acetone	$(CH_3)_2CO$	58.08	Roth
Chloroform	$CHCl_3$	119.38	Roth
Ethanol	C_2H_5OH	46.07	Roth

B. Prokaryotic cell strains and plasmid

The strains of bacterial cells used for heterologous expression and the plasmids used for in the study of the proteins mentioned in this thesis are listed in the Table 2. below along with a short description of their specific usage.

Table 2. Bacterial cell strains and plasmids used for cloning along with their specific usage

Cell strains	Application
<i>Escherichia coli</i> BL21(DE3) ¹	Common expression strain
<i>Escherichia coli</i> Δ iscR ²	Expression strain with deletion in the Iron-sulfur regulator
Stellar cells ³	High copy number cloning strain
Rosetta Gami-B (DE3) pLysS ¹	Expression strain with T7 lysozyme expression to suppress basal expression of T7 RNA polymerase prior to induction
<i>Escherichia coli</i> BL21(DE3) CC5 ⁶	Expression strain with extra chaperon 5 plasmid
Plasmids	Application
p7xC3H ²⁸	Plasmid with T7 promoter and C-terminal 3C protease site followed by decaHis-tag
p7xNH3 ²⁸	Plasmid with T7 promoter and N-terminal decaHis-tag followed by 3C protease site
pASG-IBA3 ⁴	Plasmid with Tet promoter and C-terminal Strep-tagII
pET21 α (+) ⁵	Commonly used plasmid with T7 promoter

Sources: ¹ ThermoFisher Scientific, Carlsbad, CA, USA; ² Provided by the lab of Prof. Volker Mueller, Goethe Uni., Frankfurt, Germany; ³ Clontech Laboratories, Inc., Mountain View, CA, USA; ⁴ IBA Lifesciences GmbH, Göttingen, Germany; ⁵ Merck KGaA, Darmstadt, Germany; ⁶ Provided by Dr. Lisa Jödicke, MPI-BP, Frankfurt, Germany

C. PCR

Oligonucleotides with overlap extension were synthesized using Eurofins Genomics GmbH (Ebersberg, Germany). The reactions were set up in 0.2 ml sterile PCR tubes on ice by mixing the components summarized in Table 3. PCR was carried out using Phusion DNA polymerase (ThermoFisher Scientific) in a T Gradient thermocycler (Biometra) according to the protocol in Table 4.

Table 3. PCR reagents

Components	Volume	Final concentration
5x Phusion HF	10 μ l	1x
10 mM dNTPs	1 μ l	200 μ M
10 μ M forward primer	2.5 μ l	0.5 μ M
10 μ M reverse primer	2.5 μ l	0.5 μ M
Phusion DNA polymerase [2 U/ μ l]	0.5 μ l	1 U/50 μ l reaction
plasmid DNA	variable	10 ng
Nuclease-free water	to 50 μ l	

Table 4. PCR protocol

Steps	Temperature ($^{\circ}$ C)	Time (s)
Initial denaturation	98	30
Denaturation	98	10
Annealing	62-70	20
Extension	72	15-30 per kb
Final extension	72	600
Hold	4	∞

D. Transformation of *E. coli* cells

For plasmid DNA transformation, 2 μ l of the plasmid DNA was mixed gently with 50 μ l Stellar competent cells (Takara Bio Inc.), thawed on ice. After incubation on ice for 30 min, the cells were subjected to a heat shock at 42 °C for 90 seconds, followed by incubation on ice for 5 min. For the cell growth, 300 μ l of SOC medium (2% tryptone, 0.5% yeast extract, 10 mM NaCl, 2.5 mM KCl, 10 mM MgCl₂, 10 mM MgSO₄, 20 mM glucose) were added and the cells were incubated at 37 °C with vigorous shaking for 1 h. Positive clones were selected by spreading the cell suspension (10 - 50 μ l) onto the pre-warmed lysogeny broth (LB) agar (1% (w/v) tryptone, 0.5% (w/v) yeast extract, 1% (w/v) NaCl, 1.5% (w/v) agar) plates with an appropriate antibiotic. After overnight incubation at 37 °C, plates were visually analyzed for presence of single colonies.

In case of Ldh/EtfAB complex heterologous expression, 100 ng of plasmid DNA containing the gene coding for *lctABD* (pASG-IBA3_BAStrepIIL-Fd) was mixed with *E. coli* BL21 (DE3) Δ *iscR* competent cells. Transformation of *E. coli* BL21 (DE3) Δ *iscR* competent cells was performed in the same manner as described above.

E. Isolation of plasmid DNA from *E. coli*

After transformation, a single colony was picked by a pipette tip as an inoculum for 3 ml LB medium (1% (w/v) tryptone, 0.5% (w/v) yeast extract, 1% (w/v) NaCl) containing 50 μ g/ml carbenicillin. Cultures were incubated at 37 °C with shaking overnight and then centrifuged at 14,000 rpm for 30 min. Plasmid DNA was isolated from the *E. coli* cell pellet using the Plasmid DNA isolation kit (Qiagen) according

to the manufacturer's protocol. Plasmid DNA was eluted with 10 mM Tris-HCl (pH 8.5).

F. Determination of DNA concentration

Qualitative and quantitative analysis of genomic and plasmid DNA was performed photometrically by absorbance measurements at 260 nm using a NanoDrop spectrophotometer (ThermoFisher Scientific Inc.). 10 mM Tris-HCl (pH 8.5) served as a blank as it was used for isolation of plasmid and genomic DNA. The purity of the DNA can be estimated by the ratio of absorbance at 260 nm and 280 nm (OD_{260}/OD_{280}), which should be in the range of 1.8 - 2.0. Another indicator for the presence of contaminating substances, such as chaotropic salts and phenol is the OD_{260}/OD_{230} ratio which is expected to be around 2.0 in case of pure DNA.

G. DNA sequencing

The full-length sequences of the cloned genes were confirmed by DNA sequencing carried out by Eurofins Genomics GmbH (Ebersberg, Germany). Plasmid DNA (15 μ l of 50-100 ng/ μ l; 750-1500 ng in total) and the corresponding primers (2 μ l of 10 μ M) were premixed and sent for DNA sequencing. The results were analyzed using the MultiAlign Software²⁹.

H. In-fusion HD cloning

In-fusion HD cloning (Takara Bio USA, Inc.) is an advanced method of cloning without the use of restriction digestion enzymes. The steps used to perform the

cloning in this thesis work to create necessary clones are mentioned in the following paragraphs with a descriptive figure (Fig. 4).

- a) Select a base vector and identify the insertion site. Linearize the vector by restriction enzyme digestion or inverse PCR and purify.
- b) Design PCR primers for your gene of interest with 15-bp extensions (5') that are complementary to the ends of the linearized vector.
- c) Amplify your gene of interest with CloneAmp DNA polymerase. Verify on an agarose gel that your target DNA has been amplified and determine the integrity of the PCR product.
- d) Spin-column purify your PCR product OR treat it with Cloning Enhancer.
- e) Set up your In-Fusion cloning reaction
- f) Incubate the reaction for 15 min at 50°C, then place on ice.
- g) Transform competent cells with 2.5 µl of the reaction mixture from previous step.

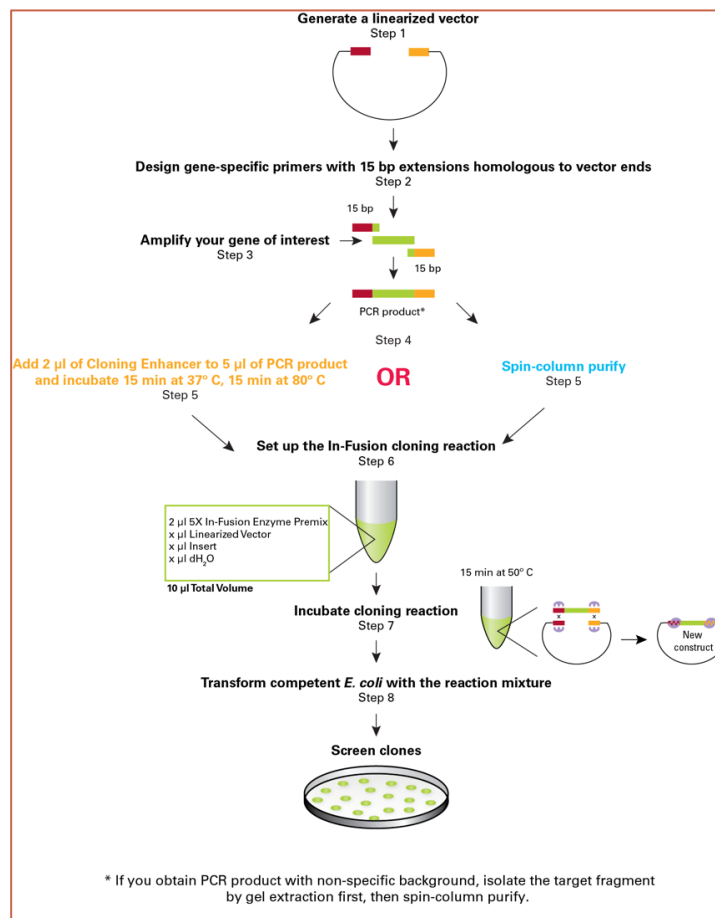


Fig. 4. In-Fusion HD cloning protocol overview. Source Takara Bio USA, Inc.

I. Site-directed mutagenesis

For the purpose of generating point mutations and nucleotide deletion from the clones, QuikChange Lightning Site-Directed Mutagenesis kit (Agilent Technologies, Inc.) was used. The components of the PCR reaction are summarized in Table. 5.

Components	Volume	Final concentration
QuikChange lightning buffer	2.5 μ l	1x
dNTP mix	0.5 μ l	N/A
forward primer	1 μ l	125 ng
reverse primer	1 μ l	125 ng
plasmid DNA	1.0 μ l	25 ng
QuikChange lightning enzyme	0.5 μ l	1 U/50 μ l reaction
Nuclease-free water	to 25 μ l	

The PCR reaction was run at 68 °C with an amplification time of 30 sec /kb of plasmid DNA. Once the PCR is done, 1 μ l of Dpn I restriction enzyme was added to digest parental methylated and hemi-methylated DNA.

J. Agarose gel electrophoresis

Five parts of the DNA sample was mixed with one part of 6X DNA Gel Loading Dye (ThermoFisher Scientific) and loaded onto a 1% (w/v) agarose gel. Electrophoresis was carried out in a tank filled with 1X TAE buffer (40 mM Tris, 20 mM acetic acid, 1 mM EDTA) at 90 V at room temperature for 1 to 1.5 hours. Visual tracking of DNA migration was possible due to the presence of bromophenol blue

and xylene cyanol FF, which co-migrate with DNA fragments of around 300 bp and 4000 bp, respectively. For DNA length estimation, GeneRuler 1 kb Plus DNA-Ladder was used as reference marker. After electrophoretic separation, the agarose gel was stained in 0.0002% (w/v) EtBr solution for 15 min. To remove the excess of the staining solution, the gel was washed in H₂O for 5 min. EtBr intercalates between the base pairs of double stranded DNA and allow visualization of DNA fragments under the UV-light using an UV transillumination gel-doc (Biorad).

K. Anaerobic heterologous gene expression

The anaerobic heterologous expression is described here with the example of Ldh/EtfAB complex.

The clone of Ldh/EtfAB complex was expressed in *E. coli* BL21 Δ *iscR* cells heterologously. The expression and purification, both were performed in an anaerobic chamber (Coy Lab Products, Inc., USA) with 95% N₂, 5% H₂. Several plasmids (pET-21 α (+), pASG-IBA3) were generated using In-Fusion HD EcoDry cloning kit (see Section VII-H), with differences in the affinity tags (Strep-tagII or decaHis-tag) and their localization at the N- or C-termini of the 3 subunits. The expression tests were performed on small scale, to find out the best possible clones for expressing the entire intact Ldh/EtfAB complex. Some clones resulted in the production of a moderately intact complex, whose purification was optimized to obtain the highest yield and quality.

Cells were grown in 800 ml Miller-LB medium in 1L culture flasks containing supplements like 2 mM of ferric ammonium citrate, 25 mM glucose, 100 μ g/ml ampicillin and 30 μ g/ml kanamycin, until the OD₆₀₀ reached 0.3 - 0.5 at 37 °C.

Afterwards 25 mM sodium fumarate was added and the culture was transferred to a 1L Schott bottle with gas-tight cap. This was bubbled for at least 20 to 30 minutes with N₂ gas to displace any trapped O₂ in the culture before induction. To accelerate this process, 2 mM L-cysteine was supplemented. After the culture was cooled down at 16 °C, 1 mM of IPTG was added to induce the plasmid to produce the protein complex. The induced culture was then incubated for the next 16 to 20 hours at 16 °C for slower and steady anaerobic production of the protein complex. Slower production methods have been shown to work better for proper folding and assembling of larger protein complexes. The culture was then harvested and cell pellet was disrupted in the French-Press under exclusion of O₂. For purification, the standard protocols for His-tag and Strep-tag affinity were used followed by gel-filtration to separate subunits or sub-complexes of the Ldh/EtfAB complex. All the purification buffers contained 20% (v/v) glycerol and 4 mM DTE to keep the enzyme stable and oxygen-free, respectively. Thus, a moderately stable complex with low-medium yield could be purified.

L. Anaerobic protein purification

a) Strep-tag affinity chromatography

For the strep-tag affinity chromatography, three buffers were prepared for this purification. The composition of these buffers, equilibration, washing, elution and regeneration, are described below in Table 6.

- 1 ml Streptactin superflow HP column (Iba GmbH) was washed and equilibrated using 5 CV of equilibration buffer.

- Afterwards, loaded the filtered supernatant on to this column for almost 2 - 4 hours using a peristaltic pump inside the anaerobic chamber.
- Once the sample was loaded for sufficient time then the column was washed with 4 CV of equilibration buffer using gravity flow.
- Once the column is washed, 4 CV of elution buffer was added to elute the strep-tagged protein complex from the affinity column.
- After the elution step, the column was regenerated using 5 CV regeneration buffer and further washed with 5 CV of wash buffer at pH 10.0 and then with 10 CV of ddH₂O and 10 CV of 70% ethanol for storage.

Table 6. Buffers for Strep-tag purification

Equilibration/ Wash	Elution	Regeneration
100 mM Tris/HCl pH 8.0	100 mM Tris/HCl pH 8.0	100 mM Tris/HCl pH 8.0
50 mM MgSO ₄	50 mM MgSO ₄	50 mM MgSO ₄
20 % (v/v) Glycerol	20 % (v/v) Glycerol	
4 mM DTT	4 mM DTT	
10 μM FAD	10 μM FAD	
	5 mM Desthiobiotin	1 mM HABA

b) Size exclusion chromatography

For size exclusion chromatography, only 1 buffer was used with the composition described in Table 7. The running buffer, ddH₂O and 70% ethanol was degassed and over-pressurized using N₂ gas for ca. 30 to 45 minutes before transferring the flasks inside the anaerobic tent. These flasks were incubated inside tent environment of 95% N₂ and 5% H₂ for at least one night while stirring on a magnetic stirrer to

VII. Materials and Methods

accelerate gas exchange. Larger volume of diluted sample from affinity chromatography was concentrated to ca. 2 to 4 mg/ml or ca to 500 μ l total volume using 70 kDa MWCO filters. The concentrated protein sample was then filtered, using 20 μ m filtration device to avoid any aggregated protein sample to be added on to SEC column, Superdex 200 Increase 10/300 GL (GE healthcare, Chicago, USA). Steps for size-exclusion chromatography are described below.

- Around 1.5 CV of deoxygenated ddH₂O was used to clean the column.
- The column was equilibrated with 1.5 to 2 CV of deoxygenated SEC buffer before loading the concentrated and filtered sample.
- The sample was loaded on the loading loop and ran using 1.5 CV of same SEC buffer to resolve proteins or protein sub-complexes based of their retention volume, V_r .
- The samples were collected and pooled from every individual peak to identify the protein composition and quality on SDS-PAGE (see Section VII-N), Native-PAGE (see Section VII-O) and calculate protein concentration (see Section VII-M).
- Protein sample was aliquoted and stored in gas-tight anaerobic vials for further use and analysis.

Table 7. Size-exclusion chromatography buffer

Contents	Concentration
Tris/HCl pH 7.5	50 mM
MgSO ₄	100 mM
Glycerol	20 % (v/v)
DTT	4 mM
FAD	10 μ M

M. Protein concentration measurement

For protein concentration measurement, Bradford assay³⁰ was used. Bovine serum albumin (BSA) (ThermoScientific) was taken as a standard. Multiple concentrations of BSA solution (1 µg/ml to 5 µg/ml) were prepared to plot a linear curve against absorbance at 595 nm using a spectrophotometer. A protein solution of nearly 1 to 2 mg/ml was prepared using dilution with protein purification buffer. The original 5x Bradford reagent was diluted to 1x using double-distilled H₂O. 1ml of this 1x Bradford reagent was added in all the cuvettes containing different BSA concentrations plus no BSA for a reagent Blank and triplicates of protein to be measured. All the cuvettes were incubated at room temperature for 10 to 15 minutes for the reaction to work. After incubation, the absorbance at 595 nm wavelength was measured using the spectrophotometer (Ultrospec 2100 pro, Amersham Biosciences). Once all the measurements were recorded then a standard curve was plotted with absorbance (595 nm) in Y-axis and BSA concentration (mg/ml) on X-axis. Only when the curve had the R² value of more than 0.98, then the concentration of protein was calculated using the absorbance.

N. Denaturing polyacrylamide gel electrophoresis

Proteins were separated by electrophoresis through the polyacrylamide gel under denaturing conditions using sodium dodecyl sulfate (SDS) according to the protocols described by Laemmli³¹. Due to an even binding of SDS to the peptides, the proteins are separated according to their molecular weight. Sample aliquots were mixed with 4x SDS sample buffer (106 mM Tris-HCl, 141 mM Tris base, pH 8.5, 2% (w/v) SDS, 10% (v/v) glycerol, 0.51 mM EDTA, 0.22 mM SERVA Blue G250, 0.175 mM

phenol red) from Invitrogen (Darmstadt, Germany) in a ratio of 1:4. The electrophoretic separation was performed using Bolt 4-12% Bis-Tris polyacrylamide gels with 1X MES or 1X MOPS SDS running buffer from Invitrogen (Darmstadt, Germany) (Table 8) at 180 V for approximately 45 to 60 minutes. Separated proteins were stained with PageBlue protein staining solution from Thermo Fisher Scientific (St. Leon-Rot, Germany) and the banding pattern was inspected and recorded.

Table 8. SDS-PAGE buffers

20X MOPS (pH 7.7)	20X MES (pH 7.3)
50 mM MOPS	50 mM MES
50 mM Tris base	50 mM Tris base
0.1% (w/v) SDS	0.1% (w/v) SDS

O. Non-denaturing polyacrylamide gel electrophoresis

To determine native mass and oligomeric states, electrophoretic separation of folded protein was carried out using non-denaturing polyacrylamide gels according to the protocol by Schägger *et al*³². The migration distances depend on the overall surface charge and the hydrodynamic radius of the protein particle in solution. Sample aliquots were mixed with 4x BN-PAGE sample buffer (50 mM Bis-Tris, pH 7.0, 50 mM NaCl, 10% (v/v) glycerol, 0.01% (w/v) bromophenol blue) in a ratio of 1:4. Two running buffers were utilized for CN-PAGE runs: 1x cathode buffer (50 mM Tricine, pH 7.0, 15 mM Bis-Tris) and 1x anode buffer (50 mM Bis-Tris, pH 7.0). The electrophoretic separation was performed using Novex 4-16% Bis-Tris

polyacrylamide gels at 150 V at room temperature for approximately 60 minutes and was continued at 4 °C at 250 V for 30 to 90 minutes.

P. Immunoblotting (Western Blot)

After electrophoretic separation of proteins via SDS-PAGE, the proteins were transferred to a PVDF membrane using the i-Blot system, Invitrogen (Darmstadt, Germany) for 7 minutes following the manufacturer's instructions. After blotting, the PVDF membrane was incubated in a 1x TBST buffer (Table 9) containing bovine serum albumin fraction (2% (w/v) BSA) at room temperature for 60 minutes in order to reduce non-specific interactions between the antibody and the proteins. Afterwards, the PVDF membrane was washed with 1x TBST buffer and incubated with the monoclonal mouse anti-Strep-TagII antibody conjugated to alkaline phosphatase (1 to 2,000 diluted in 1x TBST buffer) (Iba GmbH) at room temperature for 1 to 2 hours.

Thereafter, the membrane was washed thrice with 1x TBST buffer for 5 min and then with the alkaline phosphatase (AP) reaction buffer (Table 9).

In order to trigger a chromogenic alkaline phosphatase reaction, a development solution prepared in the AP buffer was added (250 µg/ml 5-bromo-4-chloro-3'-indolyphosphate p-toluidine salt (BCIP) and 50 µg/ml nitro-blue tetrazolium chloride (NBT)). The colorimetric reaction was stopped by addition of water. Purple bands of an insoluble precipitate are caused by the StrepII-tagged fusion protein.

Table 9. Buffers for Western blotting

10X TBST (pH 7.5)	10X AP (pH 9.5)
100 mM Tris	100 mM Tris
150 mM NaCl	100 mM NaCl
0.5% (v/v) Tween 20	5 mM MgCl ₂

Q. Chemical cross-linking

Since larger multimeric protein complexes usually stay in equilibrium with their individual subunits and sub-complexes, which can be easily detected by gel-filtration and by Native-PAGE analysis, the yield of intact complex poses an issue for electron microscopy studies. To increase the stability and thus the amount of intact protein complex, the eluant from gel-filtration can be subjected to chemical cross-linking^{33,34} procedures and then further subjected to another round of gel-filtration.

Successful cross-linking can be verified using a single dominant gel-filtration profile at the correct retention volume (V_r), corresponding to the intact protein complex and by performing an SDS-PAGE, where the individual subunit bands e.g., in our case Ldh, EtfA, EtfB, become weaker and a single smearing band of the cross-linked complex becomes stronger.

Several types of chemical cross-linkers, with variable linker lengths and different protein to cross-linker ratios relevant to this thesis work are mentioned below (Table 10). The tested cross-linkers include glutaraldehyde (GA), bis(sulfosuccinimidyl)suberate (BS³), di-methyl pimelimidate (DMP) and

dithiobis(succinimidyl propionate) (DSP). All these cross-linkers were purchased from ThermoFisher scientific, Waltham, USA.

2 cross-linker types showed promising results on the SDS-PAGE gel, as visible in the Fig. 5. Finally, 1 mM BS³ was used to stabilize the protein sample for cryo-EM experiments.

Table 10. Cross-linkers, their lengths, concentration ranges used in the experiment

Cross-linkers	Cross-linker length	Concentration range
Glutaraldehyde (GA)	7.5 Å (short)	0.0001 - 0.001 % (3 in total)
BS ³	11.4 Å (medium)	0.25 - 5 mM (6 in total)
DMP	9.2 Å (short)	6.5 - 9.2 mM (5 in total)
DSP	12 Å (medium)	0.25 - 5 mM (6 in total)

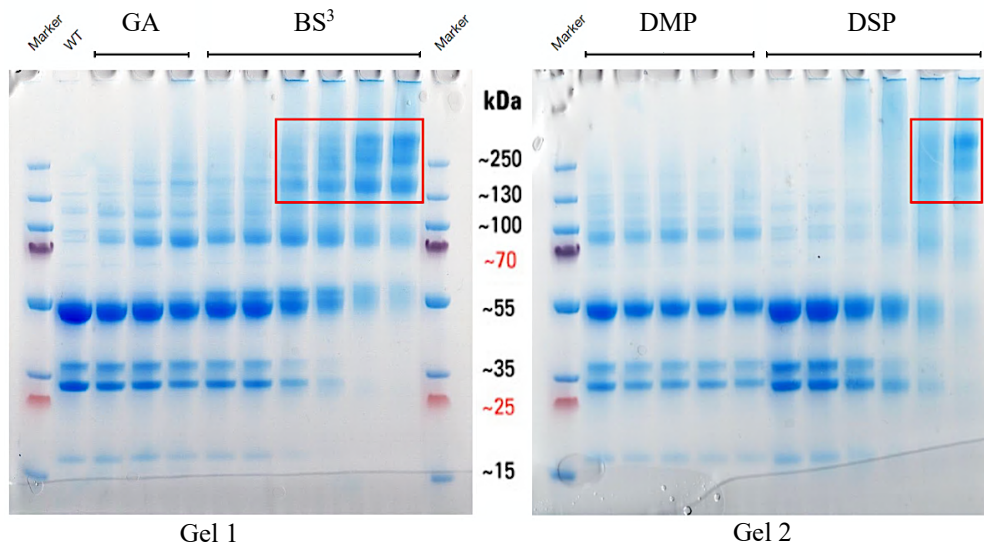


Fig. 5. SDS-PAGE gels showing effects of different chemical cross-linkers on the Ldh/EtfAB complex. Concentrations of all the cross-linkers used here are mentioned in the Table 10 above. Cross-linkers and their specific concentrations at which they show success are marked in red boxes.

R. Crystallization

Many different protein crystallization methods have been developed. They are classified in batch, vapor diffusion (VD) and dialysis methods by which in different manners the precipitant in the protein solution is slowly increased³⁵. As membrane proteins are not soluble in aqueous solution their crystallization is performed by the *in surfo* (detergent-solubilized protein) method and the *in meso* or Lipidic Cubic Phase (LCP) method³⁶. Recently, the latter method is extended by the Cubicon method³⁷ which is useful for crystallization of membrane proteins with very low yield, to mildly concentrate them in the cubic mesophase. Membrane proteins are mostly crystallized with VD or Batch methods.

Crystallization of this work was performed with diverse crystallization kits by VD either via the hanging-drop variant where the protein drop hangs on a hydrophobic glass coverslip, or via the sitting-drop variant where the drop sits in a well in the crystallization plate (Fig. 6.B). In the VP methods the water in the protein drop slowly moves via the gas phase to the bottom solution containing a higher precipitant concentration. Precipitant and protein concentrations in the drop increase which forces precipitation or crystallization (Fig. 6.A, B).

The sitting-drop method for setting up a crystallization screen is considered to be the more feasible option when using an automated crystallization robot to set up 96-well plates, whereas the hanging-drop method is preferred when setting up 24-well plates manually for scaling up crystal size or yield. In all cases, the crystallization was performed using OryxNano crystallization robot (Douglas Instruments Ltd., Hungerford, UK) (Fig. 6.C) which was inside an anaerobic chamber (Coy Laboratory Products) with an environment of 95% N₂, 5% H₂ (v/v).

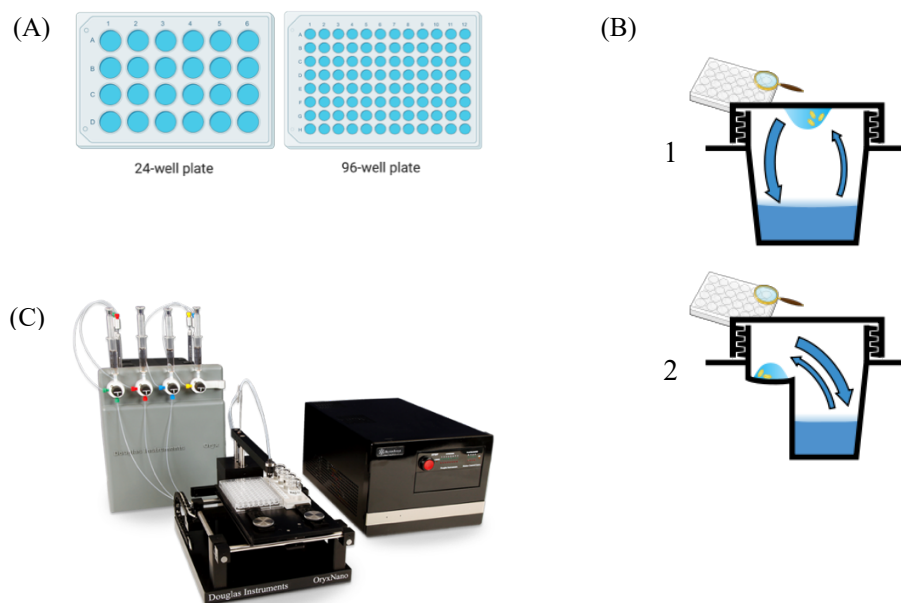


Fig. 6. (A) Crystallization plates, 24-well and 96-well, created using BioRender. (B) 1. Hanging-drop method, 2. Sitting-drop method of crystallization, source wikipedia.org. (C) Douglas Instruments OryxNano crystallization robot, source Douglas Instruments.

S. Single-particle Electron Microscopy

a) Negative-staining single-particle EM

For negative-staining, QuantiFoil 300-mesh Copper grids were prepared in advance, using Collodion solution (cellulose nitrate, 2% in amyl acetate, Sigma) as an additional support layer and then sputter-coated with 4.33 nm Carbon thread for the final Carbon film for protein sample support and distribution.

The workflow for staining the protein sample using uranyl formate (UF) on the grids, prepared in the aforementioned paragraph, is described in the diagram below.

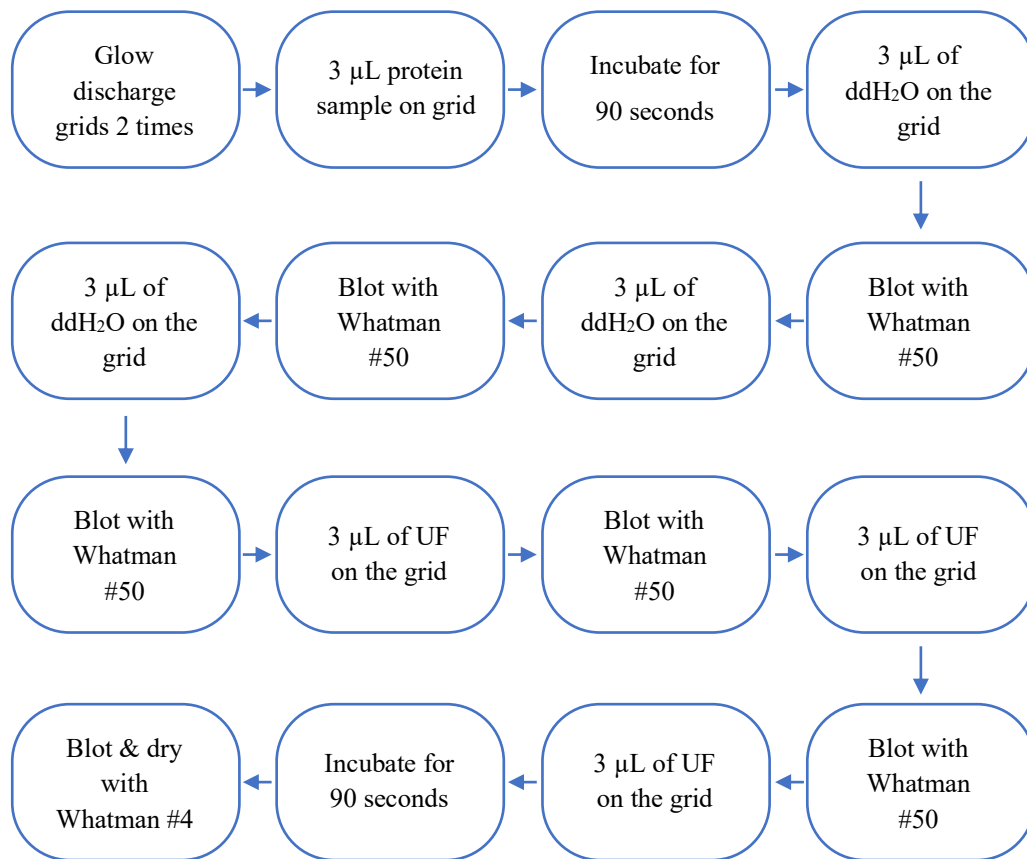


Fig. 7. Flow-diagram of Negative-staining grid preparation process

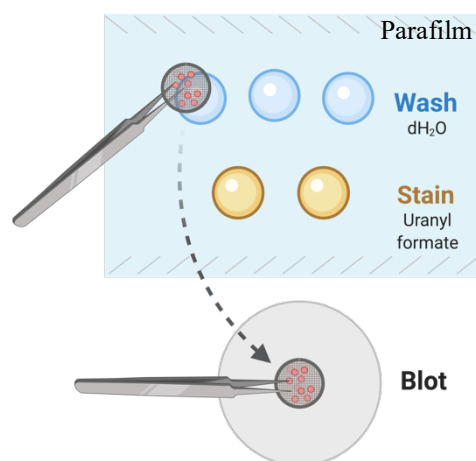


Fig. 8. Single-particle Negative-staining diagrammatic steps. Created using BioRender.com

b) Single-particle electron cryo-microscopy

For single-particle cryo-EM experiments, there are wide arrays of carbon-support variants but mostly used ones are Holey-carbon grids or Holey-carbon grids with a thin layer of Carbon back coating as a supporting material for the biological sample. Among commonly used copper or gold mesh grids with Holey-carbon film, the array of hole sizes and the hole spacing among them can also determine the differences in the outcome of sample distribution and concentration. These hole dimension and hole spacing can range from 1 μm to 4 μm . The grids used in this thesis work were C-flat R1.2/1.3-300 mesh (Protochips Inc., Morrisville, NC, USA), unless stated otherwise. These grids can be treated with chloroform for few hours to clean any manufacturing contamination and reduce any unwanted background in the images. Before loading the protein samples on to the grids, they were made hydrophilic using a Glow Discharger device (Pelco easiGlow, Ted Pella Inc., CA, USA) for 135 seconds, at 15mA current and a vacuum of 0.38 mbar. This creates a plasma in vacuum which then treats the carbon film on grids to behave hydrophilic for 15-20 minutes. This improves the protein distribution on the grids by spreading protein molecules evenly across the entire grid. These glow-discharged grids are loaded with sample (3-4 μl) and then blotted using Whatman filter paper to absorb excess sample from the grid surface, leaving only sufficient amount of protein sample inside the holes on carbon film. These grids are then plunge-frozen in to liquid ethane to avoid any crystalline ice formation in the protein buffer. This step of sample blotting and plunge-freezing is usually achieved using high speed automatic humidity and controlled plunge-freezer robots, many of which are available commercially. In this thesis work, Vitrobot Mark IV from FEI-ThermoFisher was used.

In order for these grids to be loaded on to the electron cryo-microscope, they go through a process of ‘Clipping’. In this Clipping method, a copper ring and a gold C-clip were fixed on either side of the grid, making the entire assembly known as an Autoloader grids or a Cartridge. These cartridges were then loaded on to an autoloader Cassette in order to load inside the microscope sample chamber. Each cartridge was then screened for sample and grid quality.

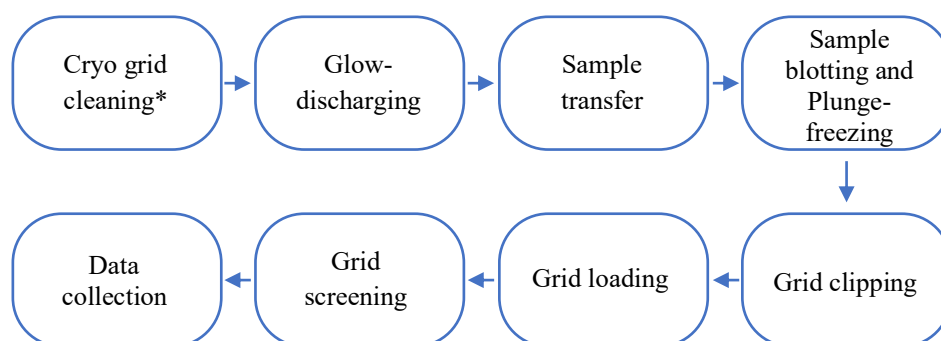


Fig. 9. Flow-diagram showing cryo-EM sample preparation steps. * refers to an optional step.

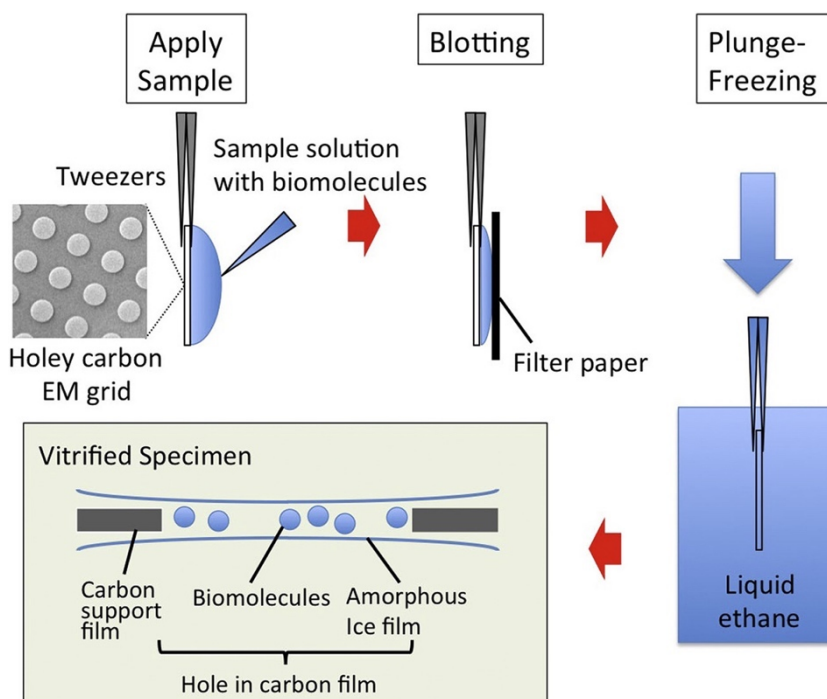


Fig. 10. General workflow for cryo-EM grid preparation³⁸.

T. Data collection and structure refinement

a) Crystallography

A general layout of crystallographic data collection and data processing is shown below (Table 11), describing the software used and their short description.

All datasets were collected at the PXII/X10SA beamline of the synchrotron Swiss Light Source (SLS) in Villigen, Switzerland. The detector used was PILATUS 6M pixel detector from Dectris (Baden-Dättwil, Switzerland). The raw data were processed with XDS/XSCALE³⁹ to extract from recorded pixel films the positions hkl and the intensity or structure factor F of each diffraction spot. For calculation an electron density by Fourier synthesis besides the structure factor amplitude F a phase is required to sum up the reflection waves correctly. The strategy of phase determination depends on the availability of a known structure. If absent, the methods of multiple isomorphous replacement and multiple anomalous dispersion are applied which calculate the phase from the differences between $F_{\text{protein+heavy atom}} - F_{\text{protein}}$ or the anomalous difference $F(hkl) - F(-h-k-l)$ at the absorption edge of a strong scatterer by using SHARP⁴⁰ and SOLOMON⁴¹. If a suitable structural template is present in the data base the molecular replacement method e.g., with PHASER⁴² is applied. After automatic or manual model building or sequence exchange the difference between the experimental F and the F calculated from the model are minimized in a process termed refinement. Program suites applied are PHENIX⁴³, CCP4⁴⁴ and BUSTER⁴⁵.

Table 11. Software and servers for data processing, refinement, and visualization

Software name	Description and Usage
XDS	Spatial correction, gain background calculation, reflection indexing, cell information, intensity integration, scaling symmetry-related reflections, and statistics
XSCALE	Scaling of the data from XDS
XDSCONV	Conversion of XSCALE data to various formats like CCP4, MTZ
UCLA-DOE LAB server	Diffraction anisotropy assessment and correction
PHASER	Phase determination by molecular replacement
SHELXD	Locating heavy atoms like Fe-S cluster in the density map
SHARP	Phase determination
SOLOMON	Phase improvement
PHENIX program suite	Restraint builder, structure refinement, validation
CCP4 program suite	Structure refinement
autoBUSTER	Structure refinement using NCS and TLS parameters
COOT	Electron density analysis, manual model building, manual model refinement
DALI server	Structure comparison calculations database
PISA server	Surface area calculation
UCSF Chimera	Structure visualization

b) Single-particle Cryo-EM

A general layout of cryo-EM data collection and data processing software and tools is given in the table below (Table 12) with short description.

All the datasets related to this thesis work were collected on Titan Krios G3i (FEI-ThermoFisher, Eindhoven, Netherlands) operating at 300 kV with a BioQuantum K3 energy filter (30 eV slit width) (Gatan Inc., USA) at a nominal magnification of 105k corresponding to a calibrated pixel size of 0.837 Å. The under-focus values were ranging from 1.2 to 2.4 μm with a 0.3 μm step in between. The

exposure rate was mostly set at ca. $15 \text{ e}^-/\text{\AA}^2/\text{second}$ with the exposure time of usually varying among proteins and datasets to set the total dose per exposure depending on the physical conditions of grids and sample.

The data quality during the collection was closely monitored using on-the-fly version of cryoSPARC⁴⁶. This software could very quickly pre-process the movies being imported continuously from the microscope data transfer server. The grid quality, ice thickness, acquirable parts of cryo-grids, particle dimensions, particle extraction box size parameters could be quickly assessed and set for the further intensive data processing.

For the more intensive data processing, the movies collected were then imported into RELION-3.1.1⁴⁷ and converted into a single stack of movies, known as a micrograph. The beam-induced motion was then corrected using Shawn Zheng's MotionCor2 algorithm⁴⁸. After motion correction, the Contrast Transfer Function parameters were estimated using Kai Zhang's Gctf⁴⁹. Micrographs that showed CTF fitting of higher than 4.5 \AA and astigmatism of more than 500 \AA were excluded from further processing. After filtering, micrographs were used for particle picking. For particle picking, crYOLO⁵⁰ with neural network denoised (JANNI) general model was used. The coordinates of particles were then imported in Relion. In Relion, these particles were extracted and then passed through several rounds of reference-free two-dimensional classification to clean and group good sets of particles based on low-resolution angular sampling and image alignments. Sets of good classes were then subjected to bias-free Initial modelling using a Stochastic Gradient Descent approach (SGD)⁴⁶. The lowpass filtered initial model along with the good classes from two-dimensional classification were used to perform a three-dimensional

classification to segregate particles among different classes based on three-dimensional angular sampling. These 3D classes were then taken for further refinement. Once the particles were initially refined, post-processing steps like Bayesian Polishing⁵¹ and CTF refinement⁵² were used to polish the refined particles and correct the CTF parameters with 3rd and 4th order aberrations⁵². Only once the particle polishing step was done, then two datasets were merged to add more particle orientations, increase the signal and final resolution. The refinement process was finalized with a Local 3D refinement job with finer angular sampling to further improve the particle alignment and then Local resolution was estimated in the cryo-EM map to correlate biological flexibility in various parts of the protein complex.

Table 12. Softwares, tools, services used for cryo-EM data collection and image processing

Software/ Tool/ Service name	Description and usage
EPU version 2.9.1	For cryo-EM data screening and collection
Leginon	For Negative-staining EM data screening and collection
cryoSPARC	Data processing, refinement
RELION-3.1.1	Data processing, refinement, local resolution estimates
UCSF Chimera	Structure visualization
UCSF ChimeraX	Structure visualization, Figure preparation
ARP/wARP web service	Model building from cryo-EM maps
SWISS-MODEL	Model building from homologous model
COOT	cryoEM map analysis, manual model building, manual model refinement

Chapter A. Pcd

1. Introduction

The major constituents of plastics are phthalate esters, which consist of phthalate esterified with dialcohols forming organic polymers (Fig. 11). Phthalates are benzene rings to which two carboxylate groups are attached either in ortho-, meta-, and para-position relative to each other. Due to the numerous advantages of plastics compared to other materials, their annual production in the 400 million tons range imposes severe environmental damages and health problems worldwide. (Thompson, 2009^{53,54}). Plastics can be mineralized by aerobic and anaerobic microorganisms⁵⁵. In both cases, phthalate esters are hydrolyzed by esterases to phthalates and alcohols. In particular, under anaerobic conditions, the decomposition of phthalates is the rate-limiting step in phthalate ester decomposition⁵⁶. While aerobic degradation involves O₂ for ring dihydroxylation thereby allowing an energetically moderate decarboxylation reaction, anaerobic degradation proceeds via CoA activation and decarboxylation to benzoyl-CoA involving an oxygen-independent unusual phthaloyl-CoA decarboxylase (Pcd)^{57,58} (Fig. 11). Pcd belongs to the UbiD family of (de)carboxylases containing prenylated FMN⁵⁹⁻⁶¹. This FMN modification is performed by UbiX-like prenyltransferases using dimethylallylmonophosphate as co-substrate for FMN⁶². Phthaloyl-CoA decarboxylation has been, at first, explored in the denitrifying bacterium *Thauera chlorobenzoica*⁶³. Accordingly, Pcd is organized as a homohexameric protein complex (M_r = 359 kDa) that binds besides the prenylated-FMN (prFMN), K⁺, and Fe²⁺ as cofactors. Oxidation of Fe²⁺ to Fe³⁺ in air results in its deactivation. The Pcd reaction was found to be irreversible; K_m

and V_{\max} for phthaloyl-CoA were 121 mM and $140 \text{ nM min}^{-1} \text{ mg}^{-1}$. A related obligate anaerobic sulfate-reducing bacterium *Desulfosarcina cetonica* also grows on phthalate⁶⁴. Interestingly, it uses an ATP-dependent phthalate-CoA ligase and not a succinyl-CoA: phthalate-CoA transferase like in denitrifying bacteria for CoA activation. *T. chlorobenzoica* Pcd could be prepared in a reasonable amount and quality for structural studies performed in cooperation with the group of Prof. Matthias Boll, Albert-Ludwigs-Universität, Freiburg.

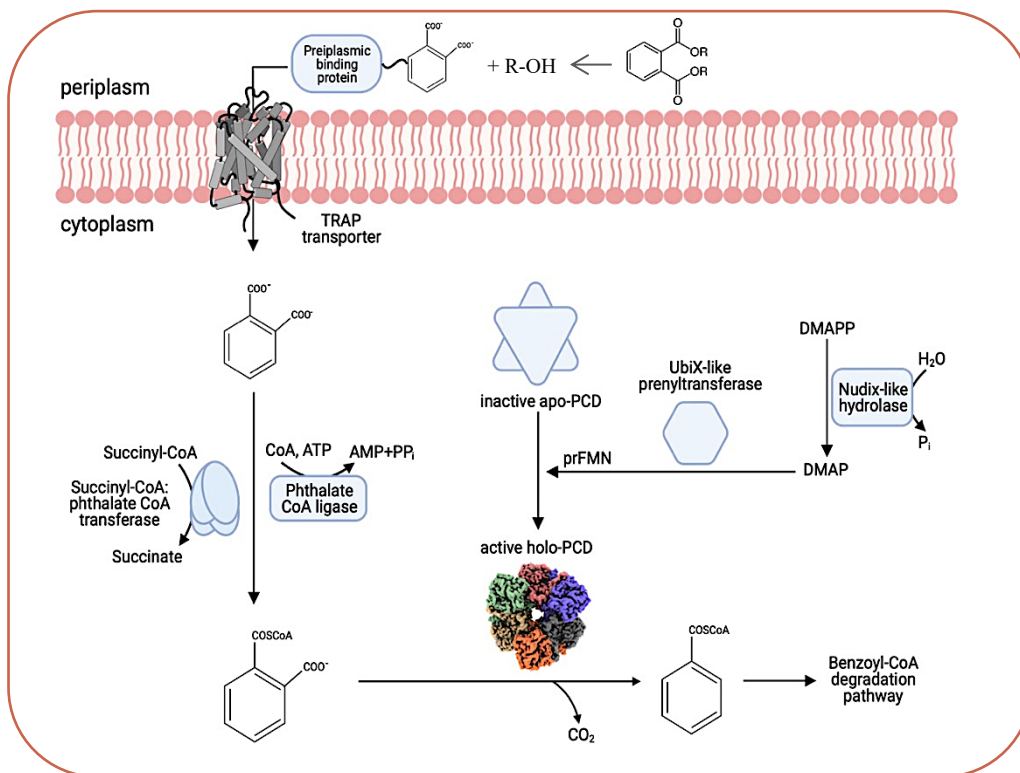


Fig. 11. Anaerobic degradation of phthalic acid, involving active holo-Pcd complex as the main degrading enzyme. Created using BioRender.com.

2. Materials and methods

2.1 Protein expression and purification

The Pcd complex was purified using the protocol described in Geiger et al.⁶⁴ and frozen aliquots were provided by Robin Geiger and Prof. Matthias Boll, Albert-Ludwigs-Universität, Freiburg. The protein sample provided was at a concentration of 10.6 mg/ml in a buffer containing 20 mM MOPS pH 7.5, 100 mM KCl, 1 mM DTT, 20% (w/v) glycerol. Lyophilized aliquots of 2-CN-benzoyl-CoA and benzoyl-CoA for protein-substrate interaction structural studies were also provided by the same group.

2.2 Single-particle negative-staining

A freshly thawed aliquot of Pcd complex with a concentration of ca. 10 mg/ml was diluted 1:10 to reach ca. 1 mg/ml, using a buffer containing 20 mM MOPS pH 7.5, 200 mM KCl, 1 mM DTT and 50 μ M SDT, for negative-staining grid preparation. The grids were glow discharged at 0.38 mbar and 15 mA for 90 seconds just before addition of the sample. Two different final dilutions, 0.01 mg/ml (1:100 dilution) and 0.05 mg/ml (1:20 dilution), were prepared to be used directly onto the grids with the same buffer. Since the Pcd complex is light- and oxygen-sensitive, the sample and grid preparations were performed in an anaerobic chamber (95% N₂, 5% H₂ v/v) and under red-light exposure; 0.75% uranyl formate (UF)⁶⁵ was used as staining agent as mentioned in the Section VII-S (a). The grids were loaded and screened on to a FEI Tecnai Spirit 120 kV microscope. Several images were collected for further analysis and as a reference to keep sample quality like homogeneity and complex intactness in check, for further cryo-EM experiments.

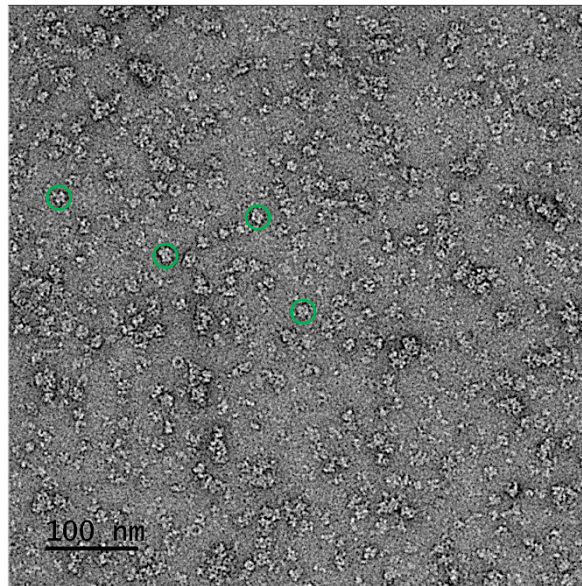


Fig. 12 Micrograph from negative-staining showing intact protein complex particles, marked in green circles

2.3 Single-particle cryo-EM sample preparation and data collection

The Pcd samples were plunge frozen using FEI Vitrobot plunge freezer at 4°C and 100% humidity, by using C-Flat R1.2/1.3, 3C-50 grids (Electron Microscopy Sciences), glow-discharged at 0.38 mbar and 15 mA for 135 seconds. The Pcd complex was thawed and prepared under anaerobic and red-light conditions inside an anaerobic chamber (95% N₂, 5% H₂ v/v) and then brought outside for freezing in gas-tight, light-impermeable vials. Likewise, cryo-grid freezing and clipping processes were always performed under red-light lamps. Freshly thawed Pcd aliquots at a concentration of ca. 10.5 mg/ml were diluted to a concentration of ca. 1.5 mg/ml (ca. 4.18 μM) using the anaerobic buffer without glycerol. 4 μl of this sample was applied to the grids and blotted for 4 seconds using Whatman filter paper #595 at a blotting force of +20 and then plunged directly into liquid ethane. Grids were

screened and images were collected on an FEI Titan Krios at 300kV equipped with a Gatan K3 Summit electron detector that operates in counting mode and with an energy filter of 30 eV slit width. A stack of 9,470 movies with 50 frames was collected over 2.65 seconds of exposure time, at a magnification of 150,000x, corresponding to a pixel size of 0.837 Å at the specimen, with a calibrated average dose of $1 \text{ e}^-/\text{Å}^2$ per frame and at defocus values of $-1.2 \text{ }\mu\text{m}$ to $-2.1 \text{ }\mu\text{m}$.

Similar conditions for freezing, clipping and image collection were used for the Pcd complex with the addition of a substrate analogue, 2-cyano-benzoyl-CoA, at a concentration of 400 μM . A stack of 7,159 movies with 50 frames was collected with the aforementioned conditions for data processing (Table 13).

The same procedure as in the aforementioned paragraph was used for the experiments with addition of 400 μM benzoyl-CoA with Pcd complex. A stack of total 11,630 movies were recorded with 50 frames keeping ca. $1 \text{ e}^-/\text{Å}^2$ per frame from 2 different grids and merged in pre-processing steps.

2.4 Single-particle cryoEM: image processing, model building and comparative analysis

All datasets of were collected using EPU version 2.9.1 in gain normalized TIFF file format. The collected movies of the empty Pcd complex and the complex supplemented with either the 2-CN-benzoyl-CoA or benzoyl-CoA were processed according to the procedure described in the Section VII-T(b)⁶⁶. The local resolution job was performed to analyze the variation in resolution at different parts of the cryo-EM map which is an indication for the biological flexibility. The chemical restraints

of the co-factor, prFMN, 2-CN-benzoyl-CoA, and benzoyl-CoA, for further manual refinement were generated using SMILES or InChI strings in elbow.phenix⁶⁷.

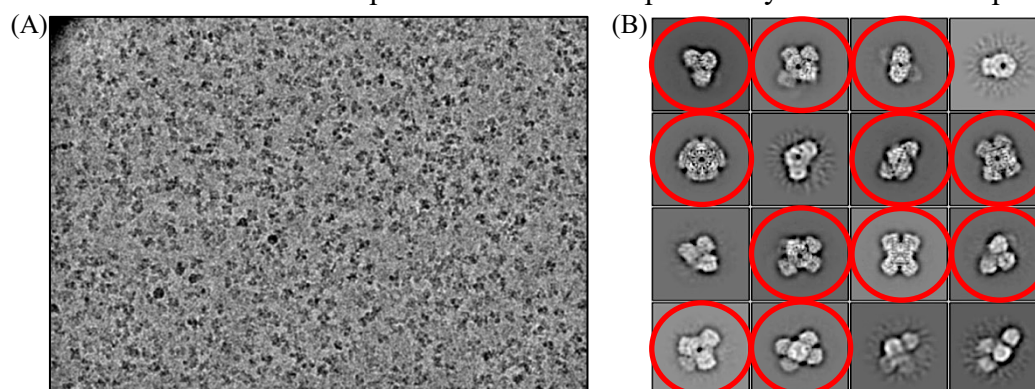
Table 13. Cryo-EM data collection analysis, refinement statistics of active holo-Pcd, Pcd-2-CN-benzoyl-CoA and Pcd-benzoyl-CoA. * refers to values which need to be further improved.

Experimental data			
Protein Ligands	Pcd complex prFMN bound	Pcd complex prFMN, 2-CN-benzoyl-CoA	Pcd complex prFMN, benzoyl-CoA
Data collection and Processing			
Microscope	FEI Titan Krios G3i	FEI Titan Krios G3i	FEI Titan Krios G3i
Voltage (kV)	300	300	300
Camera	Gatan K3 summit	Gatan K3 summit	Gatan K3 summit
Exposure time (s)	2.82	2.65	3.38
Total dose (e ⁻ /Å ²)	50.76	50.08	52.27
Dose per frame (e ⁻ /Å ²)	1.01	1.0	1.04
Defocus range	1.5-2.4	1.5-2.4	1.5-2.4
Pixel size (Å) (calibrated)	0.837	0.837	0.837
Magnification (nominal)	105,000x	105,000x	105,000x
Symmetry imposed	D3	D3	D3
No. of micrographs	9,974	6,250	6,743
Initial particle number	2,206,933	2,071,338	2,081,809
Final particle number	743,306	675,429	821,681
Map resolution (Å)	2.43	2.04	2.3
FSC threshold	0.143	0.143	0.143
Refinement			
Map-sharpneing B factor (Å ²)	-91	-61	-77
Model composition			
Chains	6	6	6
Protein (Residues)	2,985	3,114	3,114
Ligands	prFMN: 6; FE: 12; K: 6; UNK: 6	prFMN: 6; 2-CN-benzoyl-CoA: 6; FE: 12; K: 6; UNK: 6	prFMN: 6; benzoyl-CoA: 6; FE: 12; K: 6; UNK: 6
RMSD Bond Length (Å)	0.008	0.008	0.033
RMSD Bond Angles (°)	1.261	0.844	2.102
MolProbity score	3.58	2.13	3.09
Clash score	55.76*	9.35	27.81
Ramachandran plot (%)			
Favored	82.12*	97.07	93.94
Allowed	16.46	2.15	4.53
Outliers	1.42	0.78	1.53
Rotamer outliers (%)	7.23	4.21	9.72
ADP (B-factor) (min/max/mean)			
Protein	63.07/145.94/102.47	47.77/104.32/73.30	64.93/133.91/99.23
Ligand	96.97/110.46/101.90	60.71/78.61/74.23	92.19/105.86/100.71

3. Results

3.1 Single-particle cryo-EM data analysis

The multi-frame movies in different datasets were collected (as described in section 2.4 of Materials and Methods) and processed using Relion-3.1.1. The basic workflow, along with the major results, is shown in the Fig. 13.C below. According to the local resolution estimations, the model is most rigid in the center, around the threefold axis but contains flexible region at the outer edge of the monomers. Interestingly, the binding of CoA compounds, like 2CN-benzoyl-CoA and benzoyl-CoA, significantly increases the rigidity in the core part of the structure but the flexibility in the outer edge seems to be slightly increased too. This is clearly visible in the figures (Figs. 13.E, 14.C, 15.C), by increase in red color on the outer edges for more flexibility and by increase in blue color in the core threefold axes for more rigidity, in the 2nd (Fig. 14) and 3rd (Fig. 15) datasets as compared to the 1st dataset (Fig. 13). All the datasets were processed using D3-point symmetry as the *ab initio* reconstruction suggested the hexameric complex arrangement of C₃ perpendicular on C₂ axes. An exemplary micrograph from cryoEM data collection of Pcd complex is shown in Fig. 13.A. 2-D classification results depicting the useful 2-D classes are shown in Fig. 13.B. These classes were selected and then subjected for making a 3-D *ab initio* model of the complex as there were no previously known Pcd complexes.



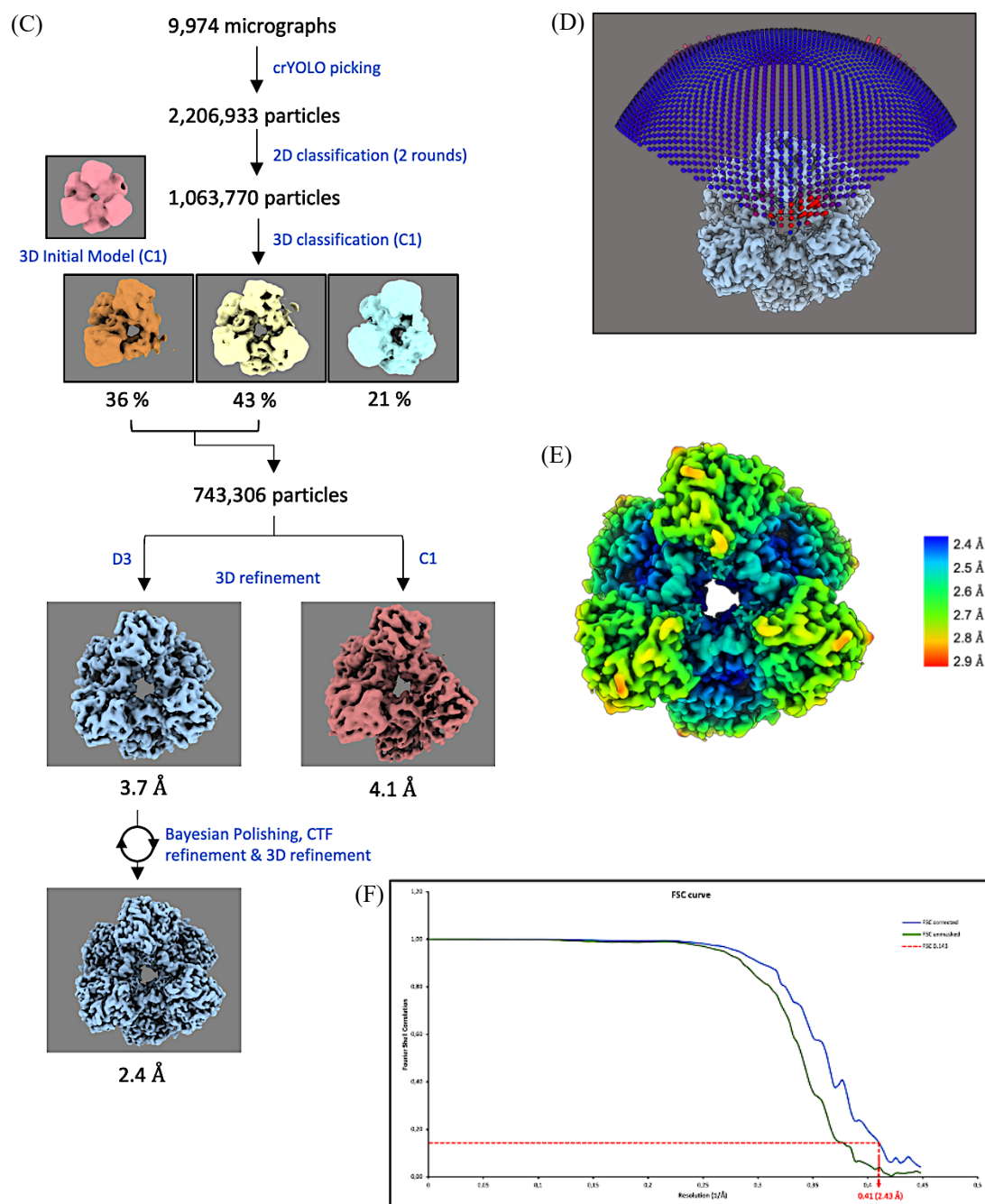


Fig. 13. (A) An exemplary cryo-EM micrograph with 5 Å low-pass filter, depicting the particle distribution and overall quality. (B) Relion 2D classes showing 11 good classes selected for further processing, are marked with red rings. (C) Relion image processing workflow used for refinement of the Pcd complex at 2.4 Å resolution. (D) Final refined cryo-EM map overlapped with the Euler angle distribution. (E) Pcd cryo-EM map color-coded with the local resolution. (F) Gold-standard FSC plot of the final Pcd map, blue curve is FSC-corrected and green curve is FSC-unmasked. Resolution estimated at FSC=0.143.

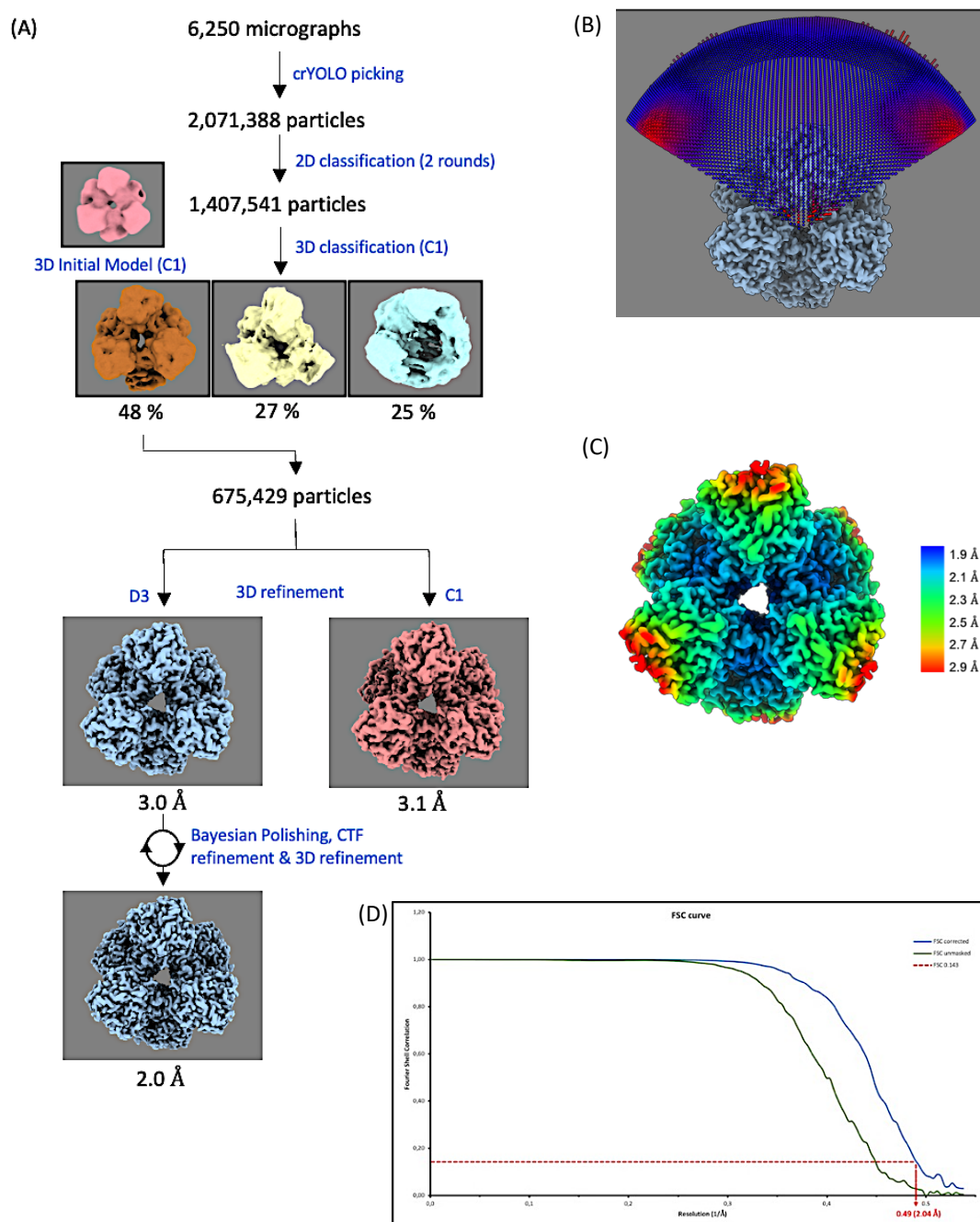


Fig. 14. (A) Relion image processing workflow used for refinement of the Pcd complex with 2-CN-benzoyl-CoA at 2.0 Å resolution. (B) Final refined cryo-EM map overlapped with the Euler angle distribution. (C) Final cryo-EM map color-coded with the local resolution. (D) Gold-standard FSC plot of the final cryo-EM map, blue curve is FSC-corrected and green curve is FSC-unmasked. Resolution estimated at FSC=0.143.

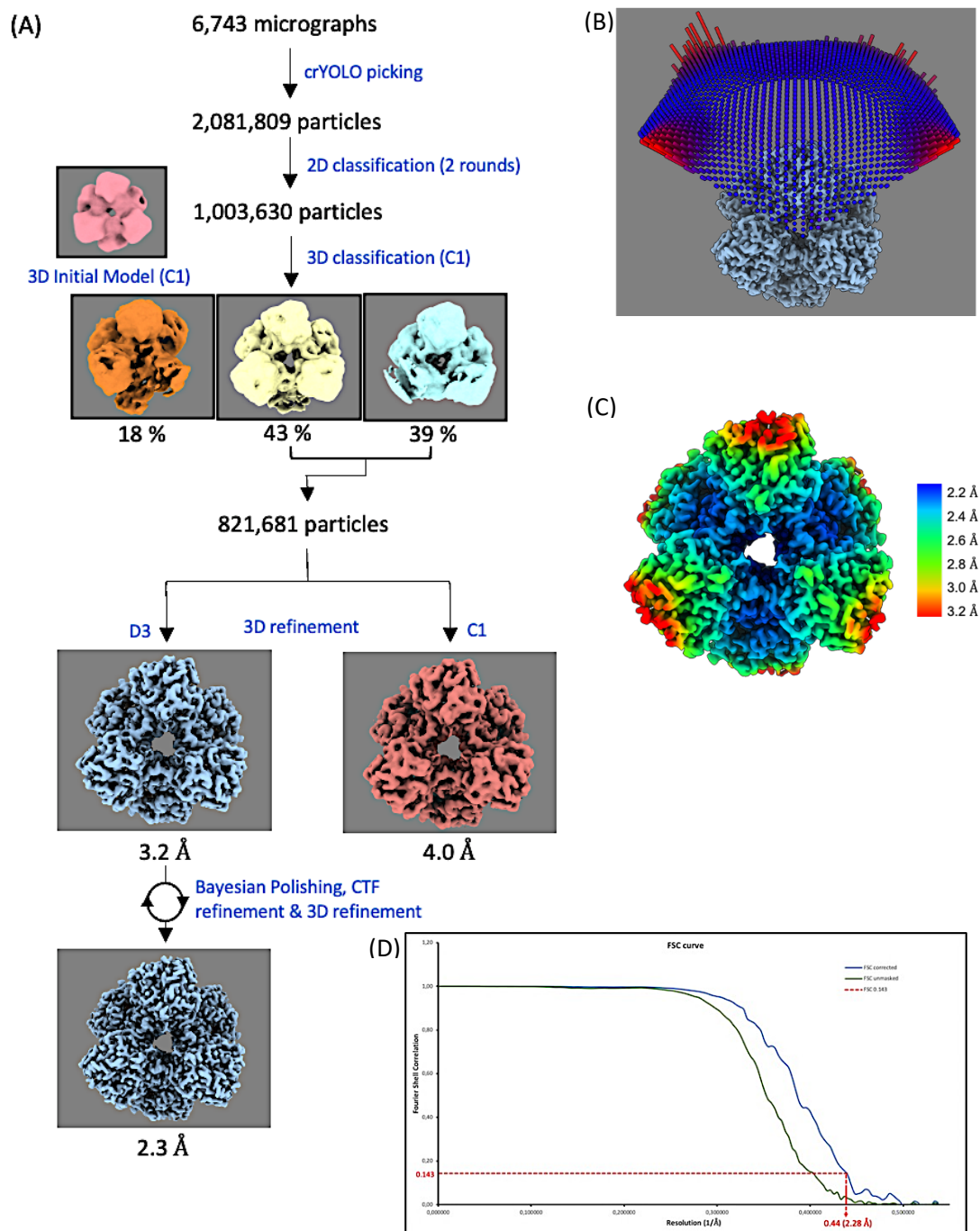


Fig. 15. (A) Relion image processing workflow used for refinement of Pcd complex with benzoyl-CoA at 2.3 Å resolution. (B) Final refined cryo-EM map overlapped with the Euler angle distribution. (C) Final cryo-EM map color-coded with the local resolution. (D) Gold-standard FSC plot of the final cryo-EM map, blue curve is FSC-corrected and green curve is FSC-unmasked. Resolution estimated at FSC=0.143.

3.2 Single-particle cryo-EM structure analysis

Overall structure:

The overall architecture and the subunit fold of Pcd from *T. chlorobenzoica* correspond to that reported for other UbiD family members⁶⁸ (Fig. 16). Briefly, each subunit is basically composed of an prFMN and an oligomerization domain with the active site localized in between (Fig. 17). The larger prFMN domain consists of two six-stranded β -sheets packed against each other to a highly distorted and split β -barrel flanked by short β -sheet and irregular elements (94 - 320) as well as an α + β -subdomain (13-93 + 322-334). The oligomerization domain (335 - 479) adopts an α + β -fold with a central five-stranded mixed β -sheet followed by an elongated C-terminal extension (480 - 527) that is two helices longer than in other UbiD enzymes and attached to the partner subunit of the Pcd dimer (Fig. 17). The oligomerization domains of the six subunits assemble around the three-fold axis and form a hexamer with a hole in its center (Fig. 16). Despite an overall similarity the oligomeric arrangement of the six subunits and the involved contact surface substantially differs among UbiD family members.

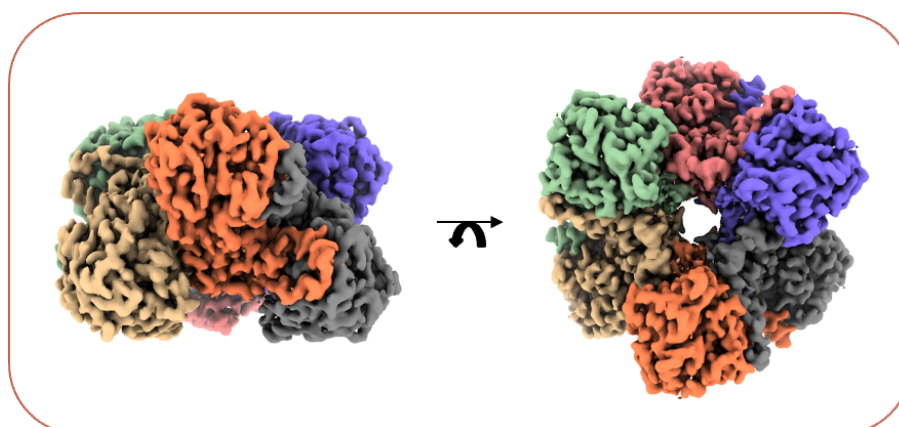


Fig. 16. cryoEM map showing overall shape and subunit arrangement from 2 different views The Pcd hexamer is built of a trimer of homodimers with a hole at the threefold axis.

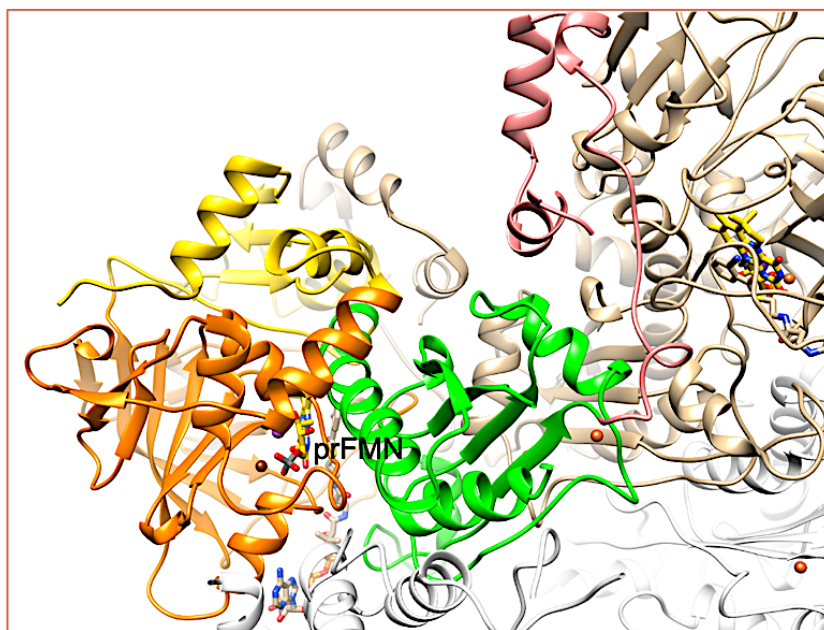


Fig. 17. Fold of a Pcd subunit. The larger split β -barrel and the small N-terminal $\alpha + \beta$ subdomain of the prFMN domains are drawn in orange and yellow, respectively; the oligomerization domain in green. The C-terminal extension (in salmon) multiply interacts with the partner subunit (in tan) of the dimer. Other dimers are partly visible in light-gray. prFMN, shown as stick model, is placed in a deep crevice between the two domains.

prFMN binding:

prFMN is embedded inside a pocket at the bottom of the active site cleft in front of the β -barrel entrance flanked by the N-terminal $\alpha + \beta$ subdomain, α -helix 189:198 and the connecting first α -helix of the oligomerization domain (Figs. 17, 18.A). The prosthetic group is completely buried except for the *re*-side of the modified isoalloxazine ring which is accessible for the substrate from bulk solvent. For binding prFMN to the protein matrix a key role is attributed to the phospho group placed at the entrance of the β -barrel which is hydrogen-bonded with His166NH, Ala222O, Tyr226OH, Glu235OE1 and His189N (Fig. 18.B). The latter is localized at the positively charged N-terminal end of helix 189 - 198. In addition, the phospho group

is coordinated with two ligands assigned as Fe^{2+} and K^+ ions (Fig. 18) according to biochemical data⁶³ and the structural data of other UbiD enzymes⁶⁰. K^+ is octahedrally ligated with Glu235, Ala200, Ala222, Ile167, Val219 and one phospho group (Fig. 18.B). Fe^{2+} is tetrahedrally ligated with His166, His189, Glu235 and one phospho group. In most UbiD enzymes Fe^{2+} is replaced by Mn^{2+} which is octahedrally coordinated, for example, in *A. niger* by the phospho group, His191, Asn168 (instead of His189), Glu233 and two H_2O . Due to the decreased coordination number of Fe^{2+} in Pcd the metal binding site shrinks which is reflected in a ca. 2 Å shifted ribitol and phospho groups of prFMN and a rearrangement of loop 222-229 by ca. 5 Å compared to other structurally characterized UbiD enzymes. Nevertheless, the position of the prenylated isoalloxazine ring is essentially conserved. It is worth to note that ICP-MS (inductively coupled plasma-mass spectrometry) analysis reveals the binding of a second Fe^{2+} and third Fe^{2+} was found in cryo-EM densities of all 3 samples. In the cryo-EM structure two attractive positions for a metal binding site are detected. The second Fe^{2+} would be octahedrally ligated with Arg430, Asp436, Asp476O, Thr478 as well as two H_2O and the third with Glu346, Ile366, Thr342 and two H_2O .

The EM density of Pcd reveals virtually an identical structure for prFMN as the one reported in the high-resolution *A. niger* Fdc1 structure (Fig. 18). No indications were detectable for a partial prFMN ketamine configuration or a hydroxylated non-aromatic ring as found in fungal Fdc1⁶⁰. However, the quality of the map is not sufficient to definitely prove a double bond between N5 and C1' of the flavo-N5 iminium adduct. The prenylated isoalloxazine ring is present in a bent conformation with the central pyrazine ring and the fourth non-aromatic six-membered ring

protruding towards the substrate binding site in agreement with the conformation of prFMN in *A. niger* Fdc1 (Fig. 18). The bent conformation is adjusted by the specific packing of side chains of Asp337, Tyr169, Ser185 and Asn170 adjacent to the xylene and pyrimidine rings and by putting Tyr169 of a loop connecting the barrel strands 171:174 and 164:168 as a backstop for the pyrazine and non-aromatic ring.

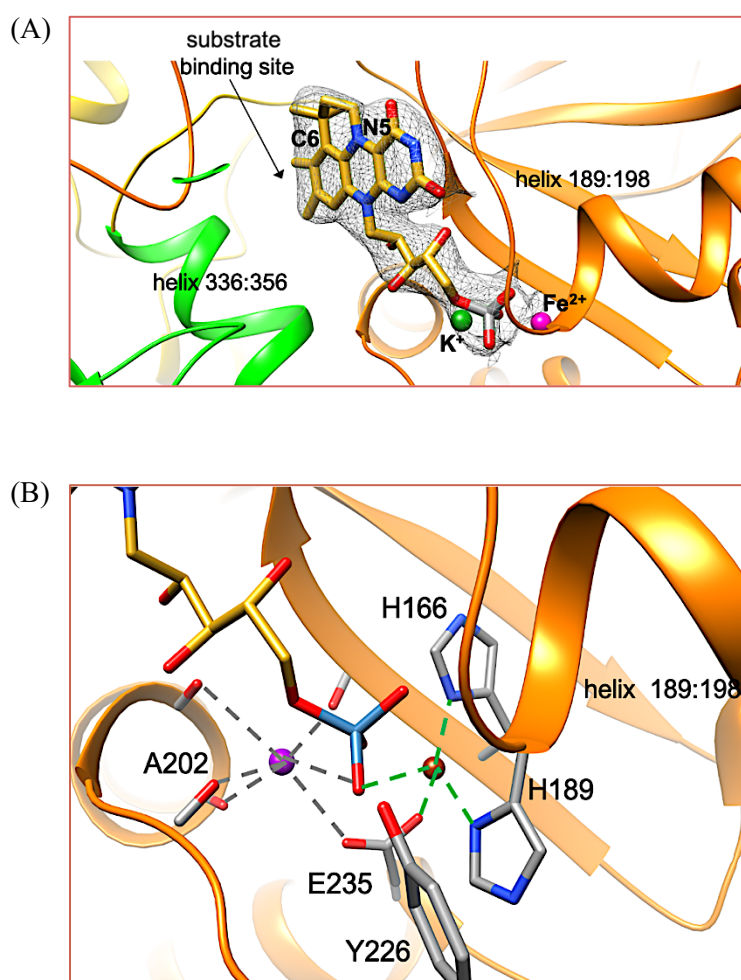


Fig. 18. prFMN binding mode. (A) Global architecture of the prFMN binding site. prFMN (prFMN contains an isoalloxazine ring that is modified by an isopentyl adduct bound to the atoms N5 and C6) is attached to the split β -barrel (orange) containing the N-terminal $\alpha + \beta$ subdomain (yellow) and the oligomerization domain (green). The density of prFMN (in grey) reveals a bent and prenylated isoalloxazine ring. (B) Surrounding of the phosphate binding site. The phosphate is anchored to the polypeptide by two functionally crucial metal ions⁶³, assigned as K⁺ (magenta ball) and Fe²⁺ (brown ball).

Binding of CN-benzoyl-CoA:

The structure of the Pcd - inhibitor complex was determined at 2.1 Å resolution based on 675,429 particles (Table 13). CN-benzoyl-CoA binding is characterized by a straight conformation until the phospho-groups and two 90° kinks before and after the ribose ring such that a hydrogen-bond is formed between the adenine ring and the ribitol (Fig. 19). The inhibitor is embedded in a 25 Å long and narrow channel lined up by the expanded linker (272-309) between the β-barrel strands 265:271 and 310:318, α-helix 189-198 and the preceding loop, the exposed linker (440-471) between strands 436:439 and 472:476 of the oligomerization domain and the loop between strands 375:380 and helix 390-400 protruding from the neighboring dimer (Fig. 19). As documented by the low rms deviations of 0.5 Å, no global conformational changes occur between the inhibitor-free and -bound Pcd structures. Only minor side chain rearrangements are detectable in the preformed substrate binding site with one exception. Segment 440-471 consisting of a short helix and an elongated loop is only visible in the map upon inhibitor binding (Fig. 19) but completely disordered in the absence of the inhibitor. Notably, its incapability to independently form a defined three-dimensional structure was predicted by the prDOS server⁶⁹ (Appendix A). Both conformational states are of functional importance. prFMN and the inhibitor can only reach their binding sites when segment 440-471 is disordered. On the other hand, its rigidification implies an increased number of CN-benzoyl-CoA – polypeptide interactions (Fig. 16) and a completely encapsulated inhibitor until the ribose group (Fig. 19). Compared to other UbiD enzymes the cleft between the domains becomes more closed (by 3-7 Å) and the

segments contacting the inhibitor are slightly sequestered from the active site crevice for providing optimal binding (Appendix B)

CN-benzoyl-CoA and prFMN are arranged in a manner that the catalytically active rings juxtapose in the center whereas the residual tail groups are directed perpendicular to each other (Fig. 19). The benzene ring of CN-benzoyl-CoA face the pyrazine and the six-membered isoprene ring of prFMN; the shortest distances of 3.2 and 3.4 Å are between C4a and C1' of prFMN and C1 and C2 of the aromatic ring, respectively (Fig. 20). The benzoyl ring is kept in its position or perhaps even pressed against prFMN by interactions with the bulky Trp289, Trp373 and Phe449 side chains. The cyano-group is contacted by Phe449, Val332, His295 and Arg171 (Fig. 20). Notably, no hydrogen-bond acceptor is placed in an appropriate distance to the CoA ester carbonyl oxygen. Moreover, Glu297, established in *A. niger* Fdc1 as catalytic acid⁶⁰, is with nearly 7 Å rather far away from C1 of the CN-benzoyl ring which might, however, change in the absence of the CN group. Surprisingly, the three acidic residues Asp372, Asp337 and Asp341 are adjacent to its nonpolar moiety of CN-benzoyl-CoA ring. The carboxylate group of Asp337 and C4 are 3 Å apart from each other.

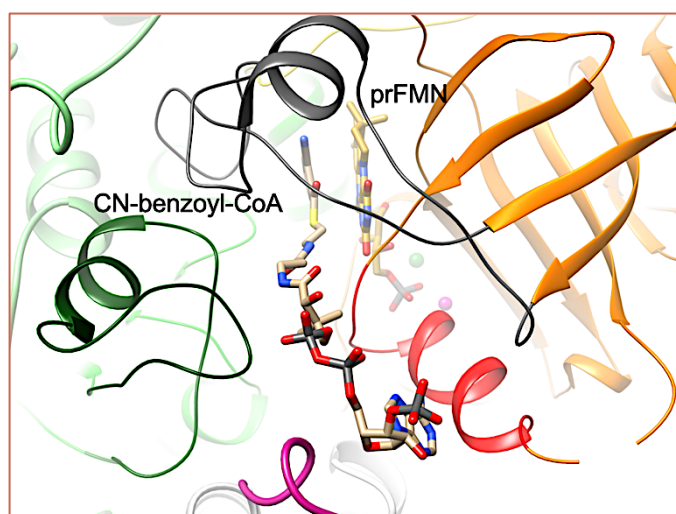


Fig. 19. Binding mode of the inhibitor CN-benzoyl-CoA. prFMN and CN-benzoyl-CoA both as stick models juxtapose each other. The inhibitor sits in a 25 Å long crevice flanked by an expanded linker (272-309) of two β -strands of the central β -barrel (gray), α -helix 189:198 and the preceding loop (red), an irregular segment (440-471) of the oligomerization domain (forest green) and a stretch of the partner dimer of the hexamer (magenta).

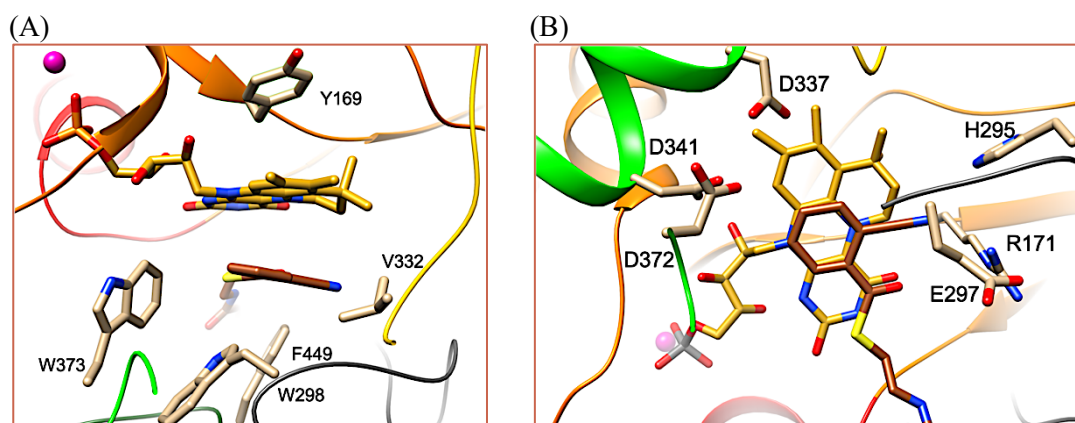


Fig. 20. The active site geometry of the isoalloxazine and 2-CN-benzoyl-CoA rings (A) and 90° rotated (B) The pyrazine of prFMN (gold) and the benzyl ring of 2-CN-benzoyl-CoA (brown) stack almost perfectly and are nearly parallel to each other. Bulky side chains hold the reaction partners in a geometry optimal for catalysis. The cyano-group of the inhibitor and most likely also the similar positioned carboxylate group of the substrate are fixed by interactions with His295 and Arg171. Asp337, Asp442 and Asp372 protrudes towards benzoyl ring of the inhibitor whereas Glu297 points away from the substrate ring.

Binding of Benzoyl-CoA:

The Pcd-benzoyl-CoA structure is globally highly related to that described for the Pcd-CN-benzoyl-CoA complex. In addition, the mutual orientation between prFMN and benzyl rings is maintained confirming the conclusions from the Pcd-CN-benzoyl-CoA complex although the product is weaker occupied than the inhibitor. The only major difference is the split conformation of the Glu297 side chain which points either away from the active site (as seen before) or alternatively towards the product ring. Then, the distance between the carboxylate oxygen and the C2 of benzoyl-CoA becomes 3.0 Å. Concomitantly, the His295 side chain, interacting with the cyano-group of CN-benzoyl-CoA in the Pcd-inhibitor complex, rotates 60° and forms a hydrogen bond with the Glu297 carboxylate group.

4. Discussion

The anaerobic degradation of industrially produced but environmentally harmful phthalate esters-based plastics involves a phthaloyl-CoA decarboxylase for executing the crucial non-oxidative aromatic decarboxylation reaction (Fig. 11). The homo-hexameric enzyme belongs to the subfamily of UbiD enzymes that differs from other family members structurally characterized yet, by its large substrate, its double bond as part of an aromatic system activated by a CoA ester and the necessity of an O₂ independent maturation of its prFMN_{iminium} ring. According to the structural data CN-phthaloyl-CoA is embedded in a narrow channel fixed by multiple contacts with the protein matrix in contrast to the wide cleft found in other UbiD enzymes (Fig. 19). The tight packing of the reaction partners in a completely encapsulated active site

channel is substantially provided by an adjacent dimer involved in CoA binding and the partner subunit of the dimer that holds in place the expanded linker segments 295-305, 368-374 and 440-471 attached to CN-phthaloyl-CoA. These findings rationalize the importance of the hexameric state for some UbiD enzymes, in particular, for those binding CoA-based substrates. The described fixed active site geometry may adjust a strained ring conformation to promote catalysis.

The maturation of prFMN by oxidizing the N5-C1' single bond to an iminium double bond by O₂⁶² is not applicable in an anaerobic environment. The determined EM structure of Pcd is compatible with the established catalytically productive prFMN_{iminium} form albeit unprovable at the current resolution⁶³. One hypothesis for O₂-free maturation suggests that two irons are initially bound in the oxidation state +3. After transient binding of the premature prFMN two electrons are transferred from the N5-C1' single bond to Fe³⁺ by an unknown mechanism forming Fe²⁺. The Pcd structure highly supports an iron localized at the phosphate binding site of prFMN 12 Å apart from the N5-C1' bond while the second and third putative metal binding sites are 12 and 26 Å apart and the nature of the metal is open.

Mechanistically, the non-oxidative decarboxylation reaction of an α,β -unsaturated acid proceeds via an 1,3 dipolar cycloaddition as established for the ferulate and cinnamate decarboxylating UbiD enzyme Fdc1⁶⁰ of *A. niger*. C1' of prFMN and C _{α} of the substrate (related to the carboxylate) and C4a of prFMN and C _{β} are covalently linked in a concerted process forming a pyrrolidine adduct (Fig. 20). In contrast to a pericyclic process the 3,4 dihydroxybenzoic acid decarboxylase of *Enterobacter cloacae* decarboxylating an aromatic catechol substrate only forms a single covalent bond between the C _{α} of a quinoid species and the C1' of prFMN⁷⁰.

However, a quinoid-based mechanism is only applicable to phenolic substrates and therefore not for phthaloyl-CoA. The determined Pcd-CN-benzoyl-CoA complex provides a detailed geometric framework for the catalytic reaction based on the assumption that the substitution of the cyano-group of the inhibitor to the carboxylate group of the substrate does not induce significant conformational changes of the reaction partners. Superposition of the substrate onto the inhibitor supports a highly similar binding as the carboxylate do not interfere with the polypeptide and their negative charge can be neutralized by hydrogen-bonds with Arg171 and His295. In the Pcd-inhibitor complex the reacting atoms C1 (C_α) and C4a as well as C2 (C_β) and C1' of the facing phthalate and pyrazine rings are stacked above each other resulting in the shortest distances between these atoms of the rings (see Fig. 20). Consequently, a dipolar 1,3 cycloaddition appears to be also the most attractive option for phthalate-CoA decarboxylation (Fig. 21). Like Fdc1⁶⁰, Pcd has, potentially, the capability to perform a Michael addition reaction due to the azomethine ylide element of prFMN and to facilitate bond formation to C4a by stabilizing the negative charge at the uracil N1CO group via the conserved Ser185, Asn170 and ribitol-3-OH (Fig. 20, 21). The challenging dearomatization step might be supported by a strained pre-reaction geometry, the electron-withdrawing thioester and carboxylate groups as well as several surrounding acidic residues that might destabilize the electron-rich aromatic ring (dearomatization energy of benzene is 35 kJ/mol).

Several alternative mechanistic solutions were also checked. The most attractive scenario is based on the modification of the 1,3 cycloaddition reaction, which was stimulated by the surprising accumulation of negatively charged residues at the hydrophobic part of the phthalate ring (Figs. 20, 21). This mechanism includes an

allylic rearrangement at the unsaturated substrate ring and thus avoids the second dearomatisation step which is even more delicate than the first one due to the absence of the electron-withdrawing carboxylate group. Another feasible scenario represents an 1,5 dipolar cycloaddition, described in organic chemistry, which would place the CoA thioester into the center of catalytic process. However, this option is not favored because of the suboptimal geometry of the facing rings. The substrate thioester group faces the uracil ring of prFMN and the distances between the carbonyl carbon and C4a and between O and C1' are with 3.5 and 3.6 Å, respectively, longer than for the reacting atoms of the 1,3 cycloaddition. In addition, we searched for a possibility to involve a thioester anion transition. However, no convincing solution was found and the absence of proton donors next to the carbonyl oxygen also does not argue for such a scenario. So far, it appears that the thioester has no central catalytic function but is, of course, crucial for substrate binding as part of CoA.

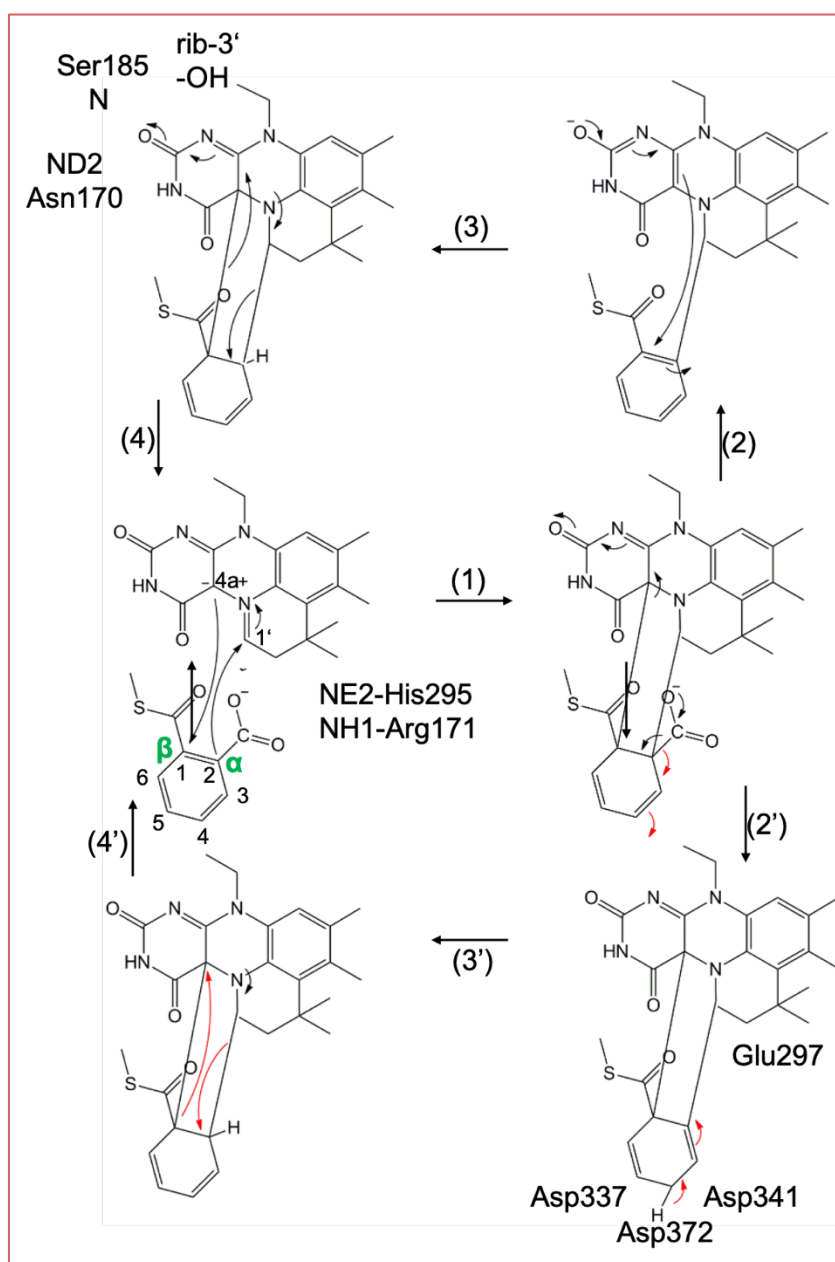


Fig. 21. Catalytic cycle of the phthaloyl-CoA decarboxylation. Two 1,3 cycloaddition reaction (1-4) are compatible with the geometry of the reaction partners. A plausible alternative is an allyl 1,3-rearrangement (1,2',3',4') which avoids the second, more challenging dearomatization step. The latter scenario was stimulated by three acidic residues next to C4 of 2-CN-phthaloyl-CoA.

Chapter B. Ldh/EtfAB

1. Introduction

Glucose fermentation generates lactate, which is further oxidized to the central cellular metabolite pyruvate. However, lactate oxidation by the standard electron acceptor NAD^+ provides a severe thermodynamic problem for all organisms. The reduction potential of pyruvate/lactate ($E_m = -190 \text{ mV}$) pair is much higher than that of the NAD^+/NADH ($E_m = -320 \text{ mV}$) pair such that the reaction cannot proceed under standard conditions. Mammals use NAD-dependent L-lactate dehydrogenase, which is located at the outer side of the inner mitochondrial membrane and associated with a monocarboxylate permease and cytochrome c oxidase, forming the “lactate oxidation complex”^{71,72}. In aerobic bacteria, the reaction is powered by a cytoplasmic FAD- or FMN-containing lactate dehydrogenase module associated with a membrane-spanning modules of the respiratory chain carrying menaquinone or ubiquinone⁷³. In anaerobic bacteria, lactate is oxidized to pyruvate by NAD^+ reduction using a reverse FBEB or electron confurcation reaction for driving this endergonic reaction⁹. Pyruvate is further degraded via acetyl-CoA to acetate. In the model organism, *Acetobacterium woodii*, Fd_{red} is generated by the Rnf complex using NADH as electron donor, coupled to the downhill transport of Na^+ into the cell⁷⁴ (Fig. 22). Ldh/EtfAB complex from *A. woodii* could be purified as moderately stable protein complex⁷⁵. Ldh, EtfA and EtfB carry one FAD each termed l-FAD, a-FAD and b-FAD. In addition, the EtfA subunit possesses an Fd-like domain with one [4Fe-4S] cluster in its N-terminus. Due to the reversibility of the reaction both bifurcation and confurcation could be experimentally

demonstrated⁷⁵. Structural and mechanistic studies were performed in cooperation with the group of Prof. Volker Müller, Goethe University, Frankfurt, Germany.

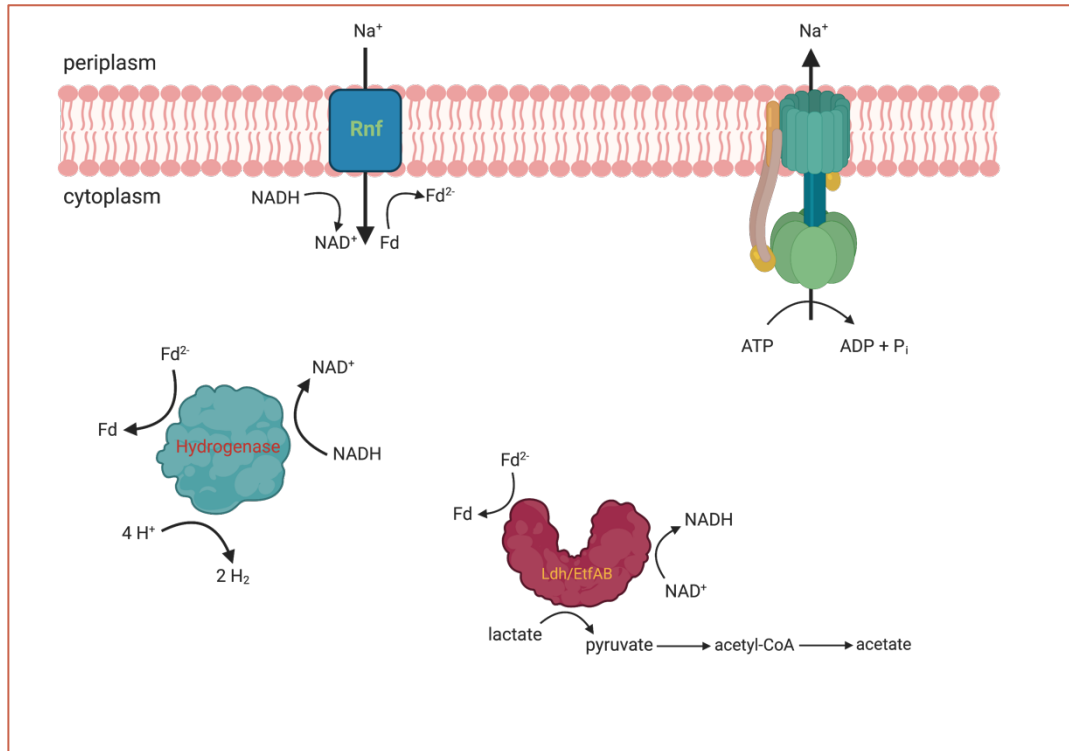


Fig. 22. Lactate fermentation pathway in *Acetobacterium woodii*, involving the Ldh/EtfAB complex. Note: protein illustrations aren't size adjusted. Created with BioRender.com

2. Materials and Methods

2.1 Gene expression, protein purification and cross-linking

Freshly purified, cross-linked (Section VII-Q) samples were provided at 4 °C by Alexander Katsyv and Prof. Volker Müller, Goethe University, Frankfurt am Main. Ldh/EtfAB complex was purified using the same protocol described in Section VII-L. Without cross-linking the proportion of intact Ldh/EtfAB complex was too low for cryo-EM studies. Several trials of cross-linking (general description in Section VII-Q) just before the EM experiment were also not successful. Sample quality was only sufficient for single-particle negative-staining and cryo-EM data collection when using 1 mM BS³ chemical cross-linker after the first size-exclusion chromatography and then purified again using a second size-exclusion chromatography to differentiate cross-linked and uncross-linked samples. The protein sample provided was at a concentration of ca. 1 mg/ml in a buffer with composition 50 mM Hepes, 150 mM NaCl, 5% glycerol, 10 uM FAD, pH 7.5.

2.2 Single-particle negative-staining

Freshly purified and cross-linked Ldh/EtfAB sample, with concentration of around 8 µM, was diluted 1:100, to reach a concentration of around 80 nM, suitable for negative-staining EM. 3 µl of the diluted protein sample was added onto the grid (as described in section VII-S(a)), stained 3 times using uranyl formate (UF) and then washed 3 times with ddH₂O, before blot drying with Whatman filter paper #40. This grid was then checked using the FEI Tecnai Spirit 120 kV microscope under low

electron dose. Several micrographs were collected manually at 42,000x magnification with a pixel size of 2.68 Å to analyze and check the sample quality, including homogeneity and particle intactness for further cryo-EM sample preparation.

2.3 Single-particle cryo-EM sample preparation and data collection

Freshly prepared BS³ cross-linked sample with a concentration of ca. 1.8 mg/ml (8.18 μM) was used to prepare cryo-grids. The grids were prepared according to the aforementioned detailed protocol described in section VII-S(b).

Grids were loaded on a Titan Krios G3i (FEI-ThermoFisher Scientific Inc., NL) operating at 300 kV equipped with a Gatan K3 direct detector and an energy filter at a slit width of 30 eV. The major change concerns the parameters of data collection. For the Ldh/EtfAB sample a stack of 9,788 movies was collected with 105 frames over 6.52 seconds of exposure time giving a high electron dose of ca. 106 e⁻/Å². The under-focus values were set between 1.2 to 2.1 μm. Further more specific details of data collection and processing can be checked from Table 14.

Table 14. Data collection, processing and refinement statistics of Ldh-Etf complex cryo-EM structure. Note: values are not final as the refinement is still ongoing.

Experimental data	
Protein	Ldh-Etf complex
State	Resting (D-state)
Data collection and Processing	
Microscope	FEI Titan Krios G3i
Voltage (kV)	300
Camera	Gatan K3 summit
Exposure time (s)	6.52
Total dose ($e^-/\text{\AA}^2$)	106.17
Dose per frame ($e^-/\text{\AA}^2$)	1.01
Defocus range	1.2-2.1
Pixel size (\AA) (calibrated)	0.837
Magnification (nominal)	105,000x
Symmetry imposed	C2
No. of micrographs	9,788
Initial particle number	5,517,853
Final particle number	674,283
Map resolution (\AA)	2.43
FSC threshold	0.143
Refinement	
Map-sharpening B factor (\AA^2)	-67
Model composition	
Chains	12
Protein (Residues)	2,136
Ligands	FAD: 6; FE: 2
RMSD Bond Length (\AA)	0.005
RMSD Bond Angles ($^\circ$)	0.969
MolProbity score	2.77
Clash score	12.52
Ramachandran plot (%)	
Favored	91.90
Allowed	8.00
Outliers	0.09
Rotamer outliers (%)	7.65
ADP (B-factor) (min/max/mean)	
Protein	55.10/151.34/90.55
Ligand	60.58/93.36/79.23

3. Results

3.1 Single-particle negative-staining and cryo-EM analysis

After diverse sample optimization attempts with changes in protein purification and protein stabilization, guided by negative-stain single-particle analysis, monodispersed samples of the Ldh/EtfAB complex from *A. woodii* were obtained in single-particle cryo-EM experiments.

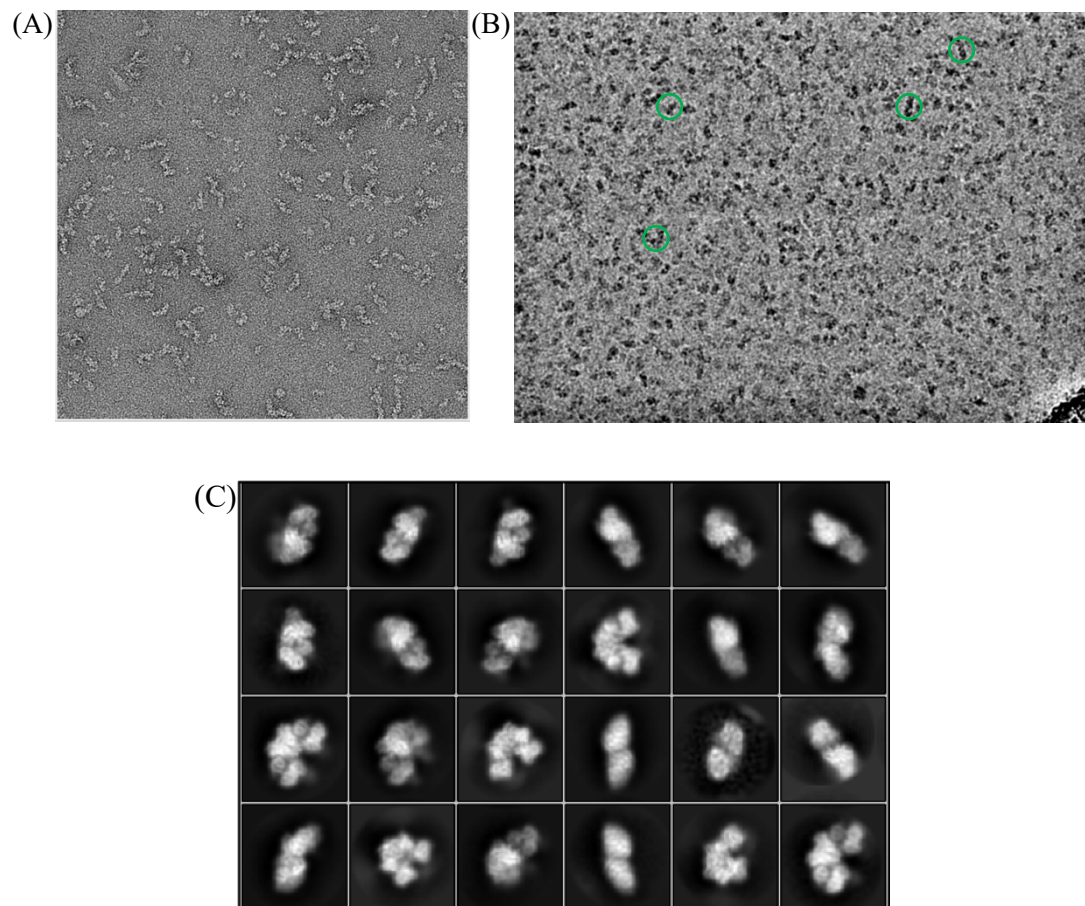


Fig. 23. (A) An exemplary micrograph from single-particle negative-staining, showing white particles on a grey background, stained using uranyl formate for staining. (B) An exemplary cryo-EM micrograph, low-pass filtered to 5 Å, few protein particles are marked by green circles. (C) Selected cryo-EM 2D classes depicting different protein orientations, produced by reference-free 2D classification in Relion.

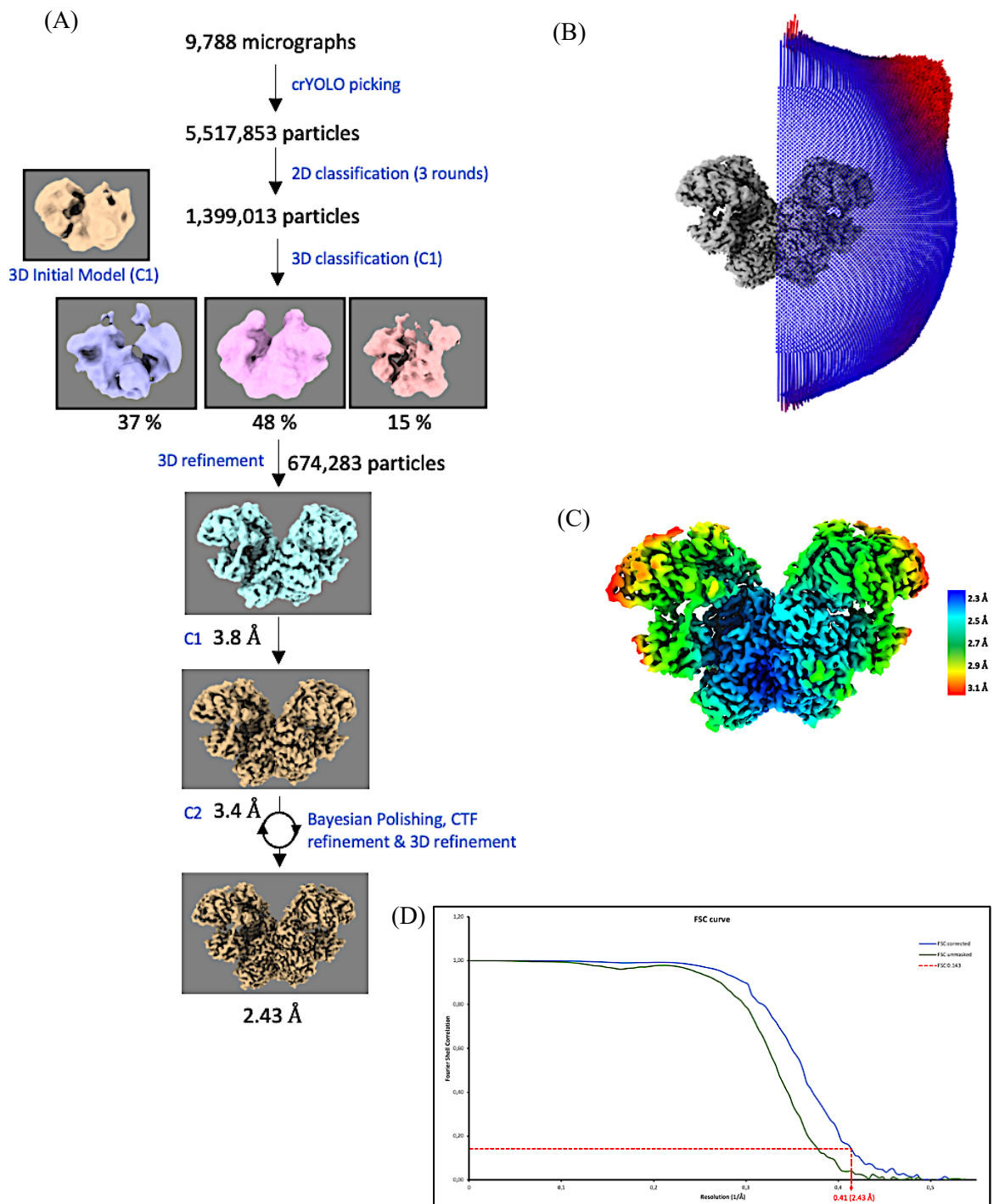


Fig. 24. (A) Relion image processing workflow for refinement of Ldh/EtfAB complex at 2.4 Å resolution. (B) Final refined cryo-EM map overlapped with the Euler angle distribution. (C) Ldh/EtfAB complex cryo-EM map color-coded with the local resolution. (D) Gold-standard FSC plot of the final cryo-EM map. Resolution estimated at FSC=0.143.

3.2 Ldh/EtfAB complex analysis

The cryo-EM structure of the Ldh/EtfAB complex from *A. woodii* was determined from a sample, cross-linked with BS³. The 2.4 Å two-fold averaged density map revealed a (Ldh/EtfAB)₂ hetero-hexamamer with a molecular mass of 252 kDa (Fig. 25), which agrees with the value derived from size-exclusion chromatography profile, native-PAGE analysis and Mass photometry.

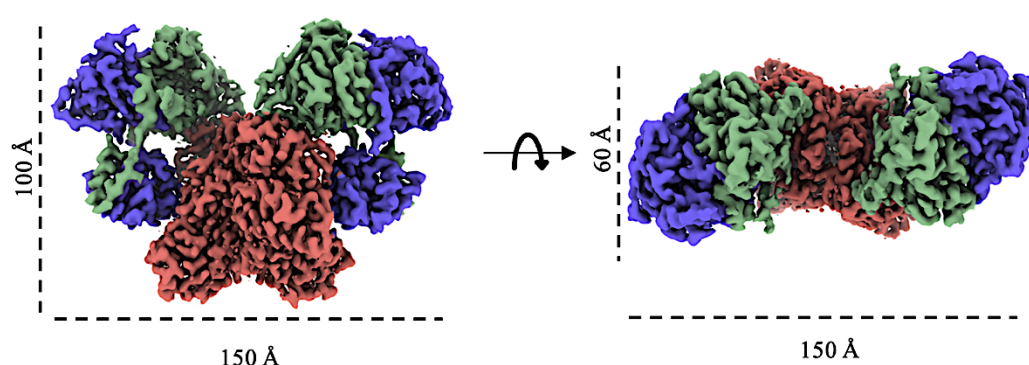


Fig. 25. Single-particle cryo-EM map showing overall complex structure, dimensions and the subunit arrangement. Ldh subunits are marked in maroon, EtfA in purple, EtfB in green.

The subunit Ldh belongs to a flavoenzyme family with p-cresol methyl hydroxylase⁷⁶, vanillyl-alcohol oxidase⁷⁷, MurB⁷⁸ and membrane-associated Ldh⁷⁹ as their prototypes⁸⁰. Their rms deviations from Ldh of *A. woodii* are 2.6 Å, 2.6 Å, 3.4 Å and 2.4 Å, respectively. Accordingly, Ldh is built of two domains, an N-terminal FAD domain (1-218) subdivided into two $\alpha + \beta$ subdomains, a cap domain (218-417) composed of an extended antiparallel β -sheet element and a C-terminal extension (417-467) attached to the FAD domain (Fig. 26). Except for membrane-associated Ldh, this flavoenzyme family operates with a homo-dimeric state as basic functional unit (Fig. 25). Its FAD (l-FAD) is embedded between the two subdomains of the FAD

domain as reported for other family members (Fig. 27). Only the isoalloxazine ring protrudes beyond the FAD domain towards the cap domain. In the (Ldh/EtfAB)₂ complex two hydrogen-bonds are formed between the flavin N3C2O group and the Gly153 CONH peptide amide and between the flavin N5 and Gly138NH. Despite the formation of van der Waals contacts to Glu37, Thr78, Leu80, Pro137, Glu139, Ala152, Glu422 and His423 (cutoff 4.0 Å) the isoalloxazine is only weakly shielded from bulk solvent compared to other family members. In front of the *si*-side of the isoalloxazine ring the FAD and cap domains line up a cavity that serves as the substrate binding site. Lactate/pyruvate can easily reach its oversized binding site by passing a wide gate framed by Gly138, Met144 and Gly329. Not surprisingly, the substrate binding sites are most related to that of the membrane-associated Ldh. Residues like Asp346, His377, Asn382, His384, Glu422 and His423 involved in lactate binding and lactate oxidation are well conserved (Appendix C). Because of the shift of helix 319:337 towards FAD the substrate-binding cavity of the membrane-associated Ldh is shrunk compared with that of the bifurcating Ldh/EtfAB. It is worth to note, that a metal binding site is reliably detected in the substrate cavity ligated by His377, His384, Glu422 and a water molecule. We tentatively assigned the metal as Fe²⁺ due to its addition during purification. Also, worth mentioning is an unexplained density in front of the 1-FAD whose profile fits to the structure of pyruvate (lactate). Its carbonyl oxygen hydrogen-bonded with H423 would be 3.6 Å apart from N5 and its carboxyl groups would be in hydrogen-bond distance to the water coordinated with the putative Fe²⁺,

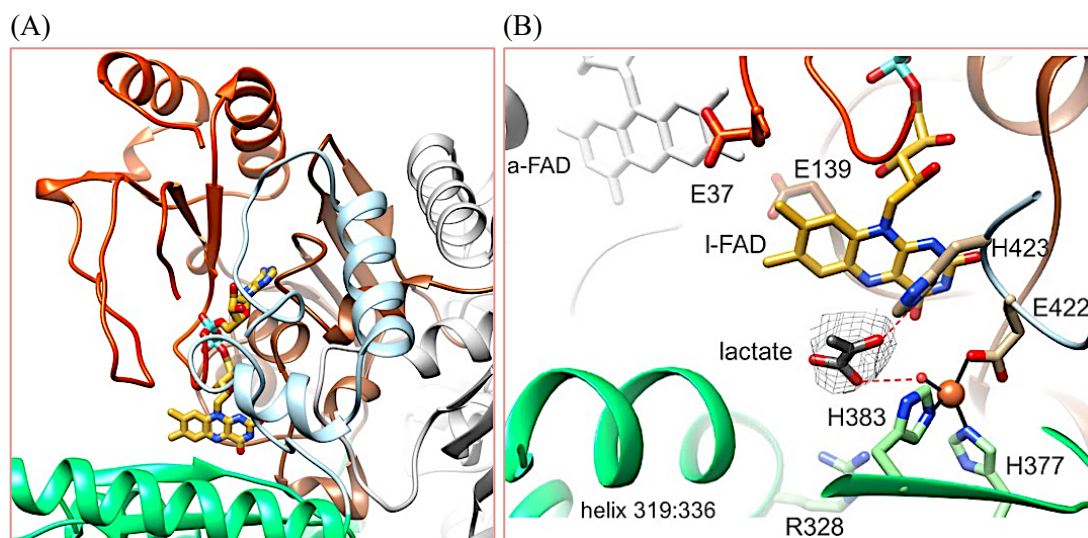


Fig. 26. Structure of the Ldh subunit. (A) Overall structure. The FAD (as stick) is sandwiched between the two subdomains (in orange and brown) of the FAD domain. The isoalloxazine ring sits between the FAD and the cap domains (green). The C-terminal extension is shown in light-blue; the partner subunit of the Ldh dimer in grey. (B) Active site region. In van der Waals contact to the N5 of the isoalloxazine is an unknown density (gray mesh), whose shape fits remarkably well with the profile of pyruvate or lactate (carbon in grey). In hydrogen-bond contact to the substrate binding site lies a binding site for a metal tentatively modelled as Fe^{2+} .

The bifurcating EtfAB module of the $(\text{Ldh/EtfAB})_2$ complex reveals the same architecture as reported for other bifurcating⁸¹⁻⁸³ and non-bifurcating EtfAB complexes. Briefly, the heterodimer is built up of a rigid base composed of the tightly associated, structurally related N-terminal domains of EtfA and EtfB termed domains I (62-269) and III (2-236) and a highly mobile domain II formed by the tightly associated C-terminal flavodoxin-like segment of EtfA (270-398) and the C-terminal arm of EtfB (237-265) (Fig. 27). The only distinguishing feature in the current structure, is the orientation of domain II relative to domain I and III base. The polypeptide environment of b-FAD is highly conserved (Appendix C, EtfB).

Prominent interactions occur between Arg205 and FAD-N5 and between Val95 of the N-terminal end of helix 95:108 and FAD-O2. Likewise, the microenvironment of a-FAD is also related to other family members but also shows a few relevant deviations. While SerA328 is further hydrogen-bonded with N5 and presumably the 2-OH ribose of FAD as well as Arg311 with the N1C2O group, the His-to-Phe exchange at position 348 and the presence several acid residues (see below) may modify physicochemical properties of the isoalloxazine ring.

The N-terminal ferredoxin domain of EtfA is highly disordered in the (Ldh/EtfAB)₂ complex and could not be traced, although the position of the ferredoxin could be clearly localized. Even the approximate position of the [4Fe-4S] cluster remains vague.

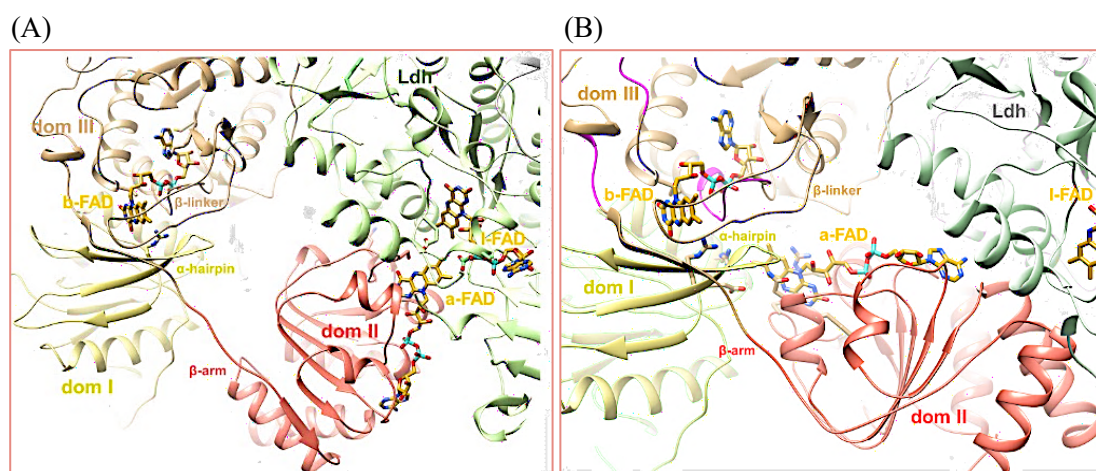


Fig. 27. Structural states of the Ldh-EtfAB complex. (A) The experimentally characterized D-state. Domain II is adjusted in a conformation that adjusts the a-FAD of domain II and the l-FAD of Ldh are in an electron-conducting distance of 3.7 Å. Domain II is spatially separated from the EtfAB base solely connected by two solvent-exposed linkers. a-FAD and b-FAD are ca. 37 Å apart from each other. EtfA domain I, EtfB domain III, EtfA domain II and Ldh are drawn in yellow, tan, salmon and light-green, respectively. (B) The modelled B-state. Domain II is rotated from the D-state to induce an electron transfer event between a-FAD and b-FAD. The isoalloxazine ring of a-FAD is positioned in a shallow crevice between domains I and III with the xylene ring pointing towards its counterpart of b-FAD.

Characteristic features of the overall structure:

The (Ldh-EtfAB)₂ complex is architecturally constructed in a manner that the Ldh dimer forms the core and two EtfAB modules are peripherally associated leading to an overall size of 150 Å x 100 Å x 60 Å (Fig. 25). Exclusively, the Ldh subunits provide the interface between the two Ldh/EtfAB protomers. In accordance with the X-ray structures of the Bcd/CarC-EtfAB complexes^{82,84}, the cryo-EM structure reveals both protomers of the (Ldh/EtfAB)₂ complex in the resting D (dehydrogenase-conducting) state (Fig. 27). In this state, domain II is essentially attached to Ldh which allows an electron transfer between l-FAD and a-FAD. In the D-state, domain II is spatially separated from the EtfAB base solely connected by two solvent-exposed linkers. a-FAD and b-FAD are ca. 37 Å apart from each other. In contrast, electrons are conducted between a-FAD and b-FAD in the B (bifurcating) state implicating a rotation of domain II and the formation of an interface between domain II and the EtfAB core (Fig. 27). No population of protein in that B-state was found by the analysis of the cryo-EM micrographs.

The D-state is characterized by two interfaces between one Ldh subunit and domain II and III of one EtfAB module (Fig. 27). In comparison, two different Bcd/CarC subunits of the Bcd/CarC-EtfAB tetramer are involved in forming two contact points to EtfAB. The first interface between Ldh and domain II of EtfA is centered around l-FAD and a-FAD which are in van der Waals contact to each other (Fig. 28). The distance of 3.7 Å between the adjacent nonpolar dimethylbenzyl moieties of the isoalloxazine rings ensures a rapid one-electron transfer. In comparison, the corresponding FADs in the Bcd/CarC-EtfAB complex are separated by a phenylalanine side chain resulting in an inter-flavin edge-to-edge distance of 8.5

Å^{82,84}. An unusual feature of the D-state of the Ldh-EtfAB complex is the presence of Glu37 and Glu139 of Ldh flanking the dimethylbenzyl groups of both FADs (Fig. 28.A). The acidic side chains may be applied to destabilize the negatively charged FAD^{•-} or FADH⁻ states. This feature is unique in dehydrogenase-EtfAB complexes or the Ldh flavoenzyme family. Cresol hydroxylase, vanillyl-alcohol oxidase and alkyldihydroxyacetonephosphate synthase/ membrane-associated Ldh use the hydrophobic residues phenylalanine, tyrosine and tryptophane that adopts a shielding function. Encapsulation of the isoalloxazine ring from bulk solvent is either provided by segments fused to the N-terminus or by an additional subunit as the cytochrome subunit of p-cresol hydroxylase. Above and underneath the isoalloxazine rings of the first interface lies a hydrophobic and hydrophilic contact patch involving the FAD and cap domains of Ldh and a single salt bridge between ArgA285 and AspC32 (Fig. 28.A).

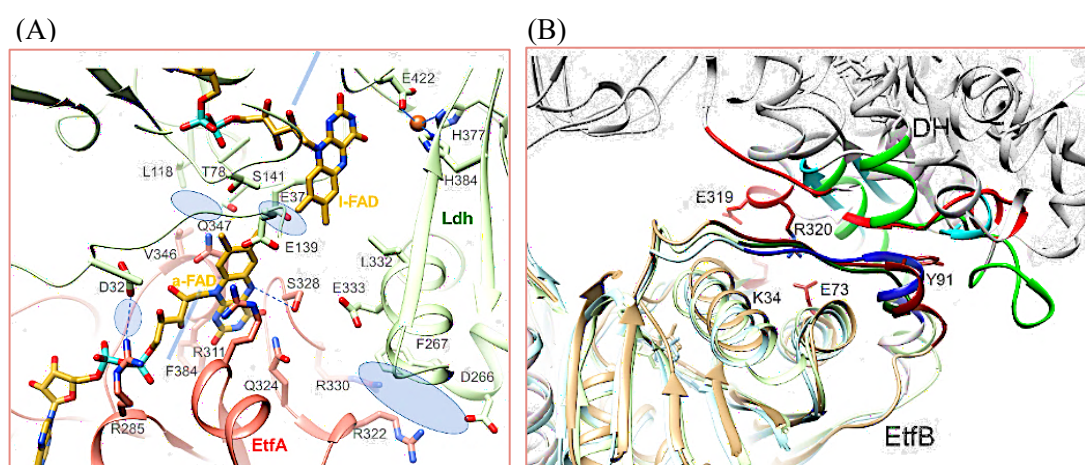


Fig. 28. The Ldh/EtfAB interfaces. (A) Contact region between Ldh and domain II in the D-state. The major contact point is formed around the α -FAD and I-FAD, which are in van der Waals contacts to each other. Three minor contact regions are marked by blue ellipses. One of them is only formed by a salt bridge between ArgA285 and AspC32. (B) Contact region between EtfB domain III and Ldh formed in B- and D-states. The EtfB domain is shown in orange; the recognition loop in red. A comparison with the Bcd/EtfAB (light blue and dark

blue) and the median chain acyl-CoA dehydrogenase-EtfAB complexes (light green and dark green) indicates high overall similarities and in the structure of the recognition loop. This is astonishing as the corresponding interface segments (red, green, blue) of the dehydrogenase subunits (grey) are completely different.

The second contact point serves as a fixed anchor between Ldh and EtfAB formed in the B- and D-state (Fig. 28.B). The static anchor is formed by a small segment (B185-B193) composed of an elongated loop and a short helix which is strictly conserved in bifurcating and non-bifurcating EtfABs and referred to as recognition loop^{85,86}. As reported for non-bifurcating EtfAB the elongated side chain of TyrB119 protrudes into hydrophobic pocket (AlaL301, ValL312, IleL314, LeuB195). A second small hydrophobic patch is formed between LeuB188, ProC273, LeuC277, ValC315 and ValC324 and two specific salt bridges are formed between LysB34 and GluC319 and between GluB73 and ArgC320 (Fig. 28.B). The limited number of hydrophobic interactions of the Ldh/EtfAB complex interface may be responsible for the found fragility of the Ldh/EtfAB hetero-hexamer.

The D-states in the Ldh/EtfAB and Bcd/CarC-EtfAB complexes are highly related although domain II is a few degrees more rotated in the latter. The resulting displacement of the isoalloxazine rings of ca. 11 Å is due to the necessity to form different interfaces between domain II and the Ldh and Bcd/CarC modules. The only major structural difference between the EtfAB modules of the Ldh/EtfAB and Bcd/CarC-EtfAB complexes is a shift of the EtfB protrusion of nearly 15 Å towards the anchor of the EtfB arm in Ldh/EtfAB which partly shields b-FAD and perhaps influences NAD⁺ binding. This substantial conformational change might also be influenced by helix 321-332 of Ldh which partly interferes with the EtfB protrusion.

In the current conformation NAD^+ cannot directly access to the frontside of b-FAD as its binding site is blocked by ThrB226 and ValB228.

4. Discussion

Enzymatic mechanism:

The $(\text{Ldh/EtfAB})_2$ complex contains two active sites 32 Å apart from each other that appears to operate independently. The presented data are compatible with a mechanistic scenario for the FAD-based electron-confurcating process starting from the D-state. (1) Lactate is first oxidized to pyruvate (-190 mV) via a hydride transfer to l-FAD. The redox potential of the Ldh reaction is 150-200 mV lower than that of the Bcd/CarC reaction, requiring differently adapted FADs. By implementing the acidic residues GluC93 and GluC139 adjacent to isoalloxazine the reduced FADH^- state might be destabilized and the redox potential decreased. (2) One electron of l-FADH^- rapidly flows to a-FAD thereby generating $\text{l-FAD}\cdot^-$ ($\text{l-FADH}\cdot$) and $\text{a-FAD}\cdot^-$ ($\text{a-FADH}\cdot$). (3) Domain II is rotated into the B-state perhaps induced by the repulsion of the negatively charged flavins, by NAD^+ and/or Fd_{red} binding. (4) Fd_{red} binding triggers a conformational change of the highly mobile ferredoxin domain of EtfA which has to be postulated to adjust an electron transfer distance between b-FAD and the [4Fe-4S] cluster in the range of 14 Å. Currently, we estimate a distance between b-FAD and the [4Fe-4S] cluster of EtfA is ca. 25 Å. Fd_{red} binds in the vicinity of the ferredoxin domain of the EtfA. As the distance between b-FAD and the [4Fe-4S] of the EtfA is ca. 25 Å in the present structure, a conformational change of the highly mobile ferredoxin domain of the EtfA has been postulated to adjust a distance of ca.

14 Å. Then, Fd_{red} fires one electron via the [4Fe-4S] cluster of EtfA to the bifurcating b-FAD. (5) If produced, the energy-rich $\text{b-FAD}\cdot^-$ is instantaneously reduced to b-FADH^- upon protonation by electron transfer from $\text{a-FAD}\cdot^-$ of domain II which already waits in the productive distance to b-FAD. Both one-electron donation processes proceed in a strictly concerted fashion. The $\text{b-FAD/b-FAD}\cdot^-$ and $\text{b-FAD}\cdot^-/\text{b-FADH}^-$ redox potentials are estimated to be < -700 mV and > 200 mV, respectively, such that the first endergonic and slow electron transfer is pulled by the second exergonic therefore termed as escapement-type mechanism. (6) The nicotinamide ring of NAD^+ attached parallel to the isoalloxazine ring becomes reduced by transferring a hydride from N5 of FADH^- to C4 of NAD^+ . (7) Perhaps upon release of NADH and/or Fd_{ox} domain II rotates back into the D-state and uptakes the remaining electron of $\text{l-FAD}\cdot^-$ ($\text{l-FADH}\cdot$). In analogy to the first round domain II carrying $\text{a-FAD}\cdot^-$ is rotated into the B-state, b-FAD is again reduced by Fd_{red} and $\text{a-FAD}\cdot^-$ and finally a second NAD^+ is reduced to NADH.

This process preferentially runs in the direction of lactate oxidation but the reverse FBEB reaction towards pyruvate reduction also proceeds albeit with a 10 times lower rate. According to the Gibbs free energy of the biochemical reaction, the thermodynamic equilibrium lies on the side of lactate and ferredoxin oxidation and the NAD^+ reduction.

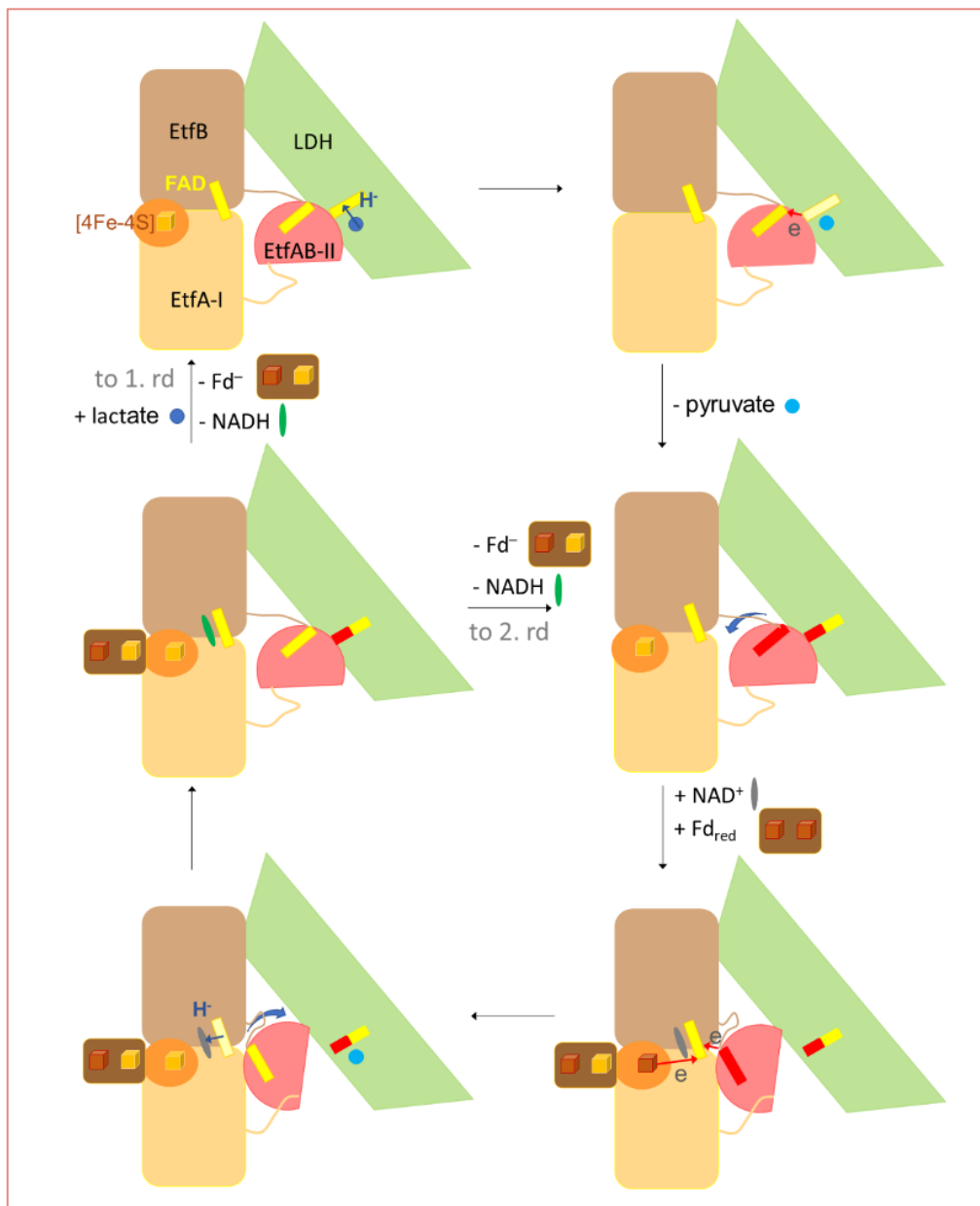


Fig. 29. Mechanism of the $(Ldh/EtfAB)_2$ reaction. The process was outlined in the direction of the thermodynamically preferred conformation direction. The cycle starts from the structurally characterized D state considered as resting state. The reduced ferredoxin Fd_{red} was written in the Fd^{2-} state and after oxidation as Fd^- . The bar of l-FAD drawn with red and yellow ends denotes in the first round $FADH\cdot$ ($FAD\cdot^-$) (red) and in the second round the oxidized FAD (yellow) state.

Chapter C. sHdrA

1. Introduction

Sulfur compounds are used in form of sulfate as electron acceptor (instead of O₂ or nitrate) and elemental sulfur (or other reduced sulfur compounds as dimethylsulfide) as electron donor in the energy metabolism of various microorganisms. One moiety of organisms uses the well-characterized dissimilatory sulfite reductase-based pathway while the other uses recently discovered Hdr (heterodisulfide reductase)-based variant^{87,88}. The Hdr-based pathway is not only present in chemoheterotrophic but also in a wide range of chemo- and photolithoautotrophic sulfur oxidizers acting as a key player for global sulfur cycling. Methanogenic heterodisulfide reductase is an FBEB enzyme that couples the exergonic reduction of the heterodisulfide of CoM-SH and CoB-SH with the endergonic reduction of ferredoxin by using H₂ as an electron donor⁸⁹. In the sulfur-oxidizing Alphaproteobacterium *Hyphomicrobium denitrificans*, operon *HdrAA'hypB1B2C1C2hyp-lbpA* was shown to be essential for the degradation of dimethylsulfide^{88,90}. It was considered that this protein complex may oxidize protein-bound sulfane to sulfite within the framework of the FBEB process. So far, a stable HdrAA'B1B2C1C2 complex could not be prepared⁹¹; however, HdrA of *H. denitrificans*, (termed sHdrA) the subunit harboring the potentially bifurcating FAD was heterologously expressed in *E. coli* BL21 Δ *iscR* strain in carboxy-terminal strep-tagged form and purified by affinity chromatography (Ernst, Kayastha et al.⁹²). In cooperation with the group of Prof. Christiane Dahl, Bonn University, structural studies were performed to gain insights into the function of the sHdrA module and the complete sHdrAA'B1B2C1C2 complex.

2. Materials and methods

2.1. Crystallization

sHdrA from *H. denitrificans* was crystallized with the sitting-drop method at 18°C in an anaerobic chamber (Coy Laboratory Products) with a gas phase of 95% N₂, 5% H₂ (v/v) equipped with an OryxNano crystallization robot (Douglas Instruments Ltd., Hungerford, UK). For crystallization, the protein was dialyzed in a solution of 20 mM Tris/HCl, pH 7.2, 50 μM FAD and concentrated to 20 mg/ml determined by the Bradford method. The quality of the sample was analyzed by SDS-PAGE. Crystals were obtained with JBScreen Pentaerythritol (Jena Bioscience) containing 100 mM MES, pH 6.5, 25% (w/v) PEP 629. As a cryo-protection, before freezing the crystals, PEP 629 concentration was increased to 35% (w/v).

2.2 Crystallography data collection, data processing, structure determination

Yellow-brownish crystals of the iron-sulfur containing flavo-protein, diffracted to ca. 1.4 Å at the beamline PXII at the Swiss-Light-Source in Villigen (Switzerland). A dataset collected at a wavelength of 1 Å was processed with XDS³⁹ (the programs are explained in section S). A second dataset was measured at the iron edge (1.739 Å) up to 2.2 Å resolution. The iron positions of the two [4Fe–4S] clusters in the asymmetric unit were identified by SHELXD⁹³. Phases were determined by using SHARP⁴⁰ and improved by SOLOMON⁴¹. The model was essentially built automatically by using ARP/wARP⁹⁴ and manually refined using COOT⁹⁵. Refinement was carried out with REFMAC5⁹⁶, phenix.refine⁴³ and autoBUSTER⁴² (Phaser; Global Phasing Ltd.,

Cambridge, UK). The quality of the model was evaluated by COOT and MOLPROBITY⁹⁷. Structure comparison calculations were performed with DALI⁹⁸ and surface area calculations by the PISA server⁹⁹. Figures for the manuscript were generated with UCSF Chimera (UCSF, San Francisco, USA)¹⁰⁰. The atomic coordinates and structure factors of sHdrA have been deposited in the Protein Data Bank and can be accessed with PDB ID: 6TJR.

3. Results

3.1 Crystallographic data analysis

The structure of sHdrA was determined at 1.4 Å resolution with R/R_{free} factors of 16.2%/19.1% (see Table 15) by using the single anomalous dispersion (SAD) method for phase determination. The data obtained by crystal diffraction was processed by using several software packages and tools as mentioned in Section 2.2 of this chapter. The results and the statistics of the analyzed data are presented in details in the following Table 15.

3.2 sHdrA structural characterization

Overall structure:

The structure of sHdrA belongs to the family of thioredoxin reductase (TrxR) (Fig. 30.A), which is, architecturally, built up of two classical dinucleotide-binding (Rossmann) domains as originally found for glutathione reductase¹⁰¹. The FAD-binding domain (2-115, 271-341) binds the FAD cofactor at the C-terminal end of the central β-sheet in the canonical manner; the isoalloxazine ring is packed between the two domains (Fig. 30.A). The [4Fe-4S] cluster binding domain (116-270) carries

the [4Fe-4S] cluster between the C-terminal central β -sheet and the N-terminal side of α -helix 180:194. The two redox centers are 9.4 Å apart from each other which allows physiological relevant electron transfer rates between them¹⁰².

Table 15. sHdrA crystallization, data collection and refinement statistics details

Crystal	sHdrA	sHdrA (SAD data)
Crystallization		
Protein solution	20 mg/mL sHdrA, 20 mM Tris-HCl, pH 7.2, 50 μ M FAD	
Crystallization conditions	0.1M MES, pH 6.5 25 % (w/v) PEP 629	
Cryogenic conditions	0.1M MES, pH 6.5 35 % (w/v) PEP 629	
Data collection		
Space group	P6 ₅	P6 ₅
Wavelength [Å]	1.0	1.739
Resolution [Å]	50.0-1.43 (1.481-1.43)	50.0-2.2
Unit cell <i>a</i> , <i>c</i> [Å]	145.6, 64.1	145.4, 64.1
Redundancy	5.8 (2.4)	14.0 (5.8)
Completeness [%]	96.70 (74.02)	94.9 (62.5)
R _{sym} [%]	4.5 (100.5)	5.6 (25.4)
I/ σ (I)	20.1(1.0)	35.5 (8.1)
CC _{1/2}	100 (40.3)	100 (96.3)
Refinement statistics		
Subunits per asym. unit	2	
No. atoms polypeptide, cofactors, solvent	5291, 206, 604	
R _{working} , R _{free} (%)	16.2 (34.5), 19.1 (34.6)	
B _{average} (Å ²) polypeptide, ligands solvent	25.4, 48.7, 33.9	
R.m.s. deviation bond lengths (Å)	0.0155	
bond angles (°)	1.63	
Ramachandran Plot favored, outliers (%)	97.0, 0.59	

The next structurally known relative of sHdrA is the core subunit of the methanogenic Hdr complex (PDB ID: 5ODC) termed mHdrA which binds FAD and the [4Fe-4S] cluster at equivalent positions¹⁰³. Their overall rms deviation is 1.5 Å (337 of 653 residues, sequence identity 32%). sHdrA, in addition, shares a high structural similarity to (low-molecular-mass) TrxR. The lowest rmsd of 3.4 Å (287 of 305; 23%) and 3.4 Å (287 of 303; 19%) has been calculated for the *Thermoplasma acidophilum* (PDB ID: 3CTY) and *Lactococcus lactis* (PDB ID: 5MH4) enzymes, respectively^{104,105}. TrxR normally contains a NADPH instead of a [4Fe-4S] cluster binding site (Fig. 30.B). An exception is the *T. acidophilum* enzyme¹⁰⁴ whose electron donor is unknown. (Low-molecular-mass) TrxR occurs in two structural forms depending on the orientation of the two domains. In the flavin-oxidizing form FADH[•] becomes oxidized after reducing the adjacent disulfide whereas in the flavin-reduced form FAD is reduced by NADPH both via hydride transfer^{106,107}. sHdrA is present in the flavin-reduced conformation.

Both, sHdrA and mHdrA form homodimers in solution characterized by an extended interface of 2470 Å² built up between the two FAD domains and separated between the two [4Fe-4S] cluster domains (Fig. 30.A). In sHdrA, the two isoalloxazine rings, the two [4Fe-4S] clusters, and the FAD and the [4Fe-4S] cluster of the counter subunits, respectively, are 18.8 Å, 11.5 Å and 17.8 Å apart from each other which allows mutual electron exchange. TrxR also oligomerizes to a homodimer, however, the orientation of two monomers differs in comparison with that of sHdrA; their two-fold axes are directed perpendicular to each other (Fig. 30.B). In TrxR, solely the FAD domains constitute the interface. The resulting contact area of 1640 Å² is significantly smaller.

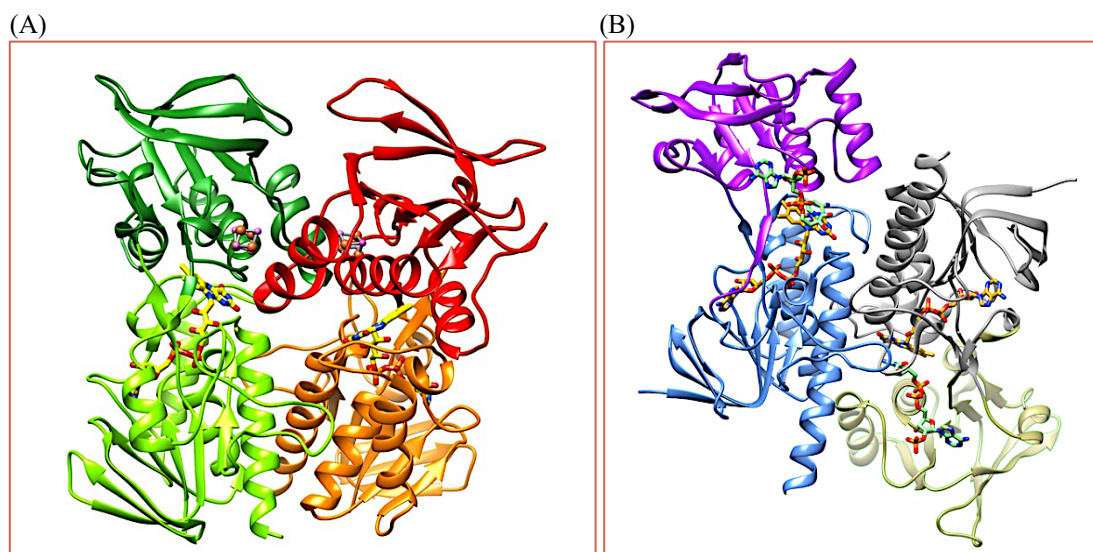


Fig. 30. (A) Structure of the HdrA dimer of *H. denitrificans*. Both FAD domains (in green and orange) and both [4Fe-4S] domains (in lime green and red) form a large contact area. Due to their parallel arrangement the two FAD and the two [4Fe-4S] clusters form an electron conducting unit, **(B) Structure of TrxR.** FAD domains (in blue and grey) form the only contact area. The NADPH domains (in magenta and olive green) do not form any contact surface and are far from each other unlike [4Fe-4S] domains of sHdrA dimer.

The FAD and [4Fe-4S] cluster binding sites:

Despite the shared overall architecture of the FAD-binding site in all TrxR family members¹⁰⁶, the polypeptide segments and relevant side chains contacting the isoalloxazine ring are subjected to substantial conformational changes (Fig. 31). Most notable are the expanded irregular segments 38-55 following strand 26:33 and the segment 131-141 linking the domain. In sHdrA and mHdrA, the isoalloxazine is essentially buried inside the polypeptide scaffold whereas especially in the reduced form of TrxR that binds NADPH the isoalloxazine is accessible from two sides. In sHdrA the isoalloxazine is in a slightly bent conformation mainly adjusted by hydrophobic side chains as Val183, Ile179, Ile322, Tyr45, Leu48 and Val49 pointing

to the *si*- and *re*-face (Fig. 31). The hydrophobic character of the FAD binding site but not individual residues are well conserved between sHdrA and mHdrA (Fig. 31). As sHdrA was produced and crystallized under anaerobic and reducing conditions its flavin is presumably in the reduced FADH⁻ state which is in line with its butterfly conformation. For mHdrA, structurally determined at lower resolution, a deviation of the isoalloxazine ring from planarity was not detectable¹⁰³.

A few but crucial polar interactions are formed between the polypeptide and the isoalloxazine ring in sHdrA (Fig. 31). The functionally important N5 is hydrogen-bonded with a water molecule which is in contact with Lys47-O, Glu137-OE1 and a second water molecule connected with Glu190-OE1. In mHdrA, Lys α 409-NZ anchored in its position by Glu358 is hydrogen-bonded with N5 and O4 (Fig. 31). In comparison, for TrxR enzymes no direct N5-polypeptide interactions but variable water-mediated hydrogen-bonds to variable polar residues are reported. The pyrimidine moiety of the three-membered ring and the protein matrix formed a hydrogen-bond between O2 and Ile322-NH positioned at the N-terminal end of helix 322:340 (see Fig. 31). These interactions are shared among TrxR family members. Moderately conserved interactions between the N3-C=O4 groups and the polypeptide in TrxR enzymes involve main chain peptide nitrogen or carbonyl groups or asparagine side chains. Notably, a further water-mediated hydrogen-bond is formed between O2 and Asp323 in sHdrA and between O2 and Lys α '524 in mHdrA. Notably, Lys α '524 points from the counter mHdrA (marked by an apostrophe) to the pyrimidine ring which is enabled by the different conformation of segment 38:55 of mHdrA compared to sHdrA.

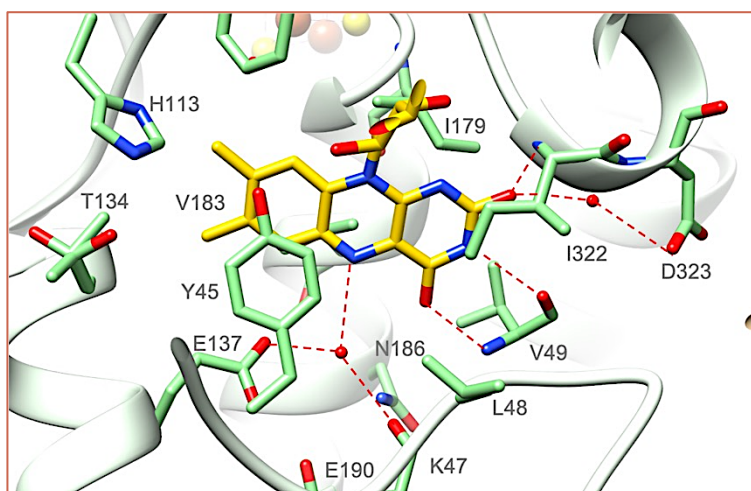


Fig. 31. Structure of the FAD binding site of sHdrA. The carbons of the FAD and the polypeptide are drawn in gold and green, respectively. Hydrogen-bonds are shown as red dashed lines. N5 of sHdrA interacts with hydrogen-bond accepting residues stabilizing FADH⁻ and FADH[•] while N5 of mHdrA is hydrogen-bonded with Lys409 stabilizing the oxidized FAD.

The X-ray structure confirmed the presence of one [4Fe-4S] cluster in line with the sequence prediction and the determined iron content of 2.5 to 3.5 molecules of irons per molecule of sHdrA monomer. The [4Fe-4S] cluster binding is well conserved in sHdrA and mHdrA. The four irons are coordinated with Cys163, Cys176, Cys180 and Cys181 and all sulfurs interact with at least one proton donor (see Fig. 32). Arg167, Arg208 and the partially positive charged N-terminal end of helices 180:195 and 212':225' provide a positively charged binding pocket.

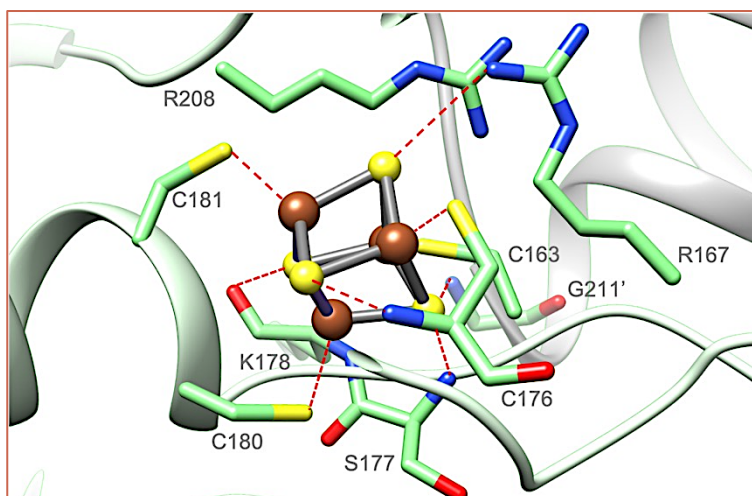


Fig. 32. Structure of the [4Fe-4S] cluster binding mode of sHdrA. The Fe and S of the [4Fe-4S] clusters are drawn in brown and yellow, respectively. The interactions between the iron of the [4Fe-4S] cluster and the polypeptide environment are shown as red dashed lines. The [4Fe-4S] cluster is primarily flanked by proton donors and positively charged residues.

4. Discussion

Transformation from an enzyme to an electron-transfer protein or vice versa:

TrxR serves as a hydride-transfer catalyst and sHdrA as an electron-transfer device despite sharing the same subunit fold. Structural features crucial for this transformation are: (1) The monomers of the sHdrA and TrxR dimers are differently arranged implicating that for sHdrA the [4Fe-4S] cluster of the two monomers become sufficiently close for providing a rapid electron transfer¹⁰⁸ (Fig. 31). Therefore, the two FAD and the two [4Fe-4S] clusters form together an electron-conducting and/or electron-storing unit. TrxR also constitutes a dimer which only involves the two FAD domains and thus allows the 66° rotation of the NADPH domain between the FAD-reducing and -oxidizing forms¹⁰⁷. (2) the NADPH binding site in TrxR was

transformed into a [4Fe-4S] cluster binding site in HdrA predominantly by prolonging helix 180:195 by one turn and by redesigning its preceding loop. In addition, the [4Fe-4S] cluster is enclosed by a reconstructed loop between strand 199:204 and helix 212:224 of both monomers (Fig. 32). The [4Fe-4S] clusters of sHdrA and mHdrA are located inside a pocket endowed with a positive electrostatic surface potential which preferentially stabilizes the reduced $[\text{Fe}^{3+}, 3\text{Fe}^{2+}]$ state. The thus predicted high redox potential is in agreement with the EPR spectroscopically determined value of -185 mV which is significantly higher as the normal value for [4Fe-4S] clusters below -300 mV^{109,110}. (3) In contrast to TrxR the isoalloxazine ring of the HdrAs is completely buried inside the protein matrix. A hydride-transferring external electron donor has therefore no access to the isoalloxazine ring.

The architecture of sHdr:

Structural data about the entire sHdr complex are not available yet. A purification of a sHdr complex with an acceptable quality succeeded for the enzyme form *A. aeolicus* which was composed of subunits HdrA, HdrB1, HdrB2, HdrC1 and HdrC2⁹¹. The corresponding genes are equivalently arranged in the same operon of all sulfur-oxidizing microorganisms containing *shdr* genes^{87,88,90,111}. In addition, the recently determined heterohexameric Hdr(ABC)₂ complex of methanogenic archaea¹⁰³ suggests as major constituent of the overall sHdr complex an asymmetric Hdr(AA'B₁B₂C₁C₂) complex. Its molecular mass of 225.3 kDa calculated for the *H. denitrificans* heterohexamer from the genome sequence is similar to 240 kDa derived from a Blue-native PAGE gel of the *A. aeolicus* enzyme⁹¹. Model building was performed by calculating the structure of the individual subunits by the Swiss Server¹¹²

and by superimposed them onto the corresponding subunits of the methanogenic Hdr(ABC)₂ complex (Fig. 33). The sequence identities between sHdrC1(C2) and mHdrC are 18.7 (34.7) % and between sHdrB1(B2) and mHdrB 21.5 (32.4) %. The model structure of the Hdr(AA'B₁B₂C₁C₂) complex of *H. denitrificans* allows an analysis of the HdrA-HdrC and HdrB-HdrC interfaces which reveals a high degree of conservation and only shows a few collisions. In addition, the contacting loop 250-255 is partly disordered in isolated HdrA but is presumably rigidified when interacting with HdrC1(C2). Finally, the sHdrA-sHdrC1(C2) interface does not involve the ferredoxin insertion/extension domains of mHdrA¹⁰³ truncated in sHdrA such that the contact area is not reduced. All these points support the reliability of the heterohexameric model.

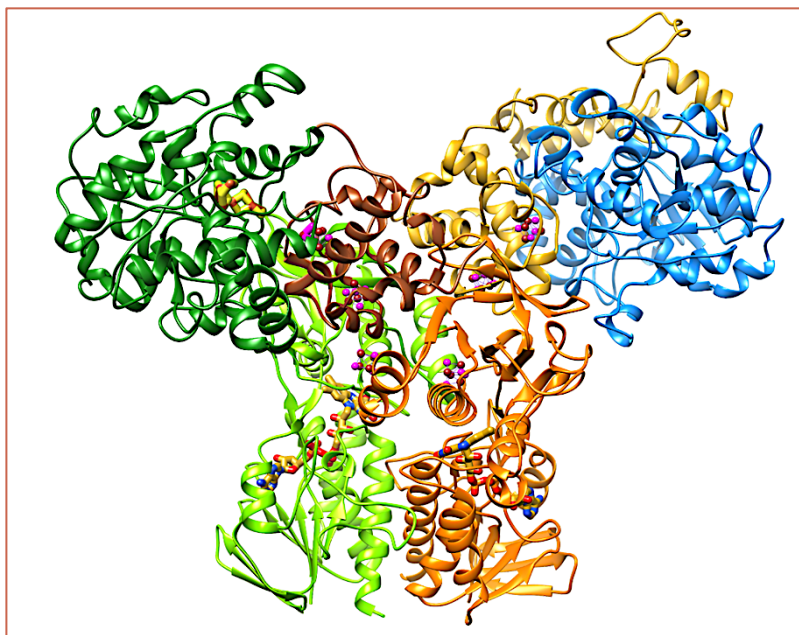


Fig. 33. Postulated model of the sHdr complex. The structures of the sHdrC1 (in brown), sHdrC2 (in gold), sHdrB1 (in dark green) and sHdrB2 (in blue) were calculated with the SwissProt server using mHdrC and mHdrB as template and integrated together with the experimentally determined sHdrA into the mHdr hexamer. HdrC2 and HdrB2 form one branch due to their closer relationship with mHdrB.

The heterohexameric architecture indicates that sHdrC1/C2 serve as redox relay between sHdrA and sHdrB1/B2. The strictly conserved eight cysteines suggest two [4Fe-4S] cluster as mHdrC. The role of the catalytic subunits HdrB1/B2 remains unknown. However, the 10 cysteines of the CCG recognition motif ligating the two noncubane [4Fe-4S] clusters in mHdrB are conserved in HdrB2^{88,103}. HdrB1 contains 7 of the 10 invariant cysteines; the replacing residues serine and aspartate have also iron-ligating capacities. Thus, a catalytic function of HdrB1 and HdrB2 is highly likely.

sHdrA is not a FAD-based electron-bifurcating module:

The participation of Hdr-like modules inspires the hypothesis that flavin-based electron-bifurcation is also used as an optimization strategy in anaerobic sulfur oxidation. However, two findings exclude this type of energy coupling process^{6,14,92,113}. The eliminated ferredoxin insertion/extension domains in sHdrA compared to mHdrA is attributed to have essential functions in electron bifurcation¹⁰³.

The second argument against sHdrA as bifurcating module is related to a different environment of the isoalloxazine ring, in particular, of the critical N5 and N2-C=O1 sites in sHdrA and mHdrA. N5 of sHdrA is dominantly surrounded by negatively charged amino acids suggesting that the interacting water is partially deprotonated and preferably interacts with a protonated N5 of the semi-reduced FADH• and reduced FADH⁻ state (Fig. 31). In contrast, the N5 of mHdrA interacting with the positively charged Lys α 409, is preferentially in a deprotonated oxidized FAD state¹⁰³. In addition, the surrounding of the N2-C=O1 group appears to be more negative in sHdrA than in mHdrA due to Asp323 instead of Lys α '524

which stabilizes the neutral $\text{FADH}\cdot$ relative to the negative charged FADH^- . As a result, the redox potential of the $\text{FAD}/\text{FADH}\cdot$ pair should be higher and that of the $\text{FADH}\cdot/\text{FADH}^-$ pair lower in sHdrA than in mHdrA. The thereby increased stability of $\text{FADH}\cdot$ was experimentally demonstrated by UV/Vis spectroscopy⁹². The presence of a stable $\text{FADH}\cdot$ is incompatible with the current concept of flavin-based electron bifurcation which requires an energy-rich semiquinone to donate an electron uphill to the low-potential electron donor ferredoxin^{6,14,17}.

The reaction of the sHdr complex:

Sulfur oxidation in sulfur-oxidizing bacteria containing the *shdrA* genes start from reduced sulfur compounds e.g., thiosulfate in the case of *H. denitrificans*. The sulfur is shuttled via a cascade of sulfur transfer reactions to sulfur carrier proteins TusA or DsrE in form of a persulfide^{87,114}. It is postulated that the sHdr complex catalyzes the protein-bound sulfane sulfur to sulfite⁸⁸ and the four remaining electrons are accepted by NAD^+ via lipoamide (Fig. 34)⁹⁰. For a sound mechanistic proposal, the data base is too limited. Therefore, one scenario compatible with the currently available data is exemplarily presented which is based on the assumption that sHdrB2 acts as a disulfide/thiolate converter, sHdrB1 as redox catalyst and sHdrA as electron-conducting/ storage unit but not as hydride donor e.g. to NAD^+ (Fig. 34). sHdrB1 may bind with its two postulated iron-sulfur clusters the cysteine and the sulfane sulfur. The latter becomes oxidized via Fe-ligated sulfonate ($-\text{S}-\text{OH}$) and sulfinate ($-\text{S}-\text{O}_2^-$) to sulfite which reveals some relationships with the reaction scheme on the siroheme iron¹¹⁵. From the oxidative HdrB1/HdrB2 branch the released electrons flow via HdrA and HdrA', to the reductive HdrC2/HdrB2 branch.

HdrB2 presumably carrying two non-heme irons performs the reduction of lipoamide to dihydrolipoamide by an analogous mechanism postulated for mHdr. MHdr catalyzes the reduction of the disulfide of coenzyme M and B¹⁰³. Lipoamide disulfide is subsequently regenerated by reducing NAD⁺ with dihydrolipoamide dehydrogenase. In this reaction scheme HdrA functions as electron-carrier device via the two [4Fe-4S] clusters whereas the two FADs may have the task to store the four sulfane electrons for decoupling the two half reactions. Further studies on the entire sHdr complex are indispensable to unravel the catalytic reactions on the two active sites, the role of the prosthetic groups and the interaction of all components.

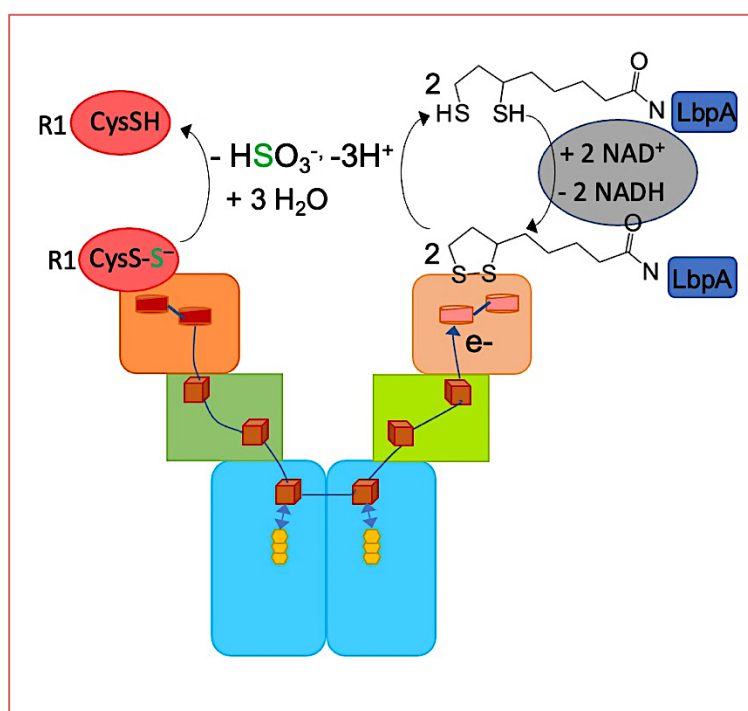


Fig. 34. Reaction scheme of the sHdr complex. Subunits HdrA, HdrC1/HdrC2 and HdrB1/B2 are shown in cyan, green (dark and light) and orange (dark and light), respectively. FAD and the iron-sulfur clusters are drawn in yellow and brown. R1 stands for a sulfur carrier protein such as TusA and DsrE (red). Lipoamide dehydrogenase is shown in gray, the lipoate binding protein (LdpA) in dark blue.

VIII. Future prospects

In case of Pcd complex, the major structural information has been extracted considering that the substrate phthaloyl-CoA is highly unstable and not available for cryo-EM experiments. Before publication, there are plans for kinetic measurements with fluorinated benzene rings of phthaloyl-CoA, to learn more about protonation sites.

In case of Ldh/EtfAB complex, the first structure in D-state (Dehydrogenase conducting) has been established. Next, a structure of the Ldh/EtfAB in complex with NAD⁺ and lactate would be planned. Cryo-EM trials to characterize the short-living B-state (bifurcation state), upon addition of substrates just before plunge-freezing the protein complex would be a challenging aim but can shed more light on the mechanism and the electron flow pathway.

The sHdrA structure showed the details of the binding sites of FAD and [4Fe-4S] cluster, independent of the interactions with rest of the complex subunits. If a suitable purification protocol is available, the entire sHdrAA'B1B2C1C2 would be an attractive target for cryo-EM structure determination to obtain a more complete mechanistic understanding.

IX. References

1. Gottschalk, G. *Bacterial Metabolism*. (Springer New York, 1986).
2. Lohmann, K. Ueber das Vorkommen und den Umsatz von Pyrophosphat im Muskel. *Die Naturwissenschaften* **16**, (1928).
3. Mitchell, P. Chemiosmotic coupling in oxidative and photosynthetic phosphorylation. *Biochimica et Biophysica Acta (BBA) - Bioenergetics* **1807**, 1507–1538 (2011).
4. Müller, V. & Hess, V. The Minimum Biological Energy Quantum. *Frontiers in Microbiology* **8**, (2017).
5. Müller, V. Bacterial Fermentation. in *eLS* (Wiley, 2001).
6. Buckel, W. & Thauer, R. K. Energy conservation via electron bifurcating ferredoxin reduction and proton/Na⁺ translocating ferredoxin oxidation. *Biochimica et Biophysica Acta - Bioenergetics* vol. 1827 (2013).
7. Hedderich, R. Energy-Converting [NiFe] Hydrogenases from Archaea and Extremophiles: Ancestors of Complex I. *Journal of Bioenergetics and Biomembranes* **36**, (2004).
8. Biegel, E., Schmidt, S., González, J. M. & Müller, V. Biochemistry, evolution and physiological function of the Rnf complex, a novel ion-motive electron transport complex in prokaryotes. *Cellular and Molecular Life Sciences* **68**, (2011).
9. Müller, V., Chowdhury, N. P. & Basen, M. Electron Bifurcation: A Long-Hidden Energy-Coupling Mechanism. *Annual Review of Microbiology* **72**, (2018).

IX. References

10. Fuchs, G., Boll, M. & Heider, J. Microbial degradation of aromatic compounds — from one strategy to four. *Nature Reviews Microbiology* **9**, (2011).
11. Li, F. *et al.* Coupled ferredoxin and crotonyl coenzyme A (CoA) reduction with NADH catalyzed by the butyryl-CoA dehydrogenase/Etf complex from *Clostridium kluyveri*. *Journal of Bacteriology* **190**, (2008).
12. Herrmann, G., Jayamani, E., Mai, G. & Buckel, W. Energy conservation via electron-transferring flavoprotein in anaerobic bacteria. *Journal of Bacteriology* vol. 190 (2008).
13. Chowdhury, N. P., Klomann, K., Seubert, A. & Buckel, W. Reduction of flavodoxin by electron bifurcation and sodium Ion-dependent reoxidation by NAD⁺ catalyzed by ferredoxin-NAD⁺ reductase (Rnf). *Journal of Biological Chemistry* **291**, (2016).
14. Nitschke, W. & Russell, M. J. Redox bifurcations: Mechanisms and importance to life now, and at its origin: A widespread means of energy conversion in biology unfolds... *BioEssays* vol. 34 (2012).
15. Baymann, F. *et al.* On the natural history of flavin-based electron bifurcation. *Frontiers in Microbiology* vol. 9 (2018).
16. Chowdhury, N. P., Kahnt, J. & Buckel, W. Reduction of ferredoxin or oxygen by flavin-based electron bifurcation in *Megasphaera elsdenii*. *FEBS Journal* **282**, (2015).
17. Lubner, C. E. *et al.* Mechanistic insights into energy conservation by flavin-based electron bifurcation. *Nature Chemical Biology* **13**, (2017).

18. Peters, J. W., Miller, A.-F., Jones, A. K., King, P. W. & Adams, M. W. Electron bifurcation. *Current Opinion in Chemical Biology* **31**, (2016).
19. Zhang, P. *et al.* Electron Bifurcation: Thermodynamics and Kinetics of Two-Electron Brokering in Biological Redox Chemistry. *Accounts of Chemical Research* **50**, (2017).
20. Fuchs, G., Boll, M. & Heider, J. Microbial degradation of aromatic compounds — from one strategy to four. *Nature Reviews Microbiology* **9**, (2011).
21. Heider, J. & Fuchs, G. Anaerobic Metabolism of Aromatic Compounds. *European Journal of Biochemistry* **243**, (1997).
22. Harwood, C. S. & Parales, R. E. The β -ketoadipate pathway and the biology of self-identity. *Annual Review of Microbiology* **50**, (1996).
23. Boll, M. Key enzymes in the anaerobic aromatic metabolism catalysing Birch-like reductions. *Biochimica et Biophysica Acta (BBA) - Bioenergetics* **1707**, (2005).
24. Boll, M. & Fuchs, G. Benzoyl-Coenzyme A Reductase (Dearomatizing), a Key Enzyme of Anaerobic Aromatic Metabolism. ATP Dependence of the Reaction, Purification and Some Properties of the Enzyme from *Thaueria Aromatica* Strain K172. *European Journal of Biochemistry* **234**, (1995).
25. Thiele, B., Rieder, O., Golding, B. T., Müller, M. & Boll, M. Mechanism of Enzymatic Birch Reduction: Stereochemical Course and Exchange Reactions of Benzoyl-CoA Reductase. *Journal of the American Chemical Society* **130**, (2008).

IX. References

26. Huwiler, S. G. *et al.* One-megadalton metalloenzyme complex in *Geobacter metallireducens* involved in benzene ring reduction beyond the biological redox window. *Proceedings of the National Academy of Sciences* **116**, (2019).
27. Kung, J. W. *et al.* Reversible Biological Birch Reduction at an Extremely Low Redox Potential. *Journal of the American Chemical Society* **132**, (2010).
28. Geertsma, E. R. & Dutzler, R. A Versatile and Efficient High-Throughput Cloning Tool for Structural Biology. *Biochemistry* **50**, (2011).
29. Corpet, F. Multiple sequence alignment with hierarchical clustering. *Nucleic Acids Research* **16**, (1988).
30. Bradford, M. A Rapid and Sensitive Method for the Quantitation of Microgram Quantities of Protein Utilizing the Principle of Protein-Dye Binding. *Analytical Biochemistry* **72**, (1976).
31. Laemmli K U. Cleavage of structural proteins during the assembly of the head of bacteriophage T4. *Nature* **227**, 680–685 (1970).
32. Wittig, I. & Schägger, H. Advantages and limitations of clear-native PAGE. *PROTEOMICS* **5**, (2005).
33. Schmidt, C. & Urlaub, H. Combining cryo-electron microscopy (cryo-EM) and cross-linking mass spectrometry (CX-MS) for structural elucidation of large protein assemblies. *Current Opinion in Structural Biology* **46**, (2017).
34. Mattson, G. *et al.* A practical approach to crosslinking. *Molecular Biology Reports* **17**, (1993).
35. McPherson, A. & Gavira, J. A. Introduction to protein crystallization. *Acta Crystallographica Section F Structural Biology Communications* **70**, (2014).

36. Caffrey, M. A comprehensive review of the lipid cubic phase or in meso method for crystallizing membrane and soluble proteins and complexes. *Acta Crystallographica Section F Structural Biology Communications* **71**, (2015).
37. Ma, P. *et al.* The cubicon method for concentrating membrane proteins in the cubic mesophase. *Nature Protocols* **12**, (2017).
38. Murata, K. & Wolf, M. Cryo-electron microscopy for structural analysis of dynamic biological macromolecules. *Biochimica et Biophysica Acta (BBA) - General Subjects* **1862**, (2018).
39. Kabsch, W. *et al.* XDS. *Acta Crystallographica Section D Biological Crystallography* **66**, (2010).
40. de La Fortelle, E. & Bricogne, G. SHARP: a maximum-likelihood heavy-atom parameter refinement program for the MIR and MAD methods. *Methods Enzymol* **276**, (1997).
41. Abrahams, J. P. & Leslie, A. G. W. Methods used in the structure determination of bovine mitochondrial F1 ATPase. *Acta Crystallographica Section D: Biological Crystallography* **52**, (1996).
42. McCoy, A. J. *et al.* Phaser crystallographic software. *Journal of Applied Crystallography* **40**, (2007).
43. Adams, P. D. *et al.* PHENIX: A comprehensive Python-based system for macromolecular structure solution. *Acta Crystallographica Section D: Biological Crystallography* **66**, (2010).
44. Winn, M. D. *et al.* Overview of the CCP4 suite and current developments. *Acta Crystallographica Section D Biological Crystallography* **67**, (2011).

IX. References

45. Smart, O. S. *et al.* Exploiting structure similarity in refinement: automated NCS and target-structure restraints in BUSTER. *Acta Crystallographica Section D Biological Crystallography* **68**, (2012).
46. Punjani, A., Rubinstein, J. L., Fleet, D. J. & Brubaker, M. A. cryoSPARC: algorithms for rapid unsupervised cryo-EM structure determination. *Nature Methods* **14**, (2017).
47. Zivanov, J. *et al.* New tools for automated high-resolution cryo-EM structure determination in RELION-3. *eLife* **7**, (2018).
48. Zheng, S. Q. *et al.* MotionCor2: Anisotropic correction of beam-induced motion for improved cryo-electron microscopy. *Nature Methods* vol. 14 (2017).
49. Zhang, K. Gctf: Real-time CTF determination and correction. *Journal of Structural Biology* **193**, (2016).
50. Wagner, T. *et al.* SPHIRE-crYOLO is a fast and accurate fully automated particle picker for cryo-EM. *Communications Biology* **2**, (2019).
51. Scheres, S. H. W. RELION: Implementation of a Bayesian approach to cryo-EM structure determination. *Journal of Structural Biology* **180**, (2012).
52. Zivanov, J., Nakane, T. & Scheres, S. H. W. Estimation of high-order aberrations and anisotropic magnification from cryo-EM data sets in RELION-3.1. *IUCrJ* **7**, (2020).
53. Net, S., Sempéré, R., Delmont, A., Paluselli, A. & Ouddane, B. Occurrence, Fate, Behavior and Ecotoxicological State of Phthalates in Different Environmental Matrices. *Environmental Science & Technology* **49**, (2015).

54. Kumar, P. Role of Plastics on Human Health. *The Indian Journal of Pediatrics* **85**, (2018).
55. Boll, M., Geiger, R., Junghare, M. & Schink, B. Microbial degradation of phthalates: biochemistry and environmental implications. *Environmental Microbiology Reports* vol. 12 3–15 (2020).
56. Gao, D.-W. & Wen, Z.-D. Phthalate esters in the environment: A critical review of their occurrence, biodegradation, and removal during wastewater treatment processes. *Science of The Total Environment* **541**, (2016).
57. Junghare, M., Spitteller, D. & Schink, B. Enzymes involved in the anaerobic degradation of ortho-phthalate by the nitrate-reducing bacterium *Azoarcus* sp. strain PA01. *Environmental Microbiology* **18**, (2016).
58. Ebenau-Jehle, C. *et al.* An unusual strategy for the anoxic biodegradation of phthalate. *The ISME Journal* **11**, (2017).
59. Cox, G. B., Young, I. G., McCann, L. M. & Gibson, F. Biosynthesis of ubiquinone in *Escherichia coli* K-12: location of genes affecting the metabolism of 3-octaprenyl-4-hydroxybenzoic acid and 2-octaprenylphenol. *Journal of bacteriology* **99**, (1969).
60. Payne, K. A. P. *et al.* New cofactor supports α,β -unsaturated acid decarboxylation via 1,3-dipolar cycloaddition. *Nature* **522**, (2015).
61. Leys, D. Flavin metamorphosis: cofactor transformation through prenylation. *Current Opinion in Chemical Biology* vol. 47 (2018).
62. White, M. D. *et al.* UbiX is a flavin prenyltransferase required for bacterial ubiquinone biosynthesis. *Nature* **522**, (2015).

63. Mergelsberg, M. *et al.* Phthaloyl-coenzyme A decarboxylase from *Thauera chlorobenzoica*: the prenylated flavin-, K⁺- and Fe²⁺-dependent key enzyme of anaerobic phthalate degradation. *Environmental Microbiology* **19**, (2017).
64. Geiger, R. A. *et al.* Enzymes involved in phthalate degradation in sulphate-reducing bacteria. *Environmental Microbiology* **21**, 3601–3612 (2019).
65. Ohi, M., Li, Y., Cheng, Y. & Walz, T. Negative staining and image classification — powerful tools in modern electron microscopy. *Biological Procedures Online* **6**, (2004).
66. Scheres, S. H. W. & Chen, S. Prevention of overfitting in cryo-EM structure determination. *Nature Methods* **9**, (2012).
67. Moriarty, N. W., Grosse-Kunstleve, R. W. & Adams, P. D. electronic Ligand Builder and Optimization Workbench (eLBOW): a tool for ligand coordinate and restraint generation. *Acta Crystallographica Section D Biological Crystallography* **65**, (2009).
68. Jacewicz, A., Izumi, A., Brunner, K., Schnell, R. & Schneider, G. Structural Insights into the UbiD Protein Family from the Crystal Structure of PA0254 from *Pseudomonas aeruginosa*. *PLoS ONE* **8**, (2013).
69. Ishida, T. & Kinoshita, K. PrDOS: Prediction of disordered protein regions from amino acid sequence. *Nucleic Acids Research* **35**, (2007).
70. Payer, S. E. *et al.* Regioselective *para*-Carboxylation of Catechols with a Prenylated Flavin Dependent Decarboxylase. *Angewandte Chemie International Edition* **56**, (2017).

71. Jacobs, R. A., Meinild, A.-K., Nordsborg, N. B. & Lundby, C. Lactate oxidation in human skeletal muscle mitochondria. *American Journal of Physiology-Endocrinology and Metabolism* **304**, (2013).
72. Hashimoto, T., Hussien, R. & Brooks, G. A. Colocalization of MCT1, CD147, and LDH in mitochondrial inner membrane of L6 muscle cells: evidence of a mitochondrial lactate oxidation complex. *American Journal of Physiology-Endocrinology and Metabolism* **290**, (2006).
73. Ma, C. *et al.* Membrane-bound l- and d-lactate dehydrogenase activities of a newly isolated *Pseudomonas stutzeri* strain. *Applied Microbiology and Biotechnology* **77**, (2007).
74. Hess, V., Schuchmann, K. & Müller, V. The Ferredoxin:NAD⁺ Oxidoreductase (Rnf) from the Acetogen *Acetobacterium woodii* Requires Na⁺ and Is Reversibly Coupled to the Membrane Potential. *Journal of Biological Chemistry* **288**, (2013).
75. Weghoff, M. C., Bertsch, J. & Müller, V. A novel mode of lactate metabolism in strictly anaerobic bacteria. *Environmental Microbiology* **17**, 670–677 (2015).
76. Cunane, L. M. *et al.* Structures of the flavocytochrome p-cresol methylhydroxylase and its enzyme-substrate complex: gated substrate entry and proton relays support the proposed catalytic mechanism. *Journal of Molecular Biology* **295**, (2000).
77. Mattevi, A. *et al.* Crystal structures and inhibitor binding in the octameric flavoenzyme vanillyl-alcohol oxidase: the shape of the active-site cavity controls substrate specificity. *Structure* **5**, (1997).

IX. References

78. Benson, T. E., Walsh, C. T. & Hogle, J. M. The structure of the substrate-free form of MurB, an essential enzyme for the synthesis of bacterial cell walls. *Structure* **4**, (1996).
79. Dym, O., Pratt, E. A., Ho, C. & Eisenberg, D. The crystal structure of D-lactate dehydrogenase, a peripheral membrane respiratory enzyme. *Proceedings of the National Academy of Sciences* **97**, (2000).
80. Fraaije, M. W., van Berkel, W. J. H., Benen, J. A. E., Visser, J. & Mattevi, A. A novel oxidoreductase family sharing a conserved FAD-binding domain. *Trends in Biochemical Sciences* **23**, (1998).
81. Chowdhury, N. P. *et al.* Studies on the mechanism of electron bifurcation catalyzed by electron transferring flavoprotein (Etf) and butyryl-CoA dehydrogenase (Bcd) of acidaminococcus fermentans. *Journal of Biological Chemistry* **289**, (2014).
82. Demmer, J. K. *et al.* Molecular basis of the flavin-based electron-bifurcating caffeyl-CoA reductase reaction. *FEBS Letters* **592**, (2018).
83. Roberts, D. L., Frerman, F. E. & Kim, J.-J. P. Three-dimensional structure of human electron transfer flavoprotein to 2.1-Å resolution. *Proceedings of the National Academy of Sciences* **93**, (1996).
84. Demmer, J. K., Pal Chowdhury, N., Selmer, T., Ermler, U. & Buckel, W. The semiquinone swing in the bifurcating electron transferring flavoprotein/butyryl-CoA dehydrogenase complex from *Clostridium difficile*. *Nature Communications* **8**, (2017).

85. Toogood, H. S., Leys, D. & Scrutton, N. S. Dynamics driving function – new insights from electron transferring flavoproteins and partner complexes. *FEBS Journal* **274**, (2007).
86. Toogood, H. S. *et al.* Extensive Domain Motion and Electron Transfer in the Human Electron Transferring Flavoprotein·Medium Chain Acyl-CoA Dehydrogenase Complex. *Journal of Biological Chemistry* **279**, (2004).
87. Dahl, C. Cytoplasmic sulfur trafficking in sulfur-oxidizing prokaryotes. *IUBMB Life* **67**, (2015).
88. Koch, T. & Dahl, C. A novel bacterial sulfur oxidation pathway provides a new link between the cycles of organic and inorganic sulfur compounds. *The ISME Journal* **12**, (2018).
89. Kaster, A.-K., Moll, J., Parey, K. & Thauer, R. K. Coupling of ferredoxin and heterodisulfide reduction via electron bifurcation in hydrogenotrophic methanogenic archaea. *Proceedings of the National Academy of Sciences* **108**, (2011).
90. Cao, X. *et al.* Lipoate-binding proteins and specific lipoate-protein ligases in microbial sulfur oxidation reveal an atypical role for an old cofactor. *eLife* **7**, (2018).
91. Boughanemi, S. *et al.* Microbial oxidative sulfur metabolism: biochemical evidence of the membrane-bound heterodisulfide reductase-like complex of the bacterium *Aquifex aeolicus*. *FEMS Microbiology Letters* **363**, (2016).
92. Ernst, C. *et al.* Structural and spectroscopic characterization of a HdrA-like subunit from *Hyphomicrobium denitrificans*. *The FEBS Journal* **288**, (2021).

IX. References

93. Schneider, T. R. & Sheldrick, G. M. Substructure solution with SHELXD. *Acta Crystallographica Section D: Biological Crystallography* **58**, (2002).
94. Langer, G., Cohen, S. X., Lamzin, V. S. & Perrakis, A. Automated macromolecular model building for X-ray crystallography using ARP/wARP version 7. *Nature Protocols* **3**, (2008).
95. Emsley, P. & Cowtan, K. Coot: Model-building tools for molecular graphics. *Acta Crystallographica Section D: Biological Crystallography* **60**, (2004).
96. Murshudov, G. N., Vagin, A. A. & Dodson, E. J. Refinement of macromolecular structures by the maximum-likelihood method. *Acta Crystallographica Section D: Biological Crystallography* vol. 53 (1997).
97. Davis, I. W. *et al.* MolProbity: All-atom contacts and structure validation for proteins and nucleic acids. *Nucleic Acids Research* **35**, (2007).
98. Holm, L. & Laakso, L. M. Dali server update. *Nucleic acids research* **44**, (2016).
99. Krissinel, E. & Henrick, K. Inference of Macromolecular Assemblies from Crystalline State. *Journal of Molecular Biology* **372**, (2007).
100. Pettersen, E. F. *et al.* UCSF Chimera--A visualization system for exploratory research and analysis. *Journal of Computational Chemistry* **25**, (2004).
101. Schulz, G. E., Schirmer, R. H., Sachsenheimer, W. & Pai, E. F. The structure of the flavoenzyme glutathione reductase. *Nature* **273**, (1978).
102. Page, C. C., Moser, C. C., Chen, X. & Dutton, P. L. Natural engineering principles of electron tunnelling in biological oxidation–reduction. *Nature* **402**, (1999).

103. Wagner, T., Koch, J., Ermler, U. & Shima, S. Methanogenic heterodisulfide reductase (HdrABC-MvhAGD) uses two noncubane [4Fe-4S] clusters for reduction. *Science* **357**, (2017).
104. Hernandez, H. H., Jaquez, O. A., Hamill, M. J., Elliott, S. J. & Drennan, C. L. Thioredoxin Reductase from *Thermoplasma acidophilum*: A New Twist on Redox Regulation. *Biochemistry* **47**, (2008).
105. Skjoldager, N. *et al.* The structure of *Lactococcus lactis* thioredoxin reductase reveals molecular features of photo-oxidative damage. *Scientific Reports* **7**, (2017).
106. Kuriyan, J. *et al.* Convergent evolution of similar function in two structurally divergent enzymes. *Nature* **352**, (1991).
107. Lennon, B. W. Twists in Catalysis: Alternating Conformations of *Escherichia coli* Thioredoxin Reductase. *Science* **289**, (2000).
108. Page, C. Mechanism for electron transfer within and between proteins. *Current Opinion in Chemical Biology* **7**, (2003).
109. Langen, R., Jensen, G. M., Jacob, U., Stephens, P. J. & Warshel, A. Protein control of iron-sulfur cluster redox potentials. *Journal of Biological Chemistry* **267**, (1992).
110. Chen, K. *et al.* Crystal structures of ferredoxin variants exhibiting large changes in [Fe-S] reduction potential. *Nature Structural Biology* (2002)
111. Liu, L.-J. *et al.* Thiosulfate Transfer Mediated by DsrE/TusA Homologs from Acidothermophilic Sulfur-oxidizing Archaeon *Metallosphaera cuprina*. *Journal of Biological Chemistry* **289**, (2014).

IX. References

112. Waterhouse, A. *et al.* SWISS-MODEL: homology modelling of protein structures and complexes. *Nucleic Acids Research* **46**, (2018).
113. Quatrini, R. *et al.* Extending the models for iron and sulfur oxidation in the extreme Acidophile *Acidithiobacillus ferrooxidans*. *BMC Genomics* **10**, (2009).
114. Tanabe, T. S., Leimkühler, S. & Dahl, C. The functional diversity of the prokaryotic sulfur carrier protein TusA. in (2019).
115. Santos, A. A. *et al.* A protein trisulfide couples dissimilatory sulfate reduction to energy conservation. *Science* **350**, (2015).

X. Appendices

Appendix A. PrDOS result of Pcd complex

PrDOS server for prediction of disordered regions in a protein. The values above 0.5 disorder probability on y-axis are predicted to be disordered regions. The segment 440 to 471 in active holo-Pcd complex was found to be disordered in cryo-EM map. Part of this segment was also predicted to be disordered and predicted to form no secondary structures (Fig. 35).

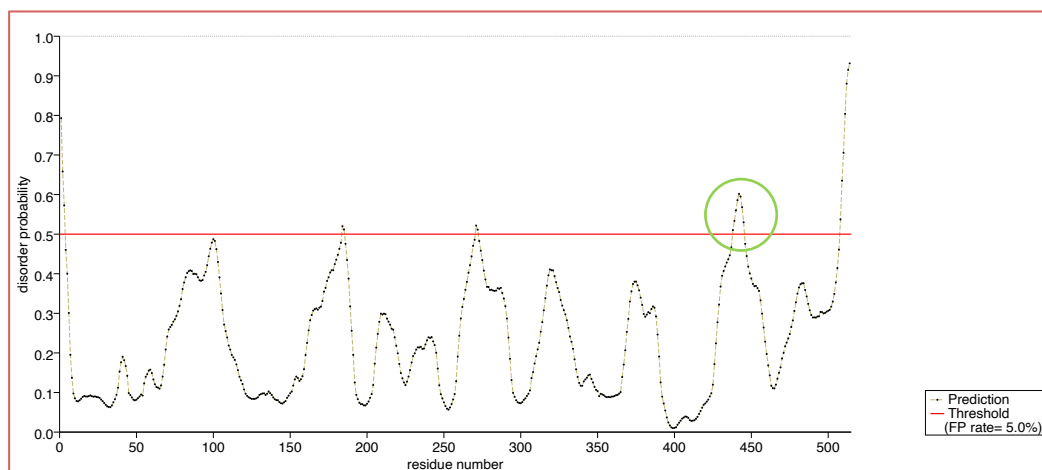
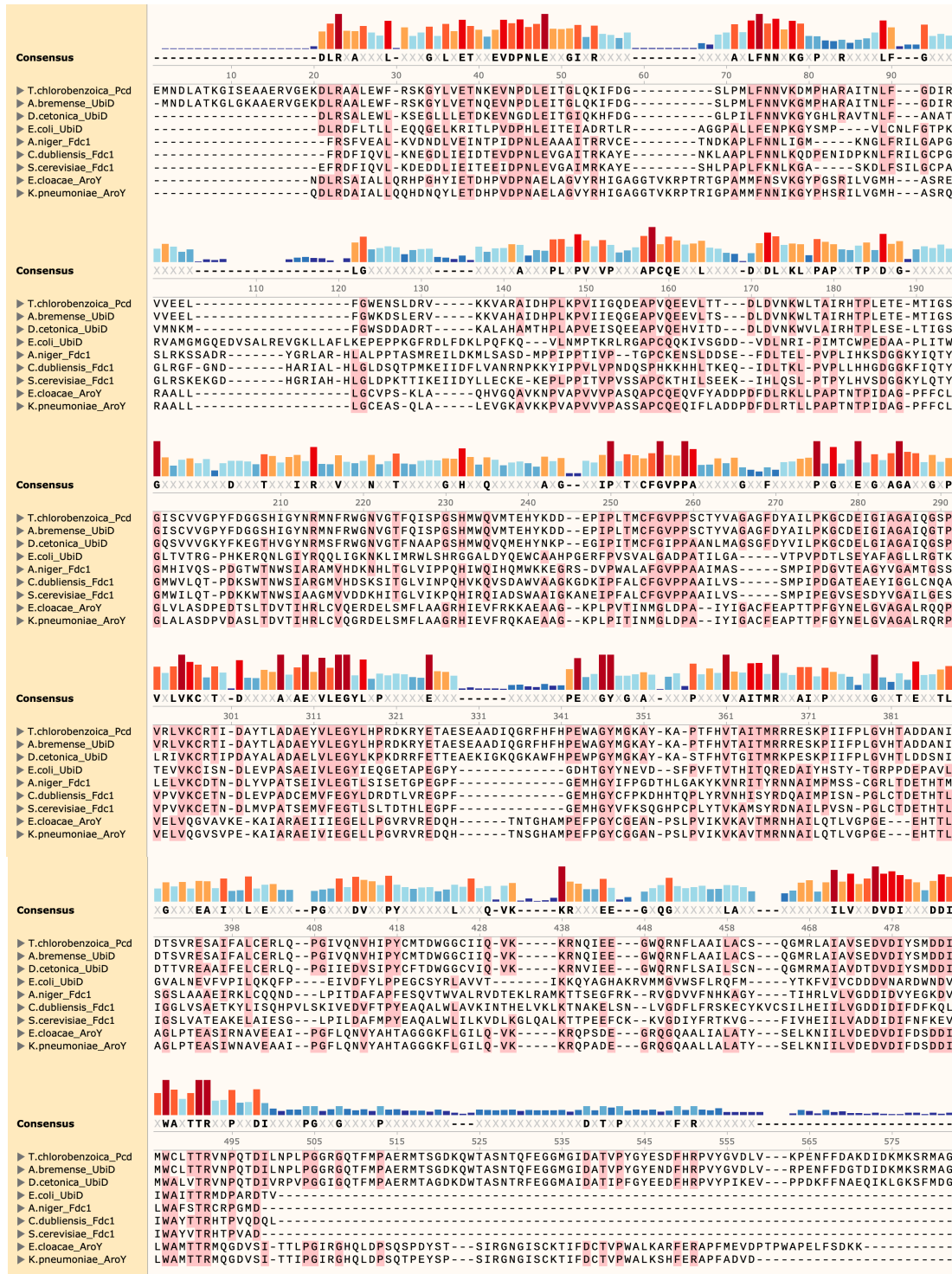


Fig. 35. PrDOS result of Pcd complex. Segment 438 to 445 (in green circle) is predicted to have high disordered probability.

Appendix B. Multiple sequence alignment of Pcd complex



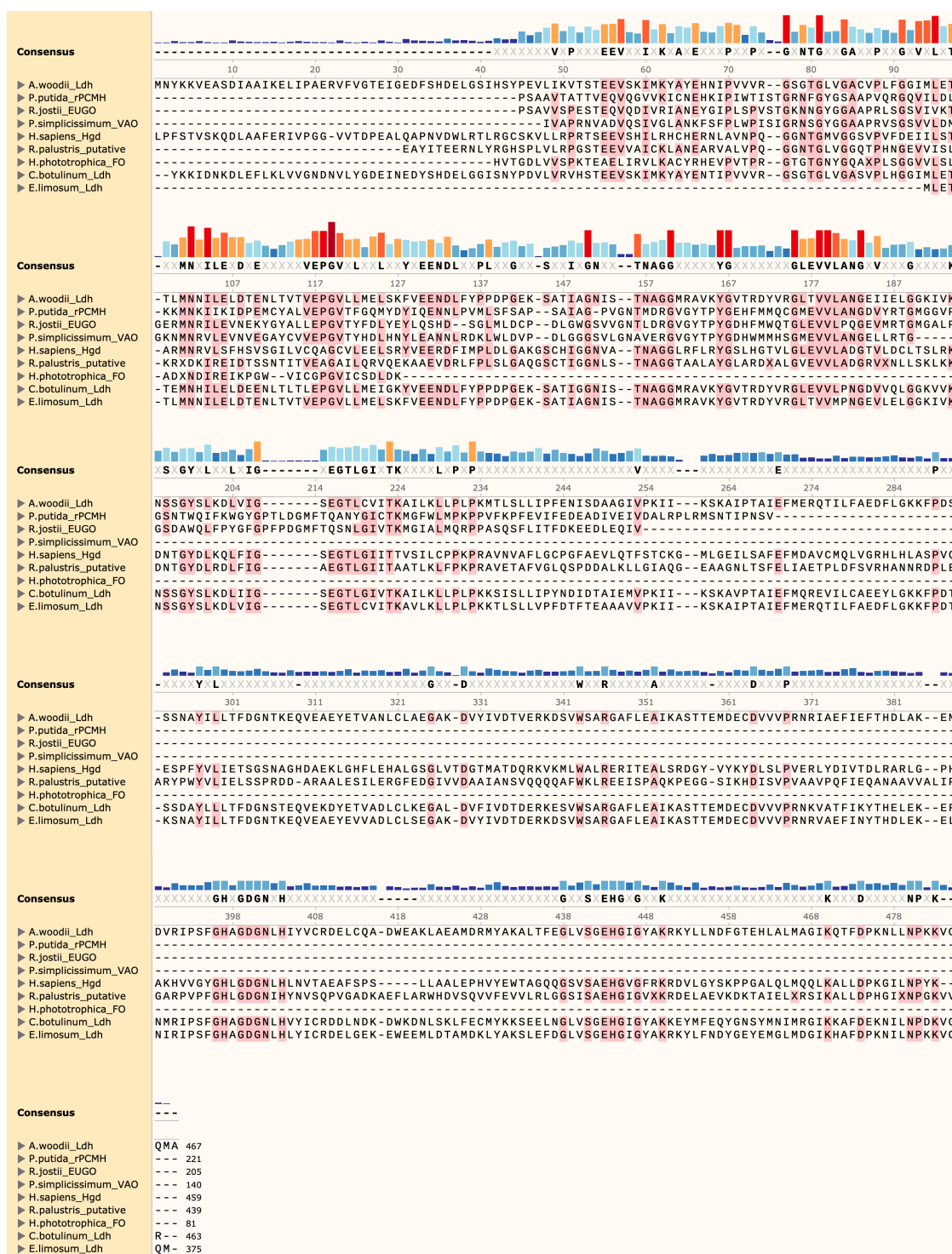
Note:

Consensus threshold: >50%

Colored peaks (from maroon to blue) represent higher to lower consensus residue percentage.

Appendix C. Multiple sequence alignment of Ldh/EtfAB complex

Lactate dehydrogenase subunit:



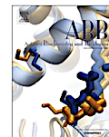
Appendix D. Review article

Archives of Biochemistry and Biophysics 701 (2021) 108796



Contents lists available at ScienceDirect

Archives of Biochemistry and Biophysics

journal homepage: www.elsevier.com/locate/yabbi

Flavins in the electron bifurcation process

Kanwal Kayastha^a, Stella Vitt^{a,b}, Wolfgang Buckel^{b,c}, Ulrich Ermler^{a,*}^a Max-Planck-Institut für Biophysik, Max-von-Laue-Str. 3, 60438, Frankfurt am Main, Germany^b Laboratorium für Mikrobiologie, Fachbereich Biologie and SYNMIKRO, Philipps-Universität, 35032, Marburg, Germany^c Max-Planck-Institut für terrestrische Mikrobiologie, Karl-von-Frisch-Str. 10, 35043, Marburg, Germany

ARTICLE INFO

Keywords:

Flavin
Electron bifurcation
Electron transfer
Redox reactions
Bioenergetics

ABSTRACT

The discovery of a new energy-coupling mechanism termed flavin-based electron bifurcation (FBEB) in 2008 revealed a novel field of application for flavins in biology. The key component is the bifurcating flavin endowed with strongly inverted one-electron reduction potentials ($FAD/FAD\bullet^- \ll FAD\bullet^-/FADH^+$) that cooperatively transfers in its reduced state one low and one high-energy electron into different directions and thereby drives an endergonic with an exergonic reduction reaction. As energy splitting at the bifurcating flavin apparently implicates one-electron chemistry, the FBEB machinery has to incorporate prior to and behind the central bifurcating flavin 2e-to-1e and 1e-to-2e switches, frequently also flavins, for oxidizing variable medium-potential two-electron donating substrates and for reducing high-potential two-electron accepting substrates. The one-electron carriers ferredoxin or flavodoxin serve as low-potential (high-energy) electron acceptors, which power endergonic processes almost exclusively in obligate anaerobic microorganisms to increase the efficiency of their energy metabolism. In this review, we outline the global organization of FBEB enzymes, the functions of the flavins therein and the surrounding of the isoalloxazine rings by which their reduction potentials are specifically adjusted in a finely tuned energy landscape.

1. Flavin-based electron bifurcation (FBEB) in biology

The term FBEB refers to an energy coupling mechanism in which an endergonic (low-potential) reduction is driven by an exergonic (high-potential) reduction; both reactions use the same electron donor endowed with an intermediate reduction potential (Fig. 1) [1–4]. The overall process often proceeds close to the thermodynamic equilibrium implicating nearly 100% energy yield. As chemical site for energy splitting serves a flavin termed bifurcating flavin. The two electrons (of its reduced state), characterized by different one-electron transition energy levels, flow into different directions and thus are available for two distinct energetically dissimilar pathways. While the electron donors and high-potential electron acceptors are rather variable, the low-potential electron acceptor is predominantly ferredoxin which can, however, be replaced by flavodoxin e.g. under iron-depleting conditions [5–8]. The FBEB process is mainly implemented into soluble multi-subunit complexes in contrast to the mechanistically related quinone-based electron bifurcation embedded into the membrane protein complexes *bc₁* and *bc_L* [9].

FBEB energy coupling has been, so far, discovered in N₂ fixation and

various degradation processes like fermentation, methanogenesis, acetogenesis, and anaerobic lactate oxidation and perhaps in sulfate reduction and benzoyl-CoA reduction (Table 1) [4,10]. It increases the efficiency of the energy metabolism in the corresponding anaerobic microorganisms operating at the thermodynamic limit of life, because the Gibbs free energy of suitable exergonic reductions is largely conserved into the electrical potential energy of reduced ferredoxin/-flavodoxin and not completely dissipated into heat [4,11]. The rescued free energy is either utilized for building up a transmembrane H⁺/Na⁺ ion gradient by reducing NAD⁺ or H⁺ via ferredoxin-NAD⁺ reductase [12] or energy-converting [NiFe]-hydrogenase [13], respectively, or for powering energetically unfavorable redox reactions as e.g. the reductive CO₂ fixation in methanogens [14,15]. Hereby, FBEB indirectly increases the amount of ATP conserved per substrate degraded and thus also provides the thermodynamic basis for microorganisms to grow on lower-energy substrates [4]. Altogether, FBEB can be considered as the third fundamental player of energy transduction to fuel endergonic processes for life besides those driven at expense of ATP and the transmembrane electrochemical potential. Due to their participation in energy metabolisms evolved on a primordial oxygen-free earth, FBEB is a

* Corresponding author.

E-mail address: ulrich.ermler@biophys.mpg.de (U. Ermler).<https://doi.org/10.1016/j.ab.2021.108796>

Received 30 October 2020; Received in revised form 1 February 2021; Accepted 3 February 2021

Available online 18 February 2021

0003-9861/© 2021 Elsevier Inc. All rights reserved.

very ancient principle of energy coupling and energy yield maximization [16,17]. FAD is one of the earliest organic molecules created in evolution and ferredoxin is discussed as energy currency before its substitution by ATP. Several comprehensive reviews analyzed the electrochemical basis of FBEB [18–20], the mode of action of FBEB enzymes [10,21] and their roles within the cellular energy metabolism including the increased ATP/metabolized substrate ratio thereby generated [4,10,11].

2. The functions of flavins in FBEB

Flavins are one of the most versatile organic catalysts in biochemistry [22–24] based on the extended delocalized electronic system of the heterocyclic isoalloxazine ring. In proteins, the tricyclic ring allows the interconversion between oxidized (F), semi-reduced (blue FH• and red F•) and reduced states (FH⁻) (Fig. 1) in energetically moderate ranges attainable for cellular redox- or photo-chemistry. Therefore, flavins are selectively applicable as two-electron or one-electron donor/acceptor devices. The flavosemiquinone FH• or F• state becomes stabilized at reduction potentials of F/FH•, F• > FH•, F•/FH⁻ favorable for one-electron processes and destabilized at inverted reduction potentials of F/FH•, F• > FH•, F•/FH⁻ which thermodynamically still permit two-electron processes. In the latter, the first endergonic electron transfer step can be formally described to be driven by the second exothermic one [18], requiring, however, the reacting atoms being in van-der-Waals contact to each other for a nucleophilic attack.

Different redox behaviors of flavins depend on their specific polypeptide environments. Although their relationship is not quantitatively understood, systematic studies revealed as major determinants specific hydrogen-bonds as well as global electrostatic and hydrophobic interactions, π - π stacking between the isoalloxazine ring and aromatic residues as well as redox-state induced conformational changes of the tricyclic ring and the contacting polypeptide. In comparison, the reduction potential of free flavins (pH 7.0, 30 °C) in aqueous solution is -219 mV for the F/FH⁻ pair and -314 and -124 mV for the F/FH• and FH•/FH⁻ pairs [25] indicating an insignificantly occupied flavosemiquinone FH• or F• state.

In FBEB, flavins are implemented at different sites of the enzyme complex provided with distinct functions. Each FBEB enzyme, per definition, contains at least one flavin that acts as the central player to couple exothermic with endothermic reduction reactions (Fig. 1) [1–3]. Its isoalloxazine ring is endowed with two one-electron redox transitions with strongly inverted electrochemical potentials for the FAD•⁻/FADH⁻ and FAD/FAD•⁻ pairs determined as ca. +345 mV and -900 mV under

photoreduction conditions [26]. Mechanistically, the first (low-energy) electron of FADH⁻ flows toward the high-potential two-electron acceptor because the free energy for activation is lower than for reducing the low-potential electron acceptor. The second (high-energy) electron moves to the low-potential one-electron carrier ferredoxin/flavodoxin (and not again to the high-potential acceptor) perhaps due to the shorter distance and the reluctance of an electron route to almost simultaneously transfer a second electron (Fig. 1). To exclude a short circuit, the two acceptors for the energetically different electrons and the electron transfer routes to them have to be positioned sufficiently far away from each other. The one-electron reduction potentials are adjusted such that the first and second electron flows uphill and downhill, respectively (Fig. 1). As a consequence, the first endothermic electron transfer step is not instantaneously reversed when coupled with the second extremely rapid exergonic one which was referred to as escapement-type mechanism [18,27]. Concurrently, the back reaction from energy-rich ferredoxin is also suppressed due to its endergonicity (Fig. 1). This strict directionality of the two single one-electron reductions is not in contradiction to the reversibility of the total FBEB process on the bifurcating FAD. In addition, the tight coupling implicates a catalytic inactivity of the FBEB reaction in the absence of one of the three substrates and thus minimizes deleterious side reactions with the energized flavosemiquinone. This kind of reaction scenario is unique in flavin biochemistry.

The exploited capability of flavins to split energy implicates a one-electron chemistry in such a way that the FBEB process has to be run through twice and requires 1e-to-2e switches for the high-potential two-electron acceptors and in some cases also 2e-to-1e switches for medium-potential two-electron donors. Bioorganic chemistry is normally based on a pairwise exchange of electrons. Flavins are well suited for these tasks when they are endowed with moderately balanced F/(FH•, F•) \leq (FH•, F•)/FH⁻ redox pair potentials because, at least, a weakly stabilized semiquinone is necessary for electron transfers. The low-potential electron acceptors, ferredoxin and flavodoxin, carrying iron/sulfur clusters and FMN, respectively, directly accept single electrons. Flavodoxins are endowed with non-inverted F/(FH•) > (FH•)/FH⁻ redox pair potential to form a stable flavosemiquinone.

3. The FBEB enzymes

The FBEB enzymes, explored so far, can be grouped into 4 classes: the bEtf (electron-transfer flavoprotein), the bNfn (NADPH dependent ferredoxin-NADH reductase), the bHdr (coenzyme M and B heterodisulfide reductase) and the bNdh (NADH dehydrogenase) classes. The

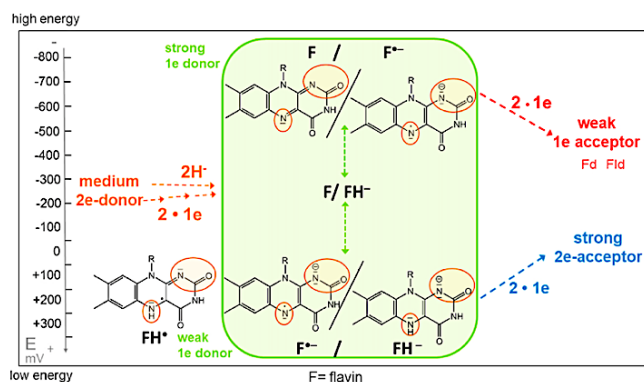


Fig. 1. The bifurcating flavin in the FBEB process. Oxidized flavin is normally present as neutral F, fully reduced flavin as FH⁻ (more rare is FH₂; pK_a 6.6 [90]) and semi-reduced flavin as blue FH• or red F• (pK_a 8.3 [90]). The N5 and N1C2 = O sites (red circle) change their protonation state and charge in the three redox states such that their microenvironment critically determines the reduction potential of the flavin (Fig. 2). In general, the proximity of positive protein charges stabilizes an electron-rich reduced state and increases the reduction potential whereas negative charges and hydrophobic surroundings favor an oxidized state. FBEB is based on the ability of flavins to split the energy of the F/F• and F•/FH⁻ one-electron redox reactions to use FH⁻ as a weak and F• as a strong electron donor. The latter reduces ferredoxin (Fd) and flavodoxin (Fld) which power endergonic reduction or uphill ion translocation processes. (For interpretation of the references to colour in this figure legend, the reader is referred to the Web version of this article.)

Table 1
The FBEB reactions and the involved enzymes.

FBEB enzymes	Reaction	Subunit composition + redox cofactors
EtfAB-Bcd	2NADH + crotonyl-CoA + Fd (2Fid) → 2NAD + butyryl-CoA + Fd ²⁻ (2Fid ⁻)	EtfA (FAD), EtfB (FAD), Bcd (FAD)
EtfAB-CarD	2NAD + butyryl-CoA + Fd ²⁻ (2Fid ⁻) → 2NADH + crotonyl-CoA + Fd	EtfA (FAD), 2[4Fe-4S], EtfB (FAD), CarD (FAD)
EtfAB-LDH	2NADH + caffeyl-CoA + Fd → 2NAD + dihydrocaffeyl-CoA + Fd ²⁻	EtfA (FAD, 1[4Fe-4S]), EtfB (FAD), LDH (FAD)
EtfABX-FixC(EtfC)	2NADH + dihydrocaffeyl-CoA + Fd → 2NAD + lactate + Fd ²⁻	EtfA (FAD, EtfB (FAD), FixC (EtfC) (FAD), EtfX (2[4Fe-4S])
NfnAB	2NADPH + NAD ⁺ + Fd → 2NADP ⁺ + 2NADH + Fd ²⁻	NfnA (FAD, [2Fe-2S]), NfnB (FAD, 2[4Fe-4S])
NfnB-DsrA*	2NAD(P)H + DsrC _{ox} + Fd → 2NAD(P) ⁺ + DsrC _{ox} + Fd ²⁻	NfnB (FAD, 4[4Fe-4S]), DsrA (siro-heme, 2 [4Fe-4S]), DsrB (siro-heme, 2[4Fe-4S]), DsrC (2 adjacent thiols)
HdrABC-MvhADG	2H ₂ + CoM-S-S-CoB + Fd → 2H ⁺ + CoM-SH + CoB-SH + Fd ²⁻	HdrA (FAD, 6[4Fe-4S]), HdrB (2 non-cubane [4Fe-4S]), HdrC (2 [4Fe-4S]), MvhA ([Ni-Fe]), MvhG (3[4Fe-4S]), MvhD (2[2Fe-2S])
HdrABC-FdhAB-MvhD	2HCOO ⁻ + CoM-S-S-CoB + Fd → 2CO ₂ + CoM-SH + CoB-SH + Fd ²⁻	HdrA (FAD, 6[4Fe-4S]), HdrB (2 non-cubane [4Fe-4S]), HdrC (2[4Fe-4S]), MvhD (2[2Fe-2S]), FdhA (MPT), FdhB (2[4Fe-4S])
HdrABC/MetFV-MvhD*	2F ₄₂₀ H ₂ + CoM-S-S-CoB + Fd → 2F ₄₂₀ + CoM-SH + CoB-SH + Fd ²⁻	HdrA (FAD, 6[4Fe-4S]), HdrB (2 non-cubane [4Fe-4S]), HdrC (2[4Fe-4S])
BamBCDEFGH*	2NADH + methylene-H ₄ F + Fd → 2NAD ⁺ + methyl-H ₄ F + Fd ²⁻	HdrA (2FAD, 4[4Fe-4S]), HdrB (2 non-cubane [4Fe-4S]), HdrC (2 [4Fe-4S]), MvhD (2[2Fe-2S]), MetV (1[4Fe-4S]), 1 Zn, MetF (2FMN)
HdrABC-FixABCD*	2F ₄₂₀ H ₂ + CoM-S-S-CoB + Fd → 2F ₄₂₀ + CoM-SH + CoB-SH + Fd ²⁻	BamE (2FAD, 6[4Fe-4S]), BamD (2 [4Fe-4S]), 2 non-cubane [4Fe-4S]), BamG (2[2Fe-2S]), BamI (2[4Fe-4S]), BamH (FAD, 2[4Fe-4S]), BamF (1[2Fe-2S]), BamC (3[4Fe-4S]), BamB (1[4Fe-4S]), WPT
HdrABC	2H ₂ + NAD ⁺ + Fd → 3H ⁺ + NADH + Fd ²⁻	HdrA (2FAD, 4[4Fe-4S]), HdrB (2 non-cubane [4Fe-4S]), HdrC (2 [4Fe-4S]), FixCD (2[4Fe-4S]), 2 [Fe-2S], FixB (2[4Fe-4S]), FixA (FAD, [2Fe-2S])
HydABC	2H ₂ + NADP ⁺ + Fd → 3H ⁺ + NADPH + Fd ²⁻	HydA (1[Fe-Fe]), 2[2Fe-2S], 3 [4Fe-4S]), HydB (FMN, 1[2Fe-2S]), 3[4Fe-4S]), HydC (1[2Fe-2S])
HytABCDE-FdhA	2HCOO ⁻ + NAD ⁺ + Fd → 2CO ₂ + NADH + H ⁺ + Fd ²⁻	HytA (1[Fe-Fe]), 2[2Fe-2S]), HytB (FMN, [2Fe-2S]), 3[4Fe-4S]), HytC (1[2Fe-2S]), HytD (1[2Fe-2S]), 2[4Fe-4S]), HytE1 (4[4Fe-4S]), HytE2 (4[4Fe-4S]), FdhA (WPT, [4Fe-4S])
HytABC-FdhF2	2HCOO ⁻ + NAD ⁺ + Fd → 2CO ₂ + NADH + H ⁺ + Fd ²⁻	HytA (1[2Fe-2S]), 4[4Fe-4S]), HytB (FMN, 1[2Fe-2S]), 3[4Fe-4S]), HytC (1[2Fe-2S]), FdhF2 (MPT, 1 [2Fe-2S]), 4[4Fe-4S])

abbreviations for the classes are derived from the protein module carrying the bifurcating flavin. Detailed structural data are available for the first three classes comprising EtfAB + Bcd (butyryl-CoA dehydrogenase) from *Acidaminococcus fermentans* [28], the EtfAB-Bcd complex from *Clostridium difficile* [29], the EtfAB-CarD (caffeyl-CoA dehydrogenase) complex of *Acetobacterium woodii* [30], the NfnAB complex from *Thermotoga maritima* [31] and *Pyrococcus furiosus* [26] and the HdrABC-MvhADG ([NiFe] hydrogenase) complex of *Methanothermococcus thermolithotrophicus* [32]. According to sequential and structural analysis, every FBEB enzyme is composed of several redox-cofactor containing building blocks that are also used by diverse non-bifurcating oxidoreductases. This is, in particular, true for the domains carrying the bifurcating flavin.

The bEtf class, so far, includes protein complexes EtfAB-Bcd (butyryl-CoA dehydrogenase) [33], EtfAB-CarD (caffeyl-CoA reductase) [34], EtfAB-LDH (lactate dehydrogenase) [35], and EtfABX-FixC (EtfC) (ubiquinone reductase) [8,36,37]. Their biochemical reactions are outlined in Table 1. EtfAB/oxidoreductases are architecturally built up of a flavin-containing multisubunit oxidoreductase core, the site of the high-potential reduction and several peripherally attached EtfAB modules [29]. Each EtfAB module is subdivided into a rigid base formed by the structurally related domains I and III from EtfA and EtfB, respectively, and a mobile FAD-carrying domain II built up of C-terminal segments from EtfA and EtfB [38]. Domain III of EtfB characterized by a distinct $\alpha\beta$ structure carries the bifurcating FAD (Fig. 2A) to which the medium-potential two-electron donor NADH is attached for hydride transfer [28]. It is worth to mention that EtfAB complexes lacking the bifurcating FAD (replaced by AMP) are also used in biology to shuttle electrons from diverse dehydrogenases to the membrane-bound respiratory chain via the FAD bound to domain II [39]. The bNfn class consists of the NfnAB complex [40] and perhaps the DsrAB (sulfite reductase)/NfnB complex (Table 1) [41]. Based on the NfnAB structure [26,31] the ferredoxin-NADP⁺ reductase-like NfnA [42] harbors an FAD and the site of the higher-potential electron acceptor NAD⁺ while NfnB contains the bifurcating FAD and the site for the two-electron donor NADPH. Architecturally, NfnB belongs to a disulfide reductase superfamily of flavoproteins (Fig. 2B) built up of two Rossmann-type $\alpha\beta$ domains and an α -helical domain. Its next relative is the dihydropyridine dehydrogenase [43]. The bHdr class consists of the HdrABC-MvhADG [44,45], HdrABC-FdhAB ([W, Se] formate dehydrogenase)-MvhD [46], HdrA2B2C2 (with F₄₂₀H₂ as electron donor) [47,48] and the putative bifurcating HdrABC-FixABCD (involved in sulfite reductase subunit DsrC reduction by NADH) [49], class II benzoyl-CoA reductase Bam [(BC)₂DEFGH]₂ [50] and methylenetetrahydrofolate reductase MetFVHdrABC-MvhD [51]; their reactions are listed in Table 1. While the high-potential reduction is localized on HdrB, the central bifurcation unit is the thioredoxin reductase subunit HdrA (Fig. 2C) [32,52]. In contrast to the first two classes, the electron donor is not NAD(P)H positioned in van der Waals contact to the bifurcating FAD, but a spatially distant two-electron donor e.g. H₂ bound to a [Ni, Fe]-hydrogenase module [44,53]. A special situation exists for QmoABC (quinone-binding membrane-spanning oxidoreductase involved in adenosine 5'-phosphosulfate reduction to sulfite via the quinol pool), which contains a potential bifurcating HdrA but no HdrB and HdrC [54]. Investigated members of the bNdh class are NAD(P)H dehydrogenase/[FeFe] hydrogenase and NAD(P)H dehydrogenase/formate dehydrogenase from several organisms with varying subunit and Fe/S cluster compositions [55-58]. The bifurcating compound has not been definitively identified in the bNdh class but a second FMN bound to the complex I-related NADH dehydrogenase module is the most attractive candidate.

The available structural data precisely reflect the functional specifications on FBEB enzymes and allow to design a general architecture (Fig. 3). FBEB enzymes are built up of a central structural unit hosting the bifurcating flavin, a two-electron donor unit as well as a high- and low-potential electron acceptor unit. The two-electron donor unit either

K. Kayastha et al.

Archives of Biochemistry and Biophysics 701 (2021) 108796

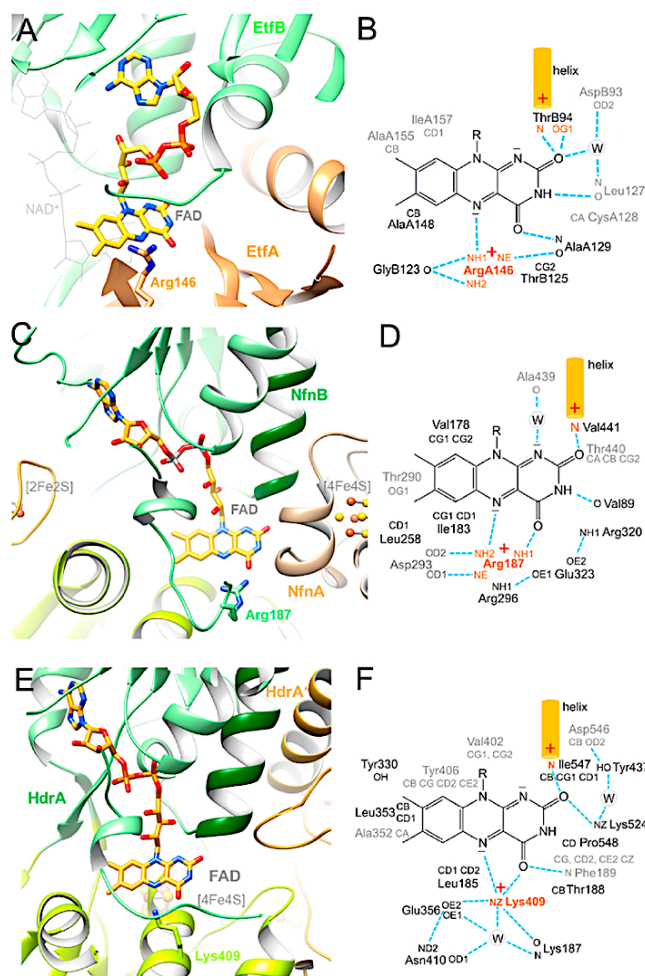


Fig. 2. Architecture of the binding sites of the bifurcating FAD. A) The bEtf class. In the EtfAB from *A. fermentans* FAD is present in an S-shaped compressed conformation with a planar isoalloxazine ring. The AMP part of NAD could be structurally identified but the ribose-nicotinamide part remains flexible and is modelled. (C) The bNfn class. In the NfnB of NfnAB from *T. maritima* the FAD is bound in an elongated conformation with a planar isoalloxazine ring. E) The bHdr class. In HdrA of HdrABC from *M. thermolithotrophicus* the FAD is bound rather similar than the one in NfnB. B, D, F) Scheme of the corresponding polypeptide-isoalloxazine interactions. Residues in front of the isoalloxazine ring (si-side) are drawn in black, those behind (re-side) in grey.

consists of NAD(PH) placed in hydride transfer distance to the bifurcating FAD or remotely a protein module with binding sites for H₂ [53], formate [46] or presumably NADH [49] as well as for the required 2e-to-1e switches such as [NiFe] or [FeFe] centers, molybdopterin or flavin, respectively (Fig. 3). The high-potential electron acceptor unit carries FAD or two non-cubane [4Fe-4S] clusters as 1e-to-2e switch that is interposed between the bifurcating FAD and the acceptor for the uptake of an electron pair. The low-potential electron-accepting structural units are ferredoxins or flavodoxins which are not part of the FBEB complex and only bound in a transient and rather unspecific manner [2]. Their exact binding positions at the surface of FBEB enzymes are therefore unknown except for NfnAB where indirect hints exist [26,31]. The central and the three peripheral redox units are connected by no,

one or several one-electron carriers which makes the distances between redox centers variable among the FBEB classes (Fig. 3).

The current structures of FBEB enzymes offered static pictures that reveal electron transfer routes between the bifurcating FAD and the three peripheral redox centers to be conductive or interrupted based on distance criteria between neighbored redox centers [59]. This finding suggests different conformational states for the three electron transfer steps whose coordination upon substrate binding/product release or redox state change is not understood yet. The available FBEB enzyme structures share the feature that the bifurcating FAD and the high potential 1e-to-2e electron switches are connected by, at least, one bridging one-electron carrier and one of the distances between the electron carriers is ca. 14 Å [59], the limit of productive electron

K. Kayastha et al.

Archives of Biochemistry and Biophysics 701 (2021) 108796

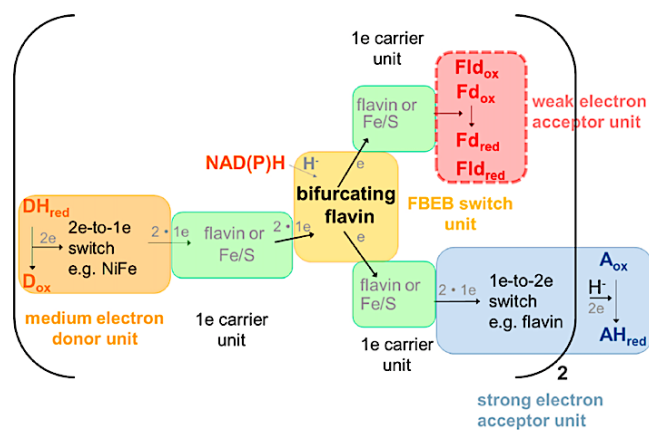


Fig. 3. Basic architecture of the FBEB machinery. The multisubunit enzyme complexes consist of a central FBEB switch unit and three peripheral redox units with binding sites for the medium electron donor, the weak and the strong electron acceptor. The central and peripheral units are mostly electronically connected by one-electron redox carriers. The weak electron acceptor, ferredoxin (Fd) or flavodoxin (Fid), is not an integral component of the FBEB complex (bordered with dashes). It transiently binds for electron uptake and is subsequently detached. Flavins can play a key role in each of the four redox units and in the connecting electron wire thereby serving as 1e-to-1e, 2e-to-1e and 1e-to-2e switches with specific redox properties governed by their global position within the FBEB complex and realized by their local protein surrounding. FBEB is initiated by reducing the bifurcating flavin either directly by NAD(P)H (or $F_{420}H_2$) via hydride transfer or by a remote two-electron donor (DH_{red}) via two single electrons. From the reduced bifurcating FADH⁻, one electron flows to the 1e-to-2e switch of the strong electron acceptor unit and the second towards the weak electron acceptor unit, Fd or Fid. This process runs twice (indicated by the “2” right below of the parenthesis). Finally, the two-electron high-potential acceptor (A_{ox}) is reduced.

transfer, or longer. In contrast, the distance between the bifurcating FAD and the next one-electron carrier along the low-potential route appears to be rather short [26,28,29,31]. Thus, distance modulation might be used for gating FBEB processes including the suppression of unfavorable back and side reactions under turnover conditions but also in the absence of one of the three substrates.

4. Characteristics of the bifurcating FAD

Structurally different FBEB subunits share the feature that the bifurcating FADs are attached to the C-terminal end of a parallel β -sheet of an open $\alpha\beta$ structure (Fig. 2). The isoalloxazine rings thereby protrude beyond the FAD-binding domain and are flanked by other redox cofactor carrying domains and/or subunits which might be beneficial for conducting electrons into different directions. In the bEtf class, the isoalloxazine ring sits between EtfB and EtfA [28–30] (Fig. 2a), in the bNfn class between all three domains of the disulfide reductase module adjacent to NfnA [26,31] (Fig. 2b) and in the bHdr class between the two $\alpha\beta$ domains of HdrA close to the partner subunit HdrB (Fig. 2c) [32]. The conformations of the entire FAD substantially differ in the three FBEB classes, however, the isoalloxazine ring is always planar.

To qualitatively assess the stability of the FAD, FADH[•]/FAD^{•-} and FADH⁻ states and thus their approximate redox behavior, the microenvironment of the bifurcating FAD was carefully analyzed. Although energetic, entropic and kinetic factors in their entirety have to be considered, two features adjacent to the N5 and N1–C2=O sites of FAD shared by all FBEB enzymes structurally characterized may play a pronounced role. The N5 site is contacted by positively charged residues, for example Arg146 in EtfAB of *A. fermentans* [28], Arg187 in NfnAB of *T. maritima* [31] and LysA409 in HdrABC of *M. thermolithotrophicus* [32] (see Fig. 2) which are strictly conserved among their bifurcating family members [60,61]. Additional interactions between O4 of FAD, main chain carboxyl oxygens, as well as two acidic residues (Asp293 and GluA356, respectively) in case of NfnB and HdrA and the mobile arginine/lysine side chains restrict the space of freedom for the latter and make larger redox state-induced conformational changes unlikely (Fig. 2). The charged and proton-donating guanidinium/ammonium groups neutralize negatively charged FAD^{•-} and FADH⁻ and form preferably a hydrogen-bond with the proton-accepting FAD and FAD^{•-}, respectively. Various data support the importance of N5-polypeptide

interactions for the physicochemical properties of FAD. (I) Based on site-directed mutagenesis experiments, the Arg136 exchange by glutamine and lysine in the *C. difficile* EtfAB-Bcd complex (equivalent to Arg146 in the *A. fermentans* enzyme, Fig. 32A) results in its disassembly [29], however, the corresponding exchange of Arg203 to alanine, glutamine and lysine in the EtfAB/CarD complex maintains its integrity and exhibits a complete loss of the FBEB activity [30]. (II) Biochemical studies on *M. elsdenii* EtfAB revealed a higher affinity of the bifurcating flavin in the oxidized FAD than in the reduced FADH⁻ state [62], tentatively interpreted by increased guanidinium-N5 interactions. (III) The catalytically relevant lysine in methanogenic HdrABC in front of N5 is exchanged in the sulfur-oxidizing *Hyphomicrobium denitrificans* HdrABC by a water molecule linked with a glutamate side chain which preferentially forms a hydrogen-bond with a protonated N5 [63]. The stable flavosemiquinone FADH[•] visible in the Vis spectra and the FADH[•]/FADH⁻ and FAD/FADH[•] pair potentials of ca. -165 mV and -40 mV establish the sulfur-oxidizing HdrABC as non-bifurcating enzyme and thus highlight the importance of the N5-polypeptide interactions for adjusting a stable or unstable flavosemiquinone. (IV) Mutations around N5 in other flavoenzymes resulted in significant changes of reduction potentials [64]. Likewise, the more negative FH[•]/FH⁻ potential in cryptochrome than in photolyase was attributed to a charged aspartate versus a neutral asparagine both interacting with N5, respectively [65], which underlines the strong influence of charged residues in the surrounding of N5.

The N1–C2=O site of the bifurcating FAD in the bEtf, bNfn and bHdr classes primarily interacts with the partially positively charged N-terminal end of an α -helix by a hydrogen bond with its terminal residue (Fig. 2). It is assumed that negatively charged flavin redox states are normally stabilized by this frequently found structural feature [66]. However, the limited number of further enhancing hydrogen bond interactions, even the presence of acidic residues in the second interaction shell, only suggest a moderate stabilization of negative charges at the N1–C2=O site by its direct environment in FBEB subunits (Fig. 2B, D, F). The isoalloxazine ring is more encapsulated in the Hdr than in the bEtf and bNfn classes which might, however, be equalized after NAD(P)H binding. No further conspicuous features are visible in the vicinity of the isoalloxazine ring (Fig. 2).

Various findings concerning the bifurcating flavin and FBEB in total are still enigmatic and await an answer. Its strongly inverted one-

electron reduction potential, a necessary prerequisite for the FBEB function [18], cannot be rationalized on the basis of the performed qualitative structural analysis despite the identification of common features in the flavin microenvironment of the three FBEB enzyme classes. This statement is also true when the magnitudes of the one-electron potentials are less extreme under equilibrium conditions than those determined upon photoreduction and correspond to those of quinone-based electron bifurcation [26,27,67]. One proposal to explain the extremely short-lived flavosemiquinone is related to the conserved arginine/lysine next to N5 which might impair the isoalloxazine radical delocalization. It is also not conclusively clarified whether FADH^\bullet or $\text{FAD}^{\bullet-}$ acts as an intermediate during the oxidation of FADH^- to FAD. According to the surrounding polypeptide, $\text{FAD}^{\bullet-}$ is more stable than FADH^\bullet implicating a deprotonation reaction after the first oxidation step if its rate is higher than the FADH^\bullet lifetime. The experimentally detected $\text{FAD}^{\bullet-}$ species argues for a deprotonated state, however, its generation was triggered by photoreduction of FAD and its decay was measured in an isolated and uni-directional fashion and not within a strongly cooperative FBEB event [26].

The extremely short-lived flavosemiquinone required on one side creates on the other a serious obstacle for the stepwise reduction of the bifurcating FAD by single electrons from the medium electron donor H_2 /formate in the bHdr class. We can only speculate whether $\text{FAD}^{\bullet-}$ is more stable than assumed under equilibrium conditions and FADH^\bullet (prior to deprotonation) reduce the low-potential electron acceptor or whether FAD is reduced by two cooperative one-electron transfer processes. In this context the coupling of the two FAD in the (HdABC-MvhADG)₂ complex and the interaction between the $\text{N1C2}=\text{O}$ group of FAD and the partner Lys524 only found in some structures to stabilize $\text{FAD}^{\bullet-}$ might play a role [32].

Finally, the tight coupling of the exergonic and endergonic bi-directional electron transfer requires the presence of all three

substrates to measure enzymatic activity. On the other hand, the *C. propionicum* EtfAB/Pcd (propionyl-CoA dehydrogenase) and *P. furiosus* NfnII catalyze uni-directional reactions with two substrates (reductions of acrylyl-CoA with NADH and NADP^+ with ferredoxin, respectively), although the binding modes of their central FADs are similar to those of their bifurcating counterparts [68,69]. Likewise, the *Methanosarcina acetivorans* HdrA2B2C2 can besides the FBEB reaction unidirectionally reduce CoM–SS–CoB by ferredoxin albeit with a low enzymatic activity [47]. It is, so far, obscure which factors determine cooperativity and non-cooperativity in FBEB. Bi- or uni-directionality might have its origin in properties of the central FAD (e.g. higher inverted one-electron reduction potentials for the bifurcating flavin) and/or of properties of the peripheral redox cofactors.

5. Flavins as 1e-to-2e switches for high-potential two-electron acceptors

Enzymes of the bEtf, bNfn and bNdh classes also use flavins for accepting two electrons – one in each round – from the bifurcating FAD and for, subsequently, transferring a hydride to the high-potential electron acceptor (Table 1, Fig. 3). In biochemistry, these flavins serve as typical 1e-to-2e switches found e.g. in ferredoxin- NADP^+ reductases [42] and acyl-CoA dehydrogenases [70]. Enzymes of the bHdr class are exceptional as the two 1e-to-2e switch is built up by two non-cubane [4Fe–4S] clusters which donate one electron each to the disulfide bond of CoM–SS–CoB, the high-potential electron acceptor [32,53]. Both non-cubane [4Fe–4S] clusters together fulfill the same task as FAD.

Acyl-CoA dehydrogenases, the high-potential electron acceptor modules of some bEtf class members are homotetramers; each monomer is composed of two α -helical and one nine-stranded β -barrel domains (Fig. 4A) [71]. FAD is sandwiched between two subunits with the isoalloxazine ring being attached to the front side of the β -barrel largely

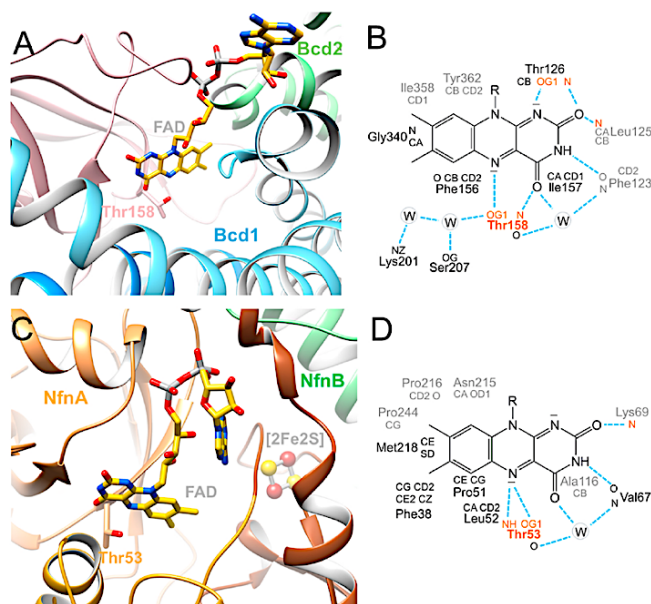


Fig. 4. High-potential 1e-to-2e switching flavins. (A) FAD-binding site in Bcd of *A. fermentans*. The slightly bent isoalloxazine ring of FAD in Bcd sits in front of a β -barrel (light pink) encapsulated by the two α -helical domains (blue and light-blue). (C) FAD-binding site in NfnA of the NfnAB complex of *T. maritima*. The planar isoalloxazine ring in NfnA sits in front of the β -barrel (orange) surrounded by the α domain (yellow) and the C-terminal extension (brown). The latter hosts the binding site of the [2Fe–2S] center. (B + D) Scheme of the corresponding polypeptide-isoalloxazine interactions. (For interpretation of the references to colour in this figure legend, the reader is referred to the Web version of this article.)

encapsulated by the α -helical domains. The FAD N5 site of *A. fermentans* Bcd interacts with Thr158-OG1 and the N1C2 = O site with Leu125-NH, Thr126-NH and Thr126-OG1 (Fig. 4B) [28]. Stabilizing an unprotonated N5 and a charged flavin state are in accordance with the spectroscopically detected flavosemiquinone anion $\text{FAD}^{\bullet-}$. The rather high and non-inverted reduction potential of the $\text{FAD}/\text{FAD}^{\bullet-}$ and $\text{FAD}^{\bullet-}/\text{FADH}^{\bullet-}$ pairs of -42 mV and -64 mV from the *A. fermentans* enzymes [72] are well suited to uptake a single electron from FAD of domain II in each round and to transfer them as hydride to crotonyl-CoA forming butyryl-CoA (-10 mV).

The FAD carrying NfnA module of the NfnAB complex, the binding site of the high-potential electron acceptor NAD^+ , is built up of a six-stranded β -barrel, an α Rossmann domain and a C-terminal extension (Fig. 4C) [73]. FAD binds at the outer surface of the β -barrel; the isoalloxazine is shielded from all three domains. The N5 site of the *T. maritima* enzyme is hydrogen-bonded with the Thr53-NH and -OG1 and the N1C2 = O site only with Lys69-NH (Fig. 4D) [31]. Therefore, the polypeptide matrix appears to preferentially interact with a deprotonated N5 and an uncharged N1C2 = O site suggesting a stabilized oxidized FAD (relative to observed FADH^{\bullet}) and FADH^{\bullet} (relative to charged $\text{FADH}^{\bullet-}$). The one-electron reduction potentials $\text{FAD}/\text{FADH}^{\bullet}$ and $\text{FADH}^{\bullet}/\text{FADH}^{\bullet-}$ of spinach ferredoxin-NADP⁺ reductase are -350 mV and -335 mV [74], and those of *Lactococcus lactis* dihydroorotate dehydrogenase are -312 mV and -297 mV [75]. The $\text{FAD}/\text{FADH}^{\bullet-}$ reduction potential of *P. furiosus* NfnI is ca. -276 mV [26]. These reduction potentials enable a hydride transfer to NAD^+ and the uptake of single electrons from the bifurcating FAD although the high reduction potential of the intervening [2Fe-2S] cluster gives rise to questions regarding the smooth electron transfer.

6. Flavins as one-electron carrier

FBEB enzymes also use flavins as electron shuttle and as low-potential electron acceptor (Fig. 3). While the one-electron reduction potential of the shuttle FAD should be in the range of the corresponding peripheral redox center unit, the low-potential flavodoxin is characterized by a low $\text{FMNH}^{\bullet}/\text{FMNH}^{\bullet-}$ reduction potential of ca. -400 mV [76] which enables the storage of free energy increments. One-electron carriers feature a stable flavosemiquinone and only use one of the two one-electron redox transitions for function.

The bEtf class harbors an FAD as electron shuttle between the bifurcating FAD and the 1e-to-2e switching FAD of the oxidoreductase domain [29,30]. Other FBEB classes use iron-sulfur clusters instead of FAD for this purpose. The shuttle FAD of the EtfA domain II is primarily attached to the C-terminal end of its central β -sheet (Fig. 5A) [28]. The N5 site of the *A. fermentans* enzyme interacts with SerA270-OG1 and the N1C2 = O site is hydrogen-bonded to the FAD ribityl-4-OH, HisA290-ND1 and ArgA253-NH, respectively. ArgA253 neutralizes, in addition, a negatively charged state due to its position at the positively charged N-terminal end of helix 253:258 and due to its guanidinium side chain being oriented coplanar to the tricyclic ring (Fig. 5B).

As FAD swings together with domain II between the B(bifurcation)- and the D (dehydrogenase, oxidoreductase)-conducting states its polypeptide surrounding substantially changes. Structural and electrochemical data for the B state of the EtfAB-Bcd complex are not available yet, but for a B-like state in the absence of the oxidoreductase module and for the ν -state (Fig. 5C + D). The one-electron reduction potentials of the EtfA FAD of separated *M. elsdenii/A. fermentans* EtfAB in the B-like state is $+81$ mV/ $+134$ mV ($\text{FAD}/\text{FAD}^{\bullet-}$) and -136 mV/ -36 mV ($\text{FAD}^{\bullet-}/\text{FADH}^{\bullet-}$) [62,72,77]. The spectroscopically detectable $\text{FAD}^{\bullet-}$ is in line with the preferred hydrogen-bond with a deprotonated N5 and

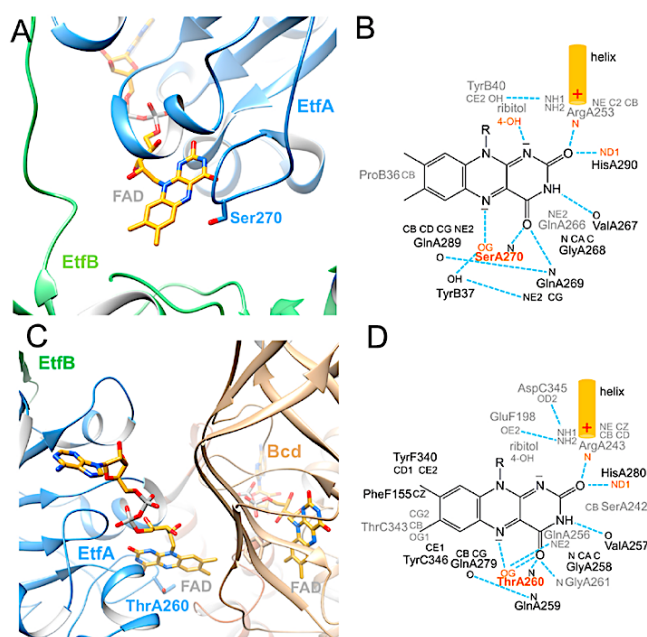


Fig. 5. Swinging FAD as electron carrier in the bEtf class. A) The FAD binding site of EtfA domain II in the B-like state of *A. fermentans*. The isoalloxazine ring is exposed from domain II and the hydrophobic dimethylbenzyl moiety is essentially surrounded by bulk solvent. FAD uptakes an electron from the bifurcating FAD in the B-state, swings with domain II to the ν -state and donates the electron to the FAD bound to Bcd (Fig. 4). B) Scheme of the polypeptide-isoalloxazine interactions. The micro-environment of FAD is ideally suited to stabilize a flavosemiquinone anion $\text{FAD}^{\bullet-}$. C) The FAD binding site of EtfA domain II in the ν -state of *C. difficile*. D) Scheme of the polypeptide-isoalloxazine interactions. The surrounding of the isoalloxazine ring becomes more hydrophobic in the D- compared with the B-like state. The labels C and F stand for two different Bcd subunits.

the capability to neutralize a negative charge at the NIC2 = O site (Fig. 5B). Several site-directed mutagenesis studies on the non-bifurcating EtfAB with a similar domain II FAD binding mode essentially confirmed the relationship between the flavin environment and the reduction potential [39,78,79]. $\text{FAD}^{\bullet-}$ of EtfA that presumably dominates in the *A. fermentans* cell under the prevailing reducing conditions [29] appears also to influence the physical properties of the bifurcating FAD [80]. In the ν -state, the reduction potential of the FAD of EtfA becomes inverted deduced from potentiometric measurements of the transient *A. fermentans* (EtfAB)₂/Bcd₄ complex [72]; the FAD/FADH⁻ reduction potential is -228 mV. This surprising finding can be qualitatively rationalized because the FAD rotates from the polar predominantly solvent-mediated domains II-III interface of the B-state (Fig. 5A + B) to a more nonpolar domain II-oxidoreductase interface of the ν -state (Fig. 5C + D) [28–30]. A non-polar surrounding stabilizes the (uncharged) oxidized FAD state and as a consequence the reduction potential of the FAD/ $\text{FAD}^{\bullet-}$ pair falls below that of $\text{FAD}^{\bullet-}$ /FADH⁻. Moreover, the conformation-dependent decrease of the reduction potential of the shuttle FAD thermodynamically facilitates its electron transfer to the 1e-to-2e switching FAD [72].

The application of flavodoxins as low-potential electron acceptors in FBEB has been, so far, demonstrated for the EtfAB/Bcd complex of *A. fermentans* [5], the EtfABX-FixC complex of *A. vinelandii* [36] and the HdrA2B2C2 complex [7]. Flavodoxins are small microbial $\alpha\beta$ proteins consisting of five parallel β -strands and five flanking α -helices (Fig. 6A) [81]. FMN is bound in the canonical fashion with the isoalloxazine ring being exposed to bulk solvent. For isoalloxazine-polypeptide interaction analysis we choose the flavodoxin of *Clostridium beijerinckii* (SNLL) which has a sequence identity of 42% to the *A. fermentans* protein applied for FBEB kinetic studies on the Etf(AB)₂/Bcd₄ complex (Fig. 6B) [5]. The N5 site weakly interacts with the polypeptide in the oxidized FMN state but forms a hydrogen bond to Gly57-O in the FMNH[•] and FMNH⁻ states thereby demonstrating the possibilities of redox-dependent conformational changes [82]. The NIC2 = O site weakly interacts with the ribitol-O2⁻ and is hydrogen bonded with main chain NH groups of Gly89, Trp90 and Gly91. The potential stabilization of negatively charged states is overcompensated by the Glu59-OE2 hydrogen-bond with N3 and the aromatic Trp90 side chain stacking to the tricyclic ring (Fig. 6) [83,84]. The resulting stabilized FMNH[•] in comparison with FMN and FMNH⁻ are reflected in reduction potentials of -92 mV and -399 mV for the FMN/FMNH[•] and FMNH[•]/FMNH⁻ pairs of the *C. beijerinckii* flavodoxin, respectively [82].

7. Cooperative versus non-cooperative one by one electron transfer reactions

The discovery of FBEB teaches us that an electron pair can be split

despite strongly inverted reduction potentials when the two one-electron steps are cooperative and diverge into two different directions from the bifurcating FADH⁻ (Fig. 1+7A). Tight coupling is ensured by the high endergonicity of the electron transfer from FADH⁻ toward the high-potential 1e-to-2e switch (FAD or two non-cubane [4Fe–4S] clusters) and the high exergonicity of the electron transfer from the flavosemiquinone to the low-potential ferredoxin/flavodoxin (Fig. 1+7A). The first rate-determining electron transfer step pulls along the second one which in return locks in the first one [18,27]. Due to the strong redox cooperativity, all three substrates – electron donor, low and high-potential electron acceptor – have to be present for measuring catalytic activity. This finding implicates that productive FBEB does not only depend on the electrochemical properties of the central bifurcating FAD but also on the spatial arrangement and the redox properties of the involved peripheral redox cofactors (Fig. 3) [67].

While cooperative bi-directional one-electron transfer on the basis of strongly inverted one-electron reduction potentials is unique for FBEB, spatial but non-cooperative electron bifurcation using rather balanced one-electron reduction potentials is also conducted in biology. In complex I, one electron smoothly flows from the NADH reduced FMN (reduction potentials of FMNH[•]/FMNH⁻ \approx -336 mV and FMN/FMNH[•] \approx -414 mV for the bovine complex I [85]) to the [4Fe–4S] cluster N3 (-160 mV in *A. aeolicus*) and the other to the [2Fe–2S] cluster N1A (-250 mV in *A. aeolicus*) [18,86] (Fig. 7B). This type of electron bifurcation reduces the production of harmful reactive oxygen species because the reduced form of N1A prevents the release of the product NAD⁺ that blocks the O₂ binding site at FMN [87]. Besides non-cooperative and cooperative bi-directional one-electron transfer scenarios cooperative (besides the conventional non-cooperative) uni-directional one-electron transfer reactions appear also to be realized in biochemistry. Naphthoyl-CoA reductase contains one FAD with a non-inverted reduction potential and one FMN with an inverted reduction potential electronically coupled by a [4Fe–4S] cluster [88,89]. An energy-rich electron is transferred from FADH⁻ to FMN and the highly unstable, short-lived FMNH[•] state is cooperatively reduced by a second low-energy electron of the system (Fig. 7C). This process allows to attain a low two-electron FMN/FMNH⁻ reduction potential of ca. -450 mV which is necessary to reductively dearomatize the inert naphthoyl ring. As mentioned, a related strategy might be applied by the HdrABC-MvhADG complex for transferring two single electrons from H₂ to the bifurcating FAD. The bifurcating flavin of the bHdr class is reduced and oxidized by 1e steps and thus differs from the bEtf and bNfn classes. For comparison, the well-established non-cooperative uni-directional 2•1e transfer from FADH⁻ is illustrated in Fig. 7D. The analyzed 2•1e-to-2e transfer processes have to be distinguished from the frequently reported 2e-to-2e reactions that are characterized by inverted F/FH[•] and FH[•]/FH⁻ reduction potentials. Here, the electrons are

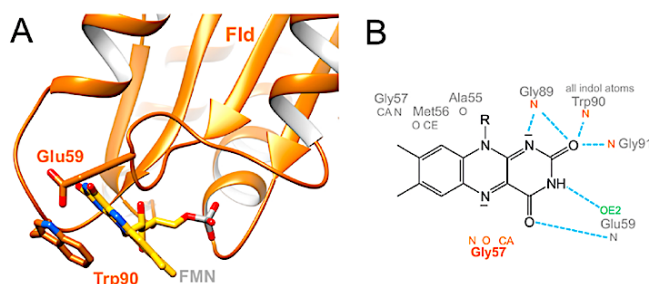


Fig. 6. Flavodoxin (Fld) of *C. beijerinckii*. A) The FMN binding site B) Scheme of the polypeptide-isoalloxazine interactions. The FMN surrounding stabilizes a neutral flavosemiquinone FH[•].

K. Kayastha et al.

Archives of Biochemistry and Biophysics 701 (2021) 108796

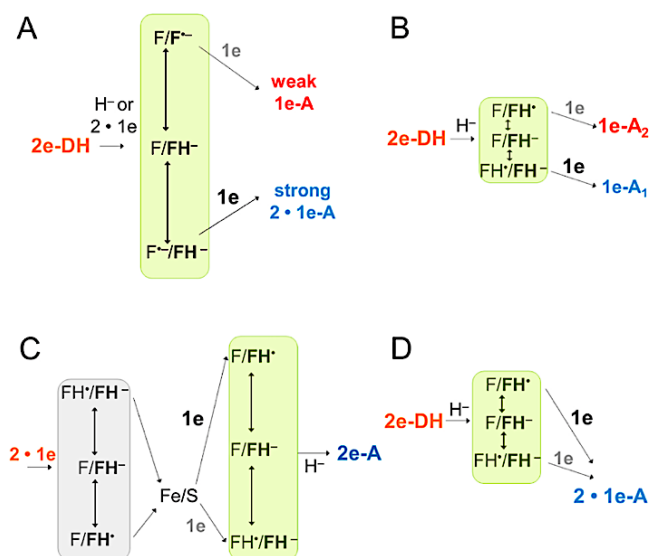


Fig. 7. Principles of flavin-dependent 2e-to-1e electron switches. The first and second electron transferred is written in bold black and grey, respectively. The flavins are abbreviated by F, the electron donor by DH and the electron acceptor by A. (A) The cooperative and bi-directional reduction process of FBEB. (B) The non-cooperative and bi-directional process as found in complex I. A moderately stable flavosemiquinone is detectable. (C) The cooperative and uni-directional reduction process as found in naphthoyl-CoA reductase. The cooperative flavin in the light-green box is an FMN, the non-cooperative one is an FAD (grey box) characterized by a detectable flavosemiquinone. (D) The normal non-cooperative and uni-directional reduction process as found in acyl-CoA dehydrogenase. In this case the reduction potentials of the one-electron transitions might be inverted. (For interpretation of the references to colour in this figure legend, the reader is referred to the Web version of this article.)

exchanged in a pairwise cooperative fashion between two substrates mostly in form of hydrides to and from the flavin.

Acknowledgement

This work was supported by the Max Planck Society and the Deutsche Forschungsgemeinschaft. We thank Hartmut Michel and Rudolf K. Thauer for long-term support. K.K. thanks Hartmut Michel and the International Max Planck Research School for funding, S.V. the Deutsche Forschungsgemeinschaft (VI 778/2-1) and W.B. Tobias Erb for support.

References

- [1] G. Herrmann, E. Jayamani, G. Mai, W. Buckel, Energy conservation via electron-transferring flavoprotein in anaerobic bacteria, *J. Bacteriol.* 190 (2008) 784–791.
- [2] F. Li, J. Hinderberger, H. Seedorf, J. Zhang, W. Buckel, R.K. Thauer, Coupled ferredoxin and crotonyl coenzyme A (CoA) reduction with NADH catalyzed by the butyryl-CoA dehydrogenase/Etf complex from *Clostridium kluyveri*, *J. Bacteriol.* 190 (2008) 843–850.
- [3] W. Nitschke, M.J. Russell, Redox bifurcations: mechanisms and importance to life now, and at its origin: a widespread means of energy conversion in biology unfolds, *Bioessays* 34 (2012) 106–109.
- [4] W. Buckel, R.K. Thauer, Energy conservation via electron bifurcating ferredoxin reduction and proton/ Na^+ translocating ferredoxin oxidation, *Biochim. Biophys. Acta* 1827 (2013) 94–113.
- [5] N.P. Chowdhury, K. Klomann, A. Seubert, W. Buckel, Reduction of flavodoxin by electron bifurcation and sodium ion-dependent reoxidation by NAD⁺ catalyzed by ferredoxin-NAD⁺ reductase (Rnf), *J. Biol. Chem.* 291 (2016) 11993–12002.
- [6] W. Thamer, I. Cirpus, M. Hans, A.J. Pierik, T. Selmer, E. Bill, D. Linder, W. Buckel, A two [4Fe-4S]-cluster-containing ferredoxin as an alternative electron donor for 2-hydroxyglutaryl-CoA dehydratase from *Acidaminococcus fermentans*, *Arch. Microbiol.* 179 (2003) 197–204.
- [7] D. Prakash, P.R. Iyer, S. Suharti, K.A. Walters, M.G. Santiago-Martinez, J. H. Golbeck, K.S. Murakami, J.G. Ferry, Structure and function of an unusual flavodoxin from the domain Archaea, *Proc. Natl. Acad. Sci. U. S. A.* 116 (2019) 25917–25922.
- [8] R.N. Ledbetter, A.M. Garcia Costas, C.E. Lubner, D.W. Mulder, M. Tokmina-Lukaszewska, J.H. Artz, A. Patterson, T.S. Magnuson, Z.J. Jay, H.D. Dunn, J. Miller, M.H. Plunkett, J.P. Hoben, B.M. Barney, R.P. Carlson, A.F. Miller, B. Bothner, P. W. King, J.W. Peters, L.C. Seefeldt, The electron bifurcating FixABCX protein complex from azotobacter vinelandii: generation of low-potential reducing equivalents for nitrogenase catalysis, *Biochemistry* 56 (2017) 4177–4190.
- [9] P. Mitchell, The protonmotive Q cycle: a general formulation, *FEBS Lett.* 59 (1975) 137–139.
- [10] W. Buckel, R.K. Thauer, Flavin-based electron bifurcation, ferredoxin, flavodoxin, and anaerobic respiration with protons (Ech) or NAD⁺ (mf) as electron acceptors: a historical review, *Front. Microbiol.* 9 (2018) 401.
- [11] V. Müller, N.P. Chowdhury, M. Bassen, Electron bifurcation: a long-hidden energy-coupling mechanism, *Annu. Rev. Microbiol.* 72 (2018) 331–353.
- [12] V. Hess, R. Gallegos, J.A. Jones, B. Barquera, M.H. Malamy, V. Müller, Occurrence of ferredoxin:NAD⁺ oxidoreductase activity and its ion specificity in several Gram-positive and Gram-negative bacteria, *PeerJ* 4 (2016) e1515.
- [13] R. Hedderich, Energy-converting [NiFe] hydrogenases from archaea and extremophiles: ancestors of complex I, *J. Bioenerg. Biomembr.* 36 (2004) 65–75.
- [14] R.K. Thauer, A.K. Kaster, H. Seedorf, W. Buckel, R. Hedderich, Methanogenic archaea: ecologically relevant differences in energy conservation, *Nat. Rev. Microbiol.* 6 (2008) 579–591.
- [15] T. Wagner, U. Emler, S. Shima, The methanogenic CO₂ reducing-and-fixing enzyme is bifunctional and contains 46 [4Fe-4S] clusters, *Science* 354 (2016) 114–117.
- [16] W.F. Martin, Hydrogen, metals, bifurcating electrons, and proton gradients: the early evolution of biological energy conservation, *FEBS Lett.* 586 (2012) 485–493.
- [17] W.F. Martin, R.K. Thauer, Energy in ancient metabolism, *Cell* 168 (2017) 953–955.
- [18] F. Baymann, B. Schoepp-Cothenet, S. Duval, M. Guiral, M. Brugna, C. Baffert, M. J. Russell, W. Nitschke, On the natural history of flavin-based electron bifurcation, *Front. Microbiol.* 9 (2018) 1357.
- [19] P. Zhang, J.L. Yuly, C.E. Lubner, D.W. Mulder, P.W. King, J.W. Peters, D. N. Beratan, Electron bifurcation: thermodynamics and kinetics of two-electron brokering in biological redox chemistry, *Acc. Chem. Res.* 50 (2017) 2410–2417.
- [20] J.L. Yuly, P. Zhang, C.E. Lubner, J.W. Peters, D.N. Beratan, Universal free-energy landscape produces efficient and reversible electron bifurcation, *Proc. Natl. Acad. Sci. U. S. A.* 117 (2020) 21045–21051.
- [21] J.W. Peters, A.F. Miller, A.K. Jones, P.W. King, M.W. Adams, Electron bifurcation, *Curr. Opin. Chem. Biol.* 31 (2016) 146–152.
- [22] C.T. Walsh, T.A. Wencewicz, Flavoenzymes: versatile catalysts in biosynthetic pathways, *Nat. Prod. Rep.* 30 (2013) 175–200.
- [23] D. Leys, N.S. Scrutton, Sweating the assets of flavin cofactors: new insight of chemical versatility from knowledge of structure and mechanism, *Curr. Opin. Struct. Biol.* 41 (2016) 19–26.
- [24] E. Romero, J.R. Gomez Castellanos, G. Gadda, M.W. Fraaije, A. Mattevi, Same substrate, many reactions: oxygen activation in flavoenzymes, *Chem. Rev.* 118 (2018) 1742–1769.
- [25] R.F. Anderson, Energetics of the one-electron reduction steps of riboflavin, FMN and FAD to their fully reduced forms, *Biochim. Biophys. Acta* 722 (1983) 158–162.
- [26] C.E. Lubner, D.P. Jennings, D.W. Mulder, G.J. Schut, O.A. Zadvornyy, J.P. Hoben, M. Tokmina-Lukaszewska, L. Berry, D.M. Nguyen, G.L. Lipscomb, B. Bothner, A. K. Jones, A.F. Miller, P.W. King, M.W.W. Adams, J.W. Peters, Mechanistic insights

- into energy conservation by flavin-based electron bifurcation, *Nat. Chem. Biol.* 13 (2017) 655–659.
- [27] A.R. Crofts, S. Hong, C. Wilson, R. Burton, D. Victoria, C. Harrison, K. Schulten, The mechanism of ubiquinol oxidation at the Qo-site of the cytochrome b_6 complex, *Biochim. Biophys. Acta* 1827 (2013) 1362–1377.
- [28] N.P. Chowdhury, A.M. Mowafy, J.K. Demmer, V. Upadhyay, S. Koelzer, E. Jayamani, J. Kahnt, M. Hornung, U. Demmer, U. Ermler, W. Buckel, Studies on the mechanism of electron bifurcation catalyzed by electron transferring flavoprotein (Etf) and butyryl-CoA dehydrogenase (Bcd) of *Acidaminococcus fermentans*, *J. Biol. Chem.* 289 (2014) 5145–5157.
- [29] J.K. Demmer, N. Pal Chowdhury, T. Selmer, U. Ermler, W. Buckel, The semiquinone swing in the bifurcating electron transferring flavoprotein/butyryl-CoA dehydrogenase complex from *Clostridium difficile*, *Nat. Commun.* 8 (2017) 1577.
- [30] J.K. Demmer, J. Bertsch, C. Oppinger, H. Wohlers, K. Kayastha, U. Demmer, U. Ermler, V. Müller, Molecular basis of the flavin-based electron-bifurcating caffeoyl-CoA reductase reaction, *FEBS Lett.* 592 (2018) 332–342.
- [31] J.K. Demmer, H. Huang, S. Wang, U. Demmer, R.K. Thauer, U. Ermler, Insights into flavin-based electron bifurcation via the NADH-dependent reduced ferredoxin: NADP oxidoreductase structure, *J. Biol. Chem.* 290 (2015) 21985–21995.
- [32] T. Wagner, J. Koch, U. Ermler, S. Shima, Methanogenic heterodisulfide reductase (HdrABC-MvhAGD) uses two noncubane [4Fe-4S] clusters for reduction, *Science* 357 (2017) 699–703.
- [33] H. Abouinanga el, O. Pinkenburg, J. Schifffels, A. El-Refai, W. Buckel, T. Selmer, Effect of an oxygen-tolerant bifurcating butyryl coenzyme A dehydrogenase/electron-transferring flavoprotein complex from *Clostridium difficile* on butyrate production in *Escherichia coli*, *J. Bacteriol.* 195 (2013) 3704–3713.
- [34] J. Bertsch, A. Parthasarathy, W. Buckel, V. Müller, An electron-bifurcating caffeoyl-CoA reductase, *J. Biol. Chem.* 288 (2013) 11304–11311.
- [35] M.C. Weghoff, J. Bertsch, V. Müller, A novel mode of lactate metabolism in strictly anaerobic bacteria, *Environ. Microbiol.* 17 (2015) 670–677.
- [36] H.D. Duan, C.E. Lubner, M. Tokmina-Lukaszewska, G.H. Gauss, B. Bothner, P. W. King, J.W. Peters, A.F. Miller, Distinct properties underlie flavin-based electron bifurcation in a novel electron transfer flavoprotein FixAB from *Rhodospseudomonas palustris*, *J. Biol. Chem.* 293 (2018) 4688–4701.
- [37] G.J. Schut, N. Mohamed-Raseek, M. Tokmina-Lukaszewska, D.W. Mulder, D.M. N. Nguyen, G.L. Lipscomb, J.P. Hoben, A. Patterson, C.E. Lubner, P.W. King, J. W. Peters, B. Bothner, A.F. Miller, M.W.W. Adams, The catalytic mechanism of electron-bifurcating electron transfer flavoproteins (ETFs) involves an intermediary complex with NAD^+ , *J. Biol. Chem.* 294 (2019) 3271–3283.
- [38] D.L. Roberts, E.E. Freman, J.J. Kim, Three-dimensional structure of human electron transfer flavoprotein to 2.1-Å resolution, *Proc. Natl. Acad. Sci. U. S. A.* 93 (1996) 14355–14360.
- [39] H.S. Toogood, D. Leys, N.S. Scrutton, Dynamics driving function: new insights from electron transferring flavoproteins and partner complexes, *FEBS J.* 274 (2007) 5481–5504.
- [40] S. Wang, H. Huang, J. Moll, R.K. Thauer, NADP^+ reduction with reduced ferredoxin and NADP^+ reduction with NADH are coupled via an electron-bifurcating enzyme complex in, *J. Bacteriol.* 192 (2010) 5115–5123.
- [41] M. Löffler, J. Feldhus, S.S. Venceslau, L. Kammler, F. Grein, L.A.C. Pereira, C. Dahl, DsrL mediates electron transfer between NADH and dSrbAB in *Allochromatium vinosum*, *Environ. Microbiol.* 22 (2020) 783–795.
- [42] P.A. Karplus, H.R. Faber, Structural aspects of plant ferredoxin : NADP^+ oxidoreductases, *Photosynth. Res.* 81 (2004) 303–315.
- [43] D. Dobritzsch, G. Schneider, K.D. Schumaker, Y. Lindqvist, Crystal structure of dihydropyrimidine dehydrogenase, a major determinant of the pharmacokinetics of the anti-cancer drug 5-fluorouracil, *EMBO J.* 20 (2001) 650–660.
- [44] R. Hedderich, A. Berkessel, R.K. Thauer, Purification and properties of heterodisulfide reductase from *Methanobacterium thermoautotrophicum* (strain Marburg), *Eur. J. Biochem.* 193 (1990) 255–261.
- [45] E. Setzke, R. Hedderich, S. Heiden, R.K. Thauer, H2: heterodisulfide oxidoreductase complex from *Methanobacterium thermoautotrophicum*. Composition and properties, *Eur. J. Biochem.* 220 (1994) 139–148.
- [46] K.C. Costa, P.M. Wong, T. Wang, T.J. Lie, J.A. Dodsworth, I. Swanson, J.A. Burn, M. Hackett, J.A. Leigh, Protein complexing in a methanogen suggests electron bifurcation and electron delivery from formate to heterodisulfide reductase, *Proc. Natl. Acad. Sci. U. S. A.* 107 (2010) 11050–11055.
- [47] Z. Yan, M. Wang, J.G. Ferry, A ferredoxin- and F420H2-dependent, electron-bifurcating, heterodisulfide reductase with homologs in the domains bacteria and archaea, *mBio* 8 (2017).
- [48] D. Prakash, S.S. Chauhan, J.G. Ferry, Life on the thermodynamic edge: respiratory growth of an acetotrophic methanogen, *Sci Adv* 5 (2019), ean9059.
- [49] A.R. Ramos, F. Grein, G.P. Oliveira, S.S. Venceslau, K.L. Keller, J.D. Wall, I. A. Pereira, The FixABCD-HdrABC proteins correspond to a novel NADH dehydrogenase/heterodisulfide reductase widespread in anaerobic bacteria and involved in ethanol metabolism in *Desulfotribia vulgaris* Hildenborough, *Environ. Microbiol.* 17 (2015) 2288–2305.
- [50] S.G. Huwiler, C. Löffler, S.E.L. Anselmann, H.J. Stark, M. von Bergen, J. Flechler, R. Rachel, M. Boll, One-megadallon metalloenzyme complex in *Geobacter metallireducens* involved in benzene ring reduction beyond the biological redox window, *Proc. Natl. Acad. Sci. U. S. A.* 116 (2019) 2259–2264.
- [51] J. Mock, S. Wang, H. Huang, J. Kahnt, R.K. Thauer, Evidence for a hexaheteromeric methylenetetrahydrofolate reductase in *Moorella thermoacetica*, *J. Bacteriol.* 196 (2014) 3303–3314.
- [52] J. Kuriyan, T.S. Krishna, L. Wong, B. Guenther, A. Pahler, C.H. Williams Jr., P. Model, Convergent evolution of similar function in two structurally divergent enzymes, *Nature* 352 (1991) 172–174.
- [53] A.K. Kaster, J. Moll, K. Parey, R.K. Thauer, Coupling of ferredoxin and heterodisulfide reduction via electron bifurcation in hydrogenotrophic methanogenic archaea, *Proc. Natl. Acad. Sci. U. S. A.* 108 (2011) 2981–2986.
- [54] A.R. Ramos, K.L. Keller, J.D. Wall, I.A. Pereira, The membrane QmoABC complex interacts directly with the dissimilatory adenosine 5'-phosphosulfate reductase in sulfate reducing bacteria, *Front. Microbiol.* 3 (2012) 137.
- [55] G.J. Schut, M.W. Adams, The iron-hydrogenase of *Thermotoga maritima* utilizes ferredoxin and NADH synergistically: a new perspective on anaerobic hydrogen production, *J. Bacteriol.* 191 (2009) 4451–4457.
- [56] K. Schuchmann, V. Müller, A bacterial electron-bifurcating hydrogenase, *J. Biol. Chem.* 287 (2012) 31165–31171.
- [57] S. Wang, H. Huang, J. Kahnt, A.P. Mueller, M. Kopke, R.K. Thauer, NADP-specific electron-bifurcating [FeFe]-hydrogenase in a functional complex with formate dehydrogenase in *Clostridium autoethanogenum* grown on CO, *J. Bacteriol.* 195 (2013) 4373–4386.
- [58] S. Wang, H. Huang, J. Kahnt, R.K. Thauer, A reversible electron-bifurcating ferredoxin- and NAD-dependent [FeFe]-hydrogenase (HydABC) in *Moorella thermoacetica*, *J. Bacteriol.* 195 (2013) 1267–1275.
- [59] C.C. Moser, J.M. Keske, K. Warncke, R.S. Farid, P.L. Dutton, Nature of biological electron transfer, *Nature* 355 (1992) 796–802.
- [60] J. Liang, H. Huang, S. Wang, Distribution, evolution, catalytic mechanism, and physiological functions of the flavin-based electron-bifurcating NADH-dependent reduced ferredoxin: NADP^+ oxidoreductase, *Front. Microbiol.* 10 (2019) 373.
- [61] A.M. Garcia Costas, S. Poudel, A.F. Miller, G.J. Schut, R.N. Ledbetter, K.R. Fixen, L. C. Seefeldt, M.W.W. Adams, C.S. Harwood, E.S. Boyd, J.W. Peters, Defining electron bifurcation in the electron-transferring flavoprotein family, *J. Bacteriol.* 199 (2017), <https://doi.org/10.1128/JB.00440-17>.
- [62] K. Sato, Y. Nishina, K. Shiga, Interaction between NADH and electron-transferring flavoprotein from *Megasphaera elsdenii*, *J. Biochem.* 153 (2013) 565–572.
- [63] C. Ernst, K. Kayastha, T. Koch, S.S. Venceslau, L.A.C. Pereira, U. Demmer, U. Ermler, C. Dahl, Structural and spectroscopic characterization of a HdrA-like subunit from *Hyphomicrobium denitrificans*, *FEBS J.* (2020), <https://doi.org/10.1111/febs.15505>.
- [64] K.Y. Yang, R.P. Swenson, Modulation of the redox properties of the flavin cofactor through hydrogen-bonding interactions with the N(5) atom: role of alphaSer254 in the electron-transfer flavoprotein from the methylotrophic bacterium W3A1, *Biochemistry* 46 (2007) 2289–2297.
- [65] V. Balland, M. Byrdin, A.P. Eker, M. Ahmad, K. Brettel, What makes the difference between a cryptochrome and DNA photolyase? A spectroelectrochemical comparison of the flavin redox transitions, *J. Am. Chem. Soc.* 131 (2009) 426–427.
- [66] Y.E. Brüggeman, A. Honegger, H. Kreuzel, A.J. Visser, C. Laane, A. Schots, R. Hilhorst, Regulation of the flavin redox potential by flavin-binding antibodies, *Eur. J. Biochem.* 249 (1997) 393–400.
- [67] J.P. Hoben, C.E. Lubner, M.W. Ratzloff, G.J. Schut, D.M.N. Nguyen, K.W. Hempel, M.W.W. Adams, P.W. King, A.F. Miller, Equilibrium and ultrafast kinetic studies manipulating electron transfer: a short-lived flavin semiquinone is not sufficient for electron bifurcation, *J. Biol. Chem.* 292 (2017) 14039–14049.
- [68] M. Hetzel, M. Brock, T. Selmer, A.J. Pierik, B.T. Golding, W. Buckel, Acryloyl-CoA reductase from *Clostridium propionicum*. An enzyme complex of propionyl-CoA dehydrogenase and electron-transferring flavoprotein, *Eur. J. Biochem.* 270 (2003) 902–910.
- [69] D.M.N. Nguyen, G.J. Schut, O.A. Zadromy, M. Tokmina-Lukaszewska, S. Poudel, G.L. Lipscomb, L.A. Adams, J.T. Dinsmore, W.J. Nixon, E.S. Boyd, B. Bothner, J. W. Peters, M.W.W. Adams, Two functionally distinct NADP^+ -dependent ferredoxin oxidoreductases maintain the primary redox balance of *Pyrococcus furiosus*, *J. Biol. Chem.* 292 (2017) 14603–14616.
- [70] C. Thorpe, J.J. Kim, Structure and mechanism of action of the acyl-CoA dehydrogenases, *Faseb. J.* 9 (1995) 718–725.
- [71] S. Djordjevic, C.P. Pace, M.T. Stankovich, J.J. Kim, Three-dimensional structure of butyryl-CoA dehydrogenase from *Megasphaera elsdenii*, *Biochemistry* 34 (1995) 2163–2171.
- [72] J. Sucharitakul, S. Buttranan, T. Wongnate, N.P. Chowdhury, M. Prongit, W. Buckel, P. Chaiyen, Modulations of the reduction potentials of flavin-based electron bifurcation complexes and semiquinone stabilities are key to control directional electron flow, *FEBS J.* (2020), <https://doi.org/10.1111/febs.15343>.
- [73] P.A. Karplus, M.J. Daniels, J.R. Herriott, Atomic structure of ferredoxin-NADP+ reductase: prototype for a structurally novel flavoenzyme family, *Science* 251 (1991) 60–66.
- [74] M.E. Corrado, A. Aliverti, G. Zanetti, S.G. Mayhew, Analysis of the oxidation-reduction potentials of recombinant ferredoxin-NADP+ reductase from spinach chloroplasts, *Eur. J. Biochem.* 239 (1996) 662–667.
- [75] A.W. Mohsen, S.E. Rigby, K.F. Jensen, A.W. Munro, N.S. Scrutton, Thermodynamic basis of electron transfer in dihydroorotate dehydrogenase B from *Lactococcus lactis*: analysis by potentiometry, EPR spectroscopy, and ENDOR spectroscopy, *Biochemistry* 43 (2004) 6498–6510.
- [76] S.G. Mayhew, G.P. Foust, V. Massey, Oxidation-reduction properties of flavodoxin from *Peptostreptococcus elsdenii*, *J. Biol. Chem.* 244 (1969) 803–810.
- [77] N.P. Chowdhury, J. Kahnt, W. Buckel, Reduction of ferredoxin or oxygen by flavin-based electron bifurcation in *Megasphaera elsdenii*, *FEBS J.* 282 (2015) 3149–3160.
- [78] T.M. Dwyer, L. Zhang, M. Muller, F. Marrugo, F. Freman, The functions of the flavin contact residues, alphaArg249 and betaTyr16, in human electron transfer flavoprotein, *Biochim. Biophys. Acta* 1433 (1999) 139–152.

K. Kayastha et al.

Archives of Biochemistry and Biophysics 701 (2021) 108796

- [79] E. Telfournier, A.W. Munro, J. Basran, M.J. Sutcliffe, S. Daff, S.K. Chapman, N. S. Scrutton, Alpha Arg-237 in *Methylophilus methylotrophus* (sp. W3A1) electron-transferring flavoprotein affords approximately 200-millivolt stabilization of the FAD anionic semiquinone and a kinetic block on full reduction to the dihydroquinone, *J. Biol. Chem.* 276 (2001) 20190–20196.
- [80] J. Sucharitakul, W. Buckel, P. Chaiyen, Rapid kinetics reveal surprising flavin chemistry in the bifurcating electron transfer flavoprotein from *Acidaminococcus fermentans*, *J. Biol. Chem.* 296 (2021), <https://doi.org/10.1074/jbc.RA120.016017>.
- [81] K.D. Watenpaugh, L.C. Sieker, L.H. Jensen, J. Legall, M. Dubourdieu, Structure of the oxidized form of a flavodoxin at 2.5-Angstrom resolution: resolution of the phase ambiguity by anomalous scattering, *Proc. Natl. Acad. Sci. U. S. A.* 69 (1972) 3185–3188.
- [82] M.L. Ludwig, K.A. Pattridge, A.L. Metzger, M.M. Dixon, M. Eren, Y. Feng, R. P. Swenson, Control of oxidation-reduction potentials in flavodoxin from *Clostridium beijerinckii*: the role of conformation changes, *Biochemistry* 36 (1997) 1259–1280.
- [83] Z. Zhou, R.P. Swenson, The cumulative electrostatic effect of aromatic stacking interactions and the negative electrostatic environment of the flavin mononucleotide binding site is a major determinant of the reduction potential for the flavodoxin from *Desulfovibrio vulgaris* [Hildenborough], *Biochemistry* 35 (1996) 15980–15988.
- [84] L.H. Bradley, R.P. Swenson, Role of glutamate-59 hydrogen bonded to N(3)H of the flavin mononucleotide cofactor in the modulation of the redox potentials of the *Clostridium beijerinckii* flavodoxin. Glutamate-59 is not responsible for the pH dependency but contributes to the stabilization of the flavin semiquinone, *Biochemistry* 38 (1999) 12377–12386.
- [85] V.D. Sled, N.I. Rudnitsky, Y. Hatefi, T. Ohnishi, Thermodynamic analysis of flavin in mitochondrial NADH:ubiquinone oxidoreductase (complex I), *Biochemistry* 33 (1994) 10069–10075.
- [86] E. Gnannt, K. Dorner, M.F.J. Strampraad, S. de Vries, T. Friedrich, The multitude of iron-sulfur clusters in respiratory complex I, *Biochim. Biophys. Acta* 1857 (2016) 1068–1072.
- [87] M. Schulte, K. Frick, E. Gnannt, S. Jurkovic, S. Burschel, R. Labatzke, K. Alerstock, D. Fiegen, D. Wohlwend, S. Gerhardt, O. Einsle, T. Friedrich, A mechanism to prevent production of reactive oxygen species by *Escherichia coli* respiratory complex I, *Nat. Commun.* 10 (2019) 2551.
- [88] M. Willstein, D.F. Bechtel, G.S. Müller, U. Demmer, L. Heimann, K. Kayastha, V. Schünemann, A.J. Pierik, G.M. Ullmann, U. Ermler, M. Boll, Low potential enzymatic hydride transfer via highly cooperative and inversely functionalized flavin cofactors, *Nat. Commun.* 10 (2019) 2074.
- [89] C. Eberlein, S. Estelmann, J. Seifert, M. von Bergen, M. Müller, R.U. Meckenstock, M. Boll, Identification and characterization of 2-naphthoyl-coenzyme A reductase, the prototype of a novel class of dearomatizing reductases, *Mol. Microbiol.* 88 (2013) 1032–1039.
- [90] S.G. Mayhew, The effects of pH and semiquinone formation on the oxidation-reduction potentials of flavin mononucleotide. A reappraisal, *Eur. J. Biochem.* 265 (1999) 698–702.

Appendix E. Naphthoyl-CoA reductase (NCR)



ARTICLE

<https://doi.org/10.1038/s41467-019-10078-3>

OPEN

Low potential enzymatic hydride transfer via highly cooperative and inversely functionalized flavin cofactors

Max Willstein¹, Dominique F. Bechtel², Christina S. Müller³, Ulrike Demmer⁴, Larissa Heimann³, Kanwal Kayastha⁴, Volker Schünemann³, Antonio J. Pierik², G. Matthias Ullmann⁵, Ulrich Ermler⁴ & Matthias Boll¹

Hydride transfers play a crucial role in a multitude of biological redox reactions and are mediated by flavin, deazaflavin or nicotinamide adenine dinucleotide cofactors at standard redox potentials ranging from 0 to -340 mV. 2-Naphthoyl-CoA reductase, a key enzyme of oxygen-independent bacterial naphthalene degradation, uses a low-potential one-electron donor for the two-electron dearomatization of its substrate below the redox limit of known biological hydride transfer processes at $E^\circ = -493$ mV. Here we demonstrate by X-ray structural analyses, QM/MM computational studies, and multiple spectroscopy/activity based titrations that highly cooperative electron transfer ($n=3$) from a low-potential one-electron (FAD) to a two-electron (FMN) transferring flavin cofactor is the key to overcome the resonance stabilized aromatic system by hydride transfer in a highly hydrophobic pocket. The results evidence how the protein environment inversely functionalizes two flavins to switch from low-potential one-electron to hydride transfer at the thermodynamic limit of flavin redox chemistry.

¹Microbiology, Faculty of Biology, University of Freiburg, Schänzlestrasse 1, 79104 Freiburg, Germany. ²Biochemistry, Faculty of Chemistry, University of Kaiserslautern, Erwin-Schrödinger-Straße 52, 67663 Kaiserslautern, Germany. ³Biophysics, Department of Physics, University of Kaiserslautern, Erwin-Schrödinger-Straße 46, 67663 Kaiserslautern, Germany. ⁴Max-Planck-Institute for Biophysics Frankfurt, Max-von-Laue-Str. 3, 60438 Frankfurt, Germany. ⁵Computational Biochemistry, University of Bayreuth, Universitätsstrasse 30, NW I, 95447 Bayreuth, Germany. Correspondence and requests for materials should be addressed to U.E. (email: ulrich.ermiler@biophys.mpg.de) or to M.B. (email: matthias.boll@biologie.uni-freiburg.de)

ARTICLE

NATURE COMMUNICATIONS | <https://doi.org/10.1038/s41467-019-10078-3>

The biodegradation of aromatic compounds to CO_2 by aerobic and anaerobic microorganisms is important for the global carbon cycle and for the elimination of persistent aromatic pollutants. In particular polycyclic aromatic hydrocarbons (PAH)s are classified as harmful for the environment and human health^{1,2}. While aerobes employ oxygenases to attack aromatic ring systems, such a strategy is no option for anaerobic bacteria. Here, enzymatic dearomatization is typically accomplished by reduction affording electron transfer at the negative redox potential limit in biology^{3–6}.

In the anaerobic degradation pathways of most monocyclic aromatic compounds, the key intermediate benzoyl-coenzyme A (CoA) serves as substrate for ATP or electron-bifurcation dependent benzoyl-CoA reductases^{7–9}. They dearomatize their substrate to a cyclic, conjugated 1,5-dienoyl-CoA at $E^\circ = -622$ mV¹⁰ in one-electron steps using either a [4Fe–4S] cluster or a tungstopterin cofactor as ultimate one-electron donors. A radical-based reaction mechanism has been proposed for enzymatic benzoyl-CoA dearomatization¹¹. Remarkably, the analogous chemical Birch reduction proceeds at harsh conditions involving cryogenic temperatures, alkali metals in ammonia as reducing agents and alcohols as proton donors¹².

During anaerobic degradation of the PAH model compound naphthalene, 2-naphthoyl-CoA reductase (NCR) reduces 2-naphthoyl-CoA (NCoA) to 5,6-dihydro-2-naphthoyl-CoA (DHNCOA), (Fig. 1)^{13–15}. To date only the NCR from the sulfate-respiring enrichment culture N47 has been studied to some extent. It belongs to a distinct subclass of the old yellow enzyme (OYE) family of flavoproteins that are composed of three domains binding FMN (flavin mononucleotide), a [4Fe–4S] cluster and either ADP or flavin adenine dinucleotide (FAD)¹³. Recent studies showed that NCoA reduction in D_2O enantioselectively yielded the product with the (5*S*, 6*S*)-configuration¹⁶. The observed defluorination of 6-F-2-NCoA to 2-NCoA by NCR is in agreement with a hydride transfer to C6 followed by protonation of the thioester-stabilized intermediate at C5 (Fig. 1)¹⁶. However, the redox potential of the NCoA/5,6-DHNCOA couple is with $E^\circ = -493$ mV¹³ outside the range of known biological hydride carriers such as NAD(P)H, flavins or deazaflavins (F420) with E° values ranging between ≈ 0 and -340 mV^{17–22}. In contrast, biological electron transfer processes below -400 mV usually involve one-electron carriers comprising metal cofactors. In addition, FMN in flavodoxins can act as low-potential one-electron carriers ($E^\circ \approx -420$ mV) that switch between stable neutral semiquinone (SQ) and unstable anionic hydroquinone (HQ) states^{23,24}. Notably, for NCR only artificial low-potential one-electron donors such as sodium dithionite or Ti(III)-citrate, but not NAD(P)H served as donors. A low-potential ferredoxin or a ferredoxin-like domain of an oxidoreductase serves most likely as natural electron donor¹⁴.

Taken these observations together, the mechanism of enzymatic naphthoyl-ring reduction has remained enigmatic. The two alternative mechanistic scenarios for naphthoyl ring dearomatization involve either a hydride transfer far below the redox window of known biological hydride-transfer reactions, or the transfer of single electrons or hydrogen atoms in a Birch reduction like manner via radical intermediates. In any scenario, catalysis at the proposed

active site FMN cofactor would involve previously unnoticed flavin redox chemistry. Here, we address this question by solving the X-ray structure of NCR with and without substrate combined with integrative electrochemical, spectroscopic and computational analyses. The results demonstrate how the protein environment functionalizes two flavin cofactors as low-potential one- and two-electron carriers that allow for hydride transfer to an aromatic ring system at the negative limit of the biological redox scale.

Results

Overall structure of NCR. The X-ray structure of NCR was determined at 2.2 Å resolution with R/R_{free} values (%) of 18.9/21.9 (for complete statistics of crystal structure analysis see Table 1). NCR is present in the crystal as a monomer modularly built up of a OYE-like TIM-barrel domain (19–359) hosting the active site FMN, an FAD binding α/β domain (401–503 + 626–674), and a second α/β domain (504–625). The [4Fe–4S] cluster is harbored in a linker region (360–400) inserted between the TIM barrel domain and the FAD binding domain (Fig. 2). This three-domain architecture is also present in the structurally characterized 2,4-dienoyl-CoA reductase (DCR, 2-*trans*-enoyl-CoA forming using NADPH as electron donor)²⁵ as well as trimethylamine²⁶ and histamine dehydrogenases²⁷ (using electron-transferring flavo-protein [ETF] as electron acceptor). The rms deviation between NCR and DCR from *E. coli* is 1.7 Å (93% of residues used) at a sequence identity of 33% (1PS9)²⁵, and that between NCR and OYE acting on non-CoA ester substrates is ca. 1.8 Å (around 53% of residues used) at a sequence identity of around 27% (e.g., 3KRU²⁸, 3HF3²⁹, and 4UTK³⁰).

Cofactor binding and electron transfer to the active site. The architecture of NCR clearly reveals a spatial separation between electron uptake at the FAD near the surface and substrate reduction at the deeply buried active site FMN cofactor.

The two flavins are electronically connected via a [4Fe–4S] cluster with edge to edge distances of 6 Å to FMN and 9 Å to FAD, respectively (Fig. 2). The FAD cofactor of NCR is located at the C-terminal end of the central β -sheet with its isoalloxazine moiety clamped between L456, W459, and L656 on the *si*-side and E541, I542, and K655 on the *re*-side (Supplementary Fig. 1b). The surrounding of the isoalloxazine by negatively charged residues (E446, E541, and D649) destabilize the FADH[–] (deprotonated FAD HQ), but not the FADH• (protonated FAD SQ) state suggesting a low-redox potential, similar to that of flavins in flavodoxins (Fig. 3).

The amide side chain of Q545 and the hydrophobic L456 and W459 point to the N5 of FAD and preferably stabilize the oxidized FAD state (Fig. 3). A distinguishing feature between DCR and NCR is the presence of an NADPH binding site in DCR which is absent in NCR. This finding can be rationalized by the exceptionally low potential of the NCoA/DHNCOA couple ($E^\circ = -493$ mV), which is ≥ 250 mV lower than for standard substrates of OYEs and far too negative for NADPH ($E^\circ \approx -360$ mV) as reductant. The bulky W459 in NCR (F424 in DCR) shifts the isoalloxazine moiety towards the *re*-side and thus totally blocks the NADPH binding site present in DCR (Supplementary Fig. 1).

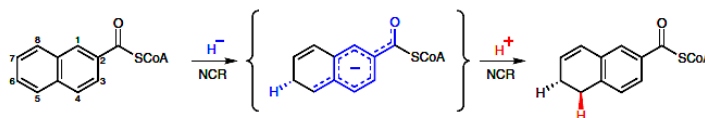


Fig. 1 Stereochemical course and potential hydride transfer mechanism of NCR. The enantioselective hydride (blue) and proton (red) transfers are shown

2

NATURE COMMUNICATIONS | (2019)10:2074 | <https://doi.org/10.1038/s41467-019-10078-3> | www.nature.com/naturecommunications

Table 1 Data collection and refinement statistics

	NCR	NCR-NCoA (soaked)	NCR-DHNCOA (co-cryst)
Data collection			
Space group	$P2_1$	$P2_1$	$I4_1$
Resolution (Å)	50–2.2	50–2.2	50–2.4
Cell dimensions			
a, b, c (Å)	82.5, 86.8, 96.9	81.7, 86.1, 96.9	176.9, 176.9, 49.2
α, β, γ (°)	90.0, 90.7, 90.0	90.0, 90.7, 90.0	90.0, 90.0, 90.0
R_{sym} (%)	7.5 (102.2) ^a	4.9 (100.9)	7.1 (95.2)
$I / \sigma I$	13.2 (1.8)	9.2 (1.0)	12.9 (2.1)
Completeness (%)	99.5 (99.7)	95.8 (91.1)	99.1 (99.8)
Redundancy	4.0 (4.1)	2.0 (2.0)	5.7 (6.1)
B-factor (Wilson plot)	42.0	49.8	59.0
Refinement			
Resolution (Å)	50.0–2.2	50.0–2.2	50.0–2.4
No. of reflections	69,124	67,470	29,943
$R_{\text{work}}/R_{\text{free}}$	18.9/21.9	18.2/22.4	23.0/27.3
No. of atoms			
Protein	10,191	10,168	5057
Ligands/ion	184	304	152
Water	187	242	27
B-factors			
Protein	52.0	62.8	93.3
FAD, [4Fe–4S], FMN, substrate	42.1, 52.6, 37.2	49.7, 61.5, 46.0, 89.7	103.8, 71.7, 62.7, 90.5
Water	43.5	58.4	76.8
R.m.s. deviations			
Bond lengths (Å)	0.015	0.015	0.004
Bond angles (°)	1.70	1.72	0.91

^aValues in parenthesis are for highest-resolution shell. Each dataset is based on one crystal

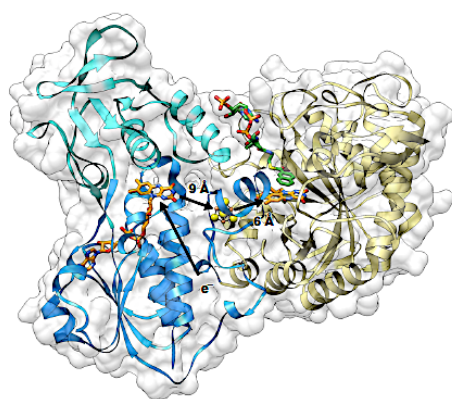


Fig. 2 Overall X-ray structure. NCR was found in the crystal structure as a monomeric enzyme in agreement with previous gel filtration data. It is composed of an OYE-like TIM barrel domain (yellow) and by two α/β domains (blue/cyan). The bound cofactors and NCoA (carbons in green) are shown as balls and sticks. A ferredoxin or ferredoxin-like domain of an oxidoreductase has been suggested as natural external electron donor; its proposed binding site is indicated by e^- /arrow

Notably, trimethylamine or histamine dehydrogenases bind ADP instead of FAD; here, electrons are directly shuttled via the [4Fe–4S] cluster to the ETF acceptor^{26,27}.

A ferredoxin or a ferredoxin-like domain of an oxidoreductase ($E \approx -500$ mV) is assumed to serve as *in vivo* electron donor

system for NCR¹⁴. Its postulated binding site is located in a flat hollow between the two α/β domains lined up by residues N540, I542, D569, M626, V653, and K655. The distance between a potential Fe/S cluster from the donor to the FAD is estimated to be below 14 Å.

The Fe/S cluster in NCR was found in the crystal structure as a cysteine-coordinated [4Fe–4S] cluster, albeit with an incomplete occupancy. Mössbauer spectroscopic analyses with ⁵⁷Fe-labeled oxidized NCR revealed spectra that were in a typical range for Fe^{2.5+} ions present in diamagnetic [4Fe–4S]²⁺ clusters. Mössbauer spectra of the dithionite reduced state were characteristic for Fe^{2.5+} and Fe²⁺ pairs of a reduced [4Fe–4S]¹⁺ cluster³¹. These results indicate the presence of an electron-transferring [4Fe–4S]^{2+/1+} cluster (for Mössbauer parameters and spectra see Supplementary Tables 1 and 2, and Supplementary Fig. 3).

The conformation and binding site of FMN is basically conserved among members of the OYE family. Thus, N5 of the isoalloxazine ring is linked with the polypeptide in all family members by a main chain amine hydrogen bond donor stabilizing the oxidized FMN state. However, two major differences between NCR and standard OYEs were identified in the polypeptide surrounding of the isoalloxazine ring that should substantially modify its electrostatic/hydrophobic properties (Fig. 4). (i) The helices 371:380 and 572:585 shield the dimethylbenzene ring from the bulk solvent in NCR; both are absent in all standard OYEs. In NCR, they build up a unique phenylalanine cluster (F375, F379, and F573) that together with the bicyclic naphthoyl-ring of the substrate form a highly hydrophobic patch (Fig. 4). (ii) In standard OYEs, two histidines and one arginine surround the pyrimidine ring of FMN thereby stabilizing anionic intermediates. From these three only the arginine is present in NCR (R245), but a hydrogen bond to the negatively charged E341 counteracts its positive charge contacting the N1–C2–O group of FMN. E341 is absent in DCR, which instead contains an extra positively charged histidine (H26) in the vicinity

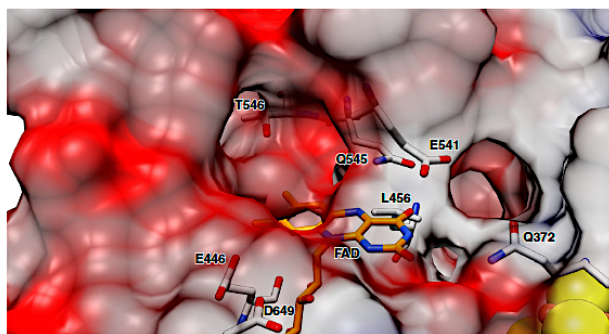


Fig. 3 Binding of the FAD cofactor. Anionic/polar residues responsible for the negative electrostatic potential are indicated. Several hydrophobic side chains around the isoalloxazine preferably stabilize the uncharged FAD and FADH• states

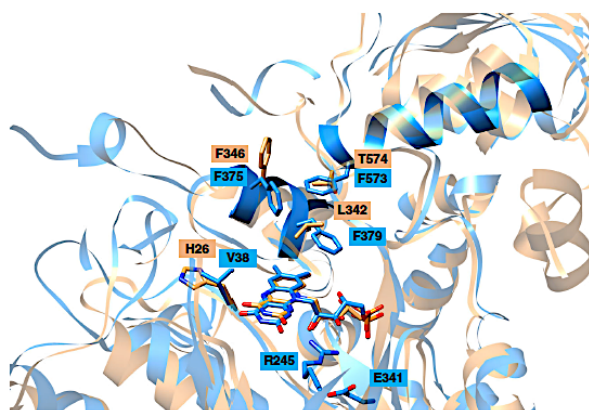


Fig. 4 Binding of the active site FMN cofactor. Overlay of NCR (blue) and DCR (amber). The FMN is shielded from bulk solvent by the two highlighted helices 371:380 and 572:585 that harbor F375, F379, and F573 creating a hydrophobic pocket absent in other OYE. The hydride-donating N5 of the FMN is in close proximity of H26 in DCR, which is replaced by a hydrophobic V38 in NCR

of FMN. These structural features largely contribute to a stabilization of the oxidized FMN state and thus to a substantial decrease of its redox potential. Electrostatic calculations gave a pKa of 8.8 for FMN indicating that FMNH⁻ rather than FMNH₂ is the catalytically relevant reduced state (pH optimum is 6.8).

Binding of NCoA/DHNCOA. The NCoA structure in complex with the substrate NCoA and the product DHNCOA were determined at 2.2 and 2.4 Å resolutions, respectively. No significant conformational changes were found between the two binary NCR complex structures and between them and the substrate-/product-free NCR as documented in rms deviations of 0.45 and 0.49 Å, respectively.

NCoA is embedded into a preformed approximately 20 Å deep cavity formed by three β-barrel strands of the TIM barrel domain, the following loops, helix 371:380 of the linker region and helix 572:585 of the second α/β domain. Its “S”-like shape is due to a kink at the cysteamine moiety and to two 90° kinks before and after the ribose of CoA (Fig. 5). The adenine base becomes thereby

attached to the pantetheine moiety. In this conformation, the phospho-ADP moiety of CoA serves as a plug to lock the entrance of the cavity. Multiple, mostly van-der-Waals contacts are formed between residues of the cavity and NCoA (Supplementary Fig. 4), which rationalizes the apparent low K_m of 1.1 μM¹⁴. The aromatic rings of NCoA are bound in an encapsulated hydrophobic pocket formed by Y82, H84, Y166, I194, V195, F375, V378, F379, and the isoalloxazine ring of FMN. The planar naphthoyl and isoalloxazine rings are oriented almost parallel to each other with the *re*-side stacked over the *si*-side, respectively. Strong π-π stacking interactions are formed between the equidistant distal phenyl and pyrazine ring atoms. Only little space is left at the cavity bottom of NCR beyond the distal phenyl ring of the substrate. This observation is in agreement with the ability of NCR to convert 6-F-NCoA but not the bulkier 2-phenanthrolyl-CoA^{14,16}.

Redox titrations. NCR (20 μM) was stepwise titrated with sodium dithionite at pH 8.0; at this pH the redox potential of

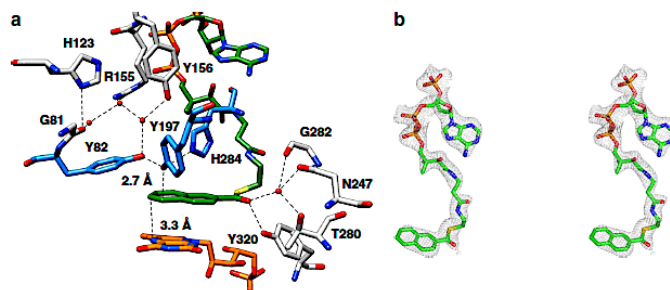


Fig. 5 Binding site of NCoA. **a** Active site geometry. The distances of hydride transfer from N5 of FMN (orange) and proton transfer from Y197 to the naphthoyl ring are indicated (carbons are shown in green). Y197 is hydrogen bonded with H284 and Y82 (all highlighted in blue), both contributing to an enhanced acidity; the proton network to the bulk solvent via bound water molecules involves Y156, R155, G81, and H123. A potential enolate intermediate at the thioester carbonyl during NCoA reduction is stabilized by Y320, G282, N247, and T280. **b** Stereo image of NCoA with the corresponding omit map (as gray meshes at a contour level of 0.5 σ). NCoA is bound in an 'S'-like conformation. Although not completely occupied, all moieties of NCoA are also clearly visible in the 2F_o-F_c electron density map at a contour level of 1 σ .

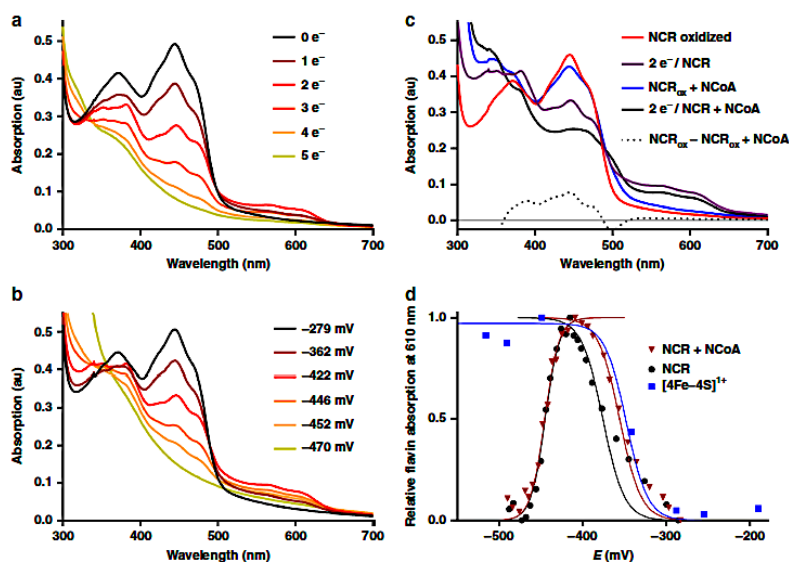


Fig. 6 Titrations of NCR (20 μ M) with dithionite at pH 8. **a** Absorption spectra after addition of stoichiometric electron equivalents. **b** Absorption spectra at defined redox potentials. **c** Absorption spectra of oxidized and two-electron reduced NCR in the absence and presence of NCoA. In the latter the signal of a charge-transfer complex between the substrate and FMN remained that allowed assigning the SQ formation to the FAD cofactor, whereas FMN remained fully oxidized. The dotted line represents the difference spectrum of oxidized NCR without NCoA minus oxidized NCR with NCoA. **d** Titration of the neutral SQ absorbance spectra of FAD in the absence (black) and presence (red) of NCoA. Formation of SQ/reduction of [4Fe-4S] was fitted to a Nernst curve with $n = 2$ electrons; reduction of SQ with $n = 3$ due to strong cooperativity of parallel FADH \bullet and FMN reduction. Titration of [4Fe-4S] cluster was followed by its $S = 1/2$ EPR spectrum (blue). Symbols represent experimental data, solid lines are fitted curves. $R^2 = 0.98$ (+NCoA)/0.78 for SQ formation; $R^2 = 0.98$ (+NCoA)/0.99 for SQ reduction. au absorbance units. Source data are provided as a Source Data file

dithionite is below -550 mV allowing for a complete reduction of all cofactors. Flavin reduction was monitored by recording UV/vis spectra; reduction of the [4Fe-4S] cluster was followed by EPR spectroscopy. Redox potentials during titrations were determined

using an Ag/AgCl reference electrode and redox-mediating dyes. This setup allowed the assignment of the number of reducing equivalents added and of the redox potentials poised to the redox states of cofactors (Fig. 6a, b). The oxidized absorption spectrum

ARTICLE

NATURE COMMUNICATIONS | <https://doi.org/10.1038/s41467-019-10078-3>

of NCR was characteristic for neutral FMN and FAD cofactors with maxima at 372 and 444 nm as reported earlier¹³.

In titrations without mediators/reference electrode, full reduction of 10 μM NCR was achieved with 25 μM of the two-electron donor dithionite, which perfectly fits to the five-electron reduction of the FMN, FAD, and $[\text{4Fe-4S}]^{2+}$ cofactors. Upon stepwise reduction, the spectrum of the oxidized flavins gradually bleached between -280 and -470 mV vs. SHE. The characteristic spectrum of a neutral SQ appeared with absorption maxima at 566 nm and 610 nm. It optimally developed after addition of two-electron equivalents at ≈ -420 mV and disappeared upon further reduction. Formation and disappearance of the SQ spectrum followed Nernst curves giving $E^{\circ} = -353 \pm 2$ mV (quinone[Q]/SQ), and $E^{\circ} = -446 \pm 1$ mV (SQ/HQ), respectively (Fig. 6d). Surprisingly, best fits were obtained for a two-electron transition ($n = 2$) for the Q/SQ couple and a three-electron transition ($n = 3$) for the SQ/HQ couple (Supplementary Fig. 5). This finding suggests a strong cooperative behavior of the three NCR cofactors in terms of joint co-reduction at highly similar apparent potentials (see below). Such cooperativity has previously only been described for the two cofactors of cytochrome *cd*³².

In the oxidized state, only a very weak $g = 2.02$ $[\text{3Fe-4S}]^{1+}$ EPR signal as substoichiometric breakdown product of the $[\text{4Fe-4S}]^{2+}$ was detected, in full agreement with Mössbauer spectroscopic data (Supplementary Fig. 3). During the reductive, dye-mediated titration, the rise of a broad rhombic $S = 1/2$ EPR signal with g values of 2.08, 1.91, and 1.8 developed and remained stable at decreasing potentials (Supplementary Fig. 6). Its formation followed a Nernst curve with $E^{\circ} = -348 \pm 10$ mV with $n = 2$ being very close to that observed for the Q/SQ couple (Fig. 6d). These results indicate that addition of two-electron equivalents reduced one flavin to the SQ and the $[\text{4Fe-4S}]$ cluster to its $+1$ state in a highly cooperative manner at highly similar potentials.

In the presence of NCoA, the absorbance spectrum of oxidized NCR was clearly affected by the formation of a shoulder around 500 nm (Fig. 6c). This broadening is assigned to a charge-transfer complex between the substrate and the active site FMN and represents a distinguishing feature of FMN compared to FAD. After reduction of NCR by two electrons in the presence of NCoA, the remaining UV/vis spectrum was dominated by the charge-transfer complex signal, whereas the features of the oxidized flavin spectrum in the absence of NCoA were almost completely lost. Moreover, the redox potentials of flavin SQ formation and reduction were only marginally affected by NCoA (Fig. 6d). Both findings clearly indicate that the observed SQ-signal derives from FAD and not from FMN and corroborate the proposed cooperative reduction of FAD to $\text{FADH}\cdot$ and the $[\text{4Fe-4S}]^{2+}$ to the $+1$ state upon addition of two-electron equivalents; in contrast the FMN remained fully oxidized.

Upon further reduction of the NCR-NCoA complex, at potentials below -420 mV, the spectra of the $\text{FADH}\cdot$ and the FMN/NCoA charge-transfer complex (at 444 nm, Supplementary Fig. 7) both simultaneously decreased. The redox potential dependent reduction of FMN to FMNH^- with virtually no intermediary SQ state fitted best to a Nernst curve with $E^{\circ} = -439 \pm 1$ mV and $n = 3$ (Supplementary Fig. 7). These values are very close to those obtained for $\text{FADH}\cdot$ reduction ($E^{\circ} = -446 \pm 1$ with $n = 3$) and indicate a strong cooperativity between the one-electron reduction of $\text{FADH}\cdot$ and the two-electron-reduction of FMN to FMNH^- . When NCoA was omitted from the redox titration assay, the reduction of FMN also followed a Nernst curve with an only slightly more negative $E^{\circ} = -445 \pm 5$ mV with $n = 3$ (Supplementary Fig. 7). Reduction of NCR by excess of the two-electron donor DHNCoA (exergonic reverse reaction) was incomplete, and the neutral flavin SQ

remained close to maximum intensity (Supplementary Fig. 8). Together with results obtained in titrations with dithionite, this finding indicates that FMN readily accepts a hydride from DHNCoA, and the FMNH^- formed reduces the FAD and the $[\text{4Fe-4S}]^{2+}$ cluster by single electrons, each.

The dependence of the extent of NCoA reduction by NCR on the redox potential poised was determined by analyzing samples by ultra performance liquid chromatography (Fig. 7a). At potentials ≥ -420 mV (two-electron reduced NCR) no conversion of NCoA was observed using established assays. Upon further reduction, the extent of NCoA conversion continuously increased and was maximal when NCR was completely reduced. The reduction of maximally 20% of the NCoA added at equal amounts to NCR can be explained by reaching thermodynamic equilibrium because E° of the NCoA/DHNCoA couple ($E^{\circ} = -493$ mV) is around 25 mV more negative than fully reduced NCR (at $E^{\circ} \approx -470$ mV). Notably, the increase of NCoA reduction extent at potentials below -400 mV almost perfectly correlated with the decrease of the $\text{FADH}\cdot$ spectrum suggesting that only the fully reduced $\text{FADH}\cdot$ is competent of supplying FMN via the $[\text{4Fe-4S}]$ cluster with single electrons for hydride transfer to NCoA.

The results obtained from titration experiments and their interpretation is summarized in Fig. 7; a corresponding electrochemical landscape for the electron transfer events is presented in Fig. 8. They suggest that the three redox cofactors transfer electrons in a highly cooperative manner as indicated by the almost identical redox potentials of the $\text{FAD}/\text{FADH}\cdot$ and $[\text{4Fe-4S}]^{2+/1+}$ ($E^{\circ} \approx -350$ mV) as well as the $\text{FADH}\cdot/\text{FADH}^-$ and FMN/FMNH^- ($E^{\circ} \approx -445$ mV) couples. Only at redox potentials below -420 mV, NCR gradually becomes competent for NCoA reduction accompanied by the cooperative ($n = 3$) reduction of the $\text{FADH}\cdot$ to FADH^- and the FMN to FMNH^- . The absence of any UV/vis feature of a flavin SQ signal at low potential suggests that the $\text{FMNH}\cdot$ is extremely instable with $E^{\circ}(\text{Q}/\text{SQ}) \ll E^{\circ}(\text{SQ}/\text{HQ})$. Such highly differing crossed-over redox potentials of the first and second electron transfer are essential for two-electron donor systems³³.

Mechanism of NCR reaction. One of the major aims of this work was to substantiate or falsify the proposed low-potential hydride transfer mechanism. Results from redox titrations already indicated a highly instable $\text{FMNH}\cdot$ that is immediately further reduced to FMNH^- , which argues for a two-electron hydride transfer process. In the NCR-NCoA complex structure, the orientation of the aromatic rings and the distance between the N5 of FMN and the C6 of NCoA of 3.3 Å are optimal for transferring a hydride. Its trajectory was simulated using quantum-mechanical (QM)/MM calculations by starting from the reduced anionic FMNH^- state. Using PyCPR³⁴, we found a transition state at 16 kcal mol⁻¹ in which the proton of FMNH^- is at half distance between N1 of FMN and C6 of NCoA, and the HOMO is delocalized over both ring systems (Fig. 9). Moreover, an intermediate with an energy of 4.5 kcal mol⁻¹ (relative to the initial state) is formed in which the hydride from FMN is already fully transferred to NCoA, but Y197 still holds its proton. In the calculation, no radical intermediate was identified, in contrast to an earlier study on the mechanism of benzoyl-CoA reduction for which a similar computational setup (conjugate peak refinement with BP86) was used³⁵. The negative charge of the transition state is delocalized over the conjugated ring system including the thioester (Fig. 1). The transition state is stabilized by hydrogen-bond interactions between the carbonyl oxygen and the Y320 hydroxy group and a polypeptide-linked water molecule (Fig. 5 and Supplementary Fig. 4). In NCR, Y197 is properly placed at the

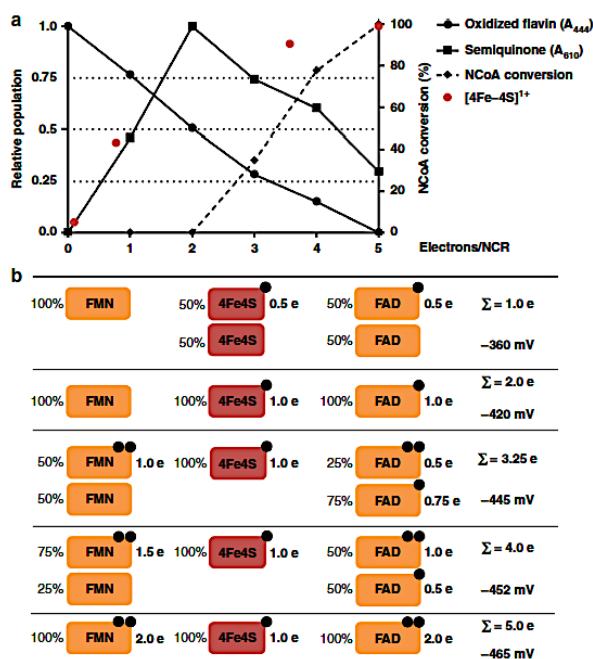


Fig. 7 Summary of redox titration experiments. **a** Relative populations of oxidized flavins, neutral SQ, $[4Fe-4S]^{1+}$ cluster and extent of NCoA reduction after addition of up to five electron equivalents to oxidized NCR. Species were determined by UV/vis spectroscopy at 444 nm (oxidized flavins), and 610 nm (neutral SQ); $[4Fe-4S]^{1+}$ cluster by EPR spectroscopy. **b** Cartoon summarizing reduction of individual NCR cofactors depending on the number of electron equivalents added/redox potential. Source data are provided as a Source Data file

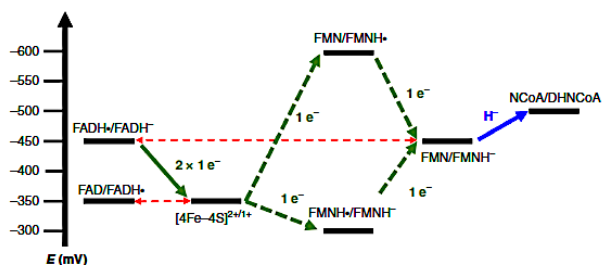


Fig. 8 Electrochemical landscape for the electron transfer reactions during NCR catalysis. After one-electron reduction of the $[4Fe-4S]$ cluster and FAD, respectively, two-single electrons are transferred to FMN to form a hydride after protonation that is subsequently transferred to NCoA. While FAD switches only between the SQ/HQ states, an FMN SQ intermediate was never observed. This finding is rationalized by largely differing crossed-over redox potentials of the two redox transitions of FMN (the values shown are minimal estimates based on the inability to observe the FMNSQ in the steady state). As a result, the second reduction drives the unfavorable first reduction resulting in the observed two-electron reduction of FMN. For the NCoA/DHNCOA couple the standard redox potential is given, which under cellular conditions will be slightly more positive

si-side of the substrate with a distance between its oxygen and C5 of 2.7 Å strongly suggesting a function as proton donor during NCoA reduction. According to QM/MM calculations Y197 transfers the proton to C5 of the 6-hydro-NCoA anion with a small barrier of only about 2 kcal/mol.

The invariant proton-donating tyrosine³⁶ is activated in all OYE members by a single interaction with a hydrogen-bond donor such as tyrosine, histidine or asparagine. NCR appears to be the only known OYE family member where the acidity of the proton-donating Y197 is increased by interactions with the two

ARTICLE

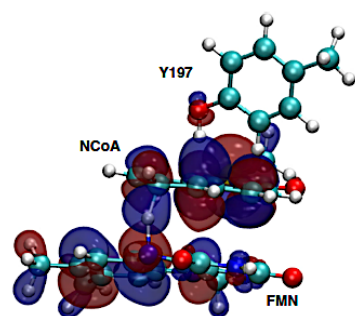
NATURE COMMUNICATIONS | <https://doi.org/10.1038/s41467-019-10078-3>

Fig. 9 Highest occupied molecular orbital (HOMO) of the transition state for the hydride transfer from FMN to NCoA. The HOMO is delocalized over both ring systems and the proton is located between N5 of FMN and C6 of NCoA. Y197 is ready to transfer its proton to the reduced NCoA

hydrogen-bond donors H284 and Y82 (Fig. 5). We calculated the protonation pattern of the active site residues at pH 7 using continuum electrostatic methods. The pK_a value of Y197 at pH = 7 is 12.6³⁷, which is low enough to donate a proton to a reduced anionic intermediate of NCoA. Its surprisingly high value is due to the desolvation effect in a rather hydrophobic active site pocket which is compensated by the local electrostatic field. H284 seems to be uncharged due to the hydrophobic surrounding and its role as proton acceptor in the hydrogen bond to the cysteamine N–H of CoA. The deprotonated state of H284 (calculated pK_a of –4.1 at pH = 7) cannot reprotonate Y197. Y82 (calculated pK_a of 16.0 at pH = 7) may donate a proton to Y197 supported by the finding that its hydroxyl group also serves as the ending point for a proton channel from bulk solvent. The proton channel extends via a water molecule bound to Y156 and two further water molecules that are hydrogen-bonded to H123 and R155 to bulk solvent (Fig. 5).

In summary, the presented structural data provide the complete molecular basis for the regio- and stereoselectivity of NCR reaction via hydride and proton transfer events. They are in full agreement with data obtained by previous vibrational circular dichroism spectroscopy analyses¹⁶.

Discussion

The presented structural, spectroscopic, and computational analyses strongly support a hydride transfer mechanism for NCR at a redox potential far below previously reported values for flavin dependent (de)hydrogenases. Consequently, the previous opinion that reversible biological electron transfer below the standard redox potential of canonical organic redox cofactors is restricted to metal cofactors or one-electron-transferring flavodoxins appears not to be valid.

The most challenging aspects of NCR catalysis is the generation of the exceptionally low-potential FMNH[–] hydride donor by a low-potential single-electron donor system. For this purpose two electronically coupled flavins are functionalized by the polypeptide surrounding in an opposite manner to low-potential one-electron (FAD) and hydride (FMN) carriers. The almost identical one-electron (FAD SQ/HQ) and two-electron (FMN/FMNH[–]) redox potentials result in the observed highly cooperative behavior ($n = 3$) of the two flavins, which is essential for the low-potential one-two-electron transfer switch. An equilibration of single electrons over the two flavin cofactors is suppressed by the crossed-over single-electron redox potential of FMN with the

$E^\circ(Q/SQ) \ll E^\circ(SQ/HQ)$ ^{33,38}, which impedes reoxidation of the FMNH[–] formed to FMNH•. The highly unfavorable first one-electron reduction of FMN ($E^\circ \ll -500$ mV) by FADH[–] via the [4Fe–4S]^{2+/1+} cluster will be greatly pulled forward by the highly exergonic second electron transfer ($E^\circ \gg -400$ mV) (Fig. 8). Most likely, the generation of the FMNH[–] state represents the rate-limiting step of the slow NCR reaction (40 nmol mg^{–1} min^{–1})¹³. Similar short-living flavin SQ states generated by a low-potential one-electron donor were proposed and identified in flavin-based electron-conformation processes. There, the second electron for reduction to the HQ state originates from a spatially separated high-potential one-electron donor^{39–41}.

The question rises whether the approximately $E^\circ = -450$ mV for the FMN/FMNH[–] couple described in this work marks the negative redox limit of enzymatic hydride transfer? Considering the lowest one-electron redox-potential for a flavodoxin FMN of around –500 mV, the border of a hydride transfer may be also anticipated in this range. At least for the even more challenging reduction of benzoyl-CoA ($E^\circ = -622$ mV) flavin mediated hydride transfer appears to be no option as benzoyl-CoA reductases employ a one-electron reduction strategy using metals as active site cofactors.

Methods

Expression and purification of NCR. NCR was heterologously produced as strep-tag fusion protein in *E. coli* using autoinduction medium inoculated with a fresh overnight culture. Cells were grown at 37 °C for four hours followed by incubation at 16 °C for 20 h. Cells were disrupted by a single passage through a french pressure cell at 11000 psi after resuspension in 2 mL of buffer A (50 mM HEPES pH 8.0, 150 mM) per g cells (wet weight). Cell debris was removed by centrifugation at 100,000g for 60 min and the supernatant was applied to streptactin affinity resin (IBA Lifesciences, Göttingen, Germany) equilibrated with buffer A using an AKTA purifier system (GE Healthcare, Solingen, Germany). Unbound proteins were washed out using buffer A and NCR was eluted with 5 mM D-threosylserine in buffer A¹⁶. For Mössbauer spectroscopy 200 μ M of ⁵⁷Fe(III)citrate were added to the growth medium instead of nonlabeled iron source. For crystallization, peak fractions after affinity chromatography were pooled and diluted with buffer H₂ (20 mM HEPES/KOH pH 8.0) to a concentration of 50 mM KCl or lower. Then the protein solution was loaded onto a Resource Q column (6 mL, GE Healthcare, Solingen, Germany) pre-equilibrated with buffer H₂. The column was washed with 6% (60 mM KCl) of buffer H₂ (20 mM HEPES/KOH pH 8.0, 1 M KCl) before bound proteins were eluted in a linear gradient of 6–10% H₂ (60–100 mM KCl). Elution fractions were pooled and concentrated and further purified by gel filtration using a Superdex 200 PG 26/600 column (320 mL, GE Healthcare, Solingen, Germany) using 20 mM HEPES/KOH pH 7.6 with 100 mM KCl. Peak fractions were pooled and concentrated to 17–30 mg/mL and frozen in liquid nitrogen and stored at –80 °C until further use (for sodium dodecyl sulfate polyacrylamide gel electrophoresis see Supplementary Fig. 9).

Redox titrations coupled to UV/vis spectroscopy. UV/vis spectroscopy was performed in an anaerobic chamber at 25 °C using a spectrophotometer (UV-1650PC, Shimadzu, Duisburg, Germany) and quartz cuvettes. All buffer and enzyme solutions were rendered anaerobic using N₂ before the experiments. All spectra were normalized for their absorption at 700 nm. For titration with sodium dithionite, NCR was diluted to a concentration of 10 μ M in assay buffer (100 mM TRIS/HCl pH 8.0) and titrated in 2 μ M steps using a freshly prepared stock solution of sodium dithionite (0.4 mM in assay buffer). For better comparison, the resulting spectra were extrapolated to a protein concentration of 20 μ M. For determination of redox potentials, NCR was diluted to a concentration of 20 μ M in buffer A (50 mM HEPES pH 8.0, 150 mM KCl) supplemented with a mix of redox mediators (Supplementary Table 3) at a concentration of 0.1 μ M each to a final volume of 2 mL⁴². The solution was constantly stirred in a fluorescence cuvette and the potential was measured using a Ag/AgCl redox electrode (InLab Redox Micro, Mettler-Toledo, Giessen, Germany) calibrated with saturated quinhydrone solutions at pH 7.0 and 4.0. All values were obtained from single determinations, and were corrected to potentials versus H₂/H⁺ using +207 mV as potential for the Ag/AgCl reference electrode. NCR was incubated for 30 min before titration with sodium dithionite in buffer A and UV/vis spectra were recorded at defined redox potentials after allowing the potential to stabilize ($\Delta E < 2$ mV/min). For titration in the presence of substrate, NCoA was added to a final concentration of 50 μ M. Data were analyzed and depicted using Prism 6 (GraphPad, San Diego, USA). For fitting of Nernst curves to data points, a modified Nernst equation was used⁴³.

Mössbauer and EPR spectroscopy. Mössbauer and EPR spectroscopic analyses are described in the Supplementary methods.

Crystallization and structure determination. Crystallization of NCR was performed with the vapor diffusion method at 4 and 20 °C. The protein solution contained 25 mg ml⁻¹ NCR, 20 mM HEPES, pH 7.5, 0.5 mM FAD and 0.5 mM FMN. The drop solution consists of 2 µl of protein solution, 1 µl of precipitate solution (composed of 17% PEG 4000 or 20% PEG3350), 0.18–0.2 M NaF and 1 µl silver bullet solution A12 or BioD4⁴⁴. The corresponding reservoir solution and 20% (w/v) glycerol served for cryo-protection. Data were collected at the Swiss-Light-Source, Villigen at a wavelength of 1 Å and processed with XDS⁴⁵ (Table 1). Phases were determined by molecular replacement using PHASER⁴⁶ integrated into PHENIX⁴⁷. A suitable model was prepared by taking DCR of *E. coli* (1P59) without residues 517–553 and by partially pruned side chains using the phenix_sculptor script (option Schwarzenbacher)⁴⁸. After refining the obtained model with REFMAC⁴⁹ and PHENIX, ARP/WARP⁵⁰ was used for amino acid exchange and further refinement. After completing manual model building with COOT⁵¹ refinement was terminated with BUSTER (Phaser, Global Phasing Ltd.) using NCS and TLS parameters⁵². Moreover, NCR crystals were soaked with 0.5 mM NCoA (pH 6.5–7.0) for 2 h at 4 °C and frozen. The X-ray structure was refined with BUSTER using the coordinates of the substrate-free NCR as starting model. Although not completely occupied, all component parts of NCoA were clearly visible in the 2F_o–F_c electron density map at a contour level of 1σ. The composite omit map at a contour level of 0.5σ is shown in Fig. 5b. Co-crystallization between NCR and NCoA (5 mM) or DHNCoA (5 mM) was performed in an anaerobic tent (95% N₂, 5% H₂) to detect the influence of O₂ and crystal lattice effects for substrate/product binding. Crystals essentially grew under the same conditions (20% PEG 3350, 0.2 M NaF) but adopted a new crystal form. Refinement of the NCR–DHNCoA complex structure was performed with PHENIX. The obtained model is highly flexible and partly disordered (overall B-factor: 93.1 Å²); the B-factor around DHNCoA is with ca. 65 Å² significantly lower. In the three data sets are 95–97% of the backbone dihedral angle in favored regions and 0.0–0.2% in outlier regions.

Computational modeling. As starting model for calculations, the structure of NCR with bound NCoA substrate was used. A sphere of water with a radius of 30 Å centered at the active site of NCR was added to the system to represent the solvent. The structural model was prepared using the software CHARMM and together with its force field⁵³ analogous to the procedure in a previous publication³⁵. The FeS cluster was assumed to be reduced and its charges were taken from the literature⁵⁴. The force field parameters for NCoA were taken from analogous parameter sets in the CHARMM force field. The assignment of the protonation state of the titratable side chains was based on titration calculations using a continuum electrostatic model and Monte Carlo titrations^{55,56}. In the QM/MM calculations, the following residues comprised the QM region: the isalloxazine ring of FMN, the naphthyl-thioester part of NCoA, and side chains of Y82, H123, Y197, H284 and three active site water molecules bridging the gap between H123 and Y82. All side chains were truncated between Cα and Cβ. In the active site, Y82 and Y197 were set to their protonated state and H284 was set to its neutral form (protonated at Ne2). For FMN, the negatively charged reduced state was assumed (deprotonated N1). The QM/MM calculations were performed using pDynamo⁵⁷ together with ORCA⁵⁸. We used unrestricted DFT as QM method, namely we used the BP86 functional with the def2-SVP basis set for the search of the path and recalculated the energies using M06 with a def2-TZVP basis. The MM energies were calculated using the CHARMM27⁵⁹ force field. To model the QM/MM boundary, a link-atom scheme and electrostatic embedding was used. The QM region was surrounded by a fully flexible MM layer of 8 Å. MM atoms that had a distance of more than 8 Å from any QM atom were harmonically restrained. The force constants of the restraints were linearly increased between 8 and 16 Å from 0 to 100 kcal (mol Å)⁻¹, except for the iron-sulfur center, which was restrained by a force constant of 100 kcal (mol Å)⁻¹. Beyond 16 Å, the maximal force constant 100 kcal/(molÅ) was applied for the restraints. Using a conjugate gradient minimizer, we minimized the initial coordinates. To obtain first estimates for transition and intermediate states, we scanned the potential energy surface along the relevant bonds with a step size of 0.1–0.4 Å. The RMS gradient threshold of 0.04 kcal (mol Å)⁻¹ was used for all minimizations and surface scans. For finding reliable transition states, we started from these estimates of the intermediates and transition state and applied the PyCPR³⁴ implementation of the conjugated peak refinement method⁶⁰.

Reporting summary. Further information on research design is available in the Nature Research Reporting Summary linked to this article.

Data availability

The datasets generated and analyzed during the current study are available from the corresponding authors upon reasonable request. The source data underlying Fig. 6a–d, Fig. 7a, b and Supplementary Figs. 3, 5–9 are provided in the Source Data file. In addition, the PDB files for generating Figs. 2–5 and Supplementary Figs. 1, 2 are accessible online at the protein data bank (6QKQ, 6QKR, and 6QKX).

Received: 25 January 2019 Accepted: 12 April 2019
Published online: 06 May 2019

References

- Vila, J., Tauler, M. & Grifoll, M. Bacterial PAH degradation in marine and terrestrial habitats. *Curr. Opin. Biotechnol.* **33**, 95–102 (2015).
- Duan, L., Naidu, R., Thavamani, P., Meaklim, J. & Megharaj, M. Managing long-term polycyclic aromatic hydrocarbon contaminated soils: a risk-based approach. *Environ. Sci. Pollut. Res. Int.* **22**, 8927–8941 (2015).
- Rabus, R. et al. Anaerobic microbial degradation of hydrocarbons: from enzymatic reactions to the environment. *J. Mol. Microbiol. Biotechnol.* **26**, 5–28 (2016).
- Meckenstock, R. U. et al. Anaerobic degradation of benzene and polycyclic aromatic hydrocarbons. *J. Mol. Microbiol. Biotechnol.* **26**, 92–118 (2016).
- Boll, M., Löffler, C., Morris, B. E. & Kung, J. W. Anaerobic degradation of homocyclic aromatic compounds via arylcarboxyl-coenzyme A esters: organisms, strategies and key enzymes. *Environ. Microbiol.* **16**, 612–627 (2014).
- Fuchs, G., Boll, M. & Heider, J. Microbial degradation of aromatic compounds - from one strategy to four. *Nat. Rev. Microbiol.* **9**, 803–816 (2011).
- Kung, J. W. et al. Identification and characterization of the tungsten-containing class of benzoyl-coenzyme A reductases. *Proc. Natl Acad. Sci. USA* **106**, 17687–17692 (2009).
- Boll, M. & Fuchs, G. Benzoyl-coenzyme A reductase (dearomatizing), a key enzyme of anaerobic aromatic metabolism. ATP dependence of the reaction, purification and some properties of the enzyme from *Thauera aromatica* strain K172. *Eur. J. Biochem.* **234**, 921–933 (1995).
- Huwiler, S. G. et al. One-megadalton metalloenzyme complex in *Geobacter metallireducens* involved in benzene ring reduction beyond the biological redox window. *Proc. Natl Acad. Sci.* **116**, 2259–2264 (2019).
- Kung, J. W. et al. Reversible biological Birch reduction at an extremely low redox potential. *J. Am. Chem. Soc.* **132**, 9850–9856 (2010).
- Thiele, B., Rieder, O., Golding, B. T., Müller, M. & Boll, M. Mechanism of enzymatic Birch reduction: stereochemical course and exchange reactions of benzoyl-CoA reductase. *J. Am. Chem. Soc.* **130**, 14050–14051 (2008).
- Birch, A. J. The Birch reduction in organic synthesis. *Pure. Appl. Chem.* **68**, 553–556 (1996).
- Estelmann, S., Blank, I., Feldmann, A. & Boll, M. Two distinct old yellow enzymes are involved in naphthyl ring reduction during anaerobic naphthalene degradation. *Mol. Microbiol.* **95**, 162–172 (2015).
- Eberlein, C. et al. Identification and characterization of 2-naphthoyl-coenzyme A reductase, the prototype of a novel class of dearomatizing reductases. *Mol. Microbiol.* **88**, 1032–1039 (2013).
- Eberlein, C. et al. ATP-dependent/independent enzymatic ring reductions involved in the anaerobic catabolism of naphthalene. *Environ. Microbiol.* **15**, 1832–1841 (2013).
- Willstein, M. et al. Enantioselective enzymatic naphthoyl ring reduction. *Chem. Eur. J.* **24**, 12505–12508 (2018).
- Greening, C. et al. Physiology, biochemistry and applications of F420- and F_o-dependent redox reactions. *Microbiol. Mol. Biol. Rev.* **80**, 451–493 (2016).
- Walsh, C. T. & Wencewicz, T. A. Flavoenzymes: versatile catalysts in biosynthetic pathways. *Nat. Prod. Rep.* **30**, 175–200 (2013).
- Macheroux, P., Kappes, B. & Ealick, S. E. Flavogenomics—a genomic and structural view of flavin-dependent proteins. *FEBS J.* **278**, 2625–2634 (2011).
- Joosten, V. & van Berkel, W. J. Flavoenzymes. *Curr. Opin. Chem. Biol.* **11**, 195–202 (2007).
- Fraaije, M. W. & Mattevi, A. Flavoenzymes: diverse catalysts with recurrent features. *Trends Biochem. Sci.* **25**, 126–132 (2000).
- Ghisla, S. & Massey, V. Mechanisms of flavoprotein-catalyzed reactions. *Eur. J. Biochem.* **181**, 1–17 (1989).
- Buckel, W., Thauer, R. K. Flavin-based electron bifurcation, ferredoxin, flavodoxin, and anaerobic respiration with protons (Ech) or NAD(+) (Rnf) as electron acceptors: a historical review. *Front. Microbiol.* **9**, 401 (2018).
- Alagaratnam, S. et al. A crystallographic study of Cys69Ala flavodoxin II from *Azotobacter vinelandii*: structural determinants of redox potential. *Protein Sci.* **14**, 2284–2295 (2005).
- Hubbard, P. A., Liang, X., Schulz, H. & Kim, J. J. The crystal structure and reaction mechanism of *Escherichia coli* 2A-dienoyl-CoA reductase. *J. Biol. Chem.* **278**, 37553–37560 (2003).
- Leys, D., Basran, J., Talfourier, F., Sutcliffe, M. J. & Scrutton, N. S. Extensive conformational sampling in a ternary electron transfer complex. *Nat. Struct. Biol.* **10**, 219–225 (2003).
- Reed, T. et al. Crystal structure of histamine dehydrogenase from *Noardioides simplex*. *J. Biol. Chem.* **285**, 25782–25791 (2010).
- Adalbjornsson, B. V. et al. Biocatalysis with thermostable enzymes: structure and properties of a thermophilic 'ene'-reductase related to old yellow enzyme. *ChemBiochem* **11**, 197–207 (2010).
- Opperman, D. J. et al. Crystal structure of a thermostable old yellow enzyme from *Thermus scotoductus* SA-01. *Biochem. Biophys. Res. Commun.* **393**, 426–431 (2010).

ARTICLE

NATURE COMMUNICATIONS | <https://doi.org/10.1038/s41467-019-10078-3>

30. Werther, T. et al. Redox-dependent substrate-cofactor interactions in the Michaelis-complex of a flavin-dependent oxidoreductase. *Nat. Commun.* **8**, 16084 (2017).
31. Pandelia, M. E., Lanz, N. D., Booker, S. J. & Krebs, C. Mössbauer spectroscopy of Fe/S proteins. *Biochim. Biophys. Acta* **1853**, 1395–1405 (2015).
32. Koppenhofer, A.; Turner, K. L.; Allen, J. W.; Chapman, S. K.; Ferguson, S. J. Cytochrome cdl from *Paracoccus pantotrophus* exhibits kinetically gated, conformationally dependent, highly cooperative two-electron redox behavior. *Biochemistry* **39**, 4243–4249 (2000).
33. Baymann, F. et al. On the natural history of flavin-based electron bifurcation. *Front. Microbiol.* **9**, 1357 (2018).
34. Gisdon, F. J., Culka, M. & Ullmann, G. M. PyCPR—a python-based implementation of the conjugate peak refinement (CPR) algorithm for finding transition state structures. *J. Mol. Model.* **22**, 242 (2016).
35. Culka, M., Huwiler, S. G., Boll, M. & Ullmann, G. M. Breaking benzene aromaticity - computational insights into the mechanism of the tungsten-containing benzoyl-CoA reductase. *J. Am. Chem. Soc.* **139**, 14488–14500 (2017).
36. Williams, R. E. & Bruce, N. C. 'New uses for an Old Enzyme'—the Old Yellow Enzyme family of flavoenzymes. *Microbiology* **148**, 1607–1614 (2002).
37. Bombarda, E. & Ullmann, G. M. pH-dependent pKa values in proteins - a theoretical analysis of protonation energies with practical consequences for enzymatic reactions. *J. Phys. Chem. B* **114**, 1994–2003 (2010).
38. Nitschke, W. & Russell, M. J. Redox bifurcations: mechanisms and importance to life now, and at its origin: a widespread means of energy conversion in biology unfolds. *BioEssays* **34**, 106–109 (2012).
39. Buckel, W. & Thauer, R. K. Flavin-based electron bifurcation, a new mechanism of biological energy coupling. *Chem. Rev.* **118**, 3862–3886 (2018).
40. Lubner, C. E. et al. Mechanistic insights into energy conservation by flavin-based electron bifurcation. *Nat. Chem. Biol.* **13**, 655–659 (2017).
41. Demmer, J. K. et al. Insights into flavin-based electron bifurcation via the NADH-dependent reduced ferredoxin:NADP oxidoreductase structure. *J. Biol. Chem.* **290**, 21985–21995 (2015).
42. Ravasio, S., Curti, B. & Vanoni, M. A. Determination of the midpoint potential of the FAD and FMN flavin cofactors and of the 3Fe-4S cluster of glutamate synthase. *Biochemistry* **40**, 5533–5541 (2001).
43. Moffet, D. A., Foley, J. & Hecht, M. H. Midpoint reduction potentials and heme binding stoichiometries of de novo proteins from designed combinatorial libraries. *Biophys. Chem.* **105**, 231–239 (2003).
44. McPherson, A. & Cudney, B. Searching for silver bullets: an alternative strategy for crystallizing macromolecules. *J. Struct. Biol.* **156**, 387–406 (2006).
45. Kabsch, W. Xds. *Acta Crystallogr. D Biol. Crystallogr.* **66**, 125–132 (2010).
46. McCoy, A. J. et al. Phaser crystallographic software. *J. Appl. Crystallogr.* **40**, 658–674 (2007).
47. Afonine, P. V. et al. Phenix.model-vs-data: a high-level tool for the calculation of crystallographic model and data statistics. *J. Appl. Crystallogr.* **43**, 669–676 (2010).
48. Schwarzenbacher, R., Godzik, A., Grzechnik, S. K. & Jaroszewski, L. The importance of alignment accuracy for molecular replacement. *Acta Crystallogr. D Biol. Crystallogr.* **60**, 1229–1236 (2004).
49. Murshudov, G. N., Vagin, A. A. & Dodson, E. J. Refinement of macromolecular structures by the maximum-likelihood method. *Acta Crystallogr. D Biol. Crystallogr.* **53**, 240–255 (1997).
50. Langer, G., Cohen, S. X., Lamzin, V. S. & Perrakis, A. Automated macromolecular model building for X-ray crystallography using ARP/wARP version 7. *Nat. Protoc.* **3**, 1171–1179 (2008).
51. Emsley, P. & Cowtan, K. Coot: model-building tools for molecular graphics. *Acta Crystallogr. D Biol. Crystallogr.* **60**, 2126–2132 (2004).
52. Bricogne, G. et al. *BUSTER version 2.9*. (Global Phasing Ltd., Cambridge, United Kingdom, 2010).
53. Brooks, B. R. et al. CHARMM: A program for macromolecular energy, minimization, and dynamics calculations. *J. Comput. Chem.* **4**, 187–217 (1983).
54. Torres, R. A., Lovell, T., Noodleman, L. & Case, D. A. Density functional and reduction potential calculations of FeS₄ clusters. *J. Am. Chem. Soc.* **125**, 1923–1936 (2003).
55. Ullmann, R. T. & Ullmann, G. M. GMCT: a Monte Carlo simulation package for macromolecular receptors. *J. Comput. Chem.* **33**, 887–900 (2012).
56. Bashford, D. & Gerwert, K. Electrostatic calculations of the pKa values of ionizable groups in bacteriorhodopsin. *J. Mol. Biol.* **224**, 473–486 (1992).
57. Field, M. J. The pDynamo program for molecular simulations using hybrid quantum chemical and molecular mechanical potentials. *J. Chem. Theory Comput.* **4**, 1151–1161 (2008).
58. Neese, F. The ORCA program system. *Wiley Interdiscip. Rev. Comput. Mol. Sci.* **2**, 73–78 (2012).
59. MacKerell, A. D. et al. All-atom empirical potential for molecular modeling and dynamics studies of proteins. *J. Phys. Chem. B* **102**, 3586–3616 (1998).
60. Fischer, S. & Karplus, M. Conjugate peak refinement: an algorithm for finding reaction paths and accurate transition states in systems with many degrees of freedom. *Chem. Phys. Lett.* **194**, 252–261 (1992).

Acknowledgements

This work was funded by the German Research Foundation (DFG) within RTG 1976 (M.W. and M.B.) and SPP 1927 (M.B., A.P., V.S., and M.U.). We thank Hartmut Michel for continuous support and the staff of the SLS, Villigen for help in data collection. We thank Sina Wäldenweber for initial crystallization.

Author contributions

M.W. purified enzymes and conducted biochemical, spectroscopic, kinetic analyses. D.F.B., and A.J.P. carried out EPR spectroscopy experiments. U.D., K.K., and U.E. crystallized enzymes and analyzed X-ray structural data, C.S.M., L.H., and V.S. performed the Mössbauer spectroscopic experiments. M.U. conducted the computational studies. M.B. designed the overall project. The paper was written through contributions of all authors. All authors have given approval to the final version of the paper.

Additional information


Supplementary Information accompanies this paper at <https://doi.org/10.1038/s41467-019-10078-3>.

Competing interests: The authors declare no competing interests.

Reprints and permission information is available online at <http://npg.nature.com/reprintsandpermissions/>

Journal peer review information: *Nature Communications* thanks Ian Hillier, Hidehiko Hirakawa and the other, anonymous, reviewer(s) for their contribution to the peer review of this work. Peer reviewer reports are available.

Publisher's note: Springer Nature remains neutral with regard to jurisdictional claims in published maps and institutional affiliations.

 **Open Access** This article is licensed under a Creative Commons Attribution 4.0 International License, which permits use, sharing, adaptation, distribution and reproduction in any medium or format, as long as you give appropriate credit to the original author(s) and the source, provide a link to the Creative Commons license, and indicate if changes were made. The images or other third party material in this article are included in the article's Creative Commons license, unless indicated otherwise in a credit line to the material. If material is not included in the article's Creative Commons license and your intended use is not permitted by statutory regulation or exceeds the permitted use, you will need to obtain permission directly from the copyright holder. To view a copy of this license, visit <http://creativecommons.org/licenses/by/4.0/>.

© The Author(s) 2019

Appendix F. Caffeyl-CoA reductase (CarCDE)

 Check for updates

FEBS
Letters

 **FEBS PRESS**
science publishing by scientists

Molecular basis of the flavin-based electron-bifurcating caffeyl-CoA reductase reaction

 Julius K. Demmer¹, Johannes Bertsch², Christian Öppinger², Hannah Wohlers², Kanwal Kayastha¹, Ulrike Demmer¹, Ulrich Ermler¹ and Volker Müller²
¹ Max-Planck-Institut für Biophysik, Frankfurt am Main, Germany

² Department of Molecular Microbiology and Bioenergetics, Institute of Molecular Biosciences, Johann Wolfgang Goethe-Universität Frankfurt am Main, Germany

Correspondence

 V. Müller, Department of Molecular Microbiology and Bioenergetics, Institute of Molecular Biosciences, Johann Wolfgang Goethe-Universität Frankfurt am Main, 60438, Frankfurt, Germany
Tel: +49-69-798-29508
Fax: +49-69-798-29306

E-mail: vmueller@bio.uni-frankfurt.de and

U. Ermler, MPI für Biophysik, Max-von-Laue-Str. 3, 60438, Frankfurt am Main, Germany

 Fax: +49 69 63031 002
Tel: +49 69 63031 054

E-mail: ulrich.ermler@biophys.mpg.de

(Received 16 November 2017, revised 4 January 2018, accepted 4 January 2018, available online 1 February 2018)

doi:10.1002/1873-3468.12971

Edited by Stuart Ferguson

Flavin-based electron bifurcation (FBEB) is a recently discovered mode of energy coupling in anaerobic microorganisms. The electron-bifurcating caffeyl-CoA reductase (CarCDE) catalyzes the reduction of caffeyl-CoA and ferredoxin by oxidizing NADH. The 3.5 Å structure of the heterododecameric Car(CDE)₄ complex of *Acetobacterium woodii*, presented here, reveals compared to other electron-transferring flavoprotein/acyl dehydrogenase family members an additional ferredoxin-like domain with two [4Fe-4S] clusters N-terminally fused to CarE. It might serve, *in vivo*, as specific adaptor for the physiological electron acceptor. Kinetic analysis of a CarCDE (ΔFd) complex indicates the bypassing of the ferredoxin-like domain by artificial electron acceptors. Site-directed mutagenesis studies substantiated the crucial role of the C-terminal arm of CarD and of ArgE203, hydrogen-bonded to the bifurcating FAD, for FBEB.

Keywords: acetogenic bacteria; bioenergetics; crystal structure; electron-transferring flavoprotein/acyl-CoA dehydrogenase; ferredoxin; flavin-based electron bifurcation

A new mode of energy coupling, termed flavin-based electron bifurcation (FBEB), was recently discovered [1,2] by which energy conservation in many anaerobic microorganisms, living at the thermodynamic limit, is made possible. Such organisms include fermenting bacteria, methanogenic archaea, and acetogenic bacteria. In FBEB, a variable exergonic reduction drives the endergonic ferredoxin reduction thereby sharing the same oxidizing agent. A flavin (F) serves as coupling medium due to its capability to split a two-electron into two one-electron reduction events of distinct

energy constituted by the electronic nature of the isoalloxazine ring and the polypeptide environment. The thermodynamically unfavorable FH⁻/FH[•] oxidation is driven by a strong variable electron acceptor and the favorable FH[•]/F oxidation powers the reduction of the weak electron acceptor ferredoxin (Fd_{ox}/Fd_{red}⁻). An analogous process was reported for the membrane-spanning cytochrome bc₁ complex where quinol is both the electron donor and the site of bifurcation [3].

Several FBEB enzymes are functionally characterized to date and recently reviewed [4–6]. One of them

Abbreviations

CarCDE, electron-transferring flavoprotein/caffeyl-CoA reductase; ET, electron transfer; EtfAB/Bcd, electron-transferring flavoprotein/butyryl-CoA dehydrogenase; FBEB, flavin-based electron bifurcation.

332

FEBS Letters 592 (2018) 332–342 © 2018 Federation of European Biochemical Societies

is the FBEB caffeoyl-CoA reductase (CarCDE) which reduces 1 caffeoyl-CoA to hydrocaffeoyl-CoA ($E_0' \approx +33$ to -10 mV; based on the fumarate/succinate or crotonyl-CoA/butyryl-CoA couples) and 2 Fd_{ox} to 2 Fd_{red}^- ($E_0' \sim -450$ to -500 mV) at the expense of 2 NADH ($E_0' = -320$ mV) which are oxidized to 2 NAD^+ [7] (Fig. 1).

The CarCDE complex is composed of the acyl dehydrogenase module CarC and an electron-transferring flavoprotein module consisting of subunits CarD and CarE (Fig. 1). All three subunits contain a noncovalently bound FAD as a prosthetic group. In addition, CarE contains an N-terminal ferredoxin-like or Fd-like domain carrying two [4Fe-4S] clusters. CarCDE is a key enzyme in caffeate respiration, a novel type of anaerobic respiration in the acetogenic model bacterium *Acetobacterium woodii* (Fig. 1). With molecular hydrogen ($E_0' = -414$ mV) as electron donor, reduced ferredoxin (Fd_{red}^-), the fuel for the respiratory chain, can only be produced by the FBEB reactions of CarCDE and [FeFe] hydrogenase [8]. The functional characterization of these two soluble FBEB complexes closes the missing gap for a complete understanding of the bioenergetics of caffeate respiration in *A. woodii* [7].

Besides NADH-dependent reduced ferredoxin : NADP⁺ oxidoreductase [9–13], the biochemically and structurally best-studied FBEB system is the electron-transferring flavoprotein/butyryl-CoA dehydrogenase (EtfAB/Bcd) complex, which is an enzyme in butyrate-producing clostridia [1,2,14–19]. It couples the exergonic reduction of crotonyl-CoA to butyryl-CoA with the endergonic reduction of ferredoxin both by oxidizing of NADH to NAD⁺. The EtfAB/Bcd complex is phylogenetically related to CarCDE; CarC, CarD, and CarE correspond to Bcd, EtfB, and EtfA, respectively. In this report, the X-ray structure of caffeoyl-CoA reductase of *A. woodii*, is described and a mechanism for FBEB postulated. Based on structural

and mutational data, we focus on the function of the Fd-like domain which is absent in the EtfAB/Bcd complex.

Material and methods

Cultivation of *A. woodii* and purification of CarCDE

Acetobacterium woodii (DSM 1030) was grown at 30 °C under anaerobic conditions in 20-L flasks (Glasgerätebau Ochs, Bovenden-Lenglern, Germany) using 20 mM fructose as carbon and energy source as described previously [20,21]. At an OD₆₀₀ of ~0.3, caffeate was added to a concentration of 5 mM. Purification of the enzyme from cell paste of *A. woodii* was done as described before [7]. In addition, an iron-sulfur cluster reconstitution was performed at room temperature for 1 h under strictly anaerobic conditions using 8 mM DTT, 10 μM FAD, 2 mM cysteine, and 1.5 mM FeSO₄.

Cloning, production and analysis of site-specifically mutated CarCDE variants

The genes *carCDE* were amplified from chromosomal DNA and cloned into the expression vector pET21a *via* the restriction sites *NheI* and *NotI*. A sequence encoding Strep-tag was introduced at the 3'-end of the gene coding for CarE by using corresponding primers (Table S1) yielding pET21a_CarCDE-Strep. The resulting plasmid was the template for site-directed mutagenesis. Nucleic acid changes were introduced at desired loci in the encoding genes and ligated normally or by the Gibson-Assembly method. Plasmid generated are pET21a_CarCDE[R203A]-Strep, pET21a_CarCDE[R203Q]-Strep, pET21a_CarCDE[R203K]-Strep, pET21a_CarCDE[ΔFd]-Strep, pET21a_CarCD[AD-arm]E-Strep, and pET21a_CarCDE(C10A, C13A, C16A, C20A, C38A, C41A, C44A, C48A)-Strep (further called pET21a_CarCDE[ΔFeS]-Strep). Plasmids were transformed into *Escherichia coli* BL21(DE3)Δ*iscR* [22], which was grown

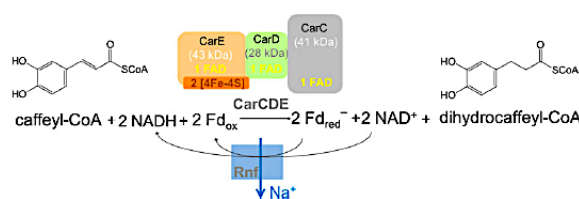


Fig. 1. Reaction of CarCDE. The FBEB enzyme CarCDE catalyzes an important process of caffeate respiration by using the energy of the enoyl carbon–carbon double bond of caffeoyl-CoA for ferredoxin reduction. The respiratory chain is rather simple and contains only two enzymes: a sodium-ion-translocating ferredoxin : NAD⁺ oxidoreductase complex [47,48] that generates an electrochemical gradient across the cell membrane and a Na⁺ F₁F₀-ATP synthase [49].

aerobically in 800 mL of LB-medium supplemented with 2 mM ammonium-iron(II) citrate, 20 mM glucose, and 100 mM MOPS/NaOH at 37 °C. At an OD₆₀₀ of 0.3–0.5, the culture was brought into an anaerobic chamber (Coy Laboratory Products, Grass Lake, MI, USA) and transferred into a sterile, anaerobic Müller-Krempel flask following supplementation of the culture with 2 mM cysteine and 20 mM fumarate. After closing the culture with a butyl stopper, the flask was cooled down to 16 °C and gene expression was induced by addition of IPTG to a final concentration of 1 mM. All steps from this point onward were done in an anoxic chamber (Coy Laboratory Products) with a gas phase of N₂/H₂ (95 : 5 [v/v]). After 16–19 h of gentle agitation cells were harvested, resuspended in 10 mL buffer W (100 mM Tris/HCl, 150 mM NaCl, 20 mM MgSO₄, 20% (v/v) glycerol, 4.4 μM resazurine, 5 μM FAD, 2 mM dithioerythritol, pH 8) and disrupted in a French press (SLM Aminco; SLM Instruments, Haverhill, MA, USA) after addition of DNase I and 0.5 mM PMSF (setting high, 1000 psi, 1 inch piston diameter). The lysate was centrifuged (2000 g, 15 min, RT) to separate undisturbed cells from the crude extract. Subsequently, the CarCDE complex was purified by affinity chromatography using Strep-Tactin high capacity material (IBA Lifesciences, Göttingen, Germany) and the elution buffer W + 2.5 mM desthiobiotin. Fractions containing CarCDE-Strep were pooled and concentrated *via* ultrafiltration (Vivaspin 6, 10 kDa Cut-off, Sartorius Stedim Biotech GmbH, Göttingen, Germany) to a volume of 500 μL. The concentrate was further separated on a buffer W-equilibrated Superose 6 10/300 GL column (GE Healthcare, Little Chalfont, UK) with a flow rate of 0.5 mL·min⁻¹. The concentration of proteins was measured according to Bradford [23]. The integrity of the enzyme complex was analyzed on a calibrated Sephacryl S300 column equilibrated with buffer W. The iron content of the purified enzyme was determined by colorimetric methods [24,25].

Assays of caffeoyl-CoA reductase activity

Kinetic measurements were routinely performed in a N₂ atmosphere at 30 °C in 1.8-mL anaerobic cuvettes (Glasgerätebau Ochs), which were sealed with rubber stoppers. A caffeoyl-CoA regeneration system was used in all measurements as previously described. Caffeoyl-CoA used in the assays was synthesized enzymatically with the caffeoyl-CoA synthetase from *A. woodii* [26]. The ferredoxin used was isolated from *Clostridium pasteurianum* as described earlier [27]. Enzyme assays for the determination of the NADH : ferredoxin:caffeoyl-CoA oxidoreductase activity contained buffer m (50 mM Tris/HCl, 20 mM MgSO₄, and 2 mM dithioerythritol, pH 7.5), 250 μM caffeate, the regeneration system, 8 μg of protein, 5 μM caffeoyl-CoA, and 20 μM ferredoxin. The FBEB reaction was started by the addition of 500 μM NADH [7]. The same assay conditions were used for the

other redox agents using instead of 20 μM ferredoxin 50 μM FAD, 50 μM FMN, 500 μM dichlorophenol indophenol and 1 mM ferricyanide (K₃Fe(CN)₆). Measurements using the methyl viologen oxidation assay were done as described earlier [7]. NADH oxidation and electron acceptor reduction were measured by UV/Vis spectroscopy (see Table 2).

Crystallization and X-ray structure determination

CarCDE was crystallized with the sitting-drop method at 20 °C in an anaerobic chamber equipped with an OryxNano crystallization robot (Douglas Instruments Ltd., Hungerford, UK). The crystallization conditions are given in Table 1. Crystals showed an anisotropic diffraction pattern and normally diffracted to ca. 5 Å. After intensive screening one crystal reached a resolution of ca. 3.5 Å at the beamline PXII at the Swiss-Light-Source in Villigen (Switzerland) and a dataset was collected. XDS [28] was used for data processing and the UCLA-DOE LAB server for anisotropic correction [29]. The resulting resolution was 3.0 Å in *a*-, 3.7 Å in *b*- and 3.5 Å in *c*-direction specified according to statistic considerations (Table 1). The structure was determined by molecular replacement using PHASER [30] and the separated Bcd and EtfAB of *Acidaminococcus fermentans* as model [15]. COOT was used for electron density analysis and model building [31]. While the quality of electron density was reasonable for CarC, sufficient for the CarDE base and domain II, it was ambiguous for the N-terminal Fd-like domain which was highly mobile and partly disordered. Refinement was performed with REFMAC [32], PHENIX [33], and BUSTER (Phaser; Global Phasing Ltd., Cambridge, UK) requiring a series of remodeling steps. A second dataset was measured at the iron edge (1.738 Å) at ca. 4.0 Å resolution using a crystal grown from a CarCDE complex solution supplemented with 2.5 mM NADH (Table 1). The sites of the four iron-sulfur clusters in the asymmetric unit could be identified by SHELXD [34] which confirmed the location of the Fd-like domain and supported its model building. The obtained coordinates of the CarCDE complex were used to determine the structure of CarCDE-NADH complex by molecular replacement. The results of the refinement are given in Table 1. Figs 3, S1 and S2 were generated with PYMOL (Schrödinger; LLC, New York, NY, USA). The atomic coordinates and structure factors of the CarCDE complex have been deposited in the Protein Data Bank, www.pdb.org with ID code 6FAH.

Results

Production of CarCDE and site-specifically mutated variants

CarCDE was initially isolated from *A. woodii* as described [7] and all crystallization attempts were performed with the obtained protein sample. The stability

J. K. Demmer *et al.*

The electron-bifurcating CarCDE complex

Table 1. Crystallographic data.

Crystal	CarCDE	CarCDE anisotropic correction	CarCDE-NADH anisotropic correction
Crystallization			
Protein solution	20–25 mg·mL ⁻¹ CarCDE, 20 mM Tris/HCl, pH 7.5, 20 mM Mg ₂ SO ₄ , 30% glycerol and 50 μM FAD		
Crystallization conditions	0.1 M Tris/HCl, pH 8.5, 30% (v/v) polyethylene glycol 4000; 200 mM Li ₂ SO ₄		0.1 M Tris/HCl, pH 6.5; 30% (v/v) polyethylene glycol 4000; 100 mM Li ₂ SO ₄ ; 2.5 mM NADH; 30% glycerol directly from the drop
Cryo conditions	Perfluoropolyether oil		
Data collection			
Space group	C2	C2	C2
Wavelength (Å)	1.0	1.0	1.739
Resolution (Å)	50.0–3.0 (3.1–3.0)	50.0–3.0 (3.08–3.01)	50.0–3.7 (3.8–3.71)
Anisotropy corr. in a,b,c		3.0, 3.7, 3.5	3.7, 4.6, 4.0
Unit cell			
a, b, c (Å)	211.5, 142.6, 101.5	211.5, 142.6, 101.5	211.1, 147.9, 103.0
β (°)	99.0	99.0	98.6
Redundancy	3.3 (3.4)	3.3 (3.3)	10.3 (10.7)
Completeness (%)	98.8 (99.1)	69.2 (3.6) ^a	71.3 (4.7) ^b
R _{sym} (%)	11.1 (434.3)	7.5 (58.9)	18.8 (261.8)
I/σ(I)	8.1 (0.43)	12.7 (70.4)	12.7 (1.0)
CC _{1/2}	99.8 (24.9)	99.8 (70.4)	99.9 (44.9)
Refinement statistics			
Mol. asym. unit		Car(CDE) ₂	Car(CDE) ₂
No. atoms		15 600, 395	15 612, 390
Polypeptide, cofactors		23.1, 28.6	25.7, 32.3
R _{working} , R _{free} (%)			
B _{average} (Å ²)		116, 92	207, 212
R.m.s. deviation			
Bond lengths (Å)		0.008	0.018
Bond angles (°)		1.15	1.06
Ramachandran plot			
Favored, outliers (%)		91.6, 0.3	90.0, 0.2

^aCompleteness > 3.6 Å is > 93%^bCompleteness > 4.6 Å is > 94%.

of the CarCDE complex and the highly O₂-sensitive [4Fe–4S] clusters could be substantially increased by adding an iron-sulfur cluster reconstitution step to the purification protocol and 30% glycerol to the enzyme solution.

For creating site-directed enzyme variants, we established a heterologous production system. The encoding CarCDE genes fused with a Strep-tag were cloned into the expression vector pET21a and expressed in the *E. coli* strain BL21(DE3)ΔiscR deregulated in iron-sulfur cluster biosynthesis. The CarCDE complex was anaerobically purified by strep-tactin affinity and Superose-6 size exclusion chromatography (Fig. 2). Its iron content was detected to be 8.3 ± 0.5 mol per mol of enzyme. Heterologously produced CarCDE catalyzes NADH-dependent reduction of caffeoyl-CoA and ferredoxin with a rate of 3.3 U·mg⁻¹ (NADH oxidation) in a coupled manner. The obtained specific FBEB activity is 97% of that measured for the enzyme

isolated from *A. woodii*. Site-specifically changed CarCDE variants were produced and analyzed by the same procedure after mutating the gene by the single nucleotide exchange method *via* corresponding primers (See Table S1 and Materials and methods). All enzyme variants produced, which were able to catalyze the FBEB reaction, showed a similar specific activity as the wild-type. The produced CarCDE variants and their kinetic behavior are summarized in Table 2.

Structure of CarCDE

Caffeoyl-CoA reductase was found in the crystal as heterododecameric Car(CDE)₄ complex. The CarC tetramer constitutes the core and four EtfAB-like modules CarDE are peripherally attached (Fig. 3A). Each CarC monomer is built up of the well-established acyl dehydrogenase fold [35]. As reported for other EtfAB family members [15,19,36–38], CarDE consists of

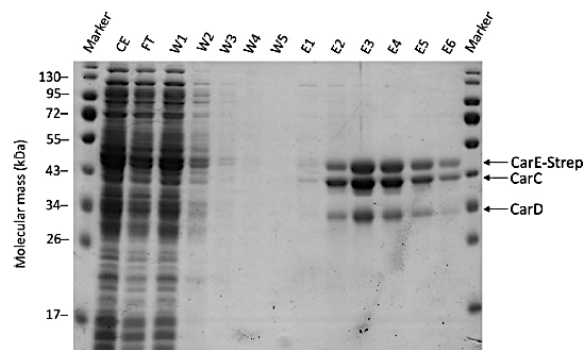


Fig. 2. Purification of Strep-tagged CarCDE from crude extract of *Escherichia coli* BL21(DE3) Δ iscR + pET21a_CarCDE-Strep verified by SDS-PAGE. Proteins were separated in 12.5% polyacrylamide gels and stained with Coomassie brilliant blue G250. CE: crude extract, FT: flow-through, W1–5: washing fractions, E1–6: elution fractions, Marker: Page-Ruler™ prestained protein marker.

Table 2. Specific activities of recombinant CarCDE and CarCDE variants with artificial electron donors/acceptors.

	WT	Δ FeS	Δ Fd	R203A	R203Q	R203K	Δ D-arm
NADH : DCPIP (600 nm)	10.5 \pm 0.1	10.9 \pm 0.6	10.3 \pm 0.2	1.5 \pm 0.2	1.5 \pm 0.1	1.4 \pm 0.2	0.9 \pm 0.1
NADH : ferricyanide (420 nm)	0.5 \pm 0.1	0.5 \pm 0.1	0.4 \pm 0.1	0.5 \pm 0.02	0.5 \pm 0.2	0.3 \pm 0.1	0.5 \pm 0.2
MV _{red} : Caffeyl-CoA (604 nm)	27.5 \pm 4.2	19.6 \pm 0.4	26.6 \pm 4.6	18.0 \pm 0.8	13.0 \pm 1.5	16.1 \pm 2.6	9.0 \pm 1.0
NADH : FMN : Caffeyl-CoA (340 nm)	1.5 \pm 0.1	1.4 \pm 0.3	1.3 \pm 0.3	1.1 \pm 0.1	1.0 \pm 0.5	1.2 \pm 0.1	0.9 \pm 0.3
NADH : FMN : Caffeyl-CoA (450 nm)	0.5 \pm 0.1	0.6 \pm 0.3	0.3 \pm 0.1	0.3 \pm 0.04	0.2 \pm 0.01	0.3 \pm 0.04	0.3 \pm 0.1
NADH : FAD : Caffeyl-CoA (340 nm)	37.0 \pm 2.1	22.3 \pm 1.1	12.3 \pm 1.2	0.6 \pm 0.1	0.5 \pm 0.04	0.5 \pm 0.1	0.6 \pm 0.1
NADH : FAD : Caffeyl-CoA (450 nm)	12.8 \pm 0.4	8.4 \pm 0.5	3.8 \pm 0.5	0.1 \pm 0.01	0.1 \pm 0.01	0.1 \pm 0.03	0.1 \pm 0.02
NADH : ferredoxin : Caffeyl-CoA (340 nm)	3.3 \pm 0.2	3.2 \pm 0.2	3.4 \pm 0.2	ND	ND	ND	ND

NADH oxidation was measured at 340 nm and flavin, DCPIP, and ferricyanide reduction at 450 nm, 600 nm, and 420 nm, respectively. MV oxidation was measured at a wavelength of 604 nm. Values are given as specific activities in U·mg⁻¹ protein. ND: not determinable. DCPIP, dichlorophenol indophenol.

domains I (E70–E275) and III (D1–D232) constituting the CarDE base and domain II composed of the C-terminal flavodoxin-like part of CarE (E276–E402) and the associated C-terminal arm of CarD (D-arm D232–D262; Fig. 3B). CarDE forms two contact points with CarC as observed in a similar manner in EtfAB/acyl dehydrogenase complexes [19,39,40]. The first interface is positioned between CarC2 and the CarDE base burying an area of 790 Å² and built up by helices C6 : C21, C39 : C46, D190 : D198, and D66 : D77 (+the preceding loop). The second contact region is formed between CarC1C2 and domain II, the buried area being 640 Å² (Fig. 3B). The FADs of CarE domain II and CarC acyl-CoA dehydrogenase, e-FAD, and c-FAD, have an edge-to-edge distance of ca. 9 Å and are bridged by the benzyl group of PheC155 of CarC1 (Fig. 3B). As an electron transfer event (ET) is possible between these FADs [41], the

found CarCDE conformation is termed as D (dehydrogenase conducting) state. E-FAD and d-FAD (bound to CarD) are ca. 40 Å aside from each other. In state D, domain II is spatially separated from the CarDE base solely connected by two solvent-exposed linkers (Fig. 3B).

A comparison of CarCDE and separated Bed and EtfAB from *A. fermentans* [15] revealed a perfect overlay between CarC and Bed as well as between the CarDE and the EtfAB bases with rms deviations of 1.4 and 1.4 Å, respectively, whereas domains II are rotated by ca. 80° relative to each other. The distance between d-FAD and e-FAD is ca. 19 Å which is slightly too long for a biologically relevant ET rate. A further rotation of domain II without multiple clashes is feasible. This CarCDE conformation is termed electron bifurcation-conducting or B-state because an ET geometry is adjusted between e-FAD of domain II and

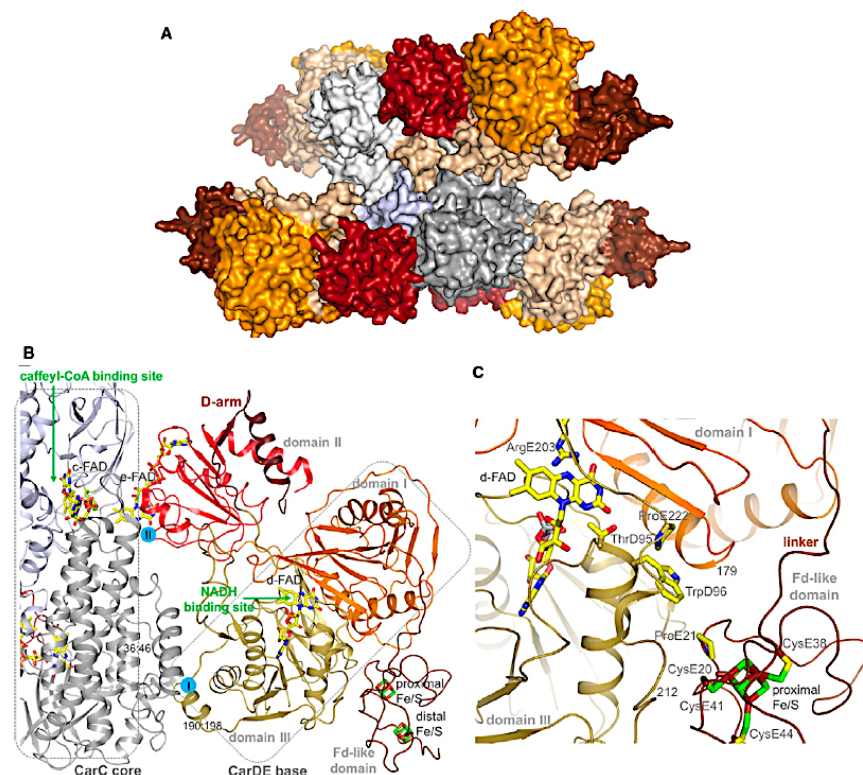


Fig. 3. Structure of CarCDE. (A) The 450 kDa heterododecameric complex. CarC1 and CarC2 is drawn in gray and white blue, CarD in wheat and domains I, II, and Fd-like of CarE in orange, red, and brown. (B) Structure of the D-state characterized by an electron-conducting conformation between c-FAD and e-FAD (shown as sticks). Each reaction requires a CarC1C2DE unit. Domain III and the D-arm of CarD are drawn in gold and dark-red, respectively. The first interface (blue circle I) between the CarC core and the CarDE base is characterized by a hydrogen bond between the C-terminal peptide carbonyl of helix C39:C46 and the N-terminal peptide amine of helix D190 : D198 and a hydrophobic patch constituted by nonpolar side chains. The second interface (blue circle II) between CarC1C2 and domain II is formed by a few hydrogen bonds between longer side chains and a small hydrophobic patch around the xylene ring of e-FAD. (C) ET between d-FAD and the proximal [4Fe-4S] cluster. The Fd-like domain-rest protein interface is formed by segments D210-D214 and E41-E43 as well as E178-E180 and E22-E23. The proximity of the NADH-binding site and especially of the anchor of the D-arm to the Fd-like domain-CarD interface does not exclude a coupling between NADH binding and an Fd-like domain rearrangement.

d-FAD, the electron-bifurcating flavin (see below). Thus, the D- and B-states differ by a rotation of domain II by ca. 90° which substantially changes the surrounding of e-FAD but not of c-FAD and d-FAD. While the CarC core-CarDE base interface is maintained in both states, the contact between the CarC core and domain II is lost in the B-state but, instead,

a new significant contact between domain II and the CarDE base is formed (Fig. S1).

The polypeptide surroundings of c-FAD, d-FAD, and e-FAD are essentially conserved compared to those of the EtfAB/Bod system [15]. The most pronounced polypeptide-d-FAD interactions are between ThrD95-N and -OG1 and O2, between Leu183-O and

N3 as well as between ArgE203-NH1 and -NH2 and the N5-C4=O4 group. The invariant ArgE203 (Fig. 3C) stabilizes oxidized FAD characterized by an unprotonated N5 and destabilizes, in particular, d-FADH⁺ containing a protonated N5. The most important polypeptide-e-FAD interactions are between ThrE327-OG1 and N5 as well as between HisE347-ND1 and ArgE310-NH1 and the N1-C2=O group which stabilized an e-FAD⁻ radical anion demonstrated for EtfAB [15].

The Fd-like domain

In contrast to the EtfAB/acyl dehydrogenases structurally characterized yet, the CarCDE complex contains a Fd-like domain carrying two [4Fe-4S] clusters [7]. The Fd-like domain is fused *via* an 11 amino acids long linker at the N-terminal end of CarE. It is located at the outer edges of the Car(CDE)₄ complex (Fig. 3A) and only loosely attached to a loop region prior to the D-arm and the C-terminal end of helix E167 : E178 (Fig. 3C). As the Fd-like domain is partially disordered, model building is not unambiguous. Fortunately, the low-resolution CarCDE-NADH structure (Fig. S2) and the structural relationship to the *Clostridium acidurici* ferredoxin (sequence identity: 40%) supports chain tracing. The two [4Fe-4S] clusters are ligated by four cysteines (Fig. 3C) which are part of the two conserved ferredoxin signature motifs CX₂CX₂CX₂CP. Notably, each motif participates in forming both [4Fe-4S] clusters (Figs 3C and S2). The distance between the two [4Fe-4S] clusters is about 9 Å. The proximal [4Fe-4S] cluster oriented to the CarDE base has the shortest distance to the bifurcating d-FAD of 19 Å which appears to be slightly too long for an efficient ET considering the 14 Å rule [41]. Interestingly, d-FAD and the proximal [4Fe-4S] cluster are bridged by TrpD96. Its aromatic indole ring has an edge-to-edge distance of ca. 7.5 Å to d-FAD and ca. 8.5 Å to the proximal [4Fe-4S] cluster (Fig. 3C). The mobile Fd-like domain can be easily displaced but considerable polypeptide rearrangements are required to adjust a distance between these two redox centers below 16 Å. Due to the short linker length an ET between the [4Fe-4S] clusters and c-FAD or e-FAD can be excluded in the D- and B-states as their distances are minimally 35 Å (Fig. 3B).

Characterization of the CarCDE variants

To explore the function of the Fd-like domain, cysteines 10, 13, 16, 20, 38, 41, 44, and 48 of the proximal and distal [4Fe-4S] clusters were exchanged to alanine

(Figs 3B and S2). Deletion of both [4Fe-4S] clusters results in a nearly complete loss of iron (0.3 ± 0.1 mol Fe per mol enzyme), but stability, subunit composition, overall protein-yield and, surprisingly, the FBEB kinetics were not affected. Subsequently, the entire Fd-like domain of CarE (residue E1-E68) was truncated. Again, stability, subunit composition, and FBEB kinetics of the CarCDE[ΔFd] complex remain unchanged, only the overall yield of the produced enzyme increased two- to threefold.

For investigating the FBEB process, the D-arm (the 32 C-terminal amino acids of CarD) was cut off. The D-arm is a part of domain II which rotates between the e-FAD-c-FAD electron-conducting D and e-FAD-d-FAD electron-conducting B-states (Figs 3B and S1). The D-arm truncation has significant negative influence on stability and yield of the CarCDE complex. Furthermore, the FBEB capability was completely lost because no NADH oxidation was detectable in the presence of caffeoyl-CoA and ferredoxin (Fig. 1). Invariant ArgE203 of CarE (Fig. 3C), whose side chain points to N5 and O4 of the bifurcating d-FAD, was exchanged against alanine, glutamine, or lysine. The resulting CarCDE(R203A, Q and K) complexes remained intact but were FBEB inactive.

Investigations of the CarCDE reaction by artificial/nonphysiological electron donors/acceptors

To further investigate the redox processes and the function of the Fd-like domain, we determined the activities of the CarCDE complex in the presence of several artificial/nonphysiological electron donors or acceptors. The data obtained are summarized in Table 2. In the presence of reduced methylviologen (MV) ($E_0' = -0.45$ V) caffeoyl-CoA could be reduced by CarCDE, CarCDE[ΔFd], and CarCDE[ΔFeS] with a specific activity of 27.5, 26.6, and 19.6 U·mg⁻¹, respectively, and by the variants CarCD[ΔD-arm]E, R203A, R203Q, and R203K with moderately decreased activities of 9–18 U·mg⁻¹. These data suggest that MV reduces c-FAD which subsequently reduces caffeoyl-CoA bound to CarC. No coupling between the low and high electron acceptor sites and no FBEB occurs. The significant decrease in activity of the residue E203 and CarCD[ΔD-arm]E variants might be explained by minor rearrangements of the domain II position relative to the CarC core due to conformational changes at the CarDE interface transmitted to the D-arm and due to its absence, respectively (Figs. 3B and S1).

Next, an FBEB experiment was performed with FAD instead of ferredoxin as low-potential electron

acceptor in the presence of caffeoyl-CoA. Both NADH oxidation and FAD reduction was observable with CarCDE and with CarCDE[ΔFd] the latter with a threefold lower rate. Notably, the NADH reduction rate with FAD is seven times higher than with ferredoxin as electron acceptor presumably due to the higher redox potential of the flavin. Unexpectedly, FMN cannot replace FAD as electron acceptor suggesting a (transient) binding site for FAD but not for FMN. Ferricyanide, like FMN, cannot serve as an electron acceptor despite its suitable redox potential. Using dichlorophenol indophenol as electron acceptor CarCDE and the CarCDE[ΔFd] variant exhibit an activity of 10.5 and 10.3 U·mg⁻¹, respectively, indicating no influence of the Fd-like domain on the catalytic process. Minor activities below 2 U·mg⁻¹ of residue E203 and the CarCD[ΔD-arm]E variants independent of the low-potential electron acceptor argue for the complete suppression of the FBEB process (Table 2).

Discussion

The FBEB mechanism

CarCDE is the first structurally characterized FBEB enzyme complex of an acetogenic bacterium. Its occurrence as a heterododecameric Car(CDE)₄ complex

allows four FBEB reactions which appear to operate independently. On the basis of the structurally detected relative geometry of the prosthetic groups and the substrate-binding sites, a mechanistic scenario could be postulated for the CarCDE reaction (Fig. 4) which is highly related to that of the bifurcating EtfAB/Bod system [15,19]. Accordingly, the electron-bifurcating d-FAD is initially reduced by NADH. In the low-resolution CarCDE structure crystallized in the presence of NADH (Table 1) extra electron density is clearly visible in front of d-FAD which could, however, not be unambiguously interpreted as NADH. Next, the first electron of d-FADH⁻ is transferred along the exergonic branch to c-FAD, which swings to domain II, from the B-state to the D-state and transfers one electron to c-FAD forming c-FADH⁻. In parallel, the remaining strong electron donor d-FADH⁻ donates an electron along the endergonic branch via two [4Fe-4S] clusters of the Fd-like domain to the unknown physiological electron acceptor. Repetition of the FBEB process affords a second reduced ferredoxin and c-FADH⁻ which transfers a hydride to caffeoyl-CoA. The FBEB inactivity in the CarCD(ΔD-arm) E variant substantiates the importance of the D-arm for the (controlled) swinging of domain II from the B- into the D-state and vice versa. It further supports the current hypothesis that NADH binding implicates an

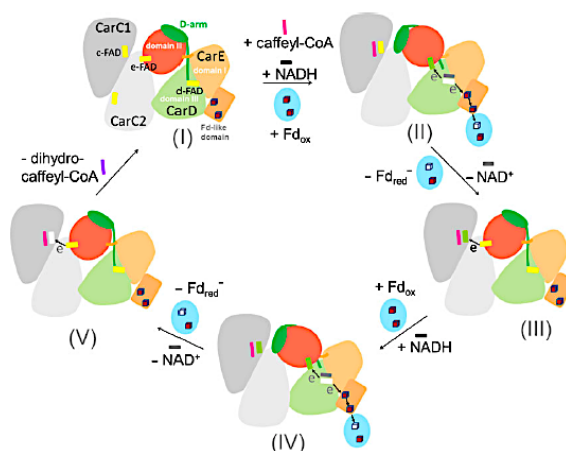


Fig. 4. Mechanism of the FBEB reaction of CarCDE. The reaction starts from the structurally characterized D-state (I) which is considered as the resting state. After NADH binding d-FAD is reduced via hydride transfer (II) and, concomitantly, domain II is rotated from the D-state (I) into the B-state (II). One electron each flows along the exergonic and endergonic branches marked by black arrows. Reduced ferredoxin (Fd_{red}⁻) and NAD⁺ are released and c-FADH⁻ is formed (III). The same FBEB process is repeated (IV + V) and finally dihydrocaffeoyl-CoA produced. The covalent linkers between domains I and II of CarE as well as domain III and the D-arm of CarD are drawn in orange and green, respectively.

outwards displacement of the D-arm anchor relative to the d-FAD-binding site. The resulting pulling force onto domain II *via* the D-arm causes its dissociation from the CarC1C2 interface [19]. The thermodynamically challenging reduction of ferredoxin requires a low d-FAD/d-FADH⁺ redox potential and it was thought that ArgE203, interacting with N5 and O4 of d-FAD, is, in particular, attractive for its adjustment. The complete FBEB inactivity of several ArgE203 variants is consistent with this idea. Moreover, an arginine or lysine in contact with the N5 and O4 atoms of the isoalloxazine ring is found in all structurally known FBEB enzymes such as EtfAB/Bcd [15,19], NADH-dependent reduced ferredoxin : NADP⁺ oxidoreductase [11,13], and heterodisulfide reductase [42].

The low-potential electron acceptor

The physiological low-potential electron acceptor for CarCDE has not been identified yet. Therefore, we analyzed the ET pathway of the endergonic branch and the FBEB reaction with artificial electron acceptors. Kinetic measurements on CarCDE and CarCDE[ΔFd] suggests that the nonphysiological ferredoxin of *C. pasteurianum* does not accept electrons *via* the Fd-like domain but directly from d-FAD because the FBEB activity is neither dependent on the [4Fe-4S] clusters nor on the presence of the Fd-like domain (Fig. 4). There are potential ferredoxin-binding sites sufficiently close to d-FAD; a ferredoxin was modeled into one of these sites in the related EtfAB complex [15]. The applicability of FAD and dichlorophenol indophenol (also bypass the [4Fe-4S] clusters of the Fd-like domain), besides ferredoxin, demonstrate the unspecificity of the low-potential electron acceptor which was also reported for the EtfAB/Bcd system [16,17]. A special FBEB reaction might exist for dichlorophenol indophenol because its reduction proceeds independent on the presence or absence of caffeoyl-CoA. We speculate that dichlorophenol indophenol is able to capture both electrons, one from e-FAD or c-FAD (after the first ET from bifurcating d-FAD) and the second (as ferredoxin) directly from d-FAD.

Nevertheless, electron supply directly from d-FAD might not be feasible if a larger protein complex acts as low-potential electron acceptor and if several workable candidates are present in the cell. Then, specificity becomes necessary and the Fd-like domain as adaptor between the residual CarCDE and, for example, a ferredoxin, a [4Fe-4S] carrying domain of the Rnf complex, or a flavodoxin of *A. woodii* would be plausible. The structural data suggest specific binding to be connected with an engagement process of the Fd-like

domain to conduct electrons along the endergonic branch.

For gaining information about Fd-like domains comparable to that of CarE, we examined the database. Accordingly, CarE of *A. woodii* shows high sequence similarities to EtfA of various Clostridia species (65–76% identity). The vast majority of the most related EtfAB proteins contains a Fd-like domain at the N terminus. A further significant resemblance was found between CarE of *A. woodii* and the family of FixB proteins (28–30% identity) also composed of members with and without a Fd-like domain. FixB proteins are involved in the anaerobic carnitine and amine/polyamine metabolism and presumably also in a FBEB event [43]. Altogether, no significant common features between EtfAB sequences with and without a Fd-like domain and between the metabolisms of the corresponding microorganisms were deducible. The Fd-like domain of CarE (E1–E52) is shared by various enzymes, the most prominent examples being RxB of the RxB complex involved in superoxide sensor SoxR reduction [44] and RnfB of the Rnf complex (41–46% identity). Rnf is involved in ET to nitrogenase, e.g., in *Rhodobacter capsulatus* [45] and in ion-gradient formation in various Clostridia and *A. woodii* [46]. Obviously, this type of Fd-like module is optimized as low-potential electron acceptor for various reactions in diverse organisms.

Acknowledgements

Work in the laboratory of VM was supported by the Deutsche Forschungsgemeinschaft, JKD thanks Rudolf K. Thauer and Hartmut Michel for financial support and KK the International Max Planck Research School for funding. We are grateful to the staff of the SLS, Villigen for help in data collection.

Author contributions

VM and UE designed the research. The enzyme was purified by JB, crystallized by JKD and UD, and its structure determined by JKD as well as refined by JKD, KK, and UE. CÖ and HW heterologously expressed the enzyme and did the mutational analysis. All authors wrote the manuscript.

References

- Herrmann G, Jayamani E, Mai G and Buckel W (2008) Energy conservation via electron-transferring flavoprotein in anaerobic bacteria. *J Bacteriol* **190**, 784–791.

- 2 Li F, Hinderberger J, Seedorf H, Zhang J, Buckel W and Thauer RK (2008) Coupled ferredoxin and crotonyl coenzyme A (CoA) reduction with NADH catalyzed by the butyryl-CoA dehydrogenase/Etf complex from *Clostridium kluyveri*. *J Bacteriol* **190**, 843–850.
- 3 Mitchell P (1975) The protonmotive Q cycle: a general formulation. *FEBS Lett* **59**, 137–139.
- 4 Buckel W, Thauer RK (2013) Energy conservation via electron bifurcating ferredoxin reduction and proton/Na⁺ translocating ferredoxin oxidation. *Biochim Biophys Acta* **1827**, 94–113.
- 5 Thauer RK, Kaster AK, Seedorf H, Buckel W and Hedderich R (2008) Methanogenic archaea: ecologically relevant differences in energy conservation. *Nat Rev Microbiol* **6**, 579–591.
- 6 Peters JW, Miller AF, Jones AK, King PW and Adams MW (2016) Electron bifurcation. *Curr Opin Chem Biol* **31**, 146–152.
- 7 Bertsch J, Parthasarathy A, Buckel W and Müller V (2013) An electron-bifurcating caffeoyl-CoA reductase. *J Biol Chem* **288**, 11304–11311.
- 8 Schuchmann K, Müller V (2012) A bacterial electron-bifurcating hydrogenase. *J Biol Chem* **287**, 31165–31171.
- 9 Wang S, Huang H, Moll J and Thauer RK (2010) NADP⁺ reduction with reduced ferredoxin and NADP⁺ reduction with NADH are coupled via an electron-bifurcating enzyme complex in *Clostridium kluyveri*. *J Bacteriol* **192**, 5115–5123.
- 10 Huang H, Wang S, Moll J and Thauer RK (2012) Electron bifurcation involved in the energy metabolism of the acetogenic bacterium *Moorella thermoacetica* growing on glucose or H₂ plus CO₂. *J Bacteriol* **194**, 3689–3699.
- 11 Demmer JK, Huang H, Wang S, Demmer U, Thauer RK and Ermler U (2015) Insights into flavin-based electron bifurcation via the NADH-dependent reduced ferredoxin:NADP oxidoreductase structure. *J Biol Chem* **290**, 21985–21995.
- 12 Demmer JK, Rupprecht FA, Eisinger ML, Ermler U and Langer JD (2016) Ligand binding and conformational dynamics in a flavin-based electron-bifurcating enzyme complex revealed by hydrogen-deuterium exchange mass spectrometry. *FEBS Lett* **590**, 4472–4479.
- 13 Lubner CE, Jennings DP, Mulder DW, Schut GJ, Zadovnyy OA, Hoben JP, Tokmina-Lukaszewska M, Berry L, Nguyen DM, Lipscomb GL *et al.* (2017) Mechanistic insights into energy conservation by flavin-based electron bifurcation. *Nat Chem Biol* **13**, 655–659.
- 14 el Aboulnaga H, Pinkenburg O, Schiffels J, El-Refai A, Buckel W and Selmer T (2013) Effect of an oxygen-tolerant bifurcating butyryl coenzyme A dehydrogenase/electron-transferring flavoprotein complex from *Clostridium difficile* on butyrate production in *Escherichia coli*. *J Bacteriol* **195**, 3704–3713.
- 15 Chowdhury NP, Mowafy AM, Demmer JK, Upadhyay V, Koelzer S, Jayamani E, Kahnt J, Hornung M, Demmer U, Ermler U *et al.* (2014) Studies on the mechanism of electron bifurcation catalyzed by electron transferring flavoprotein (Etf) and butyryl-CoA dehydrogenase (Bcd) of *Acidaminococcus fermentans*. *J Biol Chem* **289**, 5145–5157.
- 16 Chowdhury NP, Kahnt J and Buckel W (2015) Reduction of ferredoxin or oxygen by flavin-based electron bifurcation in *Megasphaera elsdenii*. *FEBS J* **282**, 3149–3160.
- 17 Chowdhury NP, Klomann K, Seubert A and Buckel W (2016) Reduction of flavodoxin by electron bifurcation and sodium ion-dependent reoxidation by NAD⁺ catalyzed by ferredoxin-NAD⁺ reductase (Rnf). *J Biol Chem* **291**, 11993–12002.
- 18 Jeong J, Bertsch J, Hess V, Choi S, Choi IG, Chang IS and Müller V (2015) Energy conservation model based on genomic and experimental analyses of a carbon monoxide-utilizing, butyrate-forming Acetogen, *Eubacterium limosum* K1ST612. *Appl Environ Microbiol* **81**, 4782–4790.
- 19 Demmer JK, Pal Chowdhury N, Selmer T, Ermler U and Buckel W (2017) The semiquinone swing in the bifurcating electron transferring flavoprotein/butyryl-CoA dehydrogenase complex from *Clostridium difficile*. *Nat Commun* **8**, 1577.
- 20 Heise R, Müller V and Gottschalk G (1992) Presence of a sodium-translocating ATPase in membrane vesicles of the homoacetogenic bacterium *Acetobacterium woodii*. *Eur J Biochem* **206**, 553–557.
- 21 Heise R, Müller V and Gottschalk G (1989) Sodium dependence of acetate formation by the acetogenic bacterium *Acetobacterium woodii*. *J Bacteriol* **171**, 5473–5478.
- 22 Akhtar MK, Jones PR (2008) Deletion of *iscR* stimulates recombinant clostridial Fe-Fe hydrogenase activity and H₂-accumulation in *Escherichia coli* BL21 (DE3). *Appl Microbiol Biotechnol* **78**, 853–862.
- 23 Bradford MM (1976) A rapid and sensitive method for the quantitation of microgram quantities of protein utilizing the principle of protein-dye binding. *Anal Biochem* **72**, 248–254.
- 24 Fish WW (1988) Rapid colorimetric micromethod for the quantitation of complexed iron in biological samples. *Methods Enzymol* **158**, 357–364.
- 25 Beinert H (1983) Semi-micro methods for analysis of labile sulfide and of labile sulfide plus sulfane sulfur in unusually stable iron-sulfur proteins. *Anal Biochem* **131**, 373–378.
- 26 Hess V, Vitt S and Müller V (2011) A caffeoyl-coenzyme A synthetase initiates caffeate activation prior to caffeate reduction in the acetogenic bacterium *Acetobacterium woodii*. *J Bacteriol* **193**, 971–978.

- 27 Schönheit P, Wascher C and Thauer RK (1978) A rapid procedure for the purification of ferredoxin from Clostridia using polyethyleneimine. *FEBS Lett* **89**, 219–222.
- 28 Kabsch W (2010) Xds. *Acta Crystallogr D Biol Crystallogr* **66**, 125–132.
- 29 Strong M, Sawaya MR, Wang S, Phillips M, Cascio D and Eisenberg D (2006) Toward the structural genomics of complexes: crystal structure of a PE/PPE protein complex from *Mycobacterium tuberculosis*. *Proc Natl Acad Sci USA* **103**, 8060–8065.
- 30 McCoy AJ, Grosse-Kunstleve RW, Adams PD, Winn MD, Storoni LC and Read RJ (2007) Phaser crystallographic software. *J Appl Crystallogr* **40**, 658–674.
- 31 Emsley P, Cowtan K (2004) Coot: model-building tools for molecular graphics. *Acta Crystallogr D Biol Crystallogr* **60**, 2126–2132.
- 32 Murshudov GN, Vagin AA and Dodson EJ (1997) Refinement of macromolecular structures by the maximum-likelihood method. *Acta Crystallogr D Biol Crystallogr* **53**, 240–255.
- 33 Adams PD, Afonine PV, Bunkoczi G, Chen VB, Davis IW, Echols N, Headd JJ, Hung LW, Kapral GJ, Grosse-Kunstleve RW *et al.* (2010) PHENIX: a comprehensive Python-based system for macromolecular structure solution. *Acta Crystallogr D Biol Crystallogr* **66**, 213–221.
- 34 Schneider TR, Sheldrick GM (2002) Substructure solution with SHELXD. *Acta Crystallogr D Biol Crystallogr* **58**, 1772–1779.
- 35 Kim JJ, Wang M and Paschke R (1993) Crystal structures of medium-chain acyl-CoA dehydrogenase from pig liver mitochondria with and without substrate. *Proc Natl Acad Sci USA* **90**, 7523–7527.
- 36 Roberts DL, Frerman FE and Kim JJ (1996) Three-dimensional structure of human electron transfer flavoprotein to 2.1-Å resolution. *Proc Natl Acad Sci USA* **93**, 14355–14360.
- 37 Roberts DL, Salazar D, Fulmer JP, Frerman FE and Kim JJ (1999) Crystal structure of *Paracoccus denitrificans* electron transfer flavoprotein: structural and electrostatic analysis of a conserved flavin binding domain. *Biochemistry* **38**, 1977–1989.
- 38 Toogood HS, van Thiel A, Basran J, Sutcliffe MJ, Scrutton NS and Leys D (2004) Extensive domain motion and electron transfer in the human electron transferring flavoprotein/medium chain Acyl-CoA dehydrogenase complex. *J Biol Chem* **279**, 32904–32912.
- 39 Leys D, Basran J, Talfournier F, Sutcliffe MJ and Scrutton NS (2003) Extensive conformational sampling in a ternary electron transfer complex. *Nat Struct Biol* **10**, 219–225.
- 40 Toogood HS, Leys D and Scrutton NS (2007) Dynamics driving function: new insights from electron transferring flavoproteins and partner complexes. *FEBS J* **274**, 5481–5504.
- 41 Page CC, Moser CC and Dutton PL (2003) Mechanism for electron transfer within and between proteins. *Curr Opin Chem Biol* **7**, 551–556.
- 42 Wagner T, Koch J, Ermler U and Shima S (2017) Methanogenic heterodisulfide reductase (HdrABC-MvhAGD) uses two noncubane [4Fe-4S] clusters for reduction. *Science* **357**, 699–703.
- 43 Ledbetter RN, Garcia Costas AM, Lubner CE, Mulder DW, Tokmina-Lukaszewska M, Artz JH, Patterson A, Magnuson TS, Jay ZJ, Duan HD *et al.* (2017) The electron bifurcating FixABCX protein complex from *Azotobacter vinelandii*: generation of low-potential reducing equivalents for nitrogenase catalysis. *Biochemistry* **56**, 4177–4190.
- 44 Koo MS, Lee JH, Rah SY, Yeo WS, Lee JW, Lee KL, Koh YS, Kang SO and Roe JH (2003) A reducing system of the superoxide sensor SoxR in *Escherichia coli*. *EMBO J* **22**, 2614–2622.
- 45 Saeki K, Kumagai H (1998) The rnf gene products in *Rhodobacter capsulatus* play an essential role in nitrogen fixation during anaerobic DMSO-dependent growth in the dark. *Arch Microbiol* **169**, 464–467.
- 46 Biegel E, Schmidt S, Gonzalez JM and Müller V (2011) Biochemistry, evolution and physiological function of the Rnf complex, a novel ion-motive electron transport complex in prokaryotes. *Cell Mol Life Sci* **68**, 613–634.
- 47 Biegel E, Müller V (2010) Bacterial Na⁺-translocating ferredoxin:NAD⁺ oxidoreductase. *Proc Natl Acad Sci USA* **107**, 18138–18142.
- 48 Schlegel K, Welte C, Deppenmeier U and Müller V (2012) Electron transport during acetoclastic methanogenesis by *Methanosarcina acetivorans* involves a sodium-translocating Rnf complex. *FEBS J* **279**, 4444–4452.
- 49 Hess V, Gonzalez JM, Parthasarathy A, Buckel W and Müller V (2013) Caffeate respiration in the acetogenic bacterium *Acetobacterium woodii*: a coenzyme A loop saves energy for caffeate activation. *Appl Environ Microbiol* **79**, 1942–1947.

Supporting information

Additional Supporting Information may be found online in the supporting information tab for this article:

Fig. S1. Cartoon representation of the B-state of CarCDE.

Fig. S2. Anomalous F⁺-F⁻ electron density around the two [4Fe-4S] clusters.

Table S1. Applied primers for site-directed mutagenesis.

XI. Acknowledgements

Throughout the work presented in this dissertation, I have received a great deal of support and help and I would like to take this opportunity to express my heartfelt gratitude.

Firstly, I would like to thank my supervisor **PD Dr. Ulrich Ermler**, from the bottom of my heart for accepting me in his group, giving me the great opportunity to work on these projects and for his constant support and encouragement during all these years.

I am grateful to **Prof. Dr. Dr. hc Hartmut Michel** and the IMPRS-MPIBP for uninterrupted funding of my research over the years. I am grateful for all the facilities and resources provided in the department for my successful Ph.D. work.

I would like to especially thank my university supervisor and collaborator, **Prof. Dr. Volker Müller** for the project and kind encouragement throughout my Ph.D. work.

I feel very fortunate to have collaborators like, **Prof. Dr. Christiane Dahl** from Bonn University, **Prof. Dr. Matthias Boll** from Freiburg University, and **Prof. Dr. Wolfgang Buckel** from Marburg University, and to get the opportunity to work on very interesting projects.

Many thanks go to **Dr. Janet Vonck** and **Deryck Mills**, who have taught and encouraged me in my initial days of cryo-EM.

A very special thanks to **Dr. Hao Xie** for supporting me in lab experiments and **Dr. Yongchan Lee** for teaching me a great deal of cryo-EM data processing.

I also thank **Ulrike Demmer** from our lab for teaching and helping with anaerobic crystallization experiments and for many other important inputs throughout these years.

XI. Acknowledgements

I really appreciate the never-ending support of **Dr. Sonja Welsch**, **Simone Prinz**, **Mark Linder** and **Dr. Susann Kaltwasser** in the central EM facility, even on weekends.

My most sincere acknowledgements are extended to **Dr. Steffen Brünle** and **Dr. Sandra Zakrzewska** for all the immense help, support and care, both scientifically and personally.

Many thanks to all the co-authors of our publications, for all their brilliant scientific inputs.

It goes without saying that the affection and support I received from my friends here in Frankfurt and in India over the past 5 years, has definitely played a very important part in helping me reach up to this point. The outings, trips, lunches, dinners and celebrations made my time in Frankfurt so memorable and joyous.

Lastly, I express my love and gratitude towards my amazing family who has encouraged me, since childhood to be in science and to always perform better in every step of life. My greatest thanks to my father, mother and brother, who taught me to not only work harder and be dedicated towards my field but also to have patience and be kind and humble. (Even though you all are thousands of kilometers away, you still inspire me to achieve new heights.)

I dedicate this thesis to my grandparents, who loved me unconditionally.

XII. Curriculum vitae

KANWAL KAYASTHA

Address: Altenhöferallee 30/ 1.02.010, 60438,
Frankfurt am Main

Date of birth: January 5th, 1992

Place of birth: Varanasi, India

Nationality: Indian

E-mail address: kanwalkayastha@gmail.com

Phone number: 017683016584



EDUCATION

From 07/2016 **Ph.D. researcher**
Max Planck Institute of Biophysics, Frankfurt am Main, Germany
Department of Molecular Membrane Biology
Supervisor: PD Dr. Ulrich Ermler
Dissertation: Structural insights on redox enzymes of anaerobic aromatic degradation and flavin-based electron bifurcation

08/2013 – 06/2015 **Master of Science, M.Sc. in Biochemistry**
Banaras Hindu University, Varanasi, India
Department of Biochemistry
Supervisor: Prof. Pramod Kumar Srivastava
Dissertation 1: Immunogenic Cell Death (ICD): A vaccination for Cancer
Supervisor: Prof. Sukh Mahendra Singh
Dissertation 2: *In vitro* action of cisplatin on macrophage activation and function. Dalton's lymphoma, its treatment with anti-cancer drug and its effect on Macrophages

08/2010 – 06/2013 **Bachelor of Science, B.Sc. (Hons.)** in Zoology
Banaras Hindu University, Varanasi, India
Department of Zoology

PROFESSIONAL EXPERIENCE

- From 10/2020 Collaborative work on “Structure determination of a Phthalate degrading protein, Phthaloyl-CoA decarboxylase (Pcd) in free and different substrates-bound states”
Publication: **Kayastha K[#]**, Geiger RA[#], Ermler U, Boll M. Enzymatic decarboxylation by phthaloyl-CoA decarboxylase (manuscript in preparation)
- 18/02/2021 Review article: Flavins in the electron bifurcation process, **Kayastha K.**, Vitt S., Buckel W., Ermler U., Archives of Biochemistry and Biophysics (2021), doi: 10.1016/j.abb.2021.108796.
- From 09/2019 Member of High-Performance Computing (HPC) cluster at Max Planck Computing and Data Facility, Garching, Germany
- 02/2018 – 11/2020 Collaborative work on “Structure determination of flavin-based electron bifurcating/confurcating protein complex, Lactate dehydrogenase/ Electron transferring Flavoprotein AB (Ldh/EtfAB) in D-state”
Publication: **Kayastha K[#]**, Katsyv A[#], Himmrichs C, Ermler U, Müller V. Electron Microscopy structure of the flavin-based electron-confurcating Ldh-EtfAB complex from *A. woodii* (manuscript in preparation)
- 05/2018 – 08/2018 Collaborative work on “Structure determination of anaerobic protein, 2-Naphthoyl-CoA reductase in apo- and substrate-bound states”
Publication: Willistein M, Bechtel DF, Müller CS, Demmer U, Heimann L, **Kayastha K**, Schünemann V, Pierik AJ, Ullmann GM, Ermler U, Boll M. Low potential enzymatic hydride transfer via highly

- cooperative and inversely functionalized flavin cofactors. Nat Commun. 2019 May 6;10(1):2074.
- 06/2018 Organized and coordinated the 1st joint PhD Student Retreat of the Max Planck Institute of Biophysics and International Max Planck Research School (IMPRS) for 30 students including 6 invited speakers, Hamburg, Germany
- 07/2017 – 11/2017 Collaborative work on “Structure determination of anaerobic flavin-based electron-bifurcating protein complex, caffeoyl-CoA reductase”
Publication: Demmer JK, Bertsch J, Öppinger C, Wohlers H, **Kayastha K**, Demmer U, Ermler U, Müller V. Molecular basis of the flavin-based electron-bifurcating caffeoyl-CoA reductase reaction. FEBS Lett. 2018 Feb;592(3):332-342.
- 10/2016 – 02/2017 Collaborative work on “Structure determination of anaerobic protein, HdrA-like subunit from *Hyphomicrobium denitrificans*”
Publication: Corvin Ernst^{1#}, **Kanwal Kayastha^{2#}**, Tobias Koch^{1§}, Sofia S. Venceslau³, Inês A. C. Pereira³, Ulrike Demmer², Ulrich Ermler² and Christiane Dahl^{1*}. Structural and spectroscopic characterization of a HdrA-like subunit from *Hyphomicrobium denitrificans*. FEBS J. 2020 Aug 4. doi: 10.1111/febs.15505.
- 05/2015 – 07/2015 Summer Training on Platelet as model for various Neurodegenerative disorders
- 05/2012 – 06/2012 Summer Training on Blood Culturing and karyotyping
- 10/2010 NIUS Training program of HBCSE by TIFR

FELLOWSHIP

- 06/2017 – 12/2019 Member of International Max Planck Research School (IMPRS) on Structure and Function of Biological Membranes

CONFERENCES AND WORKSHOPS

- 04/2021 NYSBC-NCCAT Tomography short course with hands-on practical (3 days)
- 03/2021 S2C2 cryo-EM sample preparation and data collection workshop (2 days)
- 06/2020 S2C2 cryo-EM image processing workshop (3 days)
- 03/2020 S2C2 cryo-EM specimen preparation and data collection (3 days)
- 12/2019 Cinema4D workshop for making molecular movies
- 03/2019 Symposium “Protein Folding, Aggregation and Diseases”, Goethe University, Frankfurt
- 03/2019 EUFEPS Annual Meeting 2019 Personalized medicines, Targeted therapies, Precision, drug delivery
- 09/2018 Summer School of Chemical Biology, Hirschegg, Austria
- 11/2017 GE Äkta purification system training, Munich
- 09/2017 Conference on “New horizons in membrane transport and communication”, Goethe University, Frankfurt
- 07/2017 Workshop on Project Management in Biotech Industries, SFB 807, TRAM, Goethe University, Frankfurt
- 06/2017 6th International School on Biological Crystallisation, Granada, Spain
- 12/2016 Advanced training seminar for biological security, Max Planck Institute of Biochemistry, Martinsried, Munich
- 11/2016 Advanced Biotechnologies workshop in cooperation with Malvern, MPI-BP, Frankfurt
- 09/2016 Visions in Science, Max-Planck-Gesellschaft, Berlin
- 09/2016 2nd Max Planck Career Fair, Max-Planck-Gesellschaft, Berlin

LANGUAGES

Hindi (native), English (fluent), German (beginner)

Note: # refers to co-first authorships in publications.